UNIVERSITY OF SOUTHAMPTON

Partial Discharge Signal Propagation, Modelling and Estimation in High Voltage Transformer Windings

by

Ramizi Mohamed

A thesis submitted for the degree of
Doctor of Philosophy

in the
School of Electronics and Computer Science

September 2010

UNIVERSITY OF SOUTHAMPTON

ABSTRACT

SCHOOL OF ELECTRONICS AND COMPUTER SCIENCE

Doctor of Philosophy

by Ramizi Mohamed

The thesis concerns partial discharge (PD) propagation within a high voltage transformer winding. Location of PDs and magnitude estimation are important tools for both diagnosis and prognosis of the health of large transformers. In reality there is limited access and knowledge of a winding and consequently any practical method requires the use of estimation techniques. The approach taken in this thesis is by considering lumped circuit parameter models. Firstly, a lumped capacitive parameter model was considered and secondly a transmission line lumped parameter approach developed. A technique of split winding analysis is introduced for both types of model. The derivation of the capacitive network considers the source location of a PD by defining the PD signal propagation in two directions. At the source, the currents are equal in magnitude and are attenuated as they flow in each direction. This provides information for a fixed distribution model equation. Under transmission line lumped parameter models, split winding analysis explains the development of accumulated harmonic waveforms of the PD propagation signal towards the neutral and bushing tap-point. At the source, a D'Alembert solution is employed to estimate the oscillation level and found to be in very good agreement with measured data using rectangular wave signal injection. PD signal behaviour is then considered using a time varying boundary conditions model with a principle of superposition equation of source signal. Duhamel's principle is employed to find a solution for any waveform applied to some point on the transformer winding. Under the influence of losses and distortion, an accumulated harmonic amplitude analysis from the Duhamel's principle estimates the PD propagation level. For different injection points along the transformer winding, the measured PD level at the neutral and bushing tap point caused by the accumulated harmonic amplitude reveals different patterns. As the PD injection point is altered from the bushing tap point to the neutral, the measured signals significantly change. This in turn contains information of the level of discharge signal at the source. From this analysis a technique based on minimum mean error (MME) calculation using the measurements at the bushing tap and neutral points can be used to identify the source location of PDs based on the analysis of accumulated harmonic amplitudes. With a known location, the information can then be used to estimate PD levels. As the actual charge transferred at the location

of a partial discharge cannot be measured directly, by using the D'Alembert solution, the PD source level is found to have approximately twice the apparent magnitude. By using the predominantly capacitive model derived based on split current propagation, PD estimation at higher frequencies is also possible. As a result, an estimation of PD level can be estimated for measurement signals having bandwidth of up to 150MHz.

Contents

List of Figures

List of Tables

List of Symbols

A,B,C,D,$\mathfrak{A}$,$\mathfrak{B}$	Arbitrary Constants
$\mathbf{A}$,$\mathbf{B}$,$\mathbf{C}$,$\mathbf{D}$	State matrices
An,Bn	Arbitrary constants towards Neutral
A_{isn}	Harmonic current amplitude towards neutral
$\widehat{A_{isn}}$	Harmonic current amplification factor towards neutral
A_{isb}	Harmonic current amplitude towards bushing
$\widehat{A_{isb}}$	Harmonic current amplification factor towards bushing
$A(\mathfrak{s})$	Complex transfer function: Numerator
A_s, A_{sb}, A_{sn}	Amplification factor @ gain parameter
$\boldsymbol{a}$	Unknown parameters
$\boldsymbol{a_{new}}$	Updated parameters
a_k	Set of parameters
$\boldsymbol{a_{cur}}$,$\boldsymbol{a_{min}}$	Current parameters and Minimum parameters respectively
$B(\mathfrak{s})$	Complex transfer function: Denominator
a_m, a_n	Poles coefficients
$\bar{a}_n$	Poles initial coefficients
C_B	Bushing capacitance
C_b	Series Capacitance near Bushing
C_N	Neutral capacitance
C_g, $C_g dx$	Inter-turn Capacitance @ Shunt Capacitance to Ground
C_{gr}	Resultant Inter-turn Capacitance
C_r	Resultant Series Capacitance
c	Constant variable
c_m, c_n, $\tilde{c}_n$	Residues coefficients
$c_n(t)$, $c_1(t)$	IMF signal
$\boldsymbol{D}$,$\boldsymbol{d}$	Set of matrix
$\overline{D}$	Mean winding diameter
E, a, b	Arbitrary constants
E_{sb}, F_{sb}, G_{sb}, H_{sb}	Arbitrary constants
E_{sn}, F_{sn}, G_{sn}, H_{sn}	Arbitrary constants
E_x	Intermediary sections of the windings
$F_f(x,t)$	Response to a linear system

$f(\mathfrak{s})$	Polynomial transfer function
f_C	Corner frequency
f_L	Lower frequency
f_U	Upper frequency
$\hat{f}_b(l,t)$	Step Response Function measured at Bushing
$\hat{f}_n(0,t)$	Step Response Function measured at Neutral
$G(\mathfrak{s})$	Complex transfer function
G_{dx}	Shunt conductance
$\mathcal{G}_{\mathfrak{s}}$	System gain
g	Shunt Conductance
g_{dx}	Shunt resistance per winding length
$H(\mathfrak{s})$, $h(\mathfrak{s})$	Transfer function in Laplace domain
$\lvert H(\omega)\rvert$	Voltage gain in dB @ Complex frequency response
h	Height of copper conductor
h_{1k}	Decomposed signal after k shifting process
$h_1(t)$, $h_{1k}(t)$	Time domain decomposed signal
$h(n)$	Impulse Response of recursive filter
$h(t)$	Time domain decay function
$\mathbf{I}$	Identity matrix
I	Current
I_B, I_N	Current at Bushing and Neutral respectively
$\widetilde{I_B}$, $\widetilde{I_N}$	Estimated current at bushing and neutral respectively
I_{Boff}, I_{Noff}	Current offset at bushing and neutral respectively
$i_b(x)$, $i_n(x)$	Current solution towards bushing and neutral respectively
i_c, i_C	Current flowing in shunt capacitance to ground
i_k, i_K	Current flowing in series capacitance
i_{kb}	Transmitted Current in the direction towards bushing
i_{kn}	Transmitted Current in the direction towards neutral
i_L	Current flowing in the inductor
i_n	Current towards Neutral
i''	Transmitted current
$\mathcal{J}$	Number of set of errors
K	Inter-section Capacitance or Series Capacitance along windings
K_b	Shunt Capacitance near Bushing
K_r	Resultant Inter-section Capacitance
k	Position of disc pairs @ arbitrary constant
$\mathcal{K}$, N	Number of sectional windings or disc pairs ($\mathfrak{y} = 1, 2, \ldots, K$)
k_t	Constant gradient of voltage distribution at time t
L, L_{dx}	Inductance and inductance per unit length respectively
L_0	Effective inductance from ground
l	Total length of winding

M	Mutual Inductance
ME, $\overline{ME}$	Mean error
MME	Minimum mean error
$\mathcal{M}$, $\mathcal{N}$	Matrix size
m_t	Constant gradient due to end plate
m_1, m_{1k}	Mean envelope
n	Turns in each section
$\mathfrak{n}$	Number of frequency points
$P_j(\mathfrak{s})$	Poles Laplace operator
p	Termination impedance value
Q	Apparent charge
q	Width of stack
R	Equivalent shunt resistances
$\mathfrak{R}$, $\mathfrak{r}$	Order of poles and zeros
r_{dx}	Series resistance per winding length
$r_n(t)$	Residual signal
$\hat{r}$	Radial diameter or depth of disc
SD_k	Cauchy convergence process
S_{min}	Stopage criteria
s	Harmonic order
s_o	Odd harmonic
$\mathfrak{s}$	Laplace operator
T, t	Time operator
t_d	Time delay
$U(j\omega)$	A unit input response in frequency domain
$\mathbf{u}$	State input
$u(n)$	Input Response with sample n
V_B, $V_B(t)$	Voltage level at Bushing
V_N, $V_N(t)$	Voltage level at Neutral
V_{sec}	Voltage per-section
$V(t)$	Time domain travelling wave
V, a, b	Arbitrary constants
v	Voltage along transformer windings
v_b, $v_b(x)$	Voltage in the direction towards bushing
v_n, $v_n(x)$	Voltage in the direction towards neutral
v'	Reflected wave
v''	Transmitted wave @ voltage
$v(n)$	Output Response with sample n
x	Distance along transformer winding
$\mathbf{x}$	State space
$\breve{x}$	Unknown solution matrix

x_b	$x - x'$
x_b	$\frac{x}{x'} - 1$
x'	Distance of source signal from Neutral
$x(t)$	Time domain summation of all signals
$\dot{x}$	Time derivative state
$Y(\mathfrak{s})$	Complex transfer function
y	Distance along the stack
$y(n)$	Zero Phase output response
$\mathfrak{y}$	Matrix notation of position of sectional windings
$\mathfrak{y}'$	Position of the source at $\mathfrak{y}^{th}$ disc pairs
Z_b, $Z_b(p)$	Termination impedance at Bushing
$Z_i(\mathfrak{s})$	Zeros Laplace operator
Z_n, $Z_n(p)$	Termination impedance at Neutral
Z_s,Z_{sb},Z_{sn}	Surge Impedance
Z_1, Z_2	Characteristic Impedances
$Z(p)$	Impedance between End Terminal and Ground
z_m	Zeros
Φ	Electromagnetic Flux associated with Current i''
Ψ	Electrostatic Flux associated with Voltage v''
α	Initial Distribution constant
α_B	Estimated α at bushing
α_N	Estimated α at neutral
α_b	Initial Distribution constant near Bushing
α_{beff}	Effective α towards bushing
α_{neff}	Effective α towards neutral
α_{bep}	α near End Plat at Bushing
α_{nep}	α near End Plat at Neutral
α_{eff}	Effective initial distribution constant
β	Final distribution constant
γ_s	Decay factor @ decay component
$\delta\boldsymbol{a}$	Small change of unknown parameters
δ_{al}	Steepest descent formula
δ_d	Spacer between disc
δ_t	Thickness of inter-turn insulation
$\delta(t)$	Dirac Delta function
δt	Change of time
ϵ_B	Current error at Bushing
ϵ_N	Current error at Neutral
$\overline{\epsilon_{BN}}$	Mean error of bushing and neutral terminals
$\widehat{\epsilon_B}$, $\widehat{\epsilon_N}$, $\widehat{\epsilon_{BN}}$	Matrices of errors
ζ_b, ζ_n	Half range sine cosine series function

η_k,η_l	Convergence first derivative
θ_b, θ_n	Phase Angle towards Bushing and Neutral respectively
κ	Number of non-adjacent parallel conductors
λ	Learning rate
μ, ν	Characteristic impedance equations
ξ	Damping ratio
ρ	Differential operator $\frac{\partial}{\partial t}$
σ	Standard deviation
$\sigma(\mathfrak{s})$	Rational transfer function
τ	Pulse width @ time delay operator
$\phi(w)$	Phase angle
$\phi - q - n$	Phase - Charge amplitude @ magnitude - Number
$\phi - \frac{x}{l} - n$	Phase - Ratio of distance from neutral - Number
χ^2	Chi Square function
$\psi_b(x,t)$, $\psi_n(x,t)$	Fixed distribution plus harmonic decay function
w_i, w_n	Break frequencies
$w(t)$	Time-varying Non-homogeneous input to a system
$w_{t=0}(t)$	Time-varying Non-homogeneous input, zero initial condition
ω_r	Resonance frequency
ω_{sb}, ω_{sn}	Harmonic frequency towards bushing and neutral respectively
$\omega_{x'}$	Harmonic frequency of source signal at x'
$\omega_{x'b}$	Harmonic frequency of source signal towards bushing
$\omega_{x'n}$	Harmonic frequency of source signal towards neutral
$F(x,t)$, $F(x',t)$	D'Alembert function
ε_d	Permttivity of oil
ε_t	Resultant of inter-turn permittivity (oil+solid)
φ_b, $\varphi_b(x)$, φ_n, $\varphi_n(x)$	Fixed distribution function
$\varphi_b(x,t)$, $\varphi_n(x,t)$	Time domain fixed distribution function
ϱ	Number of oil ducts
ϑ_{jj},ϑ_{jk},ϑ_{kl},ϑ_{ll}	Convergence second derivative @ Hessian matrix
$\forall\omega$	For all frequencies

Abbreviations

ANN	Artificial Neural Network
B	Bushing Terminal
CT	Current Transformer
DGA	Disolved Gas Analysis
DSO	Digital Signal Oscilloscope
EMD	Empirical Mode Decomposition
EMTP	Electromagnetic Transient Program
EP	End Plate
EWN	Evolving Wavelet Network
FFT	Fast Fourier Transform
FLVQ	Fuzzy Learning Vector Quantization
FRA	Frequency Response Analysis
GA	Genetic Algorithm
GIS	Gas Insulated System
HFCT	High Frequency Current Transformer
HHT	Hilbert Huang Transform
HPLC	High Performance Liquid Chromatography
HVDC	High Voltage Direct Current
IBVP	Initial Boundary Value Problem
IFFT	Inverse Fast Fourier Transform
IMF	Intrinsic Mode Functions
I/O SNR	Input Output Signal to Noise Ratio
KCL	Kirchoff's Current Law
KVL	Kirchoff's Voltage Law
LC	Inductance and Series Capacitance
LCK	Inductance, Series Capacitance and Shunt Capacitance
LDPE	Low-density polyethylene
LOG-LSE	Logarithmic Least Square Estimation
LVQ	Learning Vector Quantization
MAS	Multi Agent System
MBPE	Model Based Parameter Estimation
ME	Mean Error

MIMO	Multi Input Multi Output
MLE	Maximum Likelihood Estimation
MME	Minimum Mean Error
MMF	Magnetomotive Force
MSE	Mean Square Error
MTL	Multiconductor Transmission Lines
N	Neutral Terminal
NLS	Nonlinear Least Square
NLSE	Non-Linear Least Square Estimation
PD	Partial Discharge
PDE	Partial Differential Equation
PIQN	$\phi - q - n$
PSD	Power Spectrum Density
RFCT	Radio Frequency Current Transformer
RLC	Resistance, Inductance and Capacitance
RLCM	Resistance, Inductance, Capacitance and Mutual Inductance
SISO	Single Input Single Output
SNR	Signal to Noise Ratio
SP	Static Plate (also sometime known as EP)
SVD	Singular Value Decomposition
SWTF	Sectional Winding Transfer Function
TFA	Transfer Function Adjustment
UHF	Ultra High Frequency
ZPR	Zero, Poles and Residue

Declaration of Authorship

I, Ramizi Mohamed, declare that this thesis and the work presented in it are my own and has been generated by me as the result of my own original research.

"Partial Discharge Signal Propagation, Modelling and Estimation in High Voltage Transformer Windings"

and the work presented in it are my own. I confirm that:

1. This work was done wholly or mainly while in candidature for a research degree at this University;
2. Where any part of this thesis has previously been submitted for a degree or any other qualification at this University or any institution, this has been clearly stated;
3. Where I have consulted the published work of others, this is always clearly attributed;
4. Where I have quoted from the work of others, the source is always given. With the exception of such quotations, this thesis is entirely my own work;
5. I have acknowledged all main sources of help;
6. Where the thesis is based on work done by myself jointly with others, I have made clear exactly what was done by others and what I have contributed myself;
7. Parts of this work have been published as:

i. Mohamed, R. and Lewin, P. L., "Frequency Domain Modeling of High Voltage Transformers Using a Nonlinear Least-Square Estimation Technique," *16th International Symposium on High Voltage Engineering*, 24-28 August 2009, Cape Town, South Africa. pp. 297-302.

ii. Mohamed, R., Lewin, P. L. and Chen, G., "Partial Discharge Estimation in a High Voltage Transformer Using a Multi Signal Decomposition Technique," *The 9th International Conference on Properties and Applications of Dielectric Materials*, 19 - 23 July 2009, Harbin, China. pp. 425-428.

iii. Mohamed, R. and Lewin, P. L., "Partial Discharge Location in High Voltage Transformers," *IEEE Electrical Insulation Conference*, 31 May - 3 June 2009, Montreal, Canada. pp. 200-204.

iv. Mohamed, R., Markovsky, I. and Lewin, P. L., "Modeling and Parameter Estimation of High Voltage Transformer Using Rational Transfer Function State Space Approach," *IEEE 2008 Conference on Electrical Insulation and Dielectric Phenomena*, 26-29 October 2008, Quebec City, Quebec, Canada. pp. 467-470.

Signed:

Date:

Acknowledgements

First and foremost thanks to Allah s.w.t for his greatness, the most beneficient and the most merciful. I bare witness that there is no God but Allah, and Muhammad is the messengger of Allah. From him we came and to him we return. He has given me the deen, the iman and the health for me to complete the thesis and research investigation within his knowledge. My special gratitude goes to my supervisor, Professor Paul. L. Lewin. His wise supervision, support and kindness through the years has been invaluable. My thanks also to the University of Southampton and Tony Davies High Voltage Laboratory for giving me the opportunity to perform this research. Of course none of this could have been possible without the Universiti Kebangsaan Malaysia and the Malaysian Government who sponsored me throughout my time studying. Last but not least, thanks to my family, my dearest wife, Umi Kalsum Mat Noh, my lovely two daughters, Nur Farhah and Nurul Huda, and my little boy, Ahmad Azamuddin. You are the sun of my life during the day and the moon in my eyes while at night. No words describe the patience, encouragement, support and love that you have given me over the past years.

"To the readers, value the moment of your life while reading this thesis"

Chapter 1

Introduction

Transformers are important components of interconnected power systems. The design life of power transformers is usually between 20 to 35 years. In practice, with appropriate maintenance, the life of power transformers can be up to 60 years. As transformers age, the internal conditions degrade, which increases the risk of failure. Failure can occur due to external conditions triggered by extreme events like lightning strikes, switching surges or short circuits. The insulation and structure of transformers are designed to withstand such severe conditions. However as the transformer ages, insulation material degradation may reduce the withstand capability for transient overvoltages or short circuit faults.

Before a transformer reaches the point of failure, appropriate monitoring techniques are important issues. Historically, maintenance was based on a regular schedule. However, due to high costs, regular maintenance is increasingly being replaced by condition based maintenance. Therefore, reliable techniques for condition monitoring becomes an important tool to provide diagnosis of the health of a transformer and ultimately may inform assessment of future life.

1.1 Problem Statements

Partial discharge (PD) in power transformers is one of the main indicators of insulation degradation. There are many techniques for monitoring partial discharge activity in high voltage transformers such as electrical methods, acoustic methods and chemical methods. However, this research focuses on the electrical methods using radio frequency current transformers (RFCT) as sensors to measure the PDs.

Experimentally the RFCTs are located at the terminal ends of the power transformer windings, that is the high voltage bushing tap point, low voltage bushing tap point and neutral to ground connections. With reference to Figure 1.1, PD signals are generated

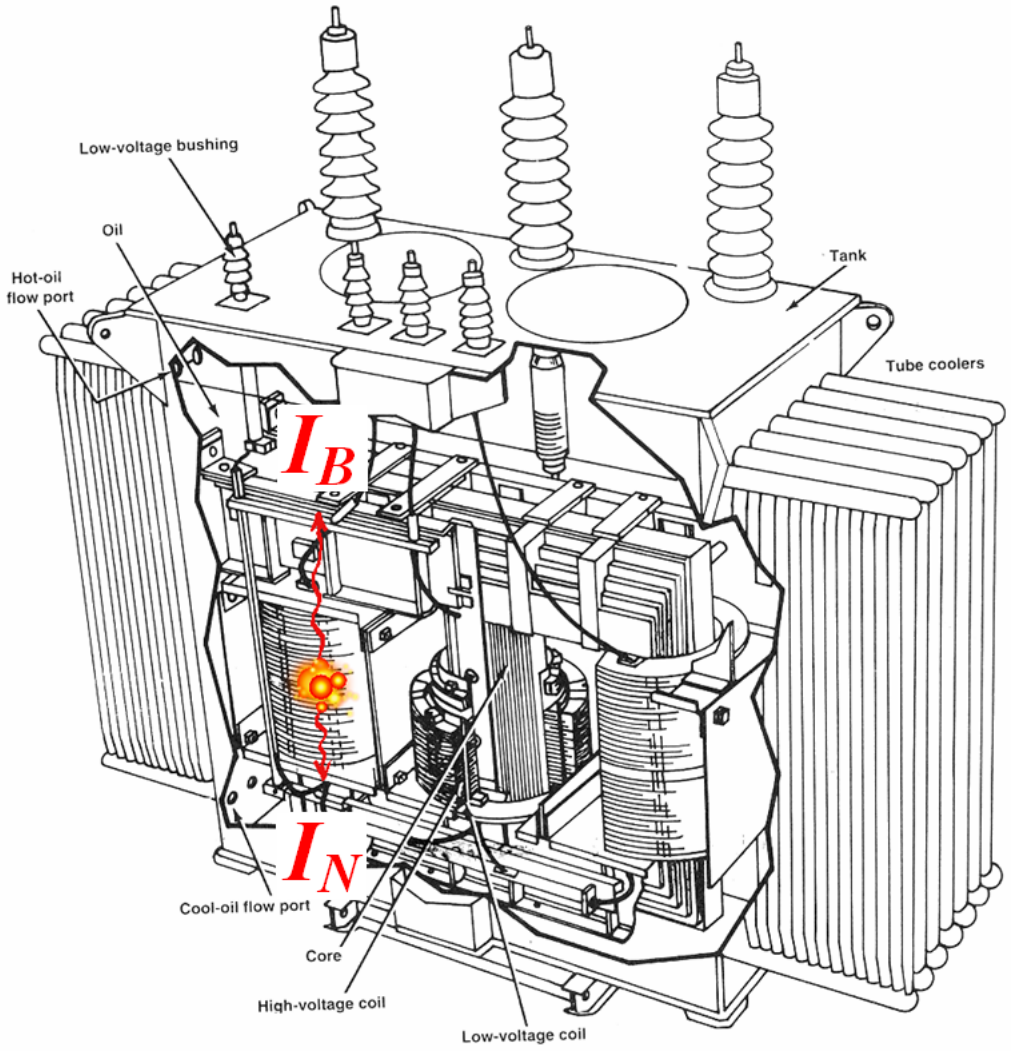

FIGURE 1.1: PD on high voltage transformer [1]

by high voltage stress of the line voltages. The radiation of discharge signals radiate through transformer oil to the tank wall, and the PD current propagates through the transformer winding to the neutral ends and bushing ends. At neutral ends to ground connections, the high transition rates of PD signals, I_N, excite the system response of the RFCTs thus the measured RFCT signals are proportional to the rate of change of currents flowing to ground. At the bushing, the high frequency PD signals, I_B, pass through the bushing to the grounded tap-point due to the bushing capacitance that acts as an equivalent high pass filter.

In partial discharge detection and identification studies, one major concern is to locate the affected PD area with precision within the transformer and to assess the severity of the degradation by estimating its PD magnitude. This can be done by estimating the original signal source in terms of its magnitude and waveshape. However, the actual charge transferred at the location of a PD cannot be measured directly. Furthermore, the transmission process of the PD signals from the source to bushing tap-point and

neutral to ground connection may be through multipath propagation. Hence PD signals may experience differing losses and attenuation from the original source point to the measuring points.

For problems associated with PD in high voltage transfomers the ability to model the transformer at high frequencies is very useful. Lumped circuit parameter models and transmission line models, are among common approaches used to represent a transformer over high frequencies. To use such models, estimation of parameters is a concern. The physical construction of a transformer, where windings are sealed in a closed enclosure, means that access to the transformer windings is very limited. Therefore, an estimation of the physical parameters is difficult and can only be based on terminal end measurements.

Typical winding parameters are represented as resistors, capacitors and inductors (RLC) in a lumped parameter model. Their values can be calculated from the physical dimensions of the high voltage transformer. However, as degraded transformers are under operation for a long period of time, the parameter values may have changed. The changes are due to the aging processes of insulation materials, electrical, thermal and mechanical stress. Therefore, physical dimensions may not be sufficient to approximate the parameters accurately and may prove unreliable for estimation of the system response of aged transformers.

1.2 Research Objectives and Scope

The main objectives of the research are to estimate and locate PD signals in a high voltage transformer using RFCTs as current sensors. Prior to estimation and localization, this research considers PD propagation modelling, investigation of high frequency transition signals, parameter estimation and partial discharge experiments.

The research focuses on modelling high voltage tranformer windings to represent high frequency PD signal propagation. Two winding types, the interleaved winding and plain winding have been considered. The approach taken is to analyze the lumped parameter model circuit arrangement using typical RLC equivalent electrical components. Due to the limited a priori knowledge of the physical parameters and the aging process of the insulation materials, the model provides an analytical solution which results in a standing wave solution. Hence the unknown parameters are defined by the standing wave parameters which can be estimated from the time domain captured PD waveforms at the windings ends.

The model derivations are based on the PD signal current divergence within a lumped parameter model which yields homogeneous partial differential equation (PDE) solutions with constant boundary conditions. This gives two sets of solutions that leads to a split

winding analysis, one solution for currents flowing towards the bushing tap-point and the other for currents flowing towards the neutral. The model also considers the solution for a PD source that yields a time varying boundary conditions model solution. This is achieved by defining the PDs as unknown source signals as an initial boundary value problem (IBVP).

This research also considers parameter estimation in the time domain and frequency domain. Time domain analysis is based on the split winding analysis model and winding distribution model. Frequency domain estimation involves a transfer function estimation technique based on nonlinear least squares. Estimation based on superposition and superimposition techniques are also explored to estimate PD waveforms. Time domain comparison and frequency domain comparison are used to investigate high frequency transition signals.

The investigation of PD signal propagation based on experimental measurement of PD signals using RFCTs has been used to validate the theoretical approach developed within this thesis.

1.3 Thesis Organization

The thesis is organized in such a way to demonstrate the steps involved in PD estimation and localization in high voltage transformers. It begins with a literature review of the background studies regarding condition monitoring and PD signal propagation studies in high voltage transformers (Chapter 2).

Chapter 3 develops a modelling technique based on a lumped capacitive model based on current divergence in transformer windings. The result yields two solutions for the voltage distribution function along the transformer winding, a solution towards the bushing tap-point and a solution towards the neutral.

Chapter 4 considers modelling high frequency signal oscillation and propagation due to transient incident waves. A split winding analysis solution is introduced which yields two standing wave solutions for transient signal propagation. The source signal is modeled and presented using a D'Alembert solution.

A time varying boundary conditions model for arbitrary applied waveforms is presented in Chapter 5. The analysis involves estimation of highly oscillatory waveforms based on Duhamel's principle which models the source signal defined by the time varying boundary conditions problem. The principle of superposition and superimposition are used to estimate the propagated signals.

Chapter 6 describes a technique for estimating the parameters based on a standing waves solution. A nonlinear least square estimation (NLSE) is used to estimate the parameters

using known equations. The estimations are based on a time domain estimation and frequency domain estimation.

Experimental models for PD signal propagation studies are presented in Chapter 7. Two types of circuit configuration and calibration techniques used to measure PD signals using the RFCTs are detailed; calibration by shunt resistor and calibration by comercial PD detector. A five RFCTs arrangement is introduced to study the PD level propagation along a transformer winding.

Chapter 8 presents a technique for PD location identification based on accumulated harmonic waveforms. Model equations based on half range sine series and quarter range sine series are used to estimate the PD levels and error calculation for PD location.

PD estimation at high frequencies based on $\phi - q - n$ pattern is presented in Chapter 9. Model equations based on predominantly capacitive regions for current divergence are derived. Results of PD estimation for different harmonic levels up to 150MHz are presented.

Finally, the conclusions and suggested future direction of the research are summarised in Chapter 10.

Chapter 2

Literature Review

Power transformers are the largest and probably the most expensive items of equipment in power systems. Obviously appropriate care and health monitoring of these assets are neccessary in order to estimate and predict their live spans. Practically the monitoring should be done over regular time intervals. This will assist in predicting any future maintenance requirements. Failure to do so may lead to catasthropic failure and may incur exessive costs. An international survey by CIGRE on large power transformers, revealed a failure rate of 1% to 2% per year [2]. This may look a relatively small quantity, however a single failure of a large power transformer causes significant disruption to utilities and is unacceptable. Since many manufacturers are merging or shutting down, repair costs are considerable. It is therefore appropriate to plan for predictive maintenance where the use of appropriate monitoring and assessment is essential.

Inspired by this, there are developing technological tools to inform maintenance. A proper method of monitoring using reliable equipment having relatively low cost is essential. Cheaper monitoring techniques have led to an opportunity to research analytical techniques. However, the reliability and robustness of techniques used are significant concerns and ultimately will determine the success of any condition monitoring activity.

2.1 Transformer Condition Monitoring

The practice of condition assessment of power transformers has increased over the last few decades. Asset health and life maintenance has become more important since economic considerations have influenced replacement policies. Maintenance practice has shifted from time based to condition based procedures in order to reduce the cost of maintenance. Most monitoring techniques are based on classical methodologies that can be categorized into two main modes of failure, internal and external causes [3, 4]. Table 2.1 shows typical causes of transformer failure that influence any condition monitoring and ultimately drive the development of higher technology tools.

TABLE 2.1: Causes of transformer failure

Internal	External
Insulation deterioration	Lightning strikes
Loss of winding clamping	System switching operations
Overheating	System overload
Oxygen	System faults (short circuit)
Moisture	
Solid contamination in the insulating oil	
Partial discharge	
Design and manufacture defects	

The classic techniques of condition monitoring are mainly focused on the insulation and winding systems. This focus still remains but has become more sophisticated and complicated. These techniques are still developing and have undergone a lot of improvements [5, 6, 7, 8]. Table 2.2 shows the typical types of monitoring techniques applicable to the insulation and winding systems.

Following deregulation of the electrical supply industry, techniques for condition monitoring have developed to allow condition based assessment of transmission and distribution assets. Over past few years condition monitoring has evolved and improved in terms of fault diagnosis [9].

A Multi Agent System (MAS) transformer condition monitoring system is one of the latest developments to provide a reliable remote monitoring system [10]. All kinds of information are monitored remotely and clustered into different layers to avoid data congestion and identify important information. The defined layers are the data monitoring layer, interpretation layer, corroboration layer and information layer. The modules in each layer require fundamental knowledge of how the plant behaves and fails. Moreover, MAS offers a flexible and extendable system framework for further integration of additional data from other sensing techniques that may develop in the future.

A comprehensive review of modern chemical and electrical diagnostic methods can be found in [11]. Among chemical methods, Disolved Gas Analysis (DGA) is the most widely used method for investigating incipient faults. The chemical method for analysing

TABLE 2.2: Transformer monitoring techniques

Insulation System	Winding System
Dissolved gas analysis	Reactance measurement
Partial discharge measurement	Low voltage impulse test
Hot spot temperature measurement	Frequency response analysis
Degree of polymerization measurement	Transfer function method
Furan analysis	
Recovery voltage measurement	
Insulation resistance measurement	
Dissipation factor measurement	

cellulose ageing by furan measurements using a High Performance Liquid Chromatography (HPLC) techique is also widely applied. An electrical method incorporating chemical and electrical methods for investigating the degree of polimerisation has also been developed. This method is based on time domain polarisation and frequency domain polarisation measurements. The time domain measurement is related to charge density of current polarisation; $j(t)_{polarisation}$; this has the effect of 'memory' over the time in a dielectric system. In frequency domain, the dissipation factor; $tan\delta$; can be measured as a function of the frequency of the test voltage.

For condition monitoring of power transformers, it has proved advantageous to implement intelligent systems [12]. Condition assessment using an intelligent neural network to identify the associated failure from DGA measurement data gives accurate diagnosis with the training data [13]. Not only that, with an appropriate feeder to the neural network using a genetic algorithm (GA) technique, the design and training process are optimized which gives an improved diagnostic result. The GA is basically used as a feedback input to the system to minimize error between input and output of the network by tuning the parameters of the neural network design.

A Wavelet network shown in Figure 2.1 also has been found to be a great tool for identifying problems with power transformers [14]. It was initially used in system identification problems in general, but the wavelets multidecomposition techniques mean that it can identify the best network parameters due to its localization property. Not only that, the robustness of the algorithms has evolved such that a new problems can be fed into the system, in this case the system is an evolving wavelet networks (EWN). Another aspect to improve the assessment capability, is the use of an intelligent decision support system based on fuzzy learning vector quantization (FLVQ) [15]. Learning vector quantization (LVQ) is defined in the learning system, where it is responsible for classifying faults due to potential insulation deterioration. Both techniques of EWN and FLVQ have a common benefit in terms of their learning algorithms, and that is adaptation to a new problem. This gives a potential benefit in adaptive learning processes where later problems can become a new learning parameter without the need to change the network design.

In diagnosing the problems associated with the cause and source of insulation failure, online or offline diagnostic techniques have been considered by employing some of the above monitoring methods [16, 17]. This aproach is becoming more widespread as condition monitoring moves to be fully computerized and incoporates multiple sensors with cross correlation data that checks validity and provides accurate diagnostic analysis [18, 19].

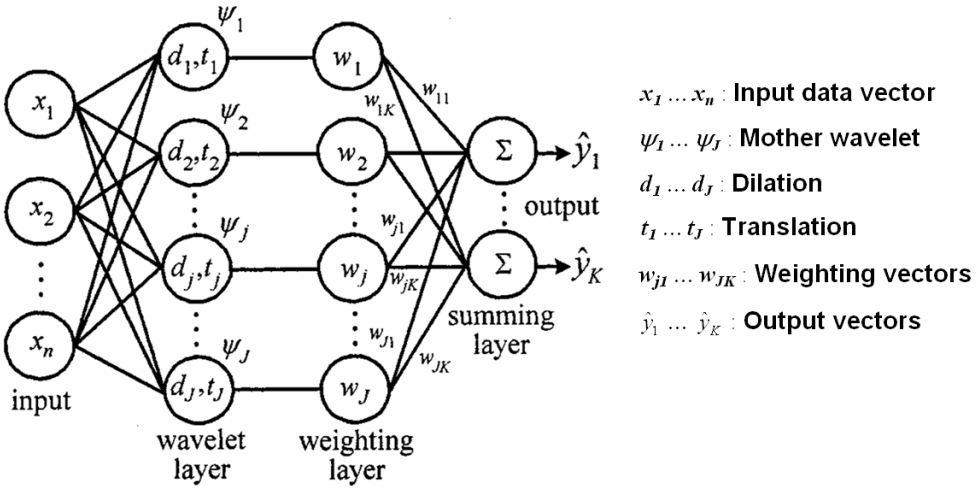

FIGURE 2.1: Evolving Wavelet Network [14]

2.2 Condition Monitoring by Partial Discharge Detection

Partial discharge is an important indicator of insulation degradation problems in a power transformer. PD phenomena are observable through electrical, mechanical, and optical means. In modern technology these are combined as a system monitoring tool where the use of electrical detection has the advantage of allowing the application of digital signal processing techniques. The combination of these technologies to measure PDs are essential, as PDs in transformers are not necessarily indicative of insulation condition. They are however an early warning of incipient problems. For insulation diagnosis it is necessary to not only know the PD magnitude but also the location of the PD source.

Partial discharges are pulses of current that occur in a transformer when the electric field strength exceeds the dielectric breakdown strength of the insulation material. This results in high frequency transient signals that propagate within transformer windings in all directions, which can propagate towards bushing tap points and neutral to ground terminals. However the PD radiation, radiates towards the transformer tank wall via the surrounding oil. Therefore PDs can be detected using non-conventional techniques such as, ultra high frequency (UHF) sensors, acoustic sensors or high frequency current transformers (HFCT) [20, 21].

Piezo-electric sensors and the use of optical fiber can also be used to detect PDs [22]. The piezoelectric sensors are connected to the outside tank to measure the acoustic wave from inside the transformer to the tank. However this system can become ineffective in high noise environments as piezoelectric sensors are sensitive to high frequency signals. To avoid this kind of problem, more advanced techniques are employed with the detection of PDs within the transformer tank wall, using fiber optic sensors as shown in Figure 2.2 [23, 24]. The system requires a sensor probe, an optical fiber linked to the sensor and high end signal processing unit. Typical epoxy-based fiber pressure sensors are used

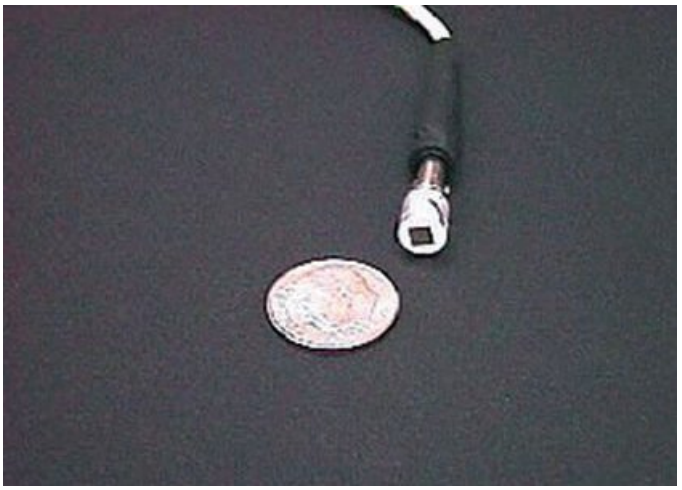

FIGURE 2.2: Epoxy-based fiber optic pressure sensor [21]

which are very small and easy to install.

The use of UHF sensors in PD monitoring is among other non-conventional techniques to detect PD propagation through the transformer oil [25, 26]. Figure 2.3 shows an example of a UHF sensor mounted on top of a transformer tank. Strathclyde University has developed a diagnostic tool for transformers which uses UHF couplers operating in frequency region of 300MHz to 1500MHz. It was initially developed for monitoring partial discharge in gas insulated system (GIS) and then applied to power transformers. The principle of recognition is based on the PD pattern, waveform recognition and the source location of PDs. The UHF sensors are mounted on the wall of the outside tank of a transformer and 'look' through dielectric windows. The sensors respond to the electromagnetic wave radiated by PDs within inside the transformer.

One very cost effective technique of PD monitoring for high voltage transformer is by applying HFCT sensors and this method has been widely used and researched [27, 28, 29].

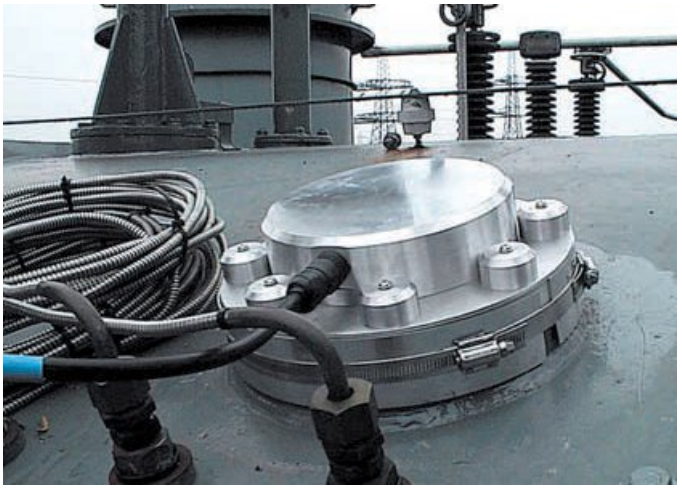

FIGURE 2.3: UHF sensor mounted on a transformer [21]

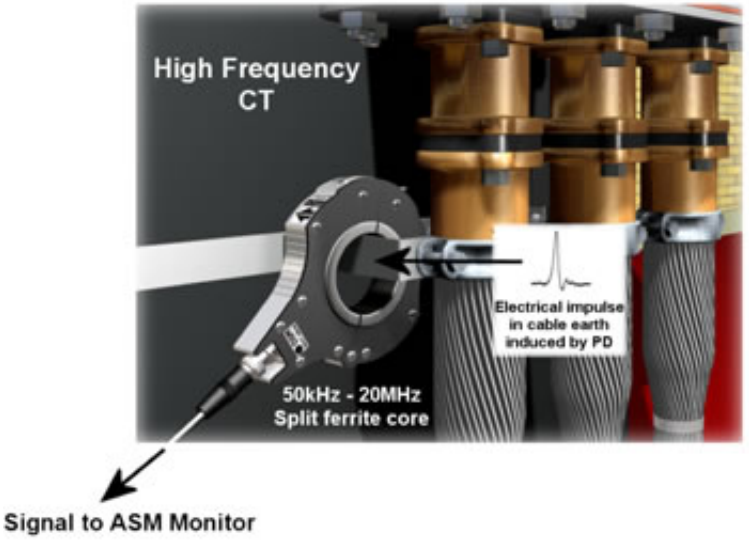

FIGURE 2.4: HFCT mounted at earth bonding point [31]

HFCTs are usually installed at the bushing tap-point terminal or the neutral to earth connection (Figure 2.4). HFCTs are very portable, cost effective and are a non-intrusive type of measurement. The use of HFCTs allows the current propagation in a conductor to be accurately measured. It is also among the safest techniques for current measurement as it has no direct contact with the winding conductors. Thus the application of CTs for discharge current measurement has great potential in facilitating PD identification even for apparatus such as high-temperature superconducting transformers [30].

2.3 High Frequency Properties of Transformers

Transfomer modelling studies are important for condition monitoring and understanding transformer behaviour at high frequency [32]. The behaviour of power transformers during operation at higher frequencies or under transient conditions is very complex and difficult to predict. The terminal response under such conditions is highly affected by nonlinear nature of loads, the core, leakage inductances, and stray capacitances distributed through the windings [33].

These are the important parameters that determine the overall frequency response which varies nonlinearly with frequency. Therefore, the challenge of modelling a large transformer will begin by estimating those parameters which are frequency dependant. These parameters will give an accurate representation of a transformer physical model when physical access to the inner structure which is contained in a closed and sealed enclosure is not possible.

The need for a wide frequency measurement range is important to determine transformer

behaviour under transient conditions. Some high voltage transformers are commonly connected to a source with high frequency harmonic content, such as a high voltage direct current (HVDC) converter station, and hence the transformer will experience a high voltage internal resonance. This happens when its natural frequency coincides with the high frequency noise generated by the collapse of the voltage during the converter switch firing sequences. These internal part winding resonances often produce transient voltages at the mid winding of a transformer that are higher than the voltage at the transformer terminals [34].

2.3.1 Transformer Modelling

In most previous studies, transformer winding parameters are determined via the physical dimensions and empirical formulas. The windings are divided into a number of parts, usually into coil section pairs having known values of physical dimension of coils, distance between coils, diameter of disc coils and insulation thickness [35, 36, 37, 38]. The solution to this is found by applying Maxwell's equations, which satisfy relevant boundary conditions for self and mutual inductance and the capacitor equation for capacitance between conductors. Such approximations often result in error in definition of the physical parameters and hence errors in the mathematical model [39]. In order to get good approximations and a more refined model, circuit parameters have to be experimentally determined. The parameter estimation techniques based on experimental measurements in either frequency domain or time domain can be used effectively to estimate these parameters.

Frequency response analysis (FRA) is a well established method that has been receiving increasing interest in the electric power industry. This technique has been proposed for model identification [40] and winding movement [41, 42, 43]. The FRA method tracks the terminal response of transformer by representing the internal impedance parameters related to inductance and capacitance with a variation of poles and zeros in its frequency domain, which attempts to relate changes in the internal condition of the transformer. These changes can be related to the change in physical parameters by means of its impedance response and its relation to the terminal frequency response [33].

2.3.2 High Frequency Transformer Winding Model

In investigating the electromagnetic transient behaviour within transformers, a high frequency transformer winding model has to be considered. At high frequency, equivalent electrical lumped parameters circuit (RLC) oftenly use to represent the equivalent model of transformer windings. Predominantly capacitive model as a representation of insulation between conductors, often considered as the model to represent the behaviour of high frequency signal propagation for initial distrbution [44]. Depending on the type of

transformer windings, the model adopted to represent high frequency phenomena may differ for different types of windings. Typical transformer type such as plain winding will have simple equivalent circuit layout which has end connection with a simple conductor arrangement between winding sections (Figure 2.5(a)). However for advanced winding layout like interleaved winding will have different equivalent circuit depending on the interleaving connection between each section (Figure 2.5(b)).

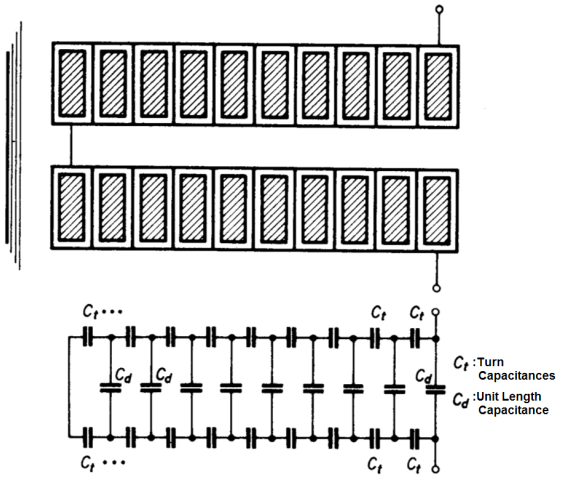

(a) Plain winding

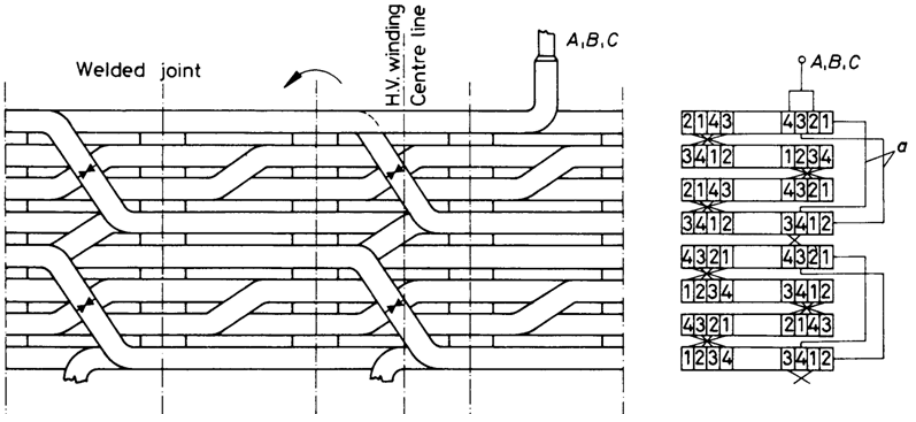

(b) Interleaved winding

FIGURE 2.5: Examples of winding layout for Plain winding and Interleaved winding [45]

In the electromagnetic transient program (EMTP), the behaviour of transformer can be determined via detailed internal winding models and terminal ends winding model. One of the ways of studying the behaviour is by looking at the impedances within transformer windings in great detail [46]. The benefit of this is that it may also define other elements of the winding such as eddy current loss due to the effective resistance of a multiturn transformer over its high frequency operating region [47].

If any case of disturbance caused by a high frequency signal from outside the transformer due to a high frequency fast transient switching operation, a lumped parameter

model may be used to represent the high frequency excitation [48]. The interpretation of signal propagation is achieved by considering the winding parameters by means of its continuous winding physical dimensions converted into electrical parameters. By finding the relative constants, it is possible to estimate the winding voltage transient distribution. Another aspect to improve this is by considering a finite element analysis with the same lumped parameter model [49]. With these higher frequency details of the stress distribution it is possible to construct a model describing high frequency transient signal propagation within transformers. The conclusion from this procedure is well suited for modelling a real transformer in cases where the frequency response mesurements do not exist.

The study of transient signals in transformer windings with EMTP studies may explain the phenomena of high frequency transient signal behaviour within a transformer winding. Other techniques for EMTP include the modal model of four terminals transformer which is useful in looking at the transfomer while loaded with terminated impedance at secondary connection [50]. In this case, the transient signal can be estimated by only measuring signals from the available transformer terminals.

By using different techniques to model high voltage transformer for the EMTP studies, it may result in different diagnostic capabilities. For example, a multi-phase network model based on the admittance matrix to represent the sectional winding impedances may result in different levels of step response or transient response in transformer windings [51]. The transient response is simulated based on high frequency signal propagation based on the measured terminal voltages of the transformer. Hence, this method allows estimation of the level of oscillation within a transformer.

The behaviour of a transformer winding at high frequencies may also differ with type of windings. It was found that there are significant difference in the response of windings in their high frequency characteristics between interleaved windings and normal plain windings [52]. With the consideration of winding transfer function, the plain winding has shown more resonant components compared to the interleaved winding. From a theoretical point of view, a frequency response transfer function is equivalent to an impulse response measurement expressed in its frequency domain. Thus by considering proper impulse response measurements, interpretation of transformer faults at high frequencies is possible [53]. The nonstationary nature of voltage and current waveforms inside the transformer winding therefore requires the model parameters to be both time and frequency dependent. However, for these techniques the parameters under consideration are estimated from detailed dimensions of the transformer windings.

There are also a few similar techniques that involve application of a capacitive network for high frequency signal oscillations. At high frequency a transformer winding will operate in its predominantly capacitive region. This can be identified either by frequency response measurements or impulse response measurements. A classical technique using

a model based power frequency equivalent circuit has been presented which has then been extended to higher frequencies by the addition of the winding capacitances and the synthesis of the frequency-dependent short-circuit branch by an RLC equivalent network [54]. The lumped parameter network has demonstrated oscillation of a very high frequency signal which is associated with the resonance frequencies of the systems.

2.3.3 Transformer Modelling for Pulse Propagation

The modelling of a transformer for pulse propagation begins with analysis using a lumped parameter circuit model [55]. Figure 2.6 shows the typical lumped parameter model for transient propagation within a single phase transformer. It was initially used to demonstrate the signal propagation under the influence of a lightning impulse. It begins by modelling the lumped circuit in a single direction of current due to the impulse applied at the bushing and travelling towards the neutral to ground connection. The technique employs of a lumped circuit parameter model by modelling the physical RLC component using a partial differential equation. The model has revealed that different RLC parameters when taken into consideration may have different transient behaviour in the system. It is also used to explore faults in a transformer winding with a simplified circuit [56].

It is also possible to study the equivalent lumped circuit parameter model using topological analysis [57]. By using the same model and with the existence of the mutual inductance between the windings, the peak resonances can be defined. The derived model can then be transformed into the time domain by using the state space equation. In finding the suitable parameter values, a method such as a genetic algorithm may be employed with an iterative learning algorithm. The reliability of the topological analysis can be clarified by considering a step response signal along a transformer winding [58]. The technique is also useful in identification of the sectional winding transfer function (SWTF), which also benefit in identifying problems associated with PDs such as localization of PD sources, discrimination between PDs inside or outside of the transformer,

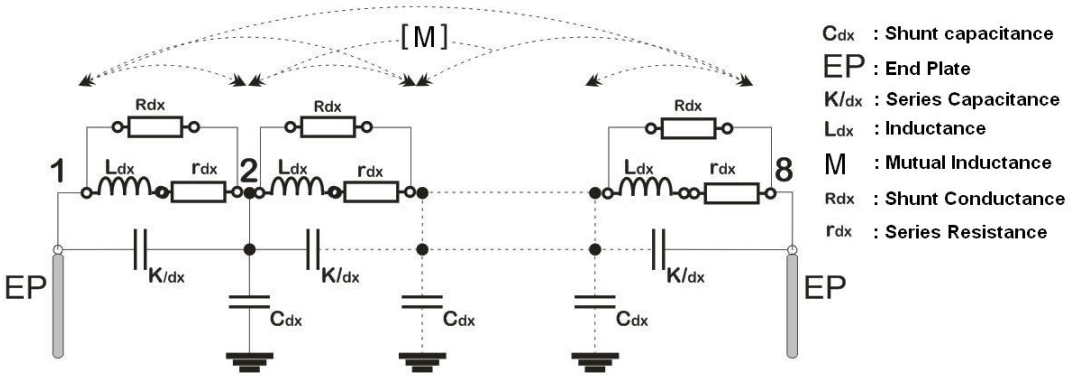

FIGURE 2.6: Equivalent lumped parameter model of a single transformer

and evaluation of actual PD amplitudes along the winding.

Another technique uses multi conductor transmission lines (MTL), as shown in Figure 2.7 to model the continuous winding by only estimating the number of turns rather than disc to disc properties [59, 60]. This is an alternative to using the lumped circuit parameter model. It is also found to have an advantage over the lumped circuit model as it is possible to locate the discharge source with its turn to turn model. The technique models the voltage and current using a voltage mode transformation technique and a current mode transformation technique. In order to apply the algorithm it is neccessary to calculate the value of interturn capacitance and ground capacitance from physical dimensions, which can be very difficult to achieve in practice.

By combining a lumped parameter model and MTL model, a hybrid model may produce better results. The lumped parameter model can be used to calculate the physical RLC parameters from winding dimensions, then the MTL can be used to simulate the propagation of PD or high transient signal within a winding of a transformer [61]. The simulation analysis is claimed to be more reliable, has a smaller computational burden and provides better accuracy over the higher frequency range.

Another hybrid model using a combination of coil-by-coil details and an inter-coil black box model has been presented [62]. Figure 2.8 shows the equivalent of hybrid model with a combination of lumped parameter model with an unknown black box model. The technique was introduced for transient propagation studies, and found to provide better analysis in revealing hidden transient signals compared to using the coil by coil model only or inter-coil black box model only. Parameter estimation of the detailed model and synthesis of the black box model are calculated based on frequency response measurements.

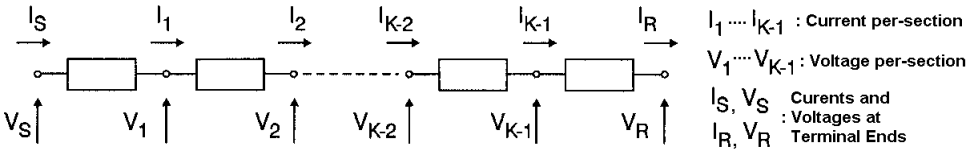

(a) Single line MTL model

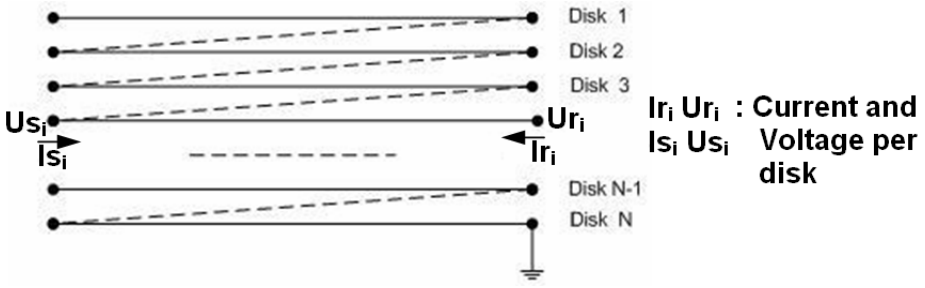

(b) MTL model

FIGURE 2.7: Variation of Multiconductor Transmission Line model [59, 60]

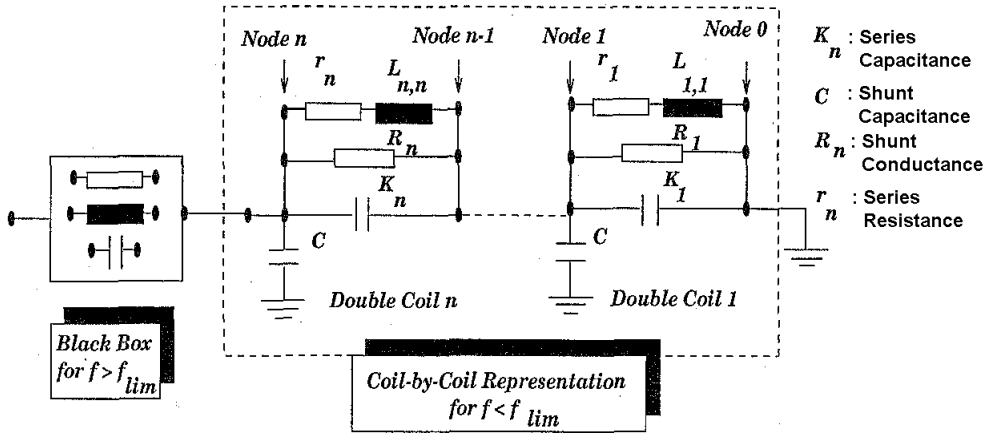

FIGURE 2.8: Equivalent hybrid lumped parameter model [62]

As different transformers consist of different types of winding arrangement, the response and the way a high frequency pulse propagates within the transformer will differ from one to another. This is simply due to the transformer construction generating a different equivalent high frequency circuit. To solve this, it may be necessary to consider a basic Norton equivalent circuit derivation which then can be associated with the transformer terminals [63]. The model consists of a set of state equations solved with the trapezoidal rule of integration in order to obtain an equivalent Norton circuit. Thus the transformer model can be easily interfaced with an electromagnetic transients program.

2.4 Partial Discharge Estimation and Localization

Partial discharge is an early warning of insulation failure. There are often PD events when a new transformer is initially tested. Hence engineers need to assess the severity of any PDs in terms of magnitude and the location. Without accessing the internal windings of the transformer, acoustic sensing may be a quick way to monitor the PDs [64, 65]. The combination between UHF sensors and acoustic sensors may yield a better understanding of the source location of PDs because more information are collected by cross correlation of PD data between sensors. In this case as variable PDs are generated, an average mesurement from the sensors is essential.

As the design of transformers is very complex, using UHF sensors may have difficulties in measuring real PD magnitudes accurately. The techniques of time of flight and time of arrival are significant and reliable as the electromagnetic waves due to a PD burst travel in a near direct path from source to the sensors. An example of UHF positions on the tank of a transformer is shown in Figure 2.9 showing the position of PD and and corresponding UHF sensors. The propagation path of electromagnetic waves in the transformer oil may experience diffraction due to obstacles where waves tend to deflected or deviated from its original path. Therefore, a spatial technique has to be identified in

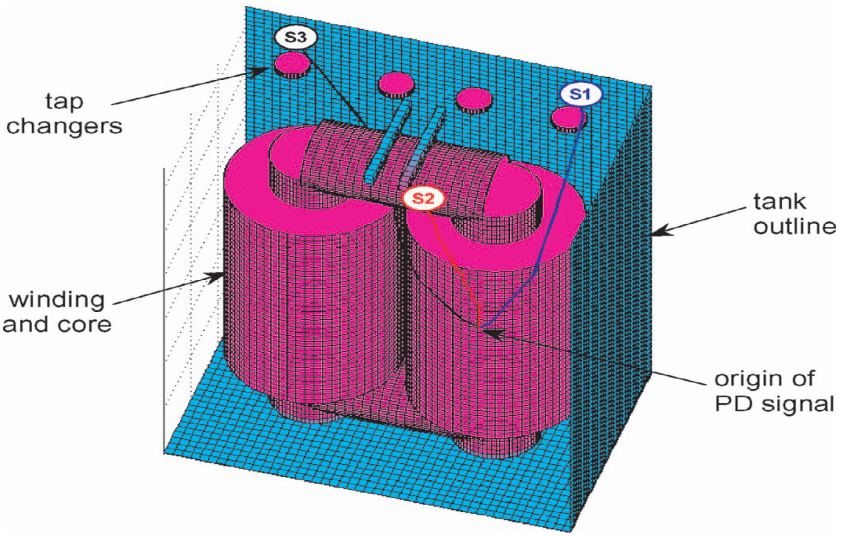

FIGURE 2.9: UHF position on a transformer tank to locate PD [25]

order to be able to identify obstacles by means of shortest path of propagation [66].

A particular problem associated with acoutic waves in transformers is from geometrical spreading of the wave from source to sensors, division of the wave among multiple paths, transmission losses in propagation from one medium to another and absorption by certain materials. However as the waves have very high frequency components, some of the wave components may have a very short wavelength compared to the dimension of the apparatus. Thus it is possible to detect this kind of wave component using suitable piezoelectric sensors that have a narrow tuned bandwidth [67, 68].

There are circumstances where PDs cannot be detected using acoustic sensors. This is when the PDs are hidden within deep inside the winding of a transformer. Hence, one possible way of detecting this is by using a lumped circuit parameter model network of RLCM parameters [69, 70]. PD localization is based on comparison of results from a real PD source with the characteristic responses of the RLCM network of the specific transformer from calibrated impulses applied at the respective bushing. This can be achieved by performing statistical analysis of the PD patterns and the PD current impulse in the frequency domain.

Electrical measurement methods are also commonly used for PD localization. Common measurement of PDs from the terminal ends of the bushing and neutral to capture PDs allows a technique to identify the transfer function of the transformer windings. This requires a knowledge base of internal parameters that can be calculated either from physical dimensions or estimated using frequency response peak resonances. The transfer function can be calculated using the model from lumped parameter analysis and a genetic algorithm has been found to be very useful in estimating the unknown lumped parameters [71]. The system for PD estimation and location is assumed to be a multi-input, multi-output system (MIMO) as shown in Figure 2.10. A deconvolution

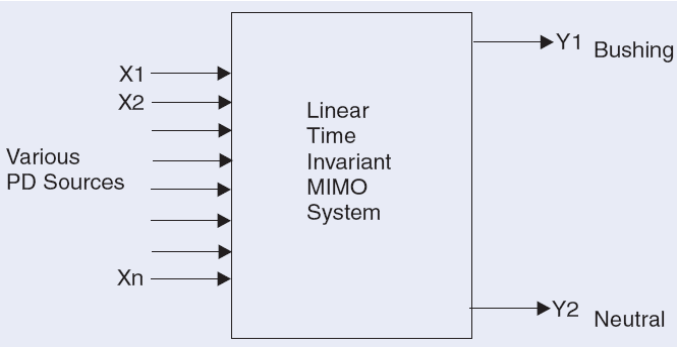

FIGURE 2.10: MIMO system for PD location by transfer function technique [71]

technique can be performed from a measured PD response based on the step response theoretical function [72, 73] in order to estimate PD severity.

As the design of a transformer can be closely modelled using lumped parameter approach, every section or disc winding in the transformer will consist of different identical RLC components which can be found by analysis of its winding based structural data [74]. It is also possible to locate and estimate PD magnitudes based on this analysis. Moving poles analysis has been found to be one of the way identifying PDs at different locations [75, 76, 77]. Where it is believed to operate under the influence of inductive elements or operate in a transmission line mode. For waves moving under the influence of the predominantly capacitive region this allows identification of the moving zeros [78, 79]. The moving poles and moving zeros analysis is the position of poles and zeros from the frequency domain analysis associated with the position of PD injection along a transformer winding. The measured PD signals at Bushing tap point and Neutral to ground connection will be the points of measurement for the analysis.

In finding the location of PDs, a capacitive operating range may be found from analysis of either the frequency response or impulse response measurements. Under a capacitive influence, waves propagate in a no loss medium. In other words the same component level of PDs will be captured at either terminal bushing or neutral end, in its oscillation propagation along the winding as shown in Figure 2.11. Hence, the distribution level can be explained as a straight line and PDs location is much easier to identify [80]. However there are circumstances where by considering the model winding under the influence of predominantly capacitive region, the winding distribution and the location of PDs will not be in a linear straight line relationship between bushing and neutral terminals [81]. The distribution curve is defined by the coefficient distribution α which is the ratio of inter-turn capacitance to inter-disk capacitance [44].

Advanced signal processing techniques are one of the most beneficial approaches for processing PD signals. As PD signals are unique and pass through multi-path mediums, they will have a certain signature associated with the original source. Therefore a feature extraction technique based on a signal template of PD signals analysed in the frequency

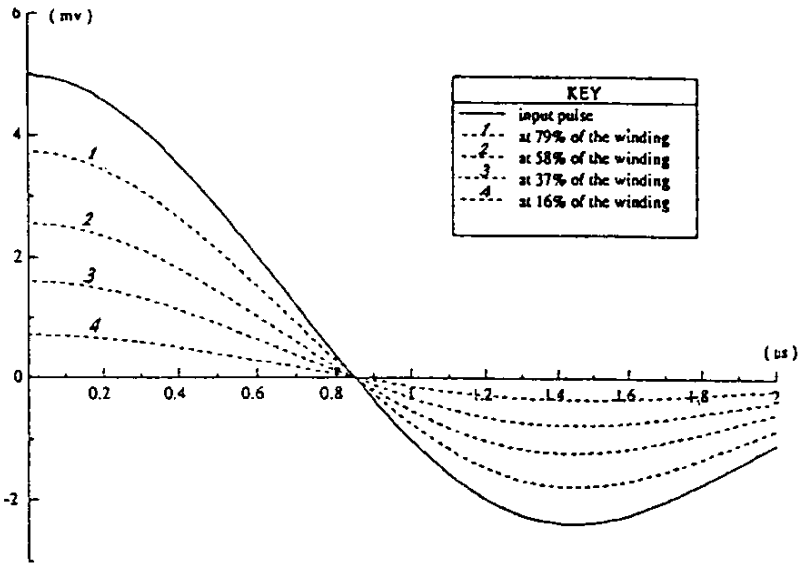

FIGURE 2.11: Time domain components of pulse distribution under predominantly capacitive region [80]

domain is possible [82]. Another feature extraction of PDs is based on power spectrum density (PSD) and is also proven to contain information about the original source [83]. It is also becomes easier to see the energy level transformation of a PD signal by using the Karhunen-Loeve-transform [84]. The energy transformation of PDs using Karhunen-Loeve theorem is clearly different with respect to the point of injection.

2.5 Parameter and Transfer Function Estimation

Parameter estimation is one of the main subjects in the study of high frequency behaviour of transformers. The parameters of interest represent the way the signal propagates from the source of a fault to the terminal measurement point. Most of the models used in translating the behaviour of high frequency signals propagating within a transformer cannot avoid utilising its physical parameters. Most of the time, the physical parameters associated with electrical properties; resistance, inductance and capacitance, can be calculated from the physical dimensions and materials of the transformer. However, some of these parameters are frequency dependant and over time parameters can change due to electrical stress and mechanical stress. It is therefore a measurement based on frequency response or impulse response that is required in order to estimate the parameters of interest.

Figure 2.12 shows an example of a three-legged transformer with its equivalent circuit parameter [85]. The magnetic circuit is shown in Figure 2.12(b), where $\mathcal{F}_{\mathcal{H}}$ and $\mathcal{F}_{\mathcal{L}}$ represent MMFs at the high and low voltage side; $\mathfrak{R}_{\mathfrak{m}}$, $\mathfrak{R}_{\mathfrak{y}}$ and $\mathfrak{R}_{\mathfrak{n}}$ represent reluctances. From Figure 2.12(c) R_H and R_L represent the winding resistances of the low voltage and high voltage; L_{sh} represents flux leakages; L_0 and R_0 represent linear inductance

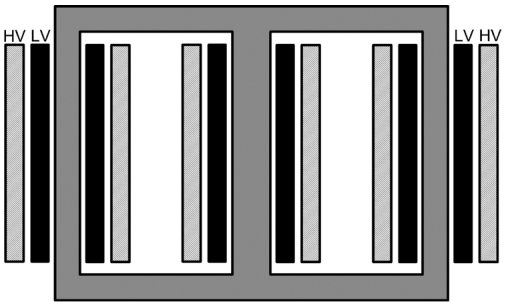

(a) Physical structure

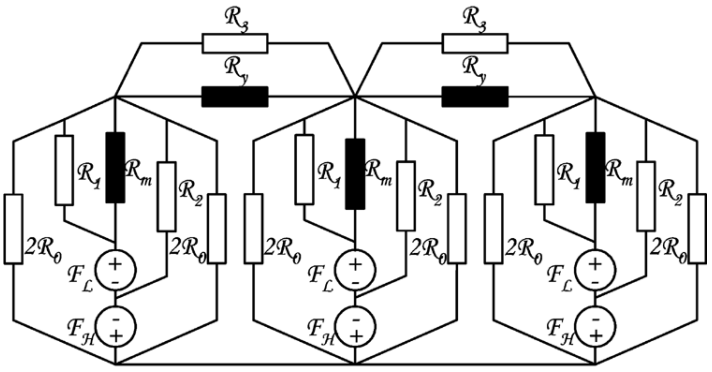

(b) Magnetic circuit

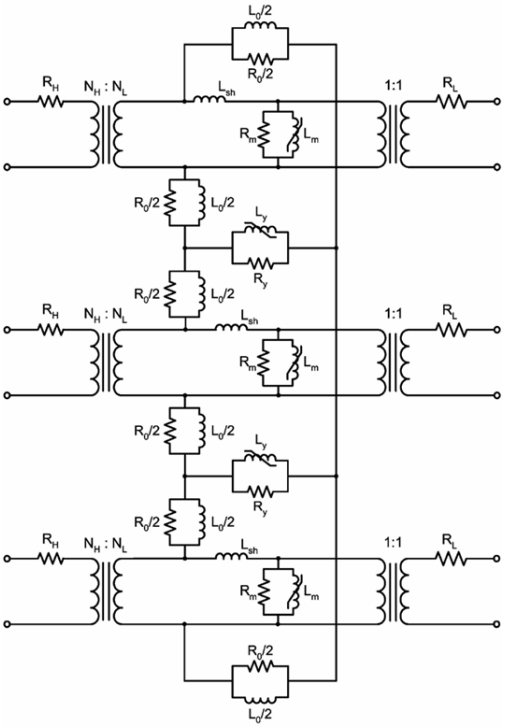

(c) Electrical equivalent circuit

FIGURE 2.12: Equivalent circuit of a three-legged stacked-core transformer [85]

and resistance; R_m and R_L represent combined resistances and saturable inductances; R_y and L_y represents the yoke section between a pair of phases.

One of the common estimations in the frequency domain is the system transfer function. The transfer function is often associated with resonant peak frequencies (poles) and resonant crest frequencies (zeros). These frequencies are analytically explained by comparison with the equivalent circuit resonant parameters of the RLC lumped parameter model. At high frequencies, the reverberation of signals are more obvious as the change between peaks and crests of the frequency response also known as poles and zeros are common. Hence the estimation of transfer function can also explain the high frequency oscillation of the transformer winding with the estimation of its transfer function coefficients.

Considerable effort has been devoted to the development of methods for transfer function estimation from frequency response observation. The frequency domain identification problem is often associated with the estimation of a rational complex function to fit a measured set of complex data or its magnitude and phase response data. The nonlinear nature of the problem has yielded different formulation and solution techniques. A linearization procedure and a complex curve fitting technique has been introduced [86] and it was then further improved [87, 88]. The proposed method was based on the least squares approach that ultimately yielded the derivation of a matrix of parameters in its linear relationship equation.

Later the formulation introduced in the form of a set of a linear equations was further developed and modified for better accuracy and smaller error for the convergence factor. It was found that a reduction of iteration number for convergence by introducing a linear least squares problem approach by singular value decomposition (SVD) [32] has improved the performance of estimation.

As frequency response is often associated with complex numbers, an estimation based on logarithmic scale can be undertaken. Similar to the linear approach, a complex logarithmic least square estimation (LOG-LSE) has been introduced [89]. The approach by the LOG-LSE has shown that the bias on the parameter estimates of the LOG-LSE decreases faster than normal input output signal to noise ratio (I/O SNR) for a nonlinear least square estimator. It was also shown that the LOG-LSE is more robust in the presence of unknown noise. The technique can be used and implemented in Matlab environment where it has been developed into a program called Transfer Function Adjustment (TFA) [90]. The process begins with the derivation of model transfer function which then is used to derive a logarithmic cost function.

High frequency signals within transformers are often contaminated by noise, which is when the use of a maximum likelihood estimator becomes particularly suitable (MLE) [91]. It has been demonstrated that under "mild conditions" in the presence of low level of noise the use of a nonlinear least squares (NLS) fitting technique for a rational transfer

function to frequency response data yields the MLE of the transfer function coefficient vector. The advantage of NLS is the ability to model a data with reasonable errors, however the only disadvantage is the difficulty of convergence to minimize the errors to a specified level. Hence an 'elemental set' of parameters comprising of a number of frequencies equal to half the number of unknown parameters to enhance the convergence factor has been introduced [91]. The use of NLS technique can be used to find a continuous time transfer function that corresponds to the complex frequency response data [92]. The NLS is used to minimising the squared norm of error between the estimated model and the measured frequency response. From the derived transfer function a simple circuit theory calculation can be used to obtain the equivalent parameter components for a transformer circuit equivalent model.

Estimation of transformer parameters can be done using time domain analysis as well as frequency domain analysis [93]. The emphasis is on the identification of the parameters through the instrumental variable method in the time domain and the maximum likelihood estimation method in the frequency domain. This method divides the estimation techniques in three major parts. First, the topology of the proposed transformer winding equivalent circuit is defined, the mathematical representation of the model is derived using state space formulations, then estimation techniques are applied to estimate the parameters in both time and frequency domain using the maximum likelihood method. Another new technique called Subspace-based identification in identifying the mathematical model of power transformers was introduced [94]. It is apparently suitable for high order structurally variable like transformers, where one of the advantage of the algorithms is its noniterative algorithm in the frequency domain.

An Artificial Neural Network (ANN) for parameter estimation has also been proposed [95]. It has been shown that the combination of genetic algorithm as parameter optimization and an artificial neural network for transfer function estimation to estimate the frequency response measurement has given a good parameter estimation in the frequency domain. The GA was used to optimise the learning process during the initial weight selection. Moreover the use of GA as a meta-heuristic robust optimization algorithm simulating the nature evolution process has widely been used in large complex problems like high order transfer function estimation. The typical structure of the GA is shown in Figure 2.13.

Other means of parameter estimation include computing techniques for reducing the computational burden and time consumption [96]. A model based parameter estimation (MBPE), based on mathematical derivation which involved fitting physically the approximated model has resulted in better accuracy of computing electromagnetic quantities from which unknown coefficients are numerically obtained. The model can then provide simple and compact representation of the functional behaviour of the quantity of interest that can be used later for interpolation or extrapolation of the fitted data.

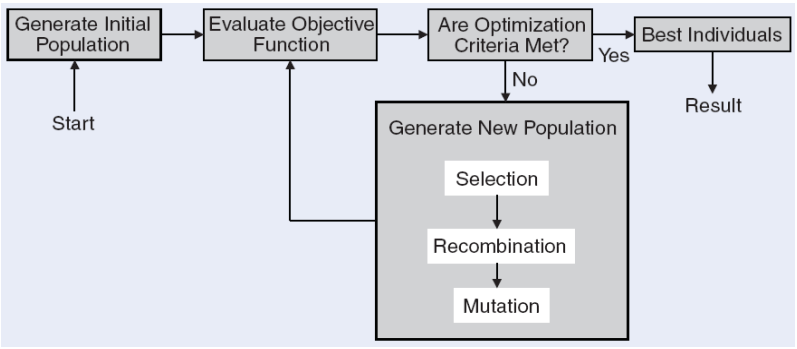

FIGURE 2.13: Structure of GA algorithm [71]

Another technique of modelling frequency response estimation for higher number of peak resonances based on rational transfer function has been introduced [97, 98]. It is called the vector fitting technique. The technique introduces a set of complex starting pole coefficients which also correspond to the order of the transfer function. As it is has an advantage of fitting higher numbers of resonances it is suitable for modelling the transfer function of a transformer response. In the normal case, peak resonances are common at high frequencies. It is has been shown that the modelling of high frequency response transfer function of transformer and transmission lines is suitable for estimating the higher number of peak resonances [99, 100].

2.6 Summary

Partial discharge monitoring in high voltage transformers has been widely investigated and has been found to be practical in giving diagnosis of transformer health. The choice of techniques in monitoring and diagnosing power transformers can be compared in terms of cost, reliability and robustness. The choice of technique relies on two diagnostic conditions, the PD magnitude and the location of fault.

In PD estimation and localization, the UHF technique may be best to determine the position of the PD source. However, in circumstances where PDs occur within deep inside of a transformer winding, electrical methods become a choice. Therefore, electrical methods are techniques that can be relied on when at high frequencies the PD energy is sustained and can be detected at the bushing and neutral ends. This estimation thus requires a suitable model to locate PDs. The main focus of PD pulse propagation involves the choice of model adopted to solve the problem. There are two models that best explain the way that PDs propagate along the transformer winding, either a lumped parameter model or a multiconductor transmission line model.

The multiconductor transmission line model has been found to be able to explain higher frequency PD phenomena then a normal lumped parameter model. It is also has the capability of modelling PD pulses with a higher number of resonances in its frequency

domain at different disc positions. However, the lumped parameter model has an advantage in terms of modelling the disc to disc parameters which can be associated directly with the position of PDs from the neutral to ground terminal. By considering the best technique in identifying the transfer function or the intermidiary frequency response of disc to disc transformer windings, it is possible to estimate and simultaneously locate the position of the PD source.

Overall, this survey has focussed on the modelling of transformers in the high frequency region and also the way that pulses propagate under such conditions. The common problem associated with modelling is parameter estimation. As transformers are always considered as a "black box" system, hence parameter estimation is an unavoidable issue when investigating the propagation of pulses under high frequency phenomena. The critical parameters under consideration are the RLCM parameters under high frequency lumped parameter model and MTL model. It can be found either by transformer physical dimensions, frequency response mesurement or impulse response measurement. As these parameters are mostly frequency dependent and change over the time, frequency response mesurement or impulse response measurement are the best choice for estimating values for a particular transformer. Therefore it is necessary to explore a reliable technique in identifying parameters with limited access and knowledge of the internal windings of a transformer.

Chapter 3

Transformer Winding Distribution

A transformer winding may be represented as a large coil consisting of several elements. Fundamentally, the transformer consists of insulation materials and copper windings placed around a laminated core. The transformer can be described using a simple equivalent circuit which results in a lumped circuit parameter model [55, 101]. Typically, insulation is modelled using an equivalent capacitor, the coil windings represented by an equivalent inductor and the losses represented as equivalent resistors.

Different winding types will produce different reponses and therefore have different equivalent circuit configurations [46]. This can be seen clearly when comparing the typical plain winding type with the interleaved winding type. The winding arrangement for both types is almost similar except the connection between the coils of the coil pairs. The choice of connection affects the interturn capacitance between coils and the interleaved winding has a higher series capacitance [45]. Thus in the case of locating a partial discharge source within the winding it is necessary to consider the detailed construction of the transformer. A good model should give an initial indication of the voltage distribution resulting from any partial discharge within the transformer through the use of transient analysis.

3.1 The Transformer Experimental Model

The experimental transformer model was developed and manufactured by Alstom and it includes an interleaved disc winding and a plain disc winding. It was further developed by the Tony Davies High Voltage Laboratory at the University of Southampton [102]. The transformer is in an oil filled tank filled with oil of specification BS148:1998 class 1. The tank was manufactured at the Stanlow Works, UK (See Appendix A). One of its

main characteristics is that it is discharge free up to applied a.c voltages of 30 kV rms.

The structure of the model contains the two types of winding (interleaved and plain disc winding). Figure 3.1 shows the cross-sectional view of the two windings wrapped around a central core that is represented using an aluminium cylinder. The upper winding is interleaved and the lower winding is plain disc. The two windings have the same construction size and use identical materials. Every pair of discs of the both windings provides a terminal as a measurement point.

Each winding consists of 7 disc pairs (14 discs) stacked on each other, where terminal leads from outside the tank are connected to each one of the disc pairs to provide external access. The winding is manufactured from a copper conductor wrapped with paper insulation, and the specification of the transformer winding meets the standard requirements of IEC27260. A cylindrical core represents the laminated iron core and is grounded. The transformer winding is confined and sealed in a thin walled aluminium cylinder so that the behaviour of the transformer modes under transient conditions is as similar to that of a real transformer as possible. The connections between winding pairs are shown in Figure 3.2

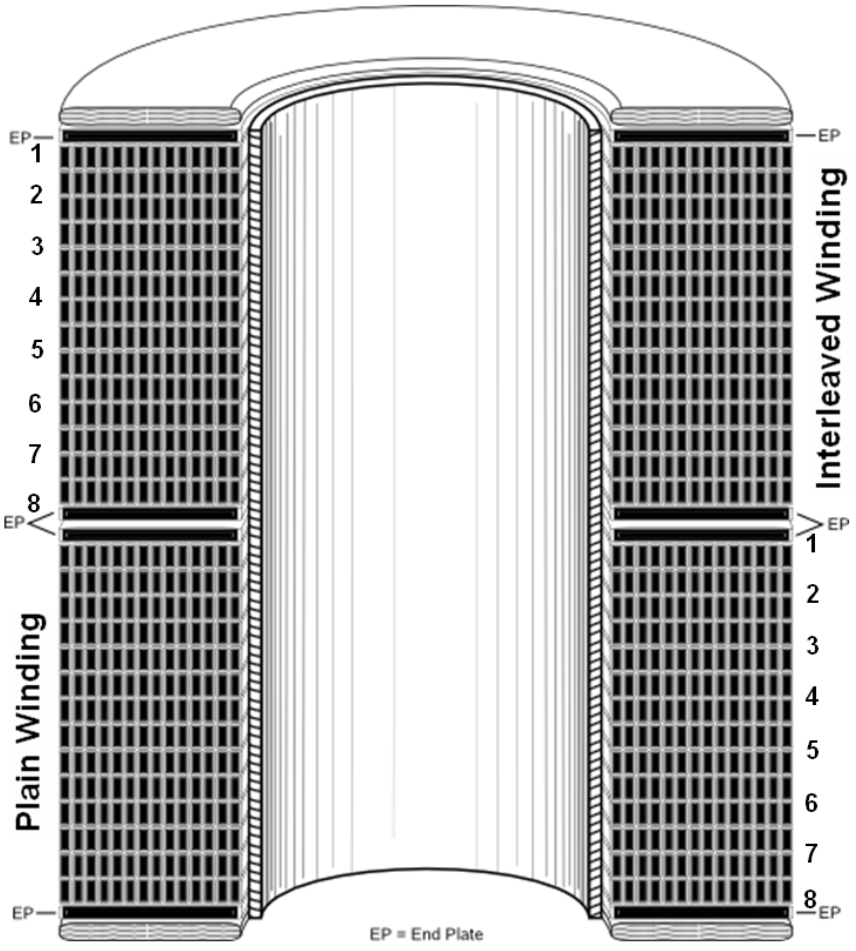

FIGURE 3.1: Crossectional view of the transformer winding model

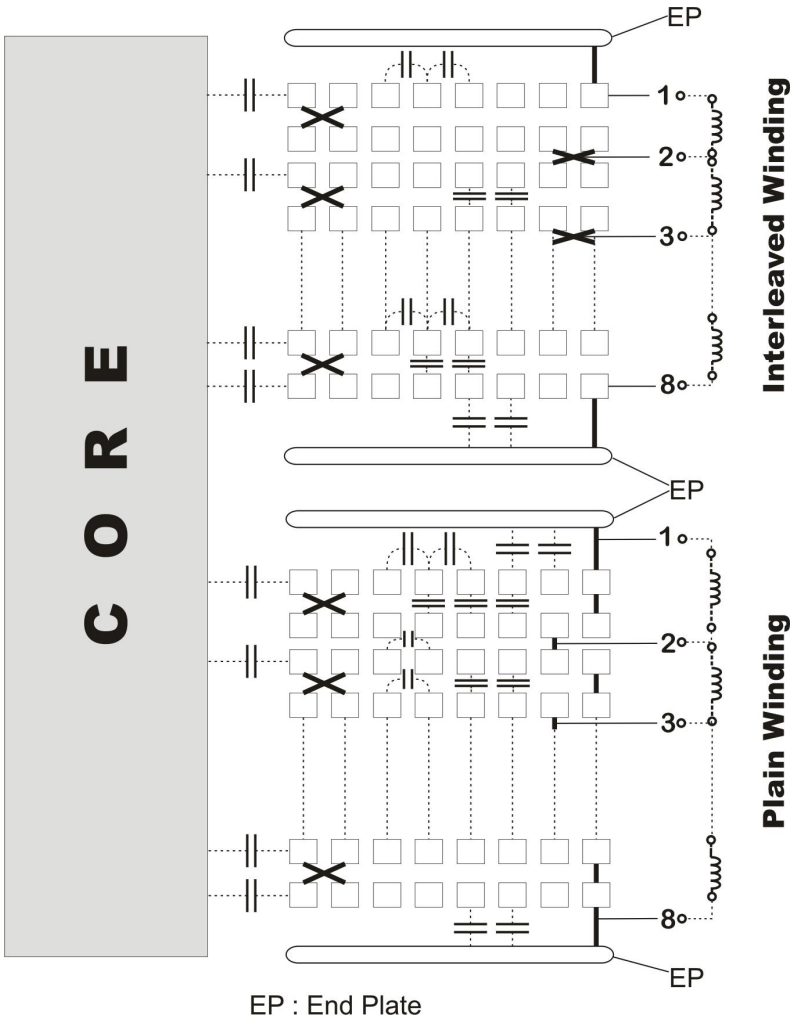

FIGURE 3.2: Capacitance and inductance arrangement on windings

3.2 Equivalent Circuit Model

In the transformer model, both windings are disc-type and each winding includes 14 discs. A pair of discs is called a 'section' where each section can be accessed externally with the direct connection from its terminals. The end connections of each winding are connected to an end plate (noted as EP in Figures 3.1 and 3.2). The use of an end plate is to support the mechanical coil stack and is also a convenient means of providing insulation to ground. It is also beneficial in reducing the end effects of the transformer winding and reduces the fundamental harmonic content. Figure 3.2 shows the arrangement of capacitance and inductance of both windings. This arrangement is based on the mechanical construction and represents the physical parameters of the winding itself. Generally, a transformer winding can be considered as an equivalent circuit of a very large inductor in series with its winding resistance. The paper insulation between the conductors can be represented as capacitances between adjacent conductors.

3.2.1 Plain Winding Series Capacitance

The schematic drawing of the disc coil of plain disc winding is shown in Figure 3.3. The capacitive elements are either of inter-turn capacitances C_g or inter-section capacitances K. To calculate the capacitance it is assumed that there is an even voltage distribution within the disc coil, hence accumulated energy can be determined using the sum of part capacitances [45].

Thus the resultant capacitance of one disc coil is:

$$C_r = C_{gr} + K_r \tag{3.1}$$

Suppose there are n turns in each section with the total of N sections per winding, the calculation of resultant inter-turn capacitance for the entire winding therefore is:

$$\sum^{N} C_{gr} = \frac{C_g}{Nn^2}(n-1) \tag{3.2}$$

whereas the resultant of inter-section capacitances are determined using:

$$\sum^{N} K_r = 4\frac{N-1}{N^2}K \tag{3.3}$$

Therefore the resultant series capacitance of the entire winding, from (3.2) and (3.3) can be described as:

$$C_r = \frac{1}{N}\left(\frac{n-1}{n^2}C_g + 4\frac{N-1}{N}K_r\right) \tag{3.4}$$

Figure 3.4 shows an example of winding dimensions for a typical single phase transformer.

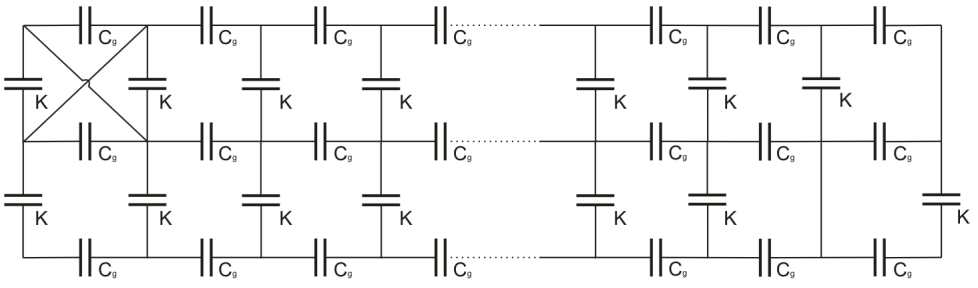

FIGURE 3.3: Schematic diagram of equivalent capacitive circuit for plain winding

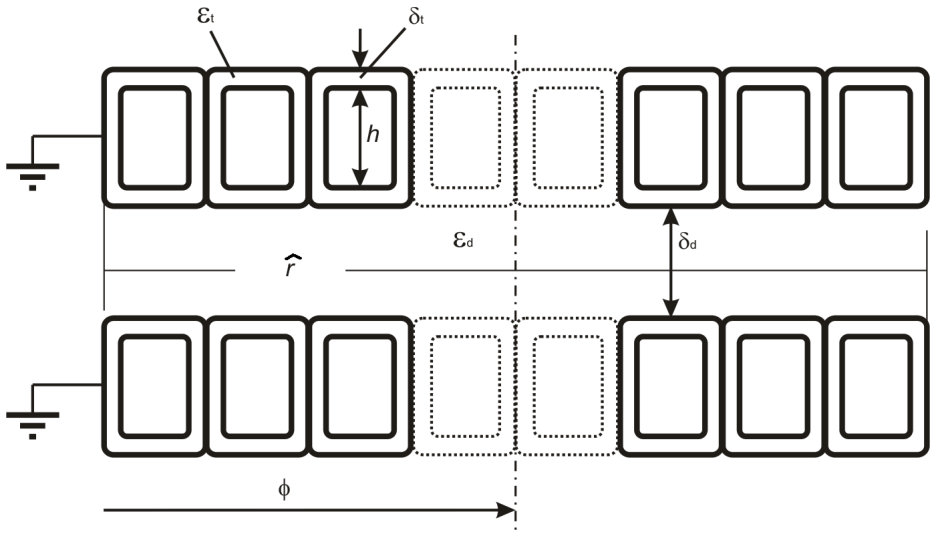

FIGURE 3.4: Winding dimensions

Where the following physical parameters are; $\overline{D}$, the mean winding diameter; h, the height of the copper conductor; $\hat{r}$, the radial diameter (or depth) of a disc; δ_t the thickness of inter-turn insulation and δ_d the spacer distance between adjacent disc. The electrical parameters are; ε_d, the permttivity of the oil and ε_t, the resultant of inter-turn permittivity of the oil plus paper insulation.

With reference to Figure 3.4, the inter-turn capacitance (C_g) and resultant inter-section capacitance (K_r) can be calculated using a known formula such that [45];

$$C_g = \varepsilon_t \varepsilon_0 \frac{D\pi(h + 2\delta_t)}{2\delta_t} = 27.8\overline{D} \frac{\varepsilon_t(h + 2\delta_t)}{2\delta_t} 10^{-12} \, F \, turn^{-1} \tag{3.5}$$

and

$$K_r = \frac{1}{3}\left[\varepsilon_0 \, D\pi \frac{r + \delta_d}{\frac{2\delta_t}{\varepsilon_t} + \frac{\delta_d}{\varepsilon_d}}\right] = 27.8\overline{D}\frac{1}{3}\frac{(\hat{r} + \delta_d)\varepsilon_t\varepsilon_d}{2\delta_t\varepsilon_d + \delta_d\varepsilon_t} 10^{-12} \, F \, section^{-1} \tag{3.6}$$

By solving Equations (3.4), (3.5) and (3.6), therefore the total series capacitance of a normal disc winding can be defined:

$$C_r = \frac{27.8\overline{D}}{N}\left[\frac{\varepsilon_t(h + 2\delta_t)}{2n\delta_t} + \frac{4}{3}\frac{(\hat{r} + \delta_d)\varepsilon_t\varepsilon_d}{2\delta_t\varepsilon_d + \delta_d\varepsilon_t}\right] 10^{-12} \, F \, winding^{-1} \tag{3.7}$$

3.2.2 Interleaved Winding Series Capacitance

By interleaving the winding end connections, the voltage distribution across the section can be made more uniform. To calculate the resultant capacitance of an interleaved winding, it is necessary to assume that the voltage distribution along the winding is linear for small values of series capacitance, and therefore intermediary voltages can be determined. Let E_x be the number of sections of from neutral to ground point, ϱ be the number of oil ducts within the windings, and κ be the number of non-adjacent parallel conductors. Therefore using similar relations as Equations (3.1) and (3.4) the series capacitance of interleaved winding can be found by [45]:

$$K = \frac{27.8\overline{D}}{N}\left[\frac{\varepsilon_t(h+2\delta_t)}{2\delta_t}\right](\kappa n - \varrho - 1)E_x^2\,10^{-12}\,F\,turn^{-1} \tag{3.8}$$

As it can be seen from Figure 3.5 the existence of conductors shorted as such at the end, reduces the inter-section capacitance. This however is dependant on the number of parallel conductors that exist to form interleaved windings. As compared to Figure 3.3 there are more parallel conductors on the edge end connections for an interleaved winding hence its radial length is less than that of a plain disc winding.

3.2.3 Series and Shunt Capacitance Calculation

According to equations (3.5) to (3.8), the interturn capacitance and intersection capacitance are dependant on the arrangement of parallel conductors between sections. This again indicates that the arrangement of plain winding differs from the interleaved winding at the connections between outer and inner points and this has a substantial effect on the values of capacitance. Table 3.1 details the parameters of the transformer winding model (further information can be found in Appendix A). Using these parameters capacitances have been calculated using Equations (3.5) and (3.8).

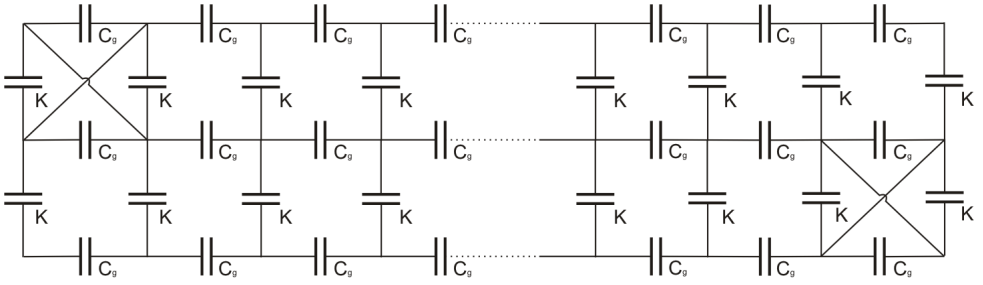

FIGURE 3.5: Schematic diagram of equivalent capacitive circuit for interleaved winding

TABLE 3.1: Calculated inter-section capacitance and inter-turn capacitance for the experimental transformer model

Parameters	**Dimensions**
$\overline{D}$: mean winding diameter	87.5mm
h: height of copper conductor	7.0 mm
$\hat{r}$: radial diameter or depth of disc	85 mm
δ_d: spacer between disc	3.0 mm
ε_d: permttivity of oil	(2.5 - 7)
δ_t: thickness of inter-turn insulation	1.0 mm
ε_t: resultant of inter-turn permittivity	2.63
N: Total number of section	14
n: Number of turn per-section	14
E_x: Intermidiary section under consideration	1 out of 14
ϱ: No of oil ducts between windings	14
Number of non-adjacent parallel conductors	
$\kappa\|_{interleaved}$:	10
$\kappa\|_{plain}$:	12
Parallel and Series Capacitance (Plain Winding)	
C_g:	28.79 pF
K:	60.010 pF
Parallel and Series Capacitance (Interleaved Winding)	
C_g:	28.79 pF
K:	257.04 pF

3.3 Travelling Waves Within a Transformer Winding

The distribution along a winding is often used to investigate the level of developed voltage inside a transformer winding. A non-invasive test can be undertaken using a traveling rectangular wave in order to validate any winding model. The application of a rectangular waveshape can be represented as a double exponential defined as [44]:

$$V(t) = V(e^{-at} - e^{-bt}) \tag{3.9}$$

in which V, a and b are arbitrary constants. The equation representing the travelling wave $V(t)$ has an impulse waveshape that is dependant on a and b. Figure 3.6 shows a typical response.

Figure 3.6 shows the principle of superposition of two exponential travelling waves, resulting in a simple impulse like wave. Note that the exponential wave at the top of the figure can be found by substituting the value of $b = \infty$, while the value of a is adjusted to give the desired wavetail. Similarly, to the bottom figure, by specifying the value of $a = \infty$, and adjusting the value of b, the wave can be explained using equation $-Ve^{-bt}$.

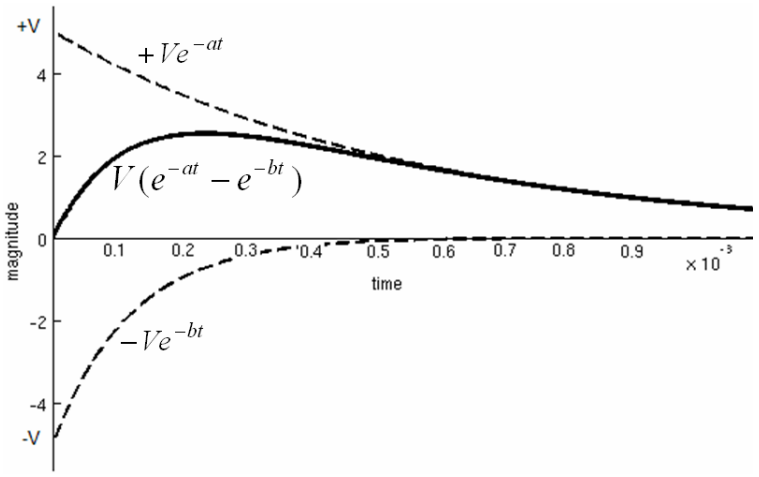

FIGURE 3.6: Superposition principle of two exponential travelling waves to represent the winding response to the application of the rectangular waveshape, $a = 2 \times 10^3$ and $b = 9 \times 10^3$

3.3.1 The influence of earth connection on travelling waves within a winding

When a travelling wave reaches a transition point, part of the wave may be reflected and the remainder pass on to another section. At the transition point itself the voltage (or current) will change in magnitude depending on the characteristics or the impedance of the terminal itself.

In the case of a transformer winding, it consists of several interconnected sections. Therefore, the equivalent circuit of a typical transformer winding is equivalent to a large inductor connected to ground. In order to study the effect different of winding configurations, let the reflected wave and the transmitted wave be denoted as v' and v'' respectively. Figure 3.7 shows the visualization of the respective transmitted and reflected wave derived from Equation (3.9).

The analytical solution for both kind of waves [44, 103], is as follows:

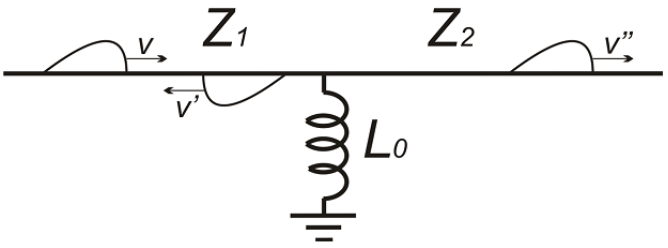

FIGURE 3.7: Reflected and transmitted wave form $v = V(e^{-at} - e^{-bt})$

$$v' = V\frac{\mu}{\nu}\left[\frac{a+\nu}{a-\mu}e^{-at} - \frac{b+\nu}{b-\mu}e^{-bt} + \frac{(a-b)(\nu+\mu)}{(a-\mu)(b-\mu)}e^{-\mu t}\right] \tag{3.10}$$

$$v'' = V\left(1+\frac{\mu}{\nu}\right)\left[\frac{a}{a-\mu}e^{-at} - \frac{b}{b-\mu}e^{-bt} - \frac{(a+b)\mu}{(a-\mu)(b-\mu)}e^{-\mu t}\right] \tag{3.11}$$

With reference to Figure 3.7, Z_1 and Z_2 are the surge line characteristic impedances derived using transmission line theory. In the case of the laboratory experiment, Z_1 and Z_2 are coaxial cables connected to the transformer winding for measurement that have a characteristic impedance of $Z_1 = Z_2 = 75\Omega$ [102] . The coefficient of ν and μ are the line impedance coefficients that are dependant on the inductance of the transformer winding and are derived as follows:

$$\begin{aligned} \nu &= \frac{Z_1 Z_2}{L_0(Z_2 - Z_1)} \\ \mu &= \frac{Z_1 Z_2}{L_0(Z_1 + Z_2)} \end{aligned} \tag{3.12}$$

Figure 3.8 shows the effective inductance under the influence of a transient incident signal. A rectangular wave was used, as the wavefront is similar to the incident wave of a dirac delta function. The response of the winding can be seen from its wavetail that represents the reverberation process of the winding at high frequency.

The result of Figure 3.8 shows a comparison of travelling waves for the interleaved and plain windings. A rectangular wave was injected at Terminal 1 (refer Figure 3.2) in each case using a function generator, and measured the response at same terminal on an oscilloscope. Theoretically, the travelling wave experiences damping dependent on the connection to ground. Due to the lower inductance of the plain winding the decay rate is faster compared to the interleaved winding, as estimated using Equation (3.11); $L_0 = 16.1mH$ for interleaved winding and $L_0 = 2.65mH$ for plain winding. Experiments revealed that the plain winding took about $45\mu s$ to decay to half value of the injected magnitude, compared to $450\mu s$ for the interleaved winding.

The plots of the calculated waveform are by using measured inductance value of $L_0 = 16.1mH$ for interleaved winding and $L_0 = 2.65mH$ for plain winding. The plots of winding response to the injection of an infinite rectangular wave shows a reduction of voltage level over time, dependant on where the signal is injected with respect to the ground connection. The distribution of inductance within the interleaved is constant with respect to the distance from the ground connection. For the plain winding the distribution of inductance is greatest towards the centre of the winding.

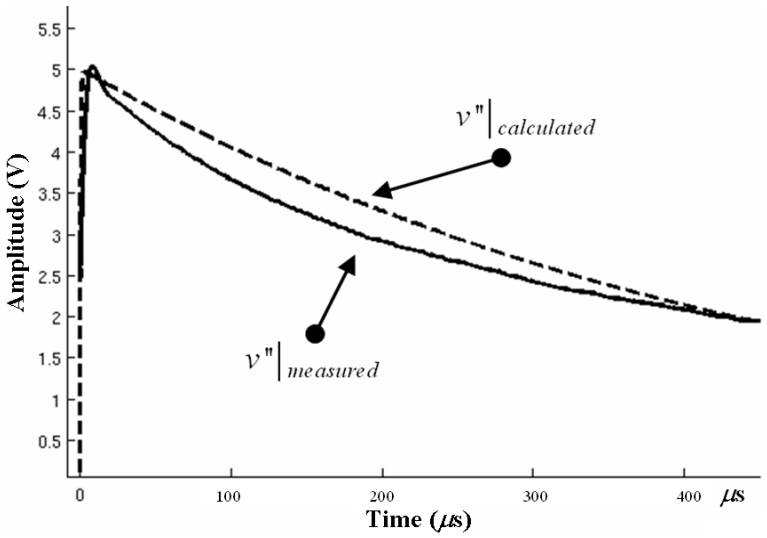

(a) Interleaved winding

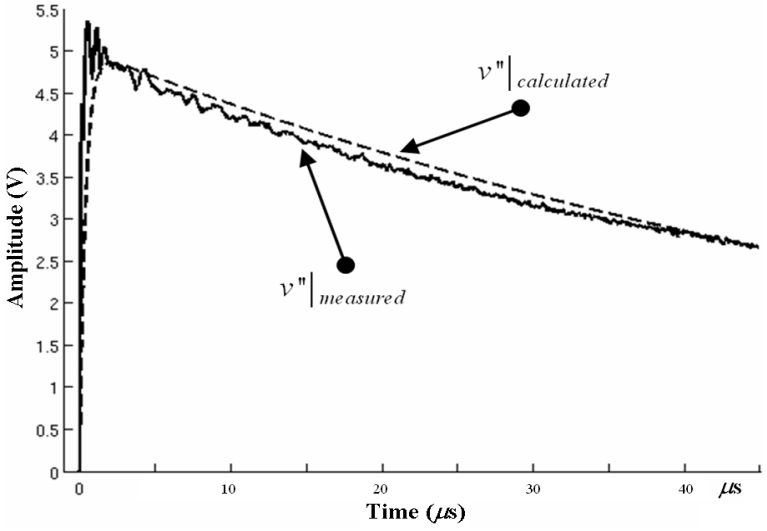

(b) Plain winding

FIGURE 3.8: Comparison of infinite rectangular wave for grounded windings. (a) Interleaved winding; $L_0 = 16.1mH$. (b) Plain winding; $L_0 = 2.65mH$

In order to investigate the amplitude of any incident wave within the winding, the same calibrated rectangular wave was injected at different positions along the winding. Obtained results are shown in Figure 3.9. Both Figure 3.9(b) and 3.9(d) are signals of the transmitted voltage level at different injection points. It is clear that the damping factor of the travelling wave is influenced by the distance between the injection point and the ground level. Thus, analytically the effective inductance at various injection points can be approximated using the same solution and obtained results are tabulated in Table 3.2.

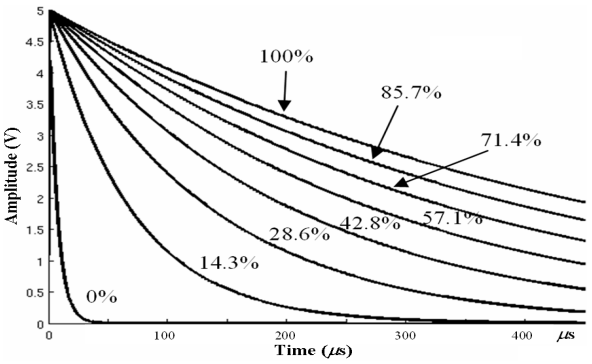

(a) Model simulation (Interleaved winding)

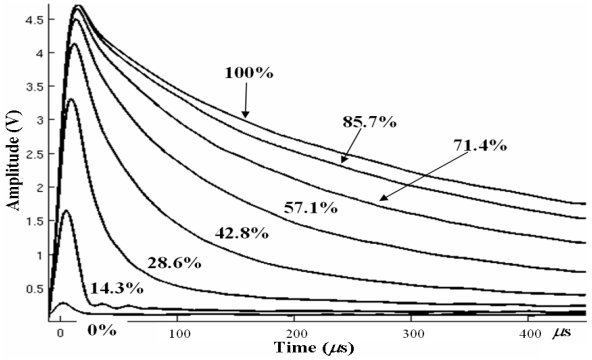

(b) Interleaved winding measurement

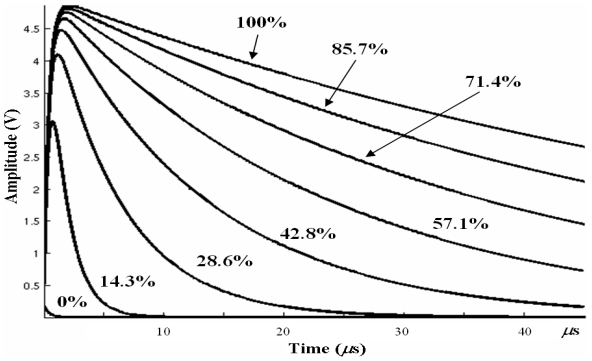

(c) Model simulation (Plain winding)

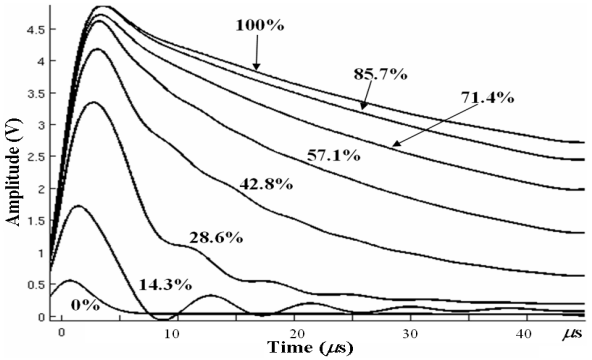

(d) Plain winding measurement

FIGURE 3.9: Comparison of response to injection of an infinite rectangular wave for grounded windings (0%: Neutral point; 100%: Bushing point). (a) Interleaved winding simulation; (b) Interleaved winding measurement; (c) Plain winding simulation and (d) Plain winding measurement

TABLE 3.2: Table of effective inductance

Position from Neutral	Interleaved winding	Plain winding
100% (Bushing)	16.1mH	2.65mH
85.7%	13.8mH	2.3mH
71.4%	11.5mH	1.7mH
57.1%	9.2mH	1.2mH
42.8%	6.9mH	0.8mH
28.6%	4.6mH	0.45mH
14.3%	2.3mH	0.15mH
0% (Neutral)	0.23mH	0.015mH

3.4 Determining the Possible Source of a Travelling Wave

The transformer winding distribution represents the voltage level for a certain disc coil or pair of disc coils. The voltage levels for interleaved winding and plain winding as seen from Figure 3.9 are similar to each other. The variation of inductance between the two is entirely due to the different connection arrangements at the winding pair end points.

To model wave propagation it is necessary to identify an equivalent circuit that represents the physical parameters of the winding. Under the influence of a transient wave the windings are represented with an equivalent circuit of capacitance, resistance and inductance in series (Figure 3.10). Different equivalent circuit arrangements can be modeled according to their physical properties and the influence of different operating frequencies [104].

With reference to Figure 3.10, N is the neutral terminal, B the bushing terminal, C_g the shunt capacitance to ground, and K the series capacitance. x is the distance at any point along the transformer winding, where $x = 0$ at neutral line and $x = l$ represents the bushing tap point.

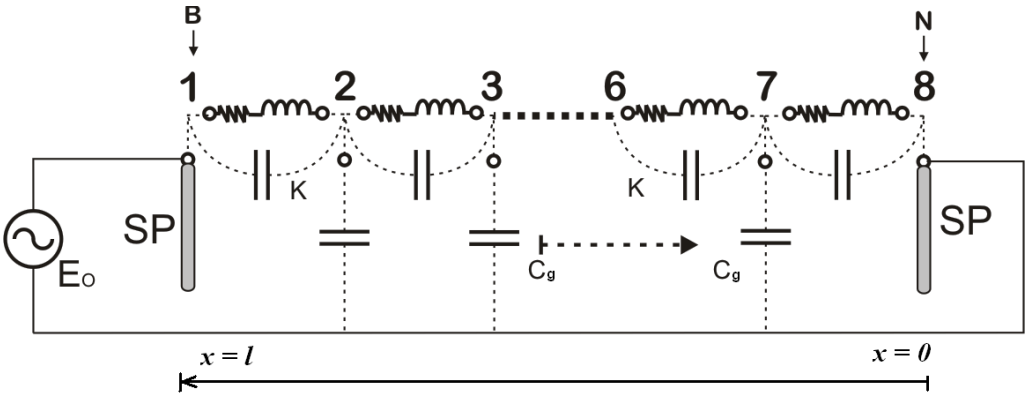

FIGURE 3.10: Equivalent inductance, resistance and capacitance in transformer winding

3.4.1 Initial Distribution Network

Suppose an infinite rectangular wave is injected from a source and travels to the terminal, the winding is considered as consisting of a network of capacitances, inductances and resistances. At the instance of injection, the incident wave of the current through the series inductance is zero. Therefore the winding acts as an instantaneous open circuit. However, the series capacitance acts as a short circuit, that allows current to flow until the capacitance achieves a fully charged condition. Therefore, at the instant of injection of a rectangular travelling wave, the equivalent circuit consists only a network of series and parallel capacitances. Figure 3.11 shows the equivalent circuit network which is also known as the initial distribution circuit. With reference to Figure 3.11, $Z(p)$ represents the impedance between the end terminal of the winding and ground.

3.4.2 The Divergence of an Incident Wave along the winding

At any instant in time, if an arbitrary input signal is applied at a point x' along the transformer winding, a current in the transformer winding will flow away from the source in two directions as shown in Figure 3.12.

With reference to Figure 3.12 i_{kn} is the transmitted signal in the direction towards neutral line (ground connection) and i_{kb} is the transmitted signal in the direction towards bushing terminal. Considering the direction towards the neutral line to be positive, the divergence of current according to Kirchoff's Current Law (KCL) can be solved by:

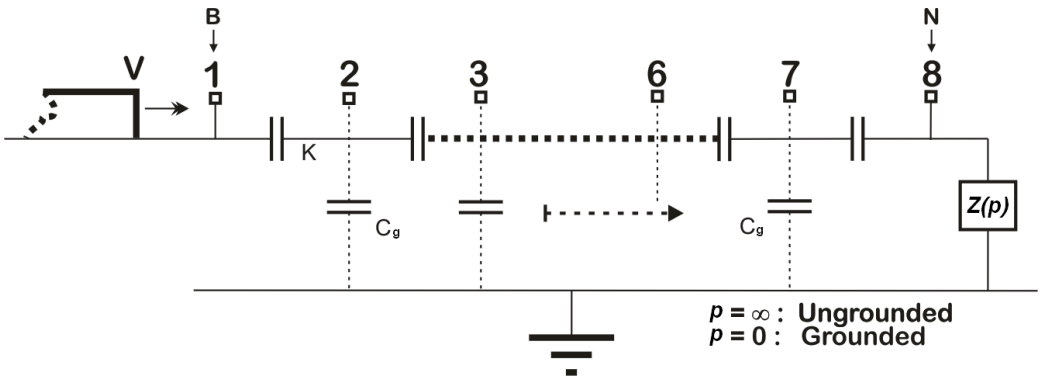

FIGURE 3.11: Initial distribution capacitive circuit

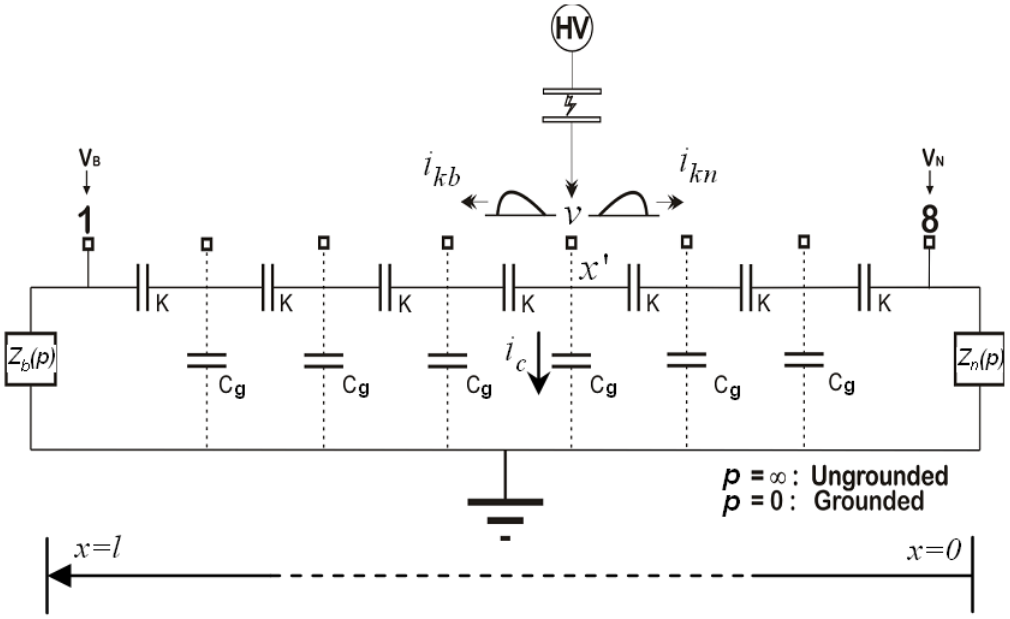

FIGURE 3.12: Current divergence for initial distribution network

$$\nabla . i = 0 \tag{3.13}$$

Hence solving Equation (3.13) for all currents, the divergence of current is define as:

$$\frac{\partial i_k}{\partial x} + i_c = 0 \tag{3.14}$$

where i_k is the current flowing in series capacitance (K) and i_c is the current flowing in shunt capacitance to ground (C_g) [55]. For which:

$$i_k = K \frac{\partial^2 v}{\partial x \partial t} \tag{3.15a}$$

$$i_c = C_g \frac{\partial v}{\partial t} \tag{3.15b}$$

By solving Equations (3.14) and (3.15), and cancelling the operator $\frac{\partial}{\partial t}$ on both sides, the following partial differential equation (PDE) is developed:

$$\frac{\partial^2 v}{\partial x^2} - \alpha^2 v = 0 \tag{3.16}$$

where the fixed distribution constant, α, is:

$$\alpha = \sqrt{\frac{C_g}{K}} \tag{3.17}$$

With reference to Figure 3.12, let v_b be the voltage distribution along transformer winding towards bushing and v_n be the voltage voltage distribution towards neutral to ground connection. Hence the terms v_b and v_n corresponds to the two different directions of current flow along the winding with respect to i_{kb} and i_{kn} respectively, i.e.

$$v_b; \qquad x' \leq x \leq l \tag{3.18a}$$

$$v_n; \qquad 0 \leq x \leq x' \tag{3.18b}$$

The solution of the PDE from Equation (3.16) will have solution towards Neutral as :

$$v_n(x) = A\, cosh(\alpha x) + B\, sinh(\alpha x) \tag{3.19}$$

and the tentative solution towards Bushing as:

$$v_b(x) = \mathfrak{A}\, cosh\,(\alpha x) - \mathfrak{B} sinh\,(\alpha x) \tag{3.20}$$

Let V_{sec} be the voltage per-section along transfomer winding and applying Kirchoff's Voltage Law (KVL) for the solution towards Bushing, the following is derived;

$$\alpha\mathfrak{A}\, sinh\,(\alpha x) - \alpha\mathfrak{B} cosh\,(\alpha x) + V_{sec} = 0 \tag{3.21}$$

Solving Equations (3.20) and (3.21) simultaneously, hence the general solution towards Bushing can be written in the form of:

$$v_b(x) = C\, sech\,(\alpha x) - D\, tanh\,(\alpha x) \tag{3.22}$$

Where the arbitrary constants of C and D are equal to:

$$C = \mathfrak{A} \tag{3.23a}$$

$$D = \frac{V_{sec}}{\alpha} \tag{3.23b}$$

The two Equations (3.19) and (3.22) are subject to boundary conditions [44]:

$$v_b(x) = V_B \qquad at \qquad x = l \tag{3.24a}$$

$$v_n(x) = V_N \qquad at \qquad x = 0 \tag{3.24b}$$

$$v_b(x) = v_n(x) \qquad at \qquad x = x' \tag{3.25a}$$

$$\frac{dv_b(x)}{dx} = \frac{dv_n(x)}{dx} \qquad at \qquad x = x' \tag{3.25b}$$

Regardless of the value of the terminal impedance at the bushing, $Z_b(p)$, and at neutral point, $Z_n(p)$, V_B and V_N are the terminal conditions considered for analysis and can be obtained from measurement. Hence According to the conditions defined in (3.24),

$$A = V_N \tag{3.26a}$$

$$C\,sech\,(\alpha l) - D\,tanh\,(\alpha l) = V_B \tag{3.26b}$$

and applying (3.25), yields:

$$C\,sech\,(\alpha x') - D\,tanh\,(\alpha x') = V_N\,cosh\,(\alpha x') + B\,sinh\,(\alpha x') \tag{3.27a}$$

$$-C\,tanh\,(\alpha x')\,sech\,(\alpha x') - D\,sech^2\,(\alpha x') = V_N\,sinh\,(\alpha x') + B\,cosh\,(\alpha x') \tag{3.27b}$$

Solving (3.26) and (3.27) simultaneously yields expressions for the variables B, C and D;

$$B = C\,sech\,(\alpha x')\,csch\,(\alpha x') - D\,sech\,(\alpha x') - V_N\,coth\,(\alpha x') \tag{3.28}$$

$$C = \frac{V_B\,cosh\,(\alpha l)\,sinh^3(\alpha x') - V_N\,sinh\,(\alpha l)\,cosh^2(\alpha x')}{sinh^3(\alpha x') - sinh\,(\alpha l)\Big[cosh^2(\alpha x') + sinh^2(\alpha x')\Big]} \tag{3.29}$$

$$D = \frac{V_B\,cosh(\alpha l)\Big[cosh^2(\alpha x') + sinh^2(\alpha x')\Big] - V_N\,cosh^2(\alpha x')}{sinh^3(\alpha x') - sinh\,(\alpha l)\Big[cosh^2(\alpha x') + sinh^2(\alpha x')\Big]} \tag{3.30}$$

The solution of Equations (3.19) and (3.22) have x' dependant terms. The distribution of the transformer winding in this case provides two solutions based on the direction of current, either towards bushing tap point or towards neutral tap point. When modelling the voltage distribution one has to consider the distance range from the identified signal source towards the ends of the winding. However an alternative solution of current divergence solution by considering the whole winding length, $l - x$, can be found in Appendix B

3.4.3 Initial Distribution Near the Bushing Terminal

The solutions from (3.19) and (3.22) require the measurement on both sides of the winding end terminals. However an estimation of winding distribution can be made by considering the terminated impedance of $Z_b(p)$ and $Z_n(p)$. By considering the PDE solution of (3.16) and rewriting the equation for the near bushing terminal:

$$\frac{\partial^2 v_n}{\partial x^2} - \frac{C_b}{K_b} v_n = 0 \tag{3.31}$$

where $\alpha = \alpha_b = \sqrt{\frac{C_b}{K_b}}$ near the bushing.

The solution of Equation (3.31) is also in the form of

$$V = A_n e^{\alpha_b x} + B_n e^{-\alpha_b x} \tag{3.32}$$

From the definition (3.15), and also using the differential operator, $\rho \equiv \frac{\partial}{\partial t}$, the currents away from the bushing are;

$$i_n = K\rho\frac{\partial v_n}{\partial x} = K\rho\alpha_b\big(A_n e^{\alpha_b x} - B_n e^{-\alpha_b x}\big) \tag{3.33}$$

By considering the case where the end termination impedance is directly grounded at the neutral end, and the applied voltage at bushing end is V_B, the boundary conditions of the solution are:

$$\begin{aligned} at \quad x = l: \qquad & v_n = V_B = A_n e^{\alpha_b l} + B_n e^{-\alpha_b l} \\ at \quad x = 0: \qquad & v_n = 0 = Z_n(p) i_n = Z_n(p)\rho\sqrt{C_b K_b}(A_n - B_n) \\ & \quad = A_n + B_n \end{aligned} \tag{3.34}$$

Solving for the two constants of A_n and B_n, yields [55];

$$A_n = \frac{V_B\big[Z_n(p)\rho\sqrt{C_b K_b} + 1\big]}{2\big[sinh\,(\alpha_b l) + Z_n(p)\rho\sqrt{C_b K_b} cosh\,(\alpha_b l)\big]} \tag{3.35}$$

$$B_n = \frac{V_B\big[Z_n(p)\rho\sqrt{C_b K_b} - 1\big]}{2\big[sinh\,(\alpha_b l) + Z_n(p)\rho\sqrt{C_b K_b} cosh\,(\alpha_b l)\big]} \tag{3.36}$$

Therefore the initial distribution equation near the bushing point is equivalent to

$$v_n(x) = V_B \frac{Z_n(p)\rho\sqrt{C_b K_b}\, cosh(\alpha_b x) + sinh(\alpha_b x)}{Z_n(p)\rho\sqrt{C_b K_b}\, cosh(\alpha_b l) + sinh(\alpha_b) l} \tag{3.37}$$

For the grounded neutral point, $Z_n = 0$, the level of distribution at $x = 0$ is theoretically $0V$, and in this case the new initial distribution is:

$$v_n(x) = V_B \frac{sinh(\alpha_b x)}{sinh(\alpha_b l)} \tag{3.38}$$

and the initial distribution equation for the ungrounded neutral, $Z_n = \infty$, becomes

$$v_n(x) = V_B \frac{cosh(\alpha_b x)}{cosh(\alpha_b l)} \tag{3.39}$$

These results were obtained taking into consideration the alternative solution in Appendix B of Equation (B.19), where voltages at the winding end terminals are measurable. The solution (B.1) will have the same solution as Equation (3.38) by considering $V_N = 0V$, Where constants C and D from Equations (B.17) and (B.18) respectively become:

$$C = \frac{V_B\Big[cos(j\alpha l)tanh(\alpha l) - sin(j\alpha l)\Big]}{tanh(\alpha l)}\Bigg|_{V_N=0V} \tag{3.40}$$

$$D = \frac{V_B\Big[cos(j\alpha l) + sin(j\alpha l)tanh(\alpha l)\Big]}{tanh(\alpha l)}\Bigg|_{V_N=0V} \tag{3.41}$$

Hence the initial distribution equation is obtained by substituting (3.40) and (3.41) into Equations (B.1) and (B.10), to give

$$v_n(x) = V_B \frac{sinh(\alpha x)}{sinh(\alpha l)}\Bigg|_{V_N=0V} \tag{3.42}$$

Therefore the solution for the source of the travelling wave near the bushing points is similar for when the source is near the bushing point.

3.4.4 The Effects of End Plates

An end plate, also known as static plate (SP), is used as a mechanical support for the transformer winding. It has a considerable benefit in equalizing the voltage distribution along the winding over the first few sections. However, it is only of benefit for short stacks of wide coils, in long stacks with narrow coils, the effect of end plates do not seem effective in equalizing the distribution between the end terminals [44].

With the experimental model, the end plate was made from an aluminium plate wrapped with crepe insulation paper. It covers the whole top and bottom of the winding stack. It is directly connected to an external terminal, which is connected to the bushing. Hence it has a response similar to the bushing tap response when a wave is injected or measured at this point.

Redrawing Figure 3.2, to include the effect of an end plate, Figure 3.13, shows an illustration of end plate to the overall winding along the whole width of the stack, $0-q$, where q is the width of the stack. However the analysis of the end plate on the overall voltage distribution is limited in terms of the terminal response measurements. As it is not possible to measure the static plate distribution along the y-axis, the analytical solution presented is based on the influence of end plate to the x-axis voltage distribution. In other words the same lumped parameter model is used for its capacitive network to study the influence of the end plate on the overall winding distribution, where the distribution can only be measured along the x-axis.

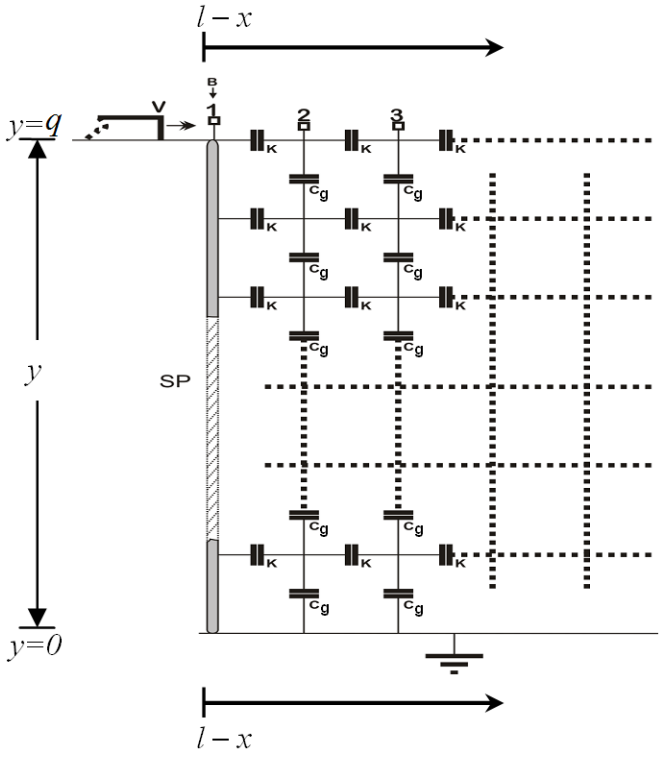

FIGURE 3.13: Effect of end plate

The end plate provides a short circuit to the nearest series capacitance to ground, C_g, from $y = 0$ to $y = q$ which reduces the capacitance near the end plate on x-axis. The end plate however has an almost negligible effect on the series capacitances, K, because the arrangement of series capacitance is perpendicular to the axis of end plate. Therefore, the nearest stack or nearest capacitance on x-axis will have the most significant effect compared to the other distributed capacitance.

Hence, α can be rewritten as α_{bep} for the end plate near the bushing where:

$$\alpha_{bep} = k\alpha(l - x) \tag{3.43}$$

where k is a constant.

Figure 3.14 shows a simulation of the effect of the static plate on the winding distribution near the bushing tap point on the x-axis for 50% of its total length l. The simulation was run in Matlab environment where the constant k was set a value of one. The simulation models a distribution for the injection of infinite rectangular wave at terminal 1.

With reference to Figure 3.15, let m_t be constant gradient of voltage distribution at time t, near the bushing tap point. The effect of m_t is to alter the value of α_{bep} such that the higher the value of m_t the higher the value of α_{bep}. Figure 3.14(a) demonstrates that, without the analysis of static plate at the bushing point, the distribution of the winding voltage is a normal transformer winding distribution that agrees with the model Equations (B.19). However, including an end plate and considering a travelling wave near the bushing the distribution approaches a constant. It can also be clearly seen in the measured distributions of Figure 3.15(a) and 3.15(b), that the distribution is flatter in the non-linear region of the winding. In the region below 70% of the winding length, the distribution is linear. m_t can be approximated using the gradient of the non-linear distribution, where from Figure 3.15;

$$m_1 > m_2 > m_3 \tag{3.44}$$

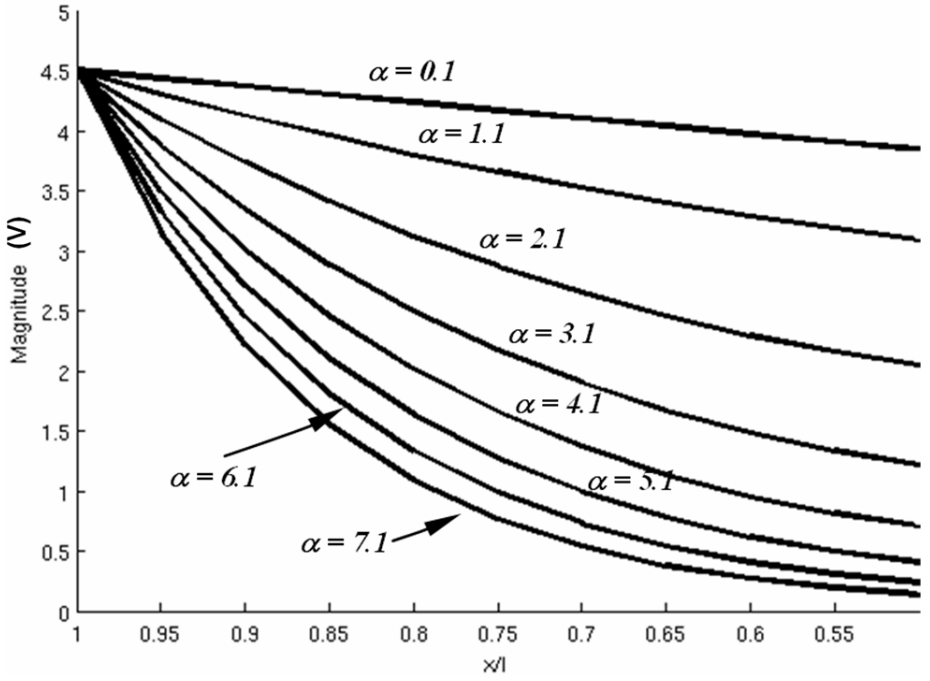

(a) Simulation without end plate

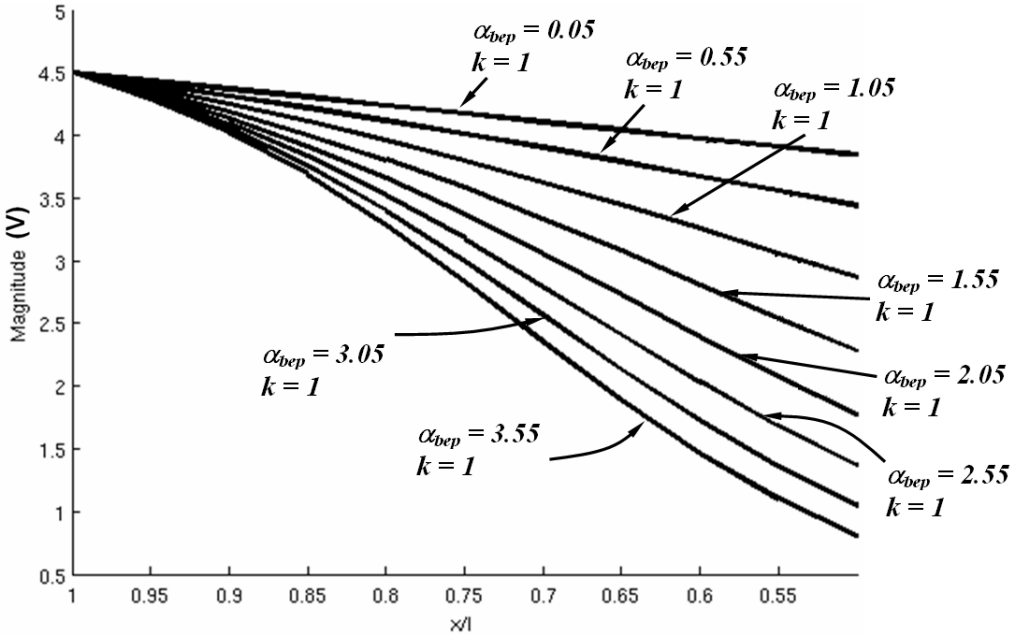

(b) Simulation with end plate

FIGURE 3.14: Effect on winding distribution near bushing of an end plate.

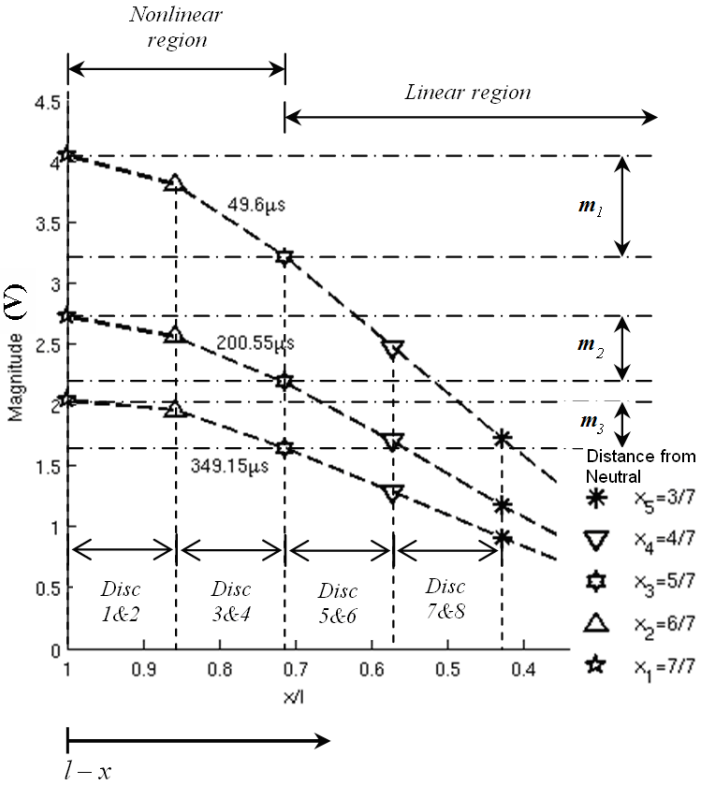

(a) Interleaved winding

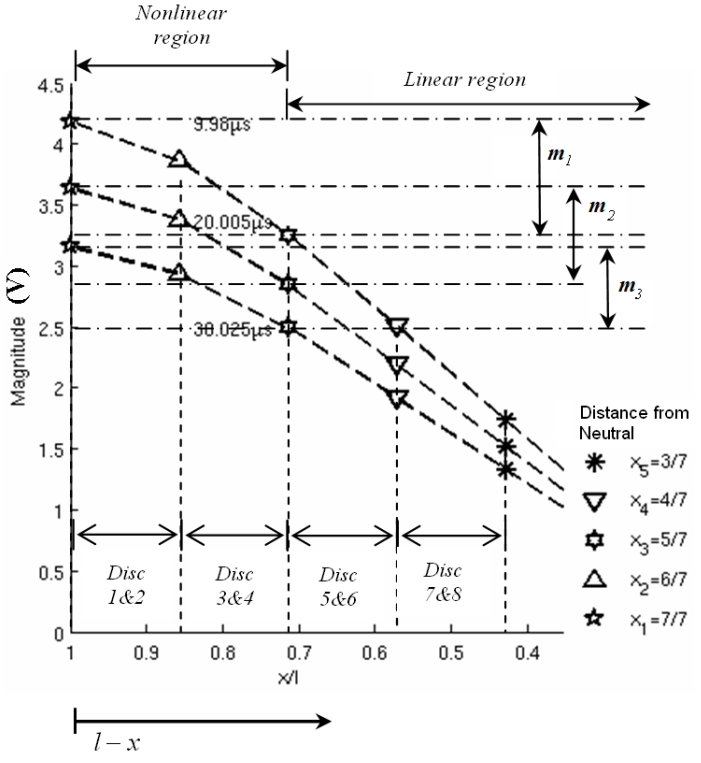

(b) Plain winding

FIGURE 3.15: Winding distribution near bushing in the presence of an end plate.

3.5 Time Domain Representation from Measurement and Voltage Distribution

A simulation was undertaken in order to model solutions of Equations (3.19) to (3.30). The source of signal is simulated using the transmitted travelling wave of Equation (3.11). The transmitted signal is modelled using different values of L_0 (effective inductance from ground), which is calculated as a coefficient at different terminals of injection [105] as shown in Table 3.2. The winding model was calculated for a ground connection, for Z_n equivalent to 0Ω. The simulation is also considered for the configuration of ungrounded winding near the bushing tap point. An infinite rectangular wave of Equation (3.9) is used to simulate the injected signal;

$$a = 0; \qquad b = 1.5 \times 10^6 \tag{3.45}$$

However, from Equation (3.9) the value of b can be of any range that resembles an infinite constant response.

Considering the injection at the bushing tap point, based on the calculated values of capacitance parameter as in Table 3.1, the fixed distribution coefficient, α is simply calculated by taking the ratio of shunt capacitance to ground (C_g) to the series capacitance along winding (K). Figure 3.16 shows the comparison of the simulation based on the calculated parameter with the real measurement of the transformer distribution using Equtions (3.42) and (3.43). For the interleaved winding the distribution plot versus the distance from neutral end connection is extracted for $50\mu s$, $200\mu s$ and $350\mu s$ time sequences (Figure 3.16(a)). While for plain winding it is extracted at $5\mu s$, $20\mu s$ and $35\mu s$ time sequences (Figure 3.16(b)). Both windings show close agreement to the calculated fixed distribution coefficients.

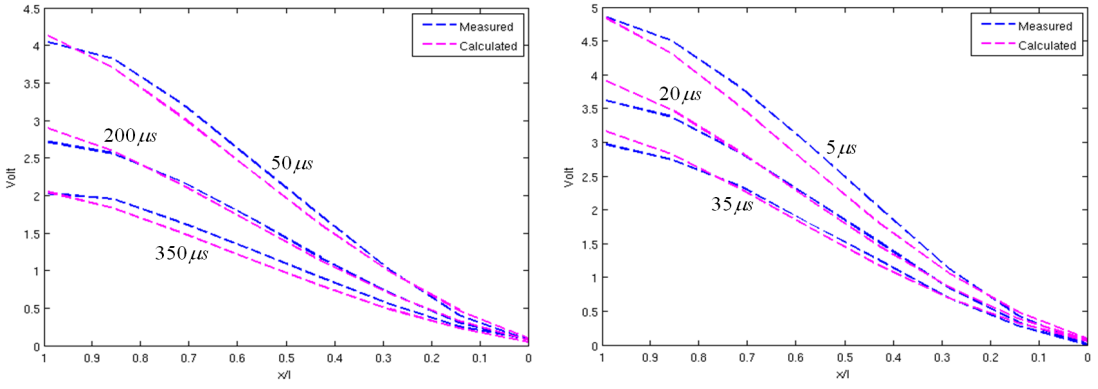

(a) Interleaved winding, $k = 5.9143; \alpha = 0.35$ (b) Plain winding, $k = 3.2714; \alpha = 0.70$

FIGURE 3.16: Winding distribution near bushing with the present of end plate

Figures 3.17 and 3.18, show the simulation results of winding voltage distribution for different sources of the infinite rectangular wave. The simulated transmitted waves are as shown in Figure 3.9(a), where the injected signal is damped by the effect of the ground connection that effects the coefficients ν and μ. Where both ν and μ are inversely proportional to the inductance value of the simulated winding that is lower at the point of injection and increases the damping of the transmitted wave.

The voltage distributions of the transformer winding are extracted by taking the level of simulated amplitude in the time domain for three different sampling times, $50\mu s$, $200\mu s$ and $350\mu s$. An experiment was undertaken on both the interleaved winding and the plain winding, to investigate the winding distribution. A 5V infinite rectangular wave with a $50ns$ rise time was injected at different terminals on the windings. The time domain responses of the windings were measured for all terminals. The transition and the amplitude of the injected wave were kept constant at all time. This is to ensure that the transformer winding will have the same excitation regardless of the different positions of injection.

The response of the transformer windings is oscillatory, hence interpolation technique is used extract the time domain fundamental waveform [106]. Then, the voltage level of the windings is extracted at different sampling times near $50\mu s$, $200\mu s$ and $350\mu s$ for interleaved winding and near $5\mu s$, $20\mu s$ and $35\mu s$ for plain winding. Figures 3.19 and 3.21 show the time domain representation of the transmitted wave injected at different source x' from neutral to ground connection for interleaved winding and plain winding respectively. The vertical dotted lines illustrate the extraction technique to determine the level of voltage at different terminals as a response of the current divergence excited by the capacitive distribution network.

Figures 3.17 and 3.18 show the pattern simulation for the model winding defined in section 3.4.2. The model uses a lower value of fixed distribution coefficient, ($\alpha = 1.5$). A similar technique is used as earlier, where the distribution is extracted for different times and plotted. As the source moves from terminal bushing to neutral ground terminal, the pattern shows the voltage level is balanced at the top of the winding close to terminal 1. At the source of $x' = 0/7$ the voltage levels are very low and approach zero.

By comparing both the simulation and measurement results, the winding distributions show very similar patterns. These initial distributions are extracted for both simulation and measurements for the $0s$ to $450\mu s$ for the interleaved winding and sampling times with 10MS/s sampling rate and $0s$ to $45\mu s$ for the plain winding. The voltage distribution of Figures 3.19(h), 3.20(h) and 3.21(h), 3.22(h) are for the ground connection simulation and measurement for the interleaved winding and plain winding respectively. The distributions are near zero and do not vary much over the sampling times $-9.4\mu s$ to $9.5\mu s$. The presence of a static plate at the neutral terminal does not significantly change the level of distribution. This is because the end neutral terminal is connected

directly to ground.

The voltages for both windings differ over instants of time but the patterns are very similar in that the measurements for both windings have almost level voltages at the top of the winding, close to bushing tap point. When the injection point is at terminal 1, it also shows that the effect of the end plate is to even out the voltage distribution, as does the end plate at the neutral point. The extraction of voltage levels at different instants of time shows that the later the time of extraction, the more the voltage level has changed.

3.6 Summary

A novel technique for determining the voltage distribution due to the injection of a rectangular wave has been derived based on the capacitive parameters of the transformer winding. The rectangular incident of instantaneous current and voltage from the injection of the infinite rectangular wave, excites the winding's capacitive elements. It is possible to derive the fixed distribution coefficent α, that is solely dependant on the inter-turn capacitance, C_g, and inter-section capacitance, K, also known as series capacitance and shunt capacitance respectively. From the dimensions of the windings, provided that there has been no displacement or winding movement, the winding voltage distribution can be estimated.

The injection of a travelling wave at an intermidiary point on the winding, has shown that the divergence of current may be represented by two PDEs. This in turn gives insight into the way that current propagates and determines the voltage distribution of the transformer winding. Without considering the end plate, however the level of distribution towards the end winding would be the same as for a long stack of windings of short diameter disc coils. From the model equation, it shows that the presence of end plates can be modelled as a short circuit effect, hence smoothing the voltage distribution near the bushing tap point. The hypothesis is that it is possible to determine the source of signal injection by undertaking simultaneous measuremements at both the bushing tap and neutral point. To illustrate this, comprehensive simulation and measurements from the experimental winding model have been undertaken as detailed in section 3.4.2.

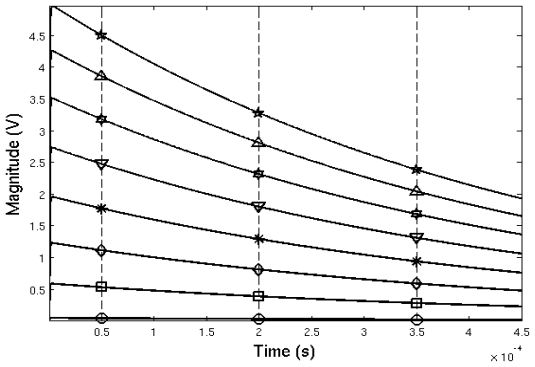

(a) $x' = 7/7$

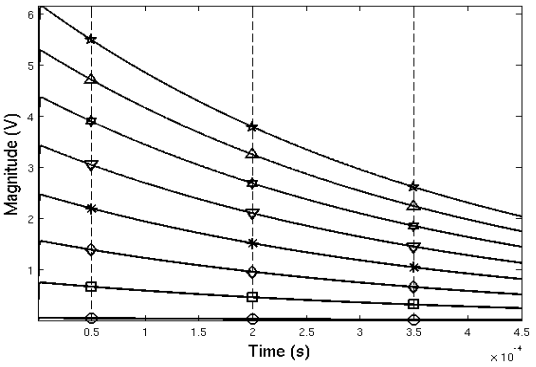

(b) $x' = 6/7$

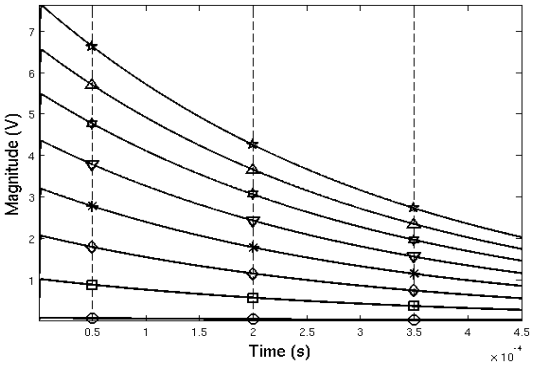

(c) $x' = 5/7$

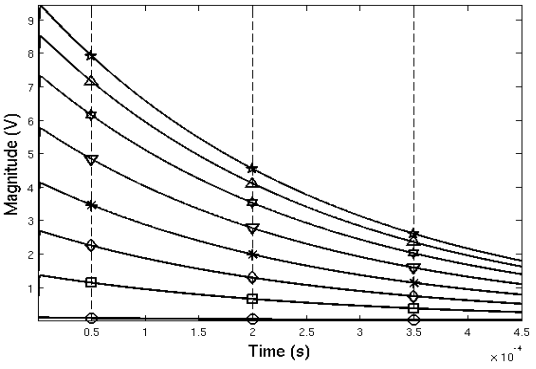

(d) $x' = 4/7$

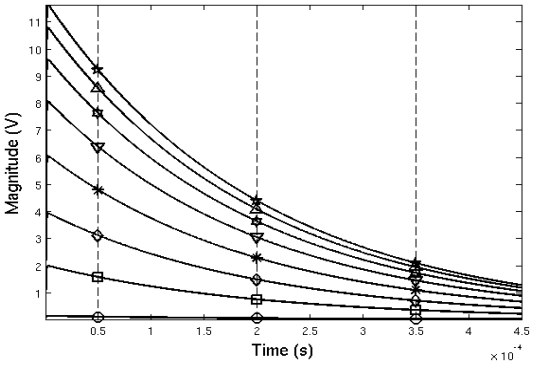

(e) $x' = 3/7$

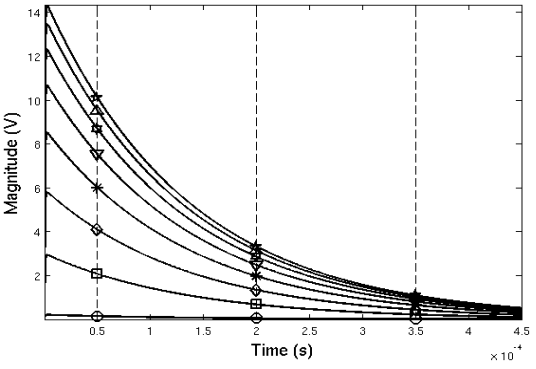

(f) $x' = 2/7$

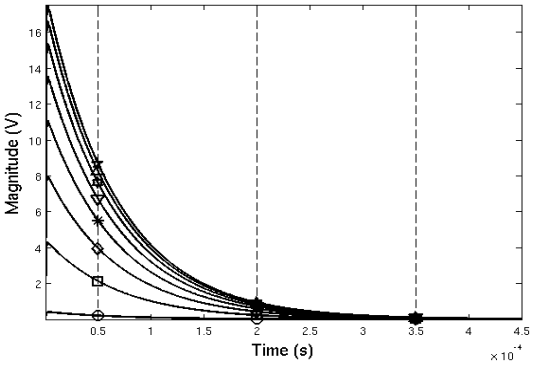

(g) $x' = 1/7$

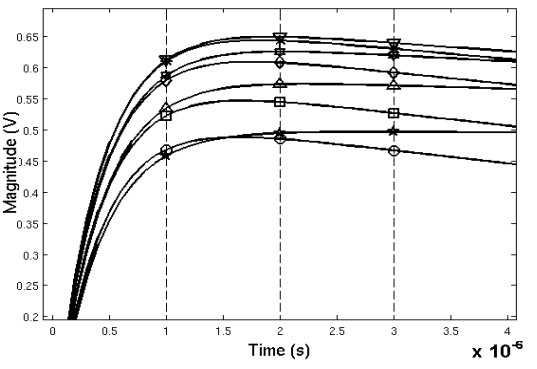

(h) $x' = 0/7$

FIGURE 3.17: Time domain fixed distribution representation; see Figure 3.18

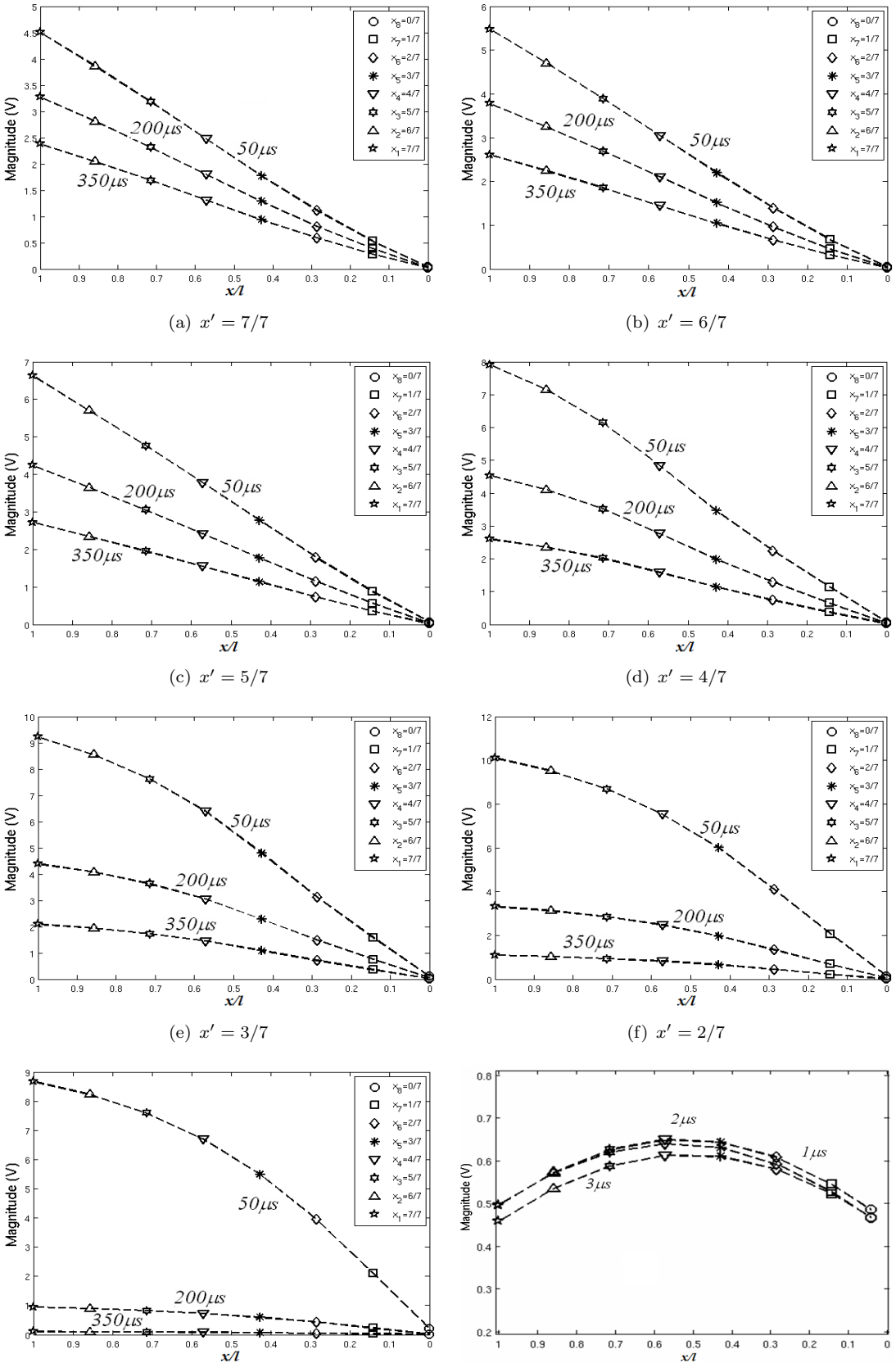

(a) $x' = 7/7$ (b) $x' = 6/7$

(c) $x' = 5/7$ (d) $x' = 4/7$

(e) $x' = 3/7$ (f) $x' = 2/7$

(g) $x' = 1/7$ (h) $x' = 0/7$

FIGURE 3.18: Fixed distribution representation; see Figure 3.17

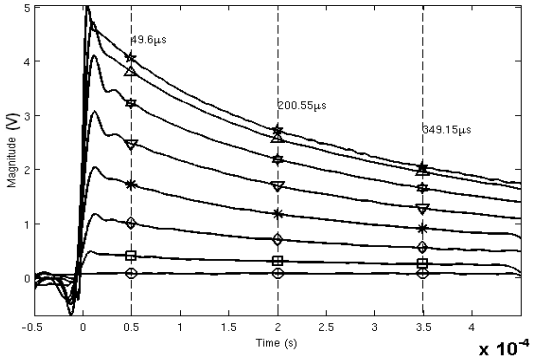

(a) $x' = 7/7$

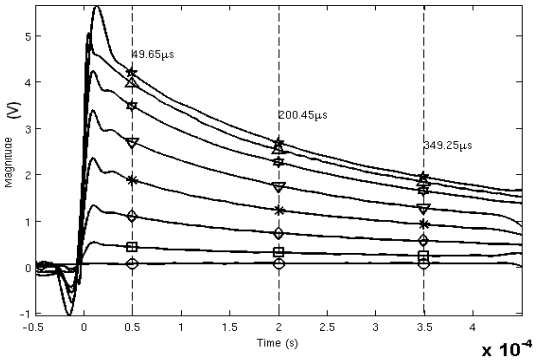

(b) $x' = 6/7$

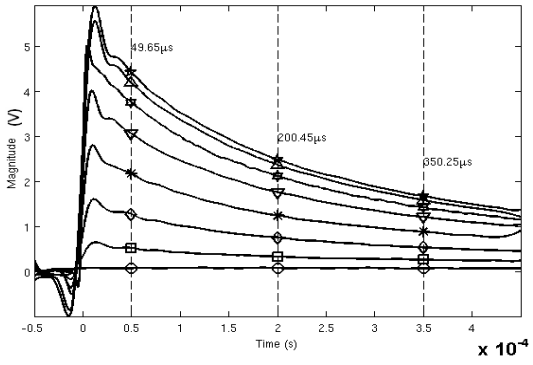

(c) $x' = 5/7$

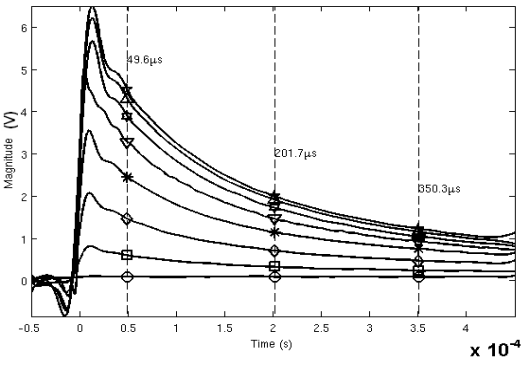

(d) $x' = 4/7$

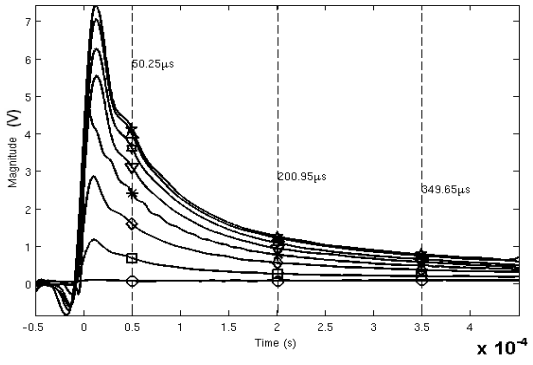

(e) $x' = 3/7$

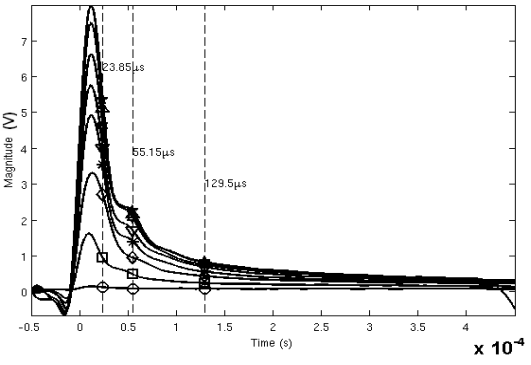

(f) $x' = 2/7$

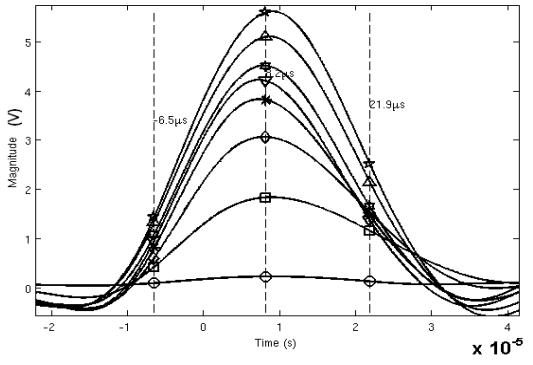

(g) $x' = 1/7$

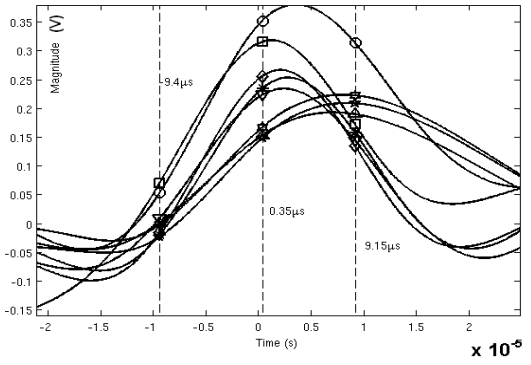

(h) $x' = 0/7$

FIGURE 3.19: Time domain fixed distribution representation of interleaved winding

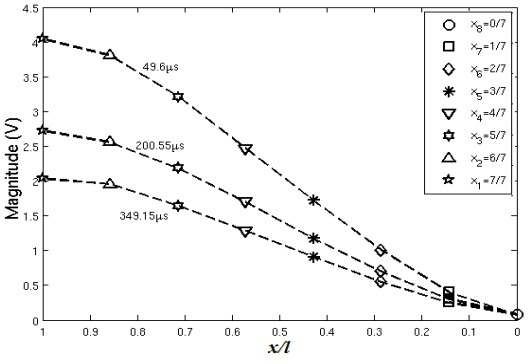

(a) $x' = 7/7$

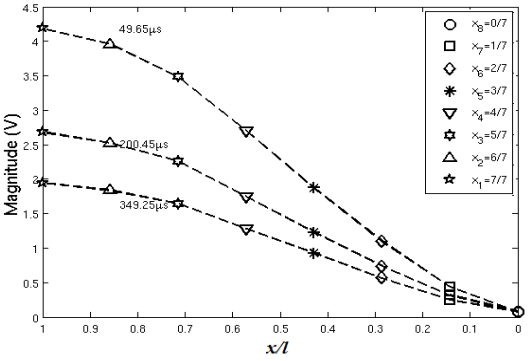

(b) $x' = 6/7$

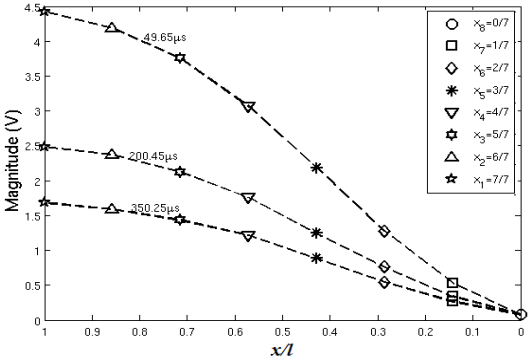

(c) $x' = 5/7$

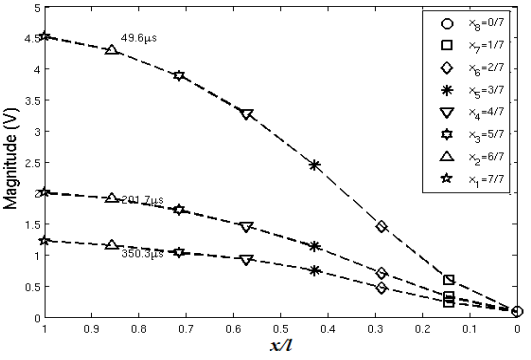

(d) $x' = 4/7$

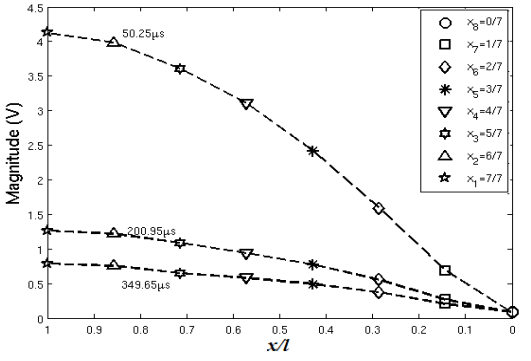

(e) $x' = 3/7$

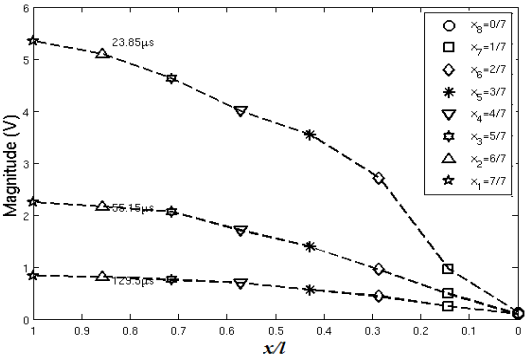

(f) $x' = 2/7$

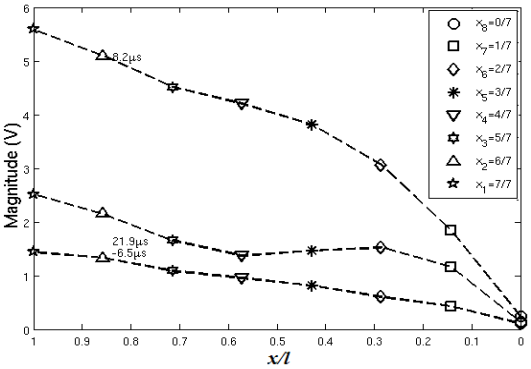

(g) $x' = 1/7$

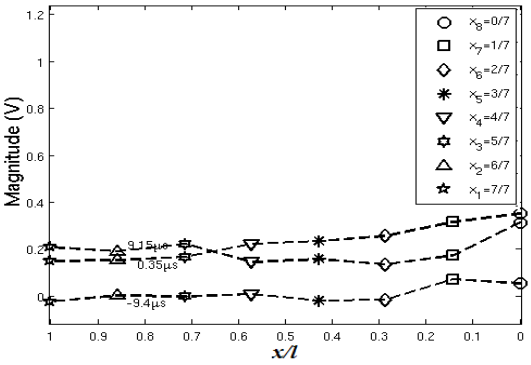

(h) $x' = 0/7$

FIGURE 3.20: Fixed distribution representation of interleaved winding from measurement

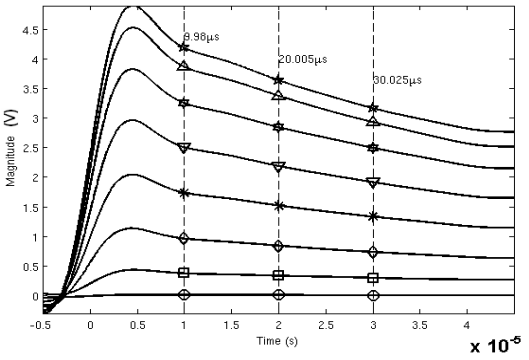

(a) $x' = 7/7$

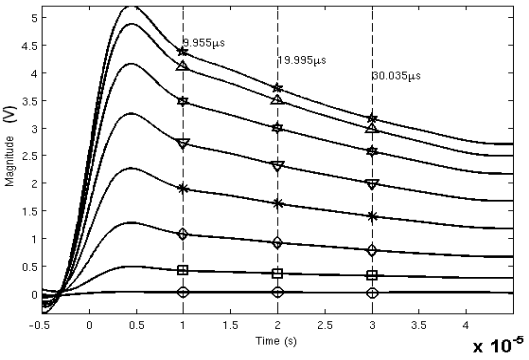

(b) $x' = 6/7$

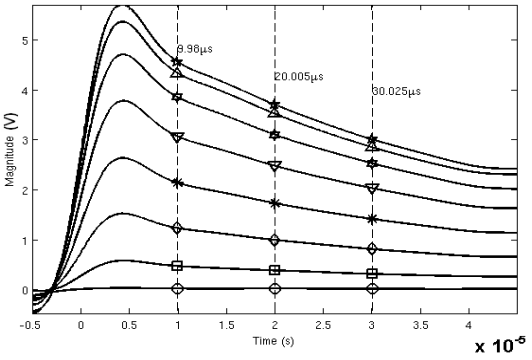

(c) $x' = 5/7$

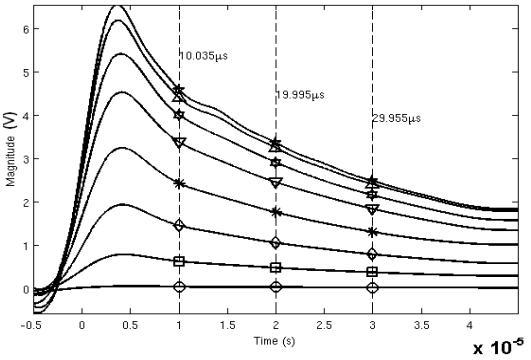

(d) $x' = 4/7$

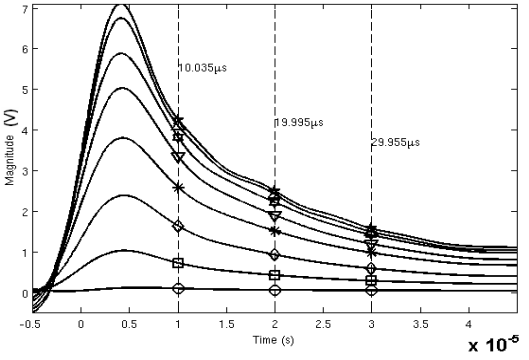

(e) $x' = 3/7$

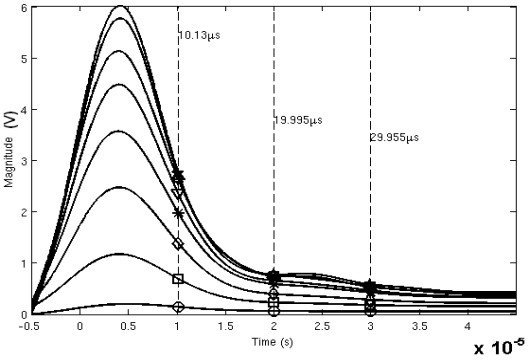

(f) $x' = 2/7$

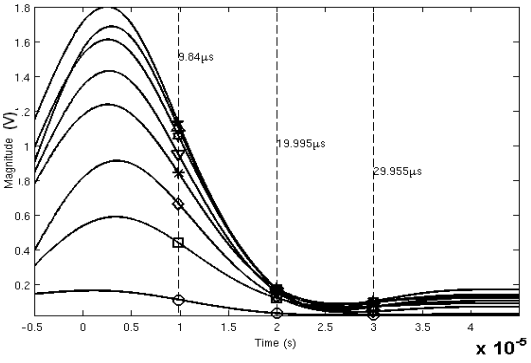

(g) $x' = 1/7$

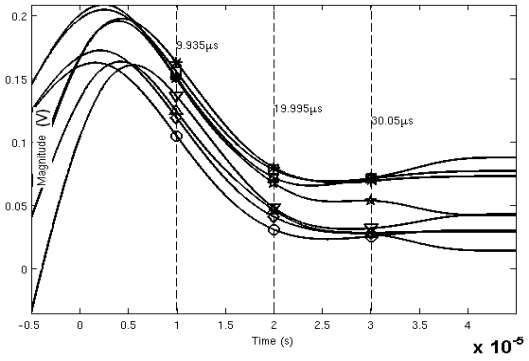

(h) $x' = 0/7$

FIGURE 3.21: Time domain fixed distribution representation of plain winding

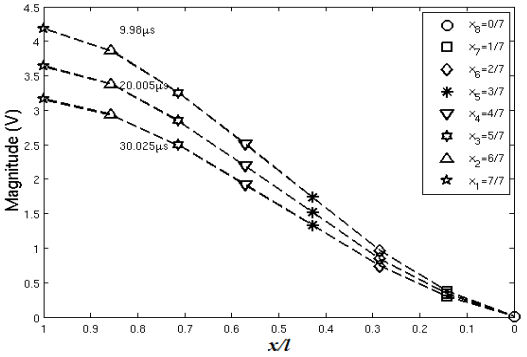

(a) $x' = 7/7$

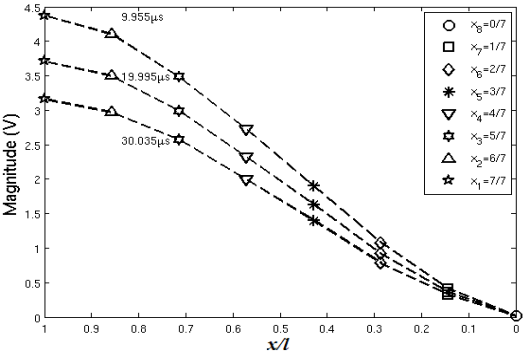

(b) $x' = 6/7$

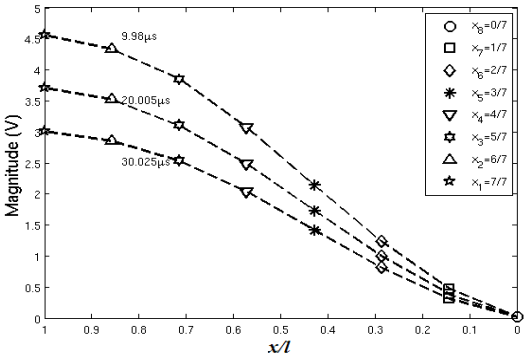

(c) $x' = 5/7$

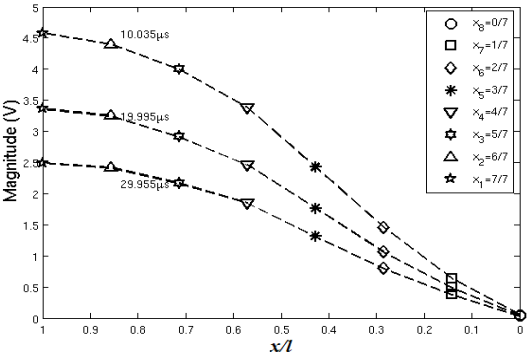

(d) $x' = 4/7$

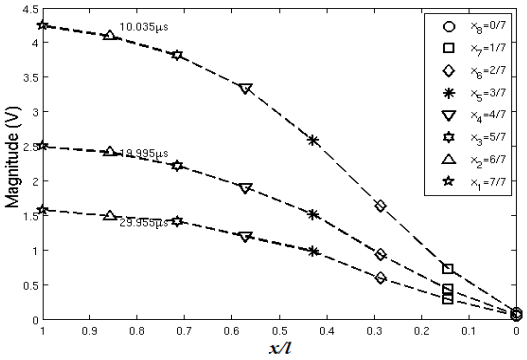

(e) $x' = 3/7$

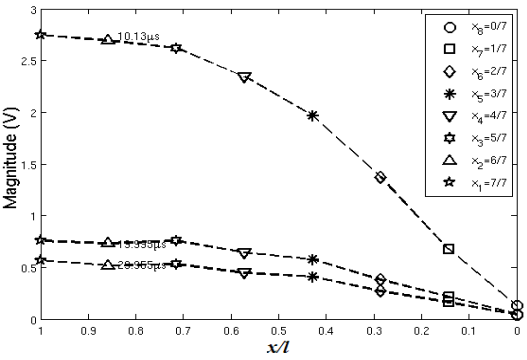

(f) $x' = 2/7$

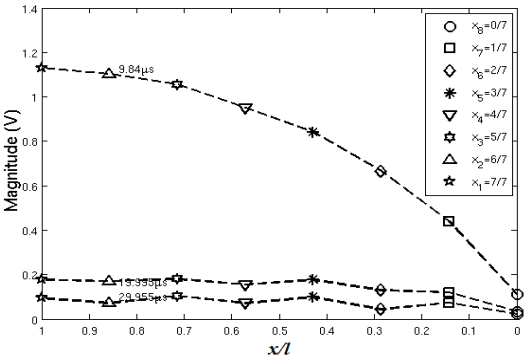

(g) $x' = 1/7$

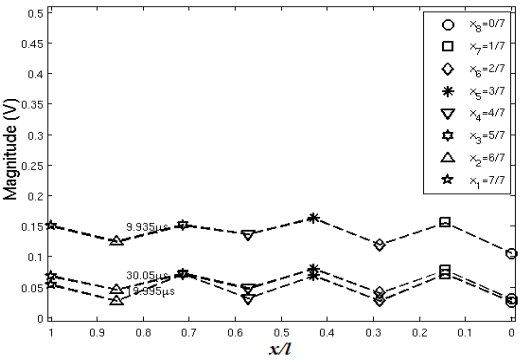

(h) $x' = 0/7$

FIGURE 3.22: Fixed distribution representation of plain winding from measurement

Chapter 4

Signal Oscillation and Propagation Within Transformer Windings

This chapter presents an oscillation model for a signal generated due to the influence of a transient incident wave source at some point along a transformer winding. As in Chapter 3, the wave under consideration is generated using an infinite rectangular wave modeled by the superposition of exponential waves. At the end of the chapter, analytical solutions and estimations are detailed that are based purely on the limited number of known parameter values for a typical transformer.

4.1 General Assumptions

The model of the transformer winding shown in Figure 4.1 is based on the lumped circuit parameter model of a single phase transformer [55]. It was based on analysis of high frequency travelling waves due to a lightning strike. The assumption was made that the wave travels in a single direction based on the fact that the lightning will strike a live line conductor and travel to ground. However in the case of partial discharge, the source of waves are from anywhere within the transformer winding itself. The source may also be very near to the bushing or the ground connection. Theoretically, signals due to partial discharge will propagate in different directions along the winding away from the source. Hence, it is possible to capture the propagated waves on either side of the terminals, bushing or neutral lines.

Due to the fact that the transformer winding is placed in a sealed enlosure and with limited access to the winding, the model presented in this section is based on several assumptions. Firstly, transient wave propagation is in two different directions away from

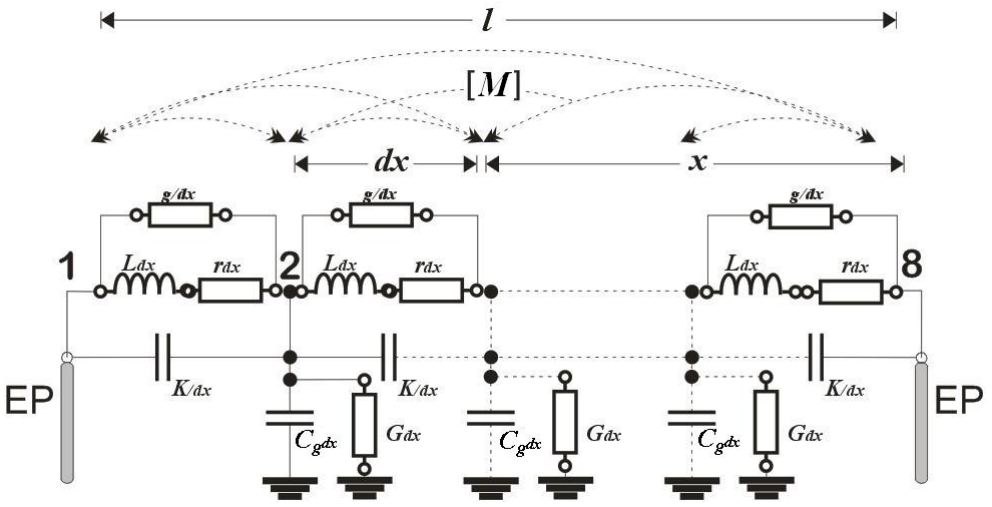

FIGURE 4.1: Lumped circuit model with mutual inductance [44, 45]

the source. Hence the signals can be simultaneously measured at the bushing and neutral terminals. Secondly, the analytical solution presented is based on a common winding construction either interleaved or plain windings. However it does not allow access to the winding from outside of the containment tank, although this capability exists in the experimental model described in Chapter 3. Finally, it must be assumed that there is limited knowledge of the transformer physical construction, hence all physical parameters have to be approximated in the derived analytical solutions.

4.2 High Frequency Transformer Equivalent Circuit Model

At high frequency, the lumped circuit model is a series connection of capacitances and inductances arranged in parallel and series respectively [48]. This is shown in Figure 4.1. At high frequencies the voltage oscillations arising in a winding are damped by the winding resistance and the core losses. If damping is also to be considered, the model of Figure 3.10 has to include resistances and ground conductances. The resistance of the winding is taken into account by a resistance, put in series with the inductance, whereas the core loss is represented by a resistance connected in parallel with them. $C_g dx$ and G_{dx} are the series of capacitance and shunt conductance to model the damping behaviour from winding to the ground. The relationship between each winding is modelled by its mutual inductance denoted as a matrix of inductance $[M]$. A section of such a model is shown in Figure 4.1, where r_{dx} is the resistance of a section of unit length of the winding, L_{dx} is inductance per unit length, K/dx is series capacitance along the winding and g/dx is the shunt conductance corresponding to the iron loss in a unit length section of the core [44, 71].

4.2.1 Initial Distribution vs Final Distribution of Voltage

Again, consider an infinite rectangular wave applied at the terminal x'. The currents at the first instance when $t = 0$ in the capacitances are infinite, and since the rate of change at this time is infinite (assuming the currents in the inductance are zero and currents in the resistances are finite), the initial distribution of the winding is equivalent to a series of capacitors. This is called initial distribution network and has been presented in sections 3.4.1 and 3.4.2.

When the signal is injected at distance x', the effective capacitance at that point differs from the whole capacitance, which effectively is a ratio of capacitance from line end to the distance of source. This is due to the effect of a number of sections seen by the traveling wave which are influenced by the resultant inter-section capacitance. Analytically this can be calculated and has been presented in 3.2.2. The effective initial distribution coefficient can be defined as;

$$\alpha_{eff} = \sqrt{\frac{C_g dx'}{\frac{K}{dx'}}} = \alpha\, dx' \tag{4.1}$$

Once the transient due to the applied infinite rectangular wave has decayed away (at $t = \infty$), the residual distribution becomes a direct current. The capacitive elements act as an open circuit and the inductive elements act as short circuits. Now, the distribution is solely dependent on the resistive elements of the parameter winding. Figure 4.2 shows the final distribution circuit which consists of resistive elements only.

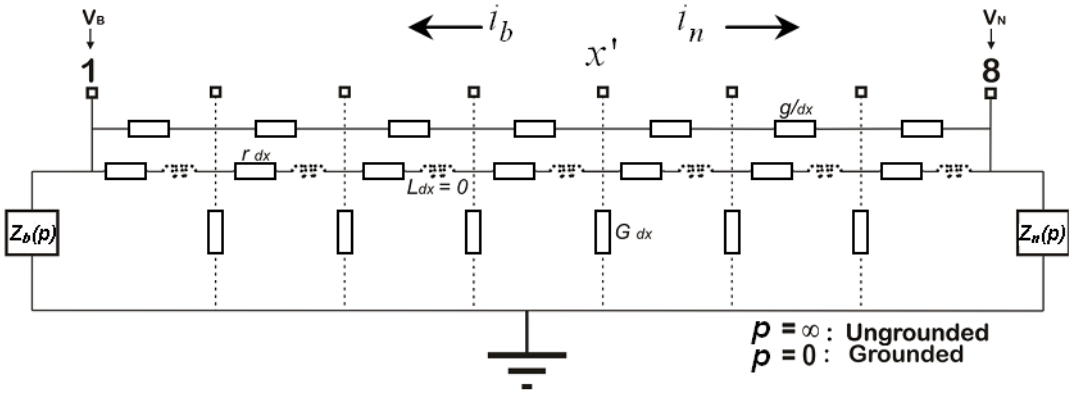

FIGURE 4.2: Resistive element of final distribution circuit

Using the similar analysis as for the initial distribution, the differential equation for the circuit is

$$\frac{\partial^2 v}{\partial x^2} - \beta^2 v = 0 \tag{4.2}$$

Where β is the final distribution coefficient that is equivalent to;

$$\beta = \sqrt{RG} \tag{4.3}$$

and R is equivalent to the shunt resistances of r_{dx} and $g/_{dx}$. Similarly, as from Equation (4.1) the effective resistances of this circuit at x' is,

$$\beta_{eff} = \sqrt{\frac{G_{dx'} r_{dx'}}{1 + r_{dx'} \frac{g}{dx'}}} = \beta\, dx' \tag{4.4}$$

Looking at the PDE of (4.2), the general solution for the final distribution has the same solution as for the initial distribution. However for a practical transformer the value of β is a very small quantity. Rewriting equations (B.15) and (B.19) for the boundary conditions at $x' = l$ and $x' = 0$ respectively, and replacing α with the final distribution coefficients, β, the solution becomes:

$$V_b = V_N cos(j\beta x) + \frac{V_B - V_N cos(j\beta l)}{sin(j\beta l)} sin(\beta x) \Bigg|_{x'=0} \tag{4.5}$$

$$V_n = V_N cosh(\beta x) - \frac{C\, sin(j\beta l) - D\, cos(j\beta l) + V_N sinh(\beta l)}{cosh(\beta l)} sinh(\beta x) \Bigg|_{x'=l} \tag{4.6}$$

The trigonometric and hyperbolic functions from the equations can be replaced with the first term of its expansion series. From equation (4.5):

$$\begin{aligned} V_b &= V_N + \frac{V_B - V_N}{j\beta l} j\beta x \\ V_b &= V_N + \big(V_B - V_N\big) \frac{x}{l} \Bigg|_{x'=0} \end{aligned} \tag{4.7}$$

And from Equation (4.6)

$$V_n = V_N - \big(jC\beta l - D + V_N \beta l\big)\beta x \tag{4.8}$$

but

$$C = \frac{V_N \beta l \left(1 - \beta^2 l^2\right)}{j\beta l} \tag{4.9a}$$

$$D = \frac{V_B \left(1 + \beta^2 l^2\right) - V_N \left(1 - \beta^2 l^2\right)}{\beta l} \tag{4.9b}$$

Therefore:

$$V_n \quad = V_N - \left[V_N \left(1 + \beta^2 l^2 - \beta^4 l^4\right) - V_B \left(1 + \beta^2 l^2\right)\right] \frac{x}{l} \Bigg|_{x'=l} \tag{4.10}$$

Hence the final distribution will practically be equivalent to a straight line between V_N and V_B, as is evident from (4.7) and (4.10) with a gradient of $\frac{x}{l}$. As discussed in [44] the following condition was suggested:

$$\textit{Initial Distribution} \approx \textit{Final Distribution} \tag{4.11}$$

Hence Figure 4.3 shows an experimental result of d.c measurement for initial distribution and final distribution of voltage extracted at $71.1\mu s$ and $403.9\mu s$ respectively.

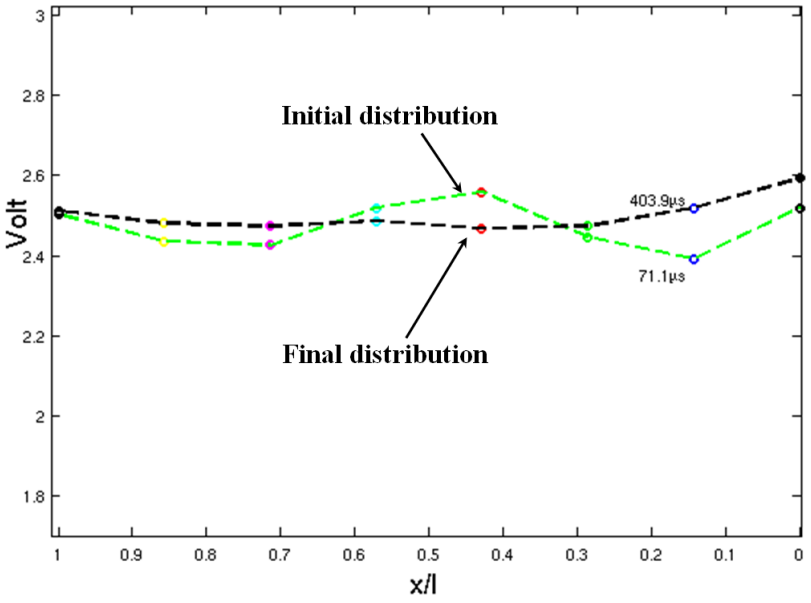

FIGURE 4.3: Initial distribution versus final distribution for d.c measurement of interleaved winding

4.3 Standing Wave Solution

The standing wave solution is for a travelling wave either under confined boundary conditions or in stationary constant position. It also can be used to solve wave motion with harmonic pairs and moving in different directions [107].

4.3.1 LCK circuit analysis

As an alternative solution to the PDEs (3.16) and (4.2), the presence of inductive elements can cause oscillations in the circuit. This is due to energy storage excited by the current-carrying conductor which tends to resist changes in the current. Figure 4.4 shows an alternative circuit solution for current propagation including the influence of inductive elements.

Based on the divergence of the current in opposite directions, the following equations are derived:

$$\frac{\partial v}{\partial x} = L\frac{\partial i_L}{\partial t} \tag{4.12a}$$

$$i_C = C_g\frac{\partial v}{\partial t} = \frac{\partial}{\partial x}(i_K + i_L) \tag{4.12b}$$

where the definition of current is:

$$i_k = K\frac{\partial^2 v}{\partial x \partial t} \tag{4.13}$$

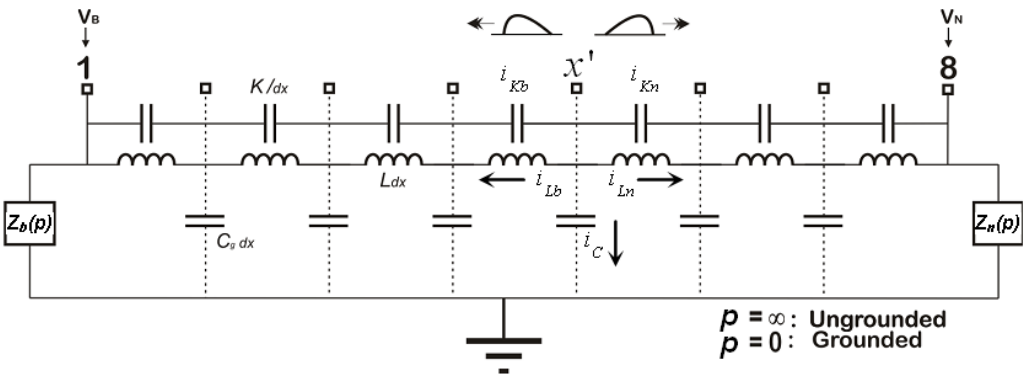

FIGURE 4.4: LCK circuit of transformer windings

Substituting for i_k into Equation (4.12b) gives:

$$\begin{aligned} C_g\frac{\partial v}{\partial t} &= \frac{\partial}{\partial x}\left(K\frac{\partial^2 v}{\partial x \partial t}\right) + \frac{\partial i_L}{\partial x} \\ C_g\frac{\partial^2 v}{\partial t^2} &= K\frac{\partial^4 v}{\partial x^2 \partial t^2} + \frac{\partial}{\partial t}\left(\frac{\partial i_L}{\partial x}\right) \end{aligned} \tag{4.14}$$

However the definition from (4.12a), yields the complete PDE describing the travelling wave towards the bushing and neutral as follows:

$$LK\frac{\partial^4 v}{\partial x^2 \partial t^2} - LC_g\frac{\partial^2 v}{\partial t^2} + \frac{\partial^2 v}{\partial x^2} = 0 \tag{4.15}$$

One major contribution of this thesis is that it introduces the use of a split winding analysis for the solution of signal propagation under impulse conditions. Fundamental to this approach is that it allows separate solutions for a signal propagating in two directions along the winding by treating the problem as two independant lumped parameter models.

4.3.2 Split winding analysis: solution towards Neutral

Equation (4.15) describes signal propagation towards the neutral and bushing tap point respectively. By considering the definition of the following [44]:

$$Initial\,distribution = Final\,distribution\; +\; Transient\,terms \tag{4.16}$$

Hence the trial solution to the PDE is in the form of:

$$\begin{aligned} \psi_n(x,t) = \varphi_n(x,t) + \sum\Big[&E_{sn}sin(\lambda x)\,cos(\omega t) + F_{sn}sin(\lambda x)\,sin(\omega t) \\ &+ G_{sn}cos(\lambda x)\,cos(\omega t) + H_{sn}cos(\lambda x)\,sin(\omega t)\Big] \end{aligned} \tag{4.17}$$

Where $\varphi_n(x,t)$ is the final fixed distribution solution towards Neutral in the form of Equation (B.1). Equation (4.17) indicates that the travelling wave consists of two main components, a fixed distribution component (first term) and harmonic signal component (second term). To obtain a solution towards neutral, assume that the initial conditions

are that the initial inductance current is zero and from solving Equations (4.12a) and (4.12b) the following are also satisfied at time equal to zero [44]:

$$\frac{\partial^2 v_n}{\partial x^2} - \frac{C_g}{K} v_n = 0 \qquad and \qquad \frac{\partial \psi_n(x,t)}{\partial t} = 0 \tag{4.18}$$

and with boundary conditions:

$$\psi_n(l,t) = V_B(t) \qquad and \qquad \psi_b(0,t) = 0; \tag{4.19}$$

By solving the initial conditions and the boundary conditions for the trial solution, thus the complete solution for a wave travelling towards the neutral is equivalent to:

$$\psi_n(x,t) = \varphi_n(x,t) + \sum_{s=1}^{\infty} \frac{2(-1)^s}{s\pi} \zeta_n sin\Big(\frac{s\pi x_n}{l}\Big) cos(\omega_{sn} t) \tag{4.20}$$

Where

$$\zeta_n = \Big\{ A\Big[cosh(\beta l) - cosh(\alpha l)\Big] + B\Big[sinh(\beta l) - sinh(\alpha l)\Big] \Big\} \tag{4.21}$$

and

$$x_n = \frac{x}{x'} - 1 \tag{4.22}$$

The constants A and B can be obtained from the solutions provided in Section 3.4.2. The full derivation of the solution can be found in Appendix C.

4.3.3 Split winding analysis: solution towards the bushing tap point

The solution of the PDE towards the bushing tap point is similar to the solution of the PDE towards the neutral as it yields fourth order linear differential equations. Except that the bushing terminal is connected via $Z_b(p)$ of Figure 4.4, where practically $Z_b(p)$ represents bushing impedance or can be replaced with an equivalent capacitor. Hence to model the bushing terminal line, it is equivalent to considering an open connection or ungrounded connection under dc conditions, unlike the neutral terminal case where $Z_n(p)$ is equivalent to zero.

Therefore the solution for the ungrounded winding can be found by replacing the half range Fourier sine series with a quarter range Fourier sine series of odd harmonics.

However the relationship of bushing to terminal harmonic order is computed by:

$$s_o = (2s - 1) \tag{4.23}$$

Using the same general solution as for the solution towards neutral, and by the definition from the Equation (4.16) [44]; the solution towards bushing tap point also comprises of a fixed final distribution component plus the harmonic standing wave;

$$\begin{aligned}\psi_b(x,t) = \varphi_b(x,t) + \sum \Big[& E_{sb} sin(\lambda x)\, cos(\omega t) + F_{sb} sin(\lambda x)\, sin(\omega t) \\ & + G_{sb} cos(\lambda x)\, cos(\omega t) + H_{sb} cos(\lambda x)\, sin(\omega t) \Big]\end{aligned} \tag{4.24}$$

Where $\varphi_b(x,t)$ is the final fixed distribution solution towards Bushing in the form of Equation (B.3), with the following initial conditions;

$$\frac{\partial^2 v_b}{\partial x^2} - \frac{C_g}{K} v_b = 0 \qquad and \qquad \frac{\partial \psi_b(x,t)}{\partial t} = 0, \tag{4.25}$$

and boundary conditions:

$$\psi_b(l,t) = V_B(t) \qquad and \qquad \psi_b(0,t) = 0; \tag{4.26}$$

Solving for the initial conditions and the boundary conditions, therefore the complete solution for the wave travelling towards bushing is (the full derivation can be found in Appendix C):

$$\psi_b(x,t) = \varphi_b(x,t) + \sum_{s_o=1}^{\infty} \frac{8l}{s_o^2 \pi^2}\, sin\Big(\frac{s_o \pi}{2}\Big)\, \zeta_b sin\Big(\frac{s_o \pi x_b}{2l}\Big) cos(\omega_{sb} t) \tag{4.27}$$

Where

$$\zeta_b = \Big\{ C\Big[\beta sin(\beta l) - \alpha sin(\alpha l)\Big) + D\Big(\alpha cos(\alpha l) - \beta cos(\beta l)\Big] \Big\} \tag{4.28}$$

and

$$x_b = x - x' \tag{4.29}$$

Again both contants C and D can be obtained by solving the solutions in Section B.1.

Both the derived solutions (4.20) and (4.27) can be further simplified to minimize the computational burden. The fixed distribution component of the equations will be almost constant, as β is very small or almost equivalent to zero. Therefore equations (4.7) and (4.10) will have a similar form and can be simplified to [44];

$$\varphi(x,t) = \varphi_n(x,t) = \varphi_b(x,t) = V_N(t) + \frac{x}{l}\Big[V_B(t) - V_N(t)\Big] \tag{4.30}$$

Which allows the solutions of (4.20) and (4.27) to be rewritten as: Solution towards neutral ($\beta \approx 0$):

$$\psi_n(x,t) = \varphi(x,t) + \sum_{s=1}^{\infty} \frac{2(-1)^s}{s\pi}\left[A\Big(1 - cosh(\alpha l)\Big) - Bsinh(\alpha l)\right] sin\Big(\frac{s\pi x_n}{l}\Big)\, cos(\omega_{sn} t) \tag{4.31}$$

Solution towards bushing tap point ($\beta \approx 0$):

$$\psi_b(x,t) = \varphi(x,t) + \sum_{s_o=1}^{\infty} \frac{8l}{s_o^2\pi^2}\, sin\frac{s_o\pi}{2}\left[D\alpha cos(\alpha l) - C\alpha sin(\alpha l)\right] sin\Big(\frac{s_o\pi x_b}{2l}\Big) cos\omega_{sb} t \tag{4.32}$$

4.3.4 The Decay Factor

The solutions provided in Sections 4.3.2 and 4.3.3 are without considering the losses within the transformer winding. If losses are considered, a full lumped circuit parameter model as shown in Figure 4.5 has to be considered [55]. Where the PDE of the circuit model is as follows [44]:

$$\begin{aligned} rK\frac{\partial^5 v}{\partial x^4 \partial t} + (1+gr)\frac{\partial^4 v}{\partial x^4} - LK\frac{\partial^4 v}{\partial x^2 \partial t^2} - (rC+gL)\frac{\partial^3 v}{\partial x^2 \partial t} \\ - rG\frac{\partial^2 v}{\partial x^2} + LC\frac{\partial^2 v}{\partial t^2} + LG\frac{\partial v}{\partial t} = 0 \end{aligned} \tag{4.33}$$

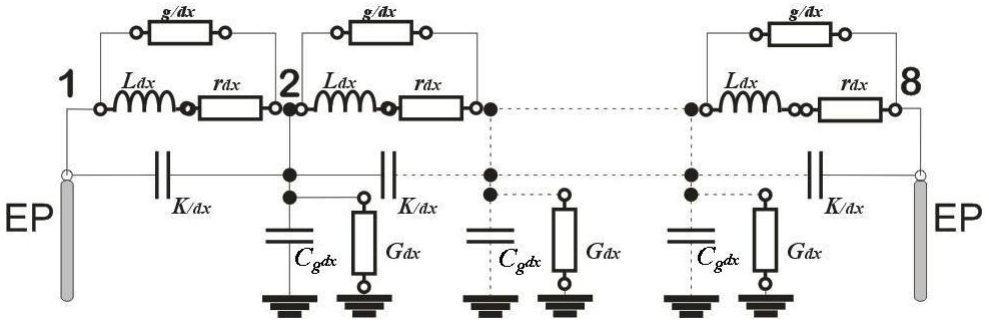

FIGURE 4.5: Lumped circuit model [44]

The decay factor can be derived from Equation (4.33). Writing the PDE in auxillary form;

$$\begin{aligned} rKa^4b \,+\, (1+gr)a^4 \,-\, LKa^2b^2 - (rC+gL)a^2b \\ - \, rGa^2 \,+\, LCb^2 \,+\, LGb = 0 \end{aligned} \tag{4.34}$$

Solving the auxillary form for b, the decay factor is equivalent to [44]:

$$\gamma_s = \frac{rKs^4\pi^4/l^4 + (rC+gL)s^2\pi^2/l^2 + LG}{2L(C + Ks^2\pi^2/l^2)} \tag{4.35}$$

Therefore, the complete solution for the wave travelling towards Neutral and towards Bushing (Equations (4.20) and (4.27) respectively) can be written by incorporating the decay term as follows:

$$\psi_n(x,t) = \varphi_n(x,t) + \sum_{s=1}^{\infty} \frac{2(-1)^s}{s\pi}\, e^{-\gamma_s t}\, \zeta_n sin\Big(\frac{s\pi x_n}{l}\Big)\, cos(\omega_{sn}t) \tag{4.36}$$

for the solution towards neutral and

$$\psi_b(x,t) = \varphi_b(x,t) + \sum_{s_o=1}^{\infty} \frac{8l}{s_o^2\pi^2}\, sin\Big(\frac{s_o\pi}{2}\Big)\, e^{-\gamma_s t}\, \zeta_b sin\Big(\frac{s_o\pi x_b}{2l}\Big) cos(\omega_{sb}t) \tag{4.37}$$

for the solution towards bushing tap point.

4.3.5 Split Winding Analysis: Infinite Rectangular Wave Response, Measurement and Simulation

Using the analysis of signal propagation developed above, the analysis of signal injection using an infinite rectangular wave source is presented here. A $50ns$ rise time for infinite rectangular wave was used in the experiment. The signal was injected at different terminals to represent varying source location x' and the corresponding response waveforms were measured in the time domain at other terminals that represent x.

The split waves originated from source x' oscillate as the waves travels further away from each other. At any point x, the voltage level is measured and estimated using the

derived model equations (4.36) and (4.37) for a solution towards the neutral and bushing respectively. The calculated solution is estimated for different value of α and β, which gives two sets of values for the two different windings. The estimated α and β for the simulation are $\alpha = 0.35$ and $\beta = 0.31$ for interleaved winding and $\alpha = 0.7$ and $\beta = 0.26$ for plain winding. Figures 4.7 and 4.9 show the experimental results of travelling waves using infinite rectangular wave injected at different x' along the two different windings. Figures 4.6 and 4.8 show the corresponding simulation results for waves calculated using split winding analysis technique for interleaved winding and plain winding respectively.

Through observation, it is obvious that both windings have a very similar pattern for travelling waves. There is very good agreement between measurement and simulation results for both type of windings by means of its oscillation patterns. However, for the plain disc winding there is a discrepancy at neutral line injection or for $x' = 0/7$, in which the measurement shows significant signal oscillations for $x = 1/7$ to $x = 7/7$. This is due to the non-uniform distribution of its mechanical construction which cause higher accumulation of harmonic waveforms propagating towards the bushing tap point compared to the interleaved winding.

4.3.6 Amplitude Distribution

Distribution in the time domain can be viewed by considering the amplitude measurement of the measured winding response. The amplitude in the time domain represents the magnitude of oscillation and is important in order to determine the level of energy in the reverberation process during signal propagation. As has been seen in previous sections the amplitude factor is determined by the choice of parameters; α and β; for the initial distribution and final distribution coefficients respectively. The amplitude factor in both directions of current propagation, can be determined from the PDE solutions;

The amplitude factor towards the neutral point is:

$$|E_{sn}| = \frac{2(-1)^s}{s\pi}\,\zeta_n sin\Big(\frac{s\pi x_n}{n}\Big) \tag{4.38}$$

and the amplitude factor towards the bushing tap point is:

$$|E_{sb}| = \frac{8l}{s_o^2\pi^2}\,sin\Big(\frac{s_o\pi}{2}\Big)\,\zeta_b sin\Big(\frac{s_o\pi x_b}{2l}\Big) \tag{4.39}$$

From equations (4.38) and (4.39), the distribution of the signal amplitude is in the range of term x_n and x_b respectively. Where both terms have x' in their equations. Figure 4.10 show the transition of amplitude distribution for both equations for different x'.

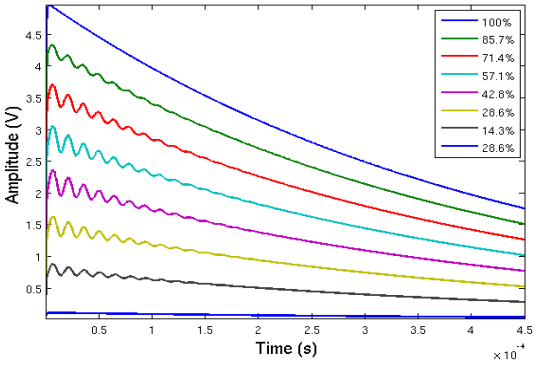

(a) $x' = 7/7$

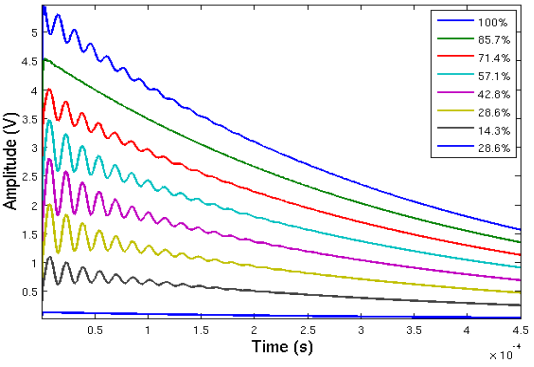

(b) $x' = 6/7$

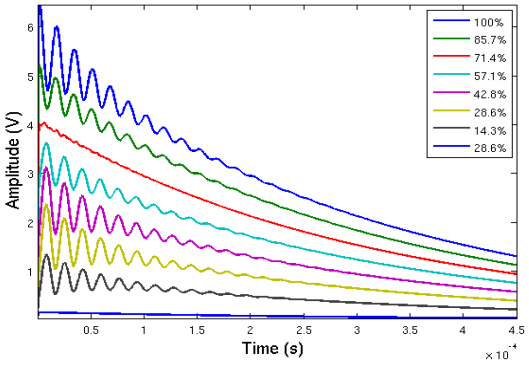

(c) $x' = 5/7$

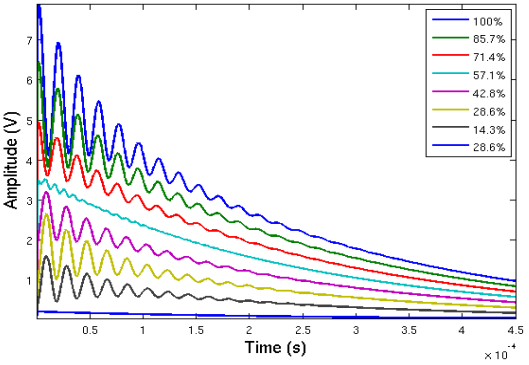

(d) $x' = 4/7$

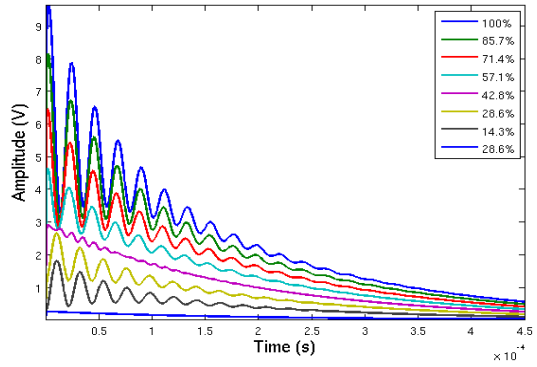

(e) $x' = 3/7$

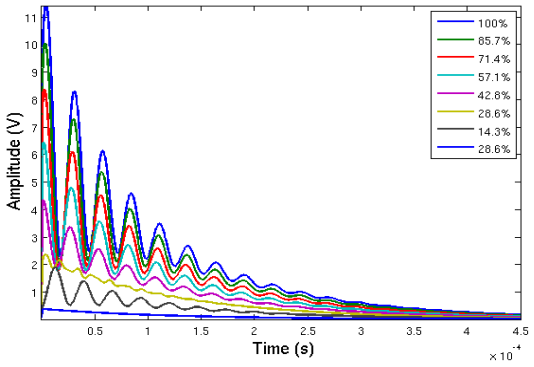

(f) $x' = 2/7$

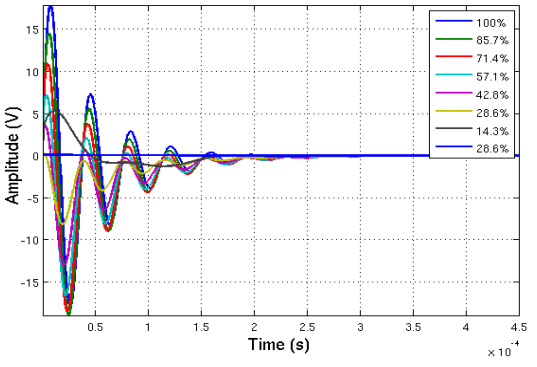

(g) $x' = 1/7$

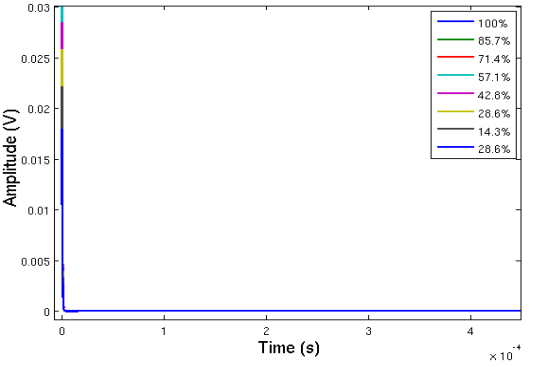

(h) $x' = 0/7$

FIGURE 4.6: Time domain response to infinite rectangular wave simulated at different x' for interleaved winding

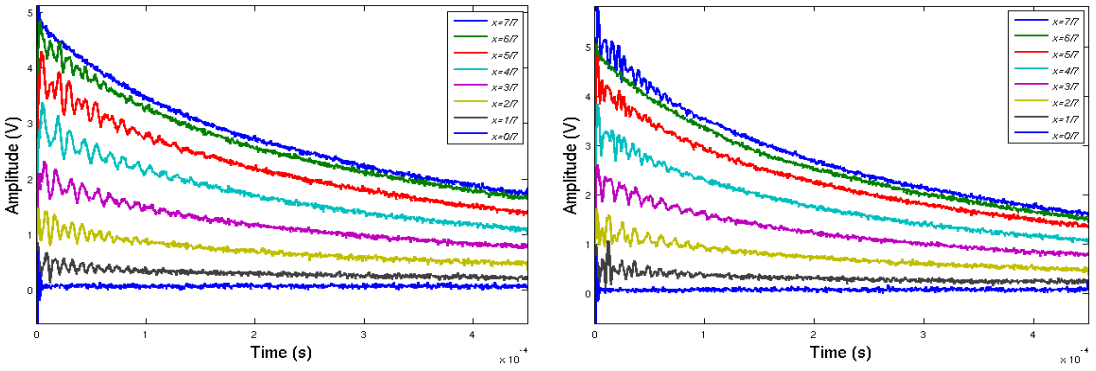

(a) $x' = 7/7$

(b) $x' = 6/7$

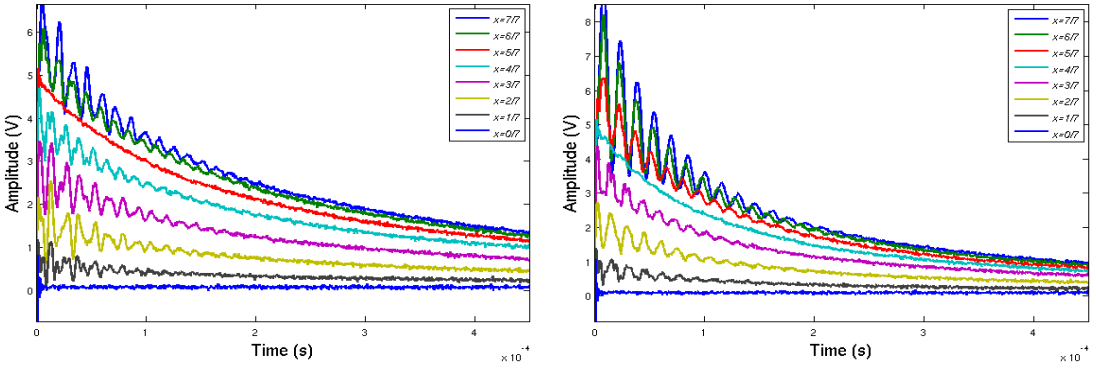

(c) $x' = 5/7$

(d) $x' = 4/7$

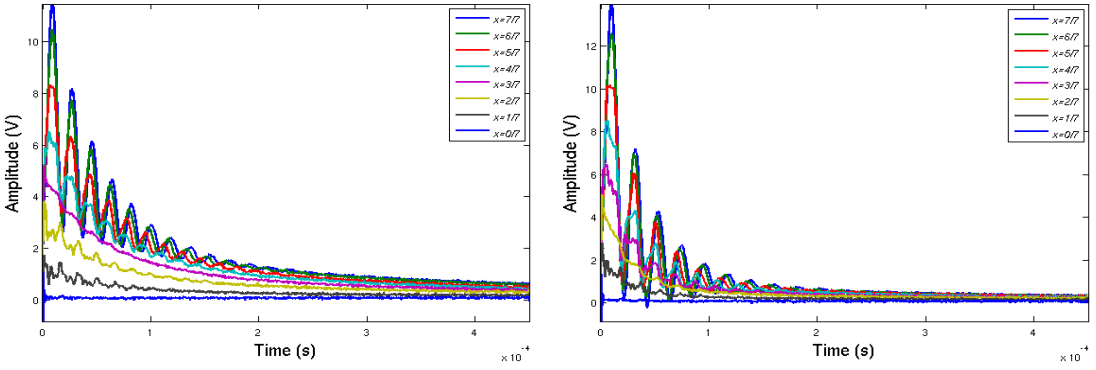

(e) $x' = 3/7$

(f) $x' = 2/7$

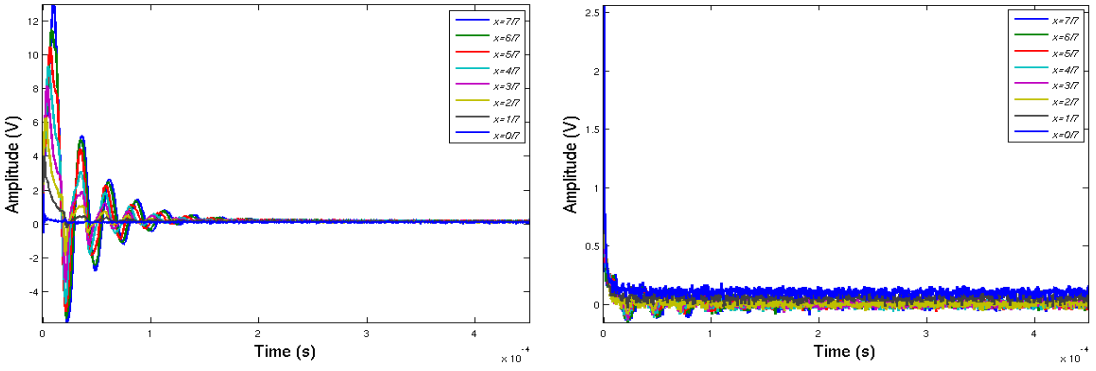

(g) $x' = 1/7$

(h) $x' = 0/7$

FIGURE 4.7: Time domain response to infinite rectangular wave measured at different x' for interleaved winding

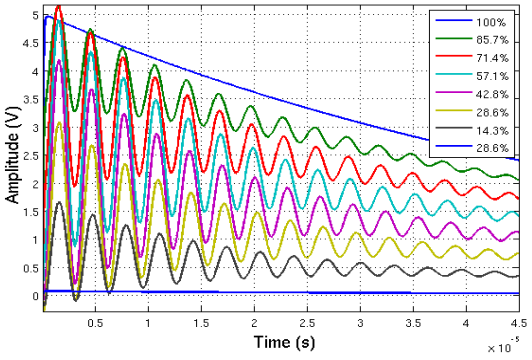

(a) $x' = 7/7$

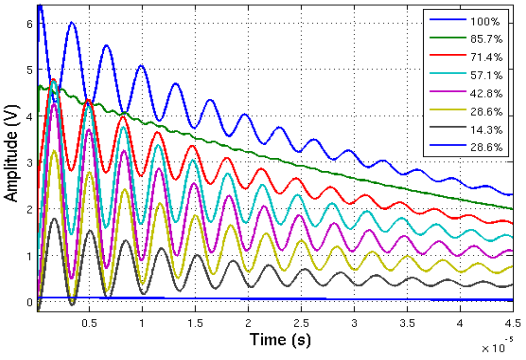

(b) $x' = 6/7$

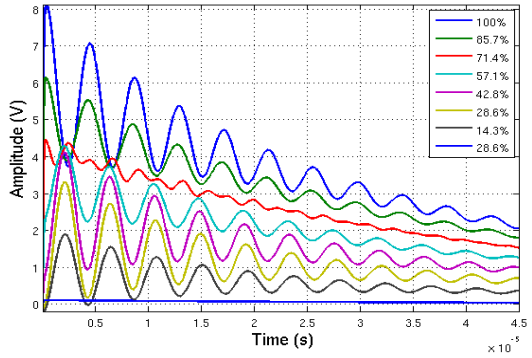

(c) $x' = 5/7$

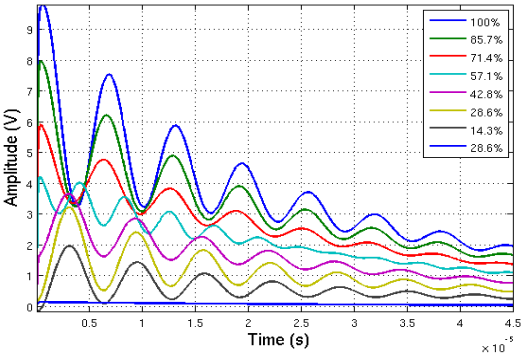

(d) $x' = 4/7$

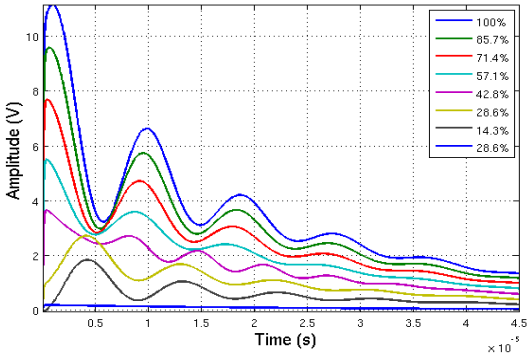

(e) $x' = 3/7$

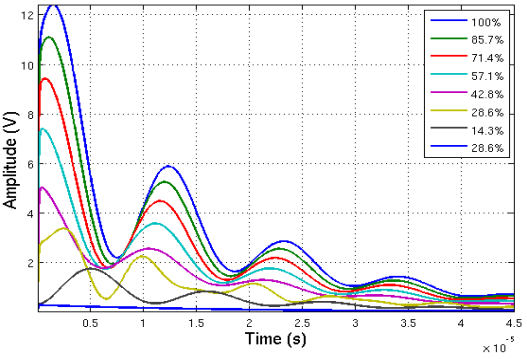

(f) $x' = 2/7$

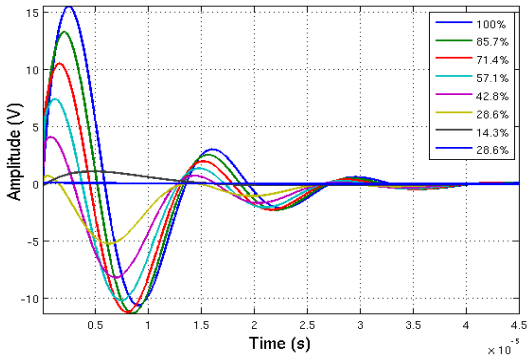

(g) $x' = 1/7$

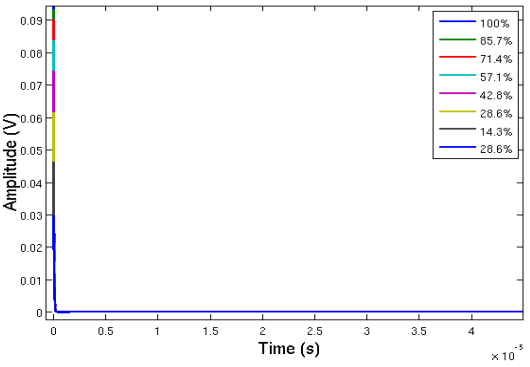

(h) $x' = 0/7$

FIGURE 4.8: Time domain response to infinite rectangular wave simulated at different x' for plain winding

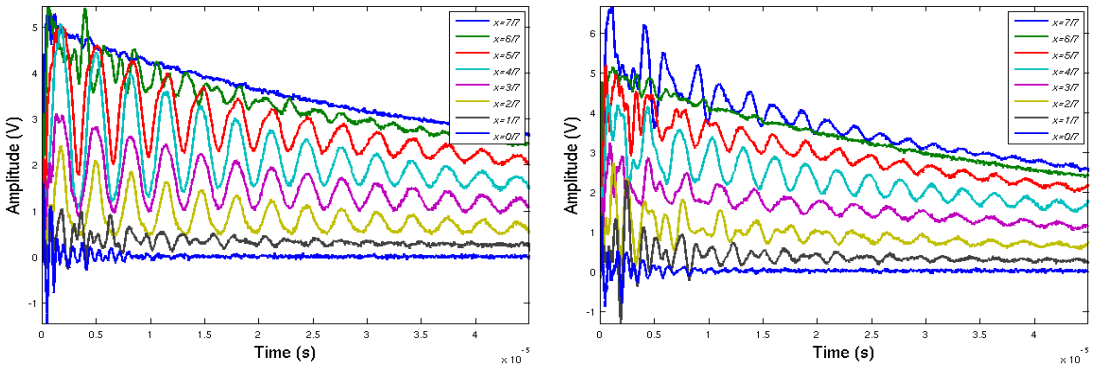

(a) $x' = 7/7$

(b) $x' = 6/7$

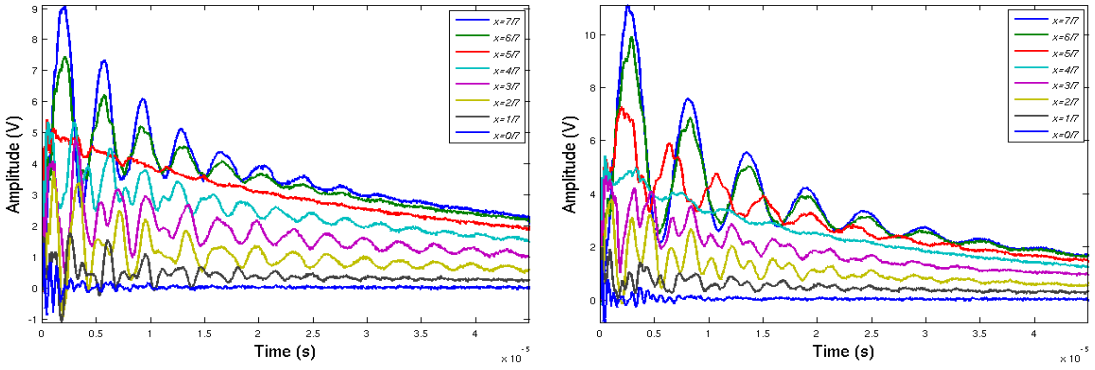

(c) $x' = 5/7$

(d) $x' = 4/7$

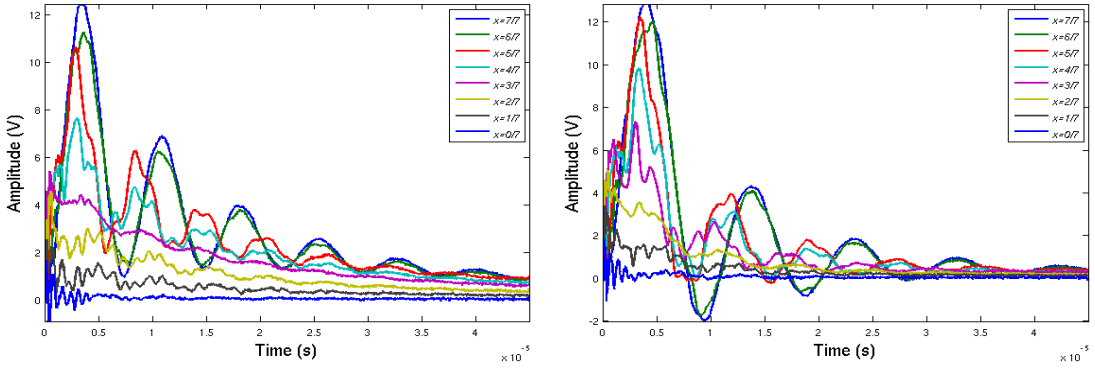

(e) $x' = 3/7$

(f) $x' = 2/7$

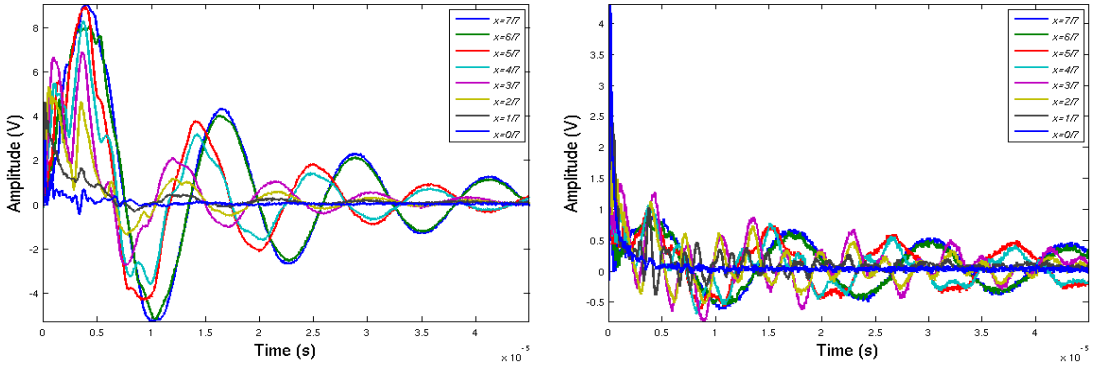

(g) $x' = 1/7$

(h) $x' = 0/7$

FIGURE 4.9: Time domain response to infinite rectangular wave measured at different x' for plain winding

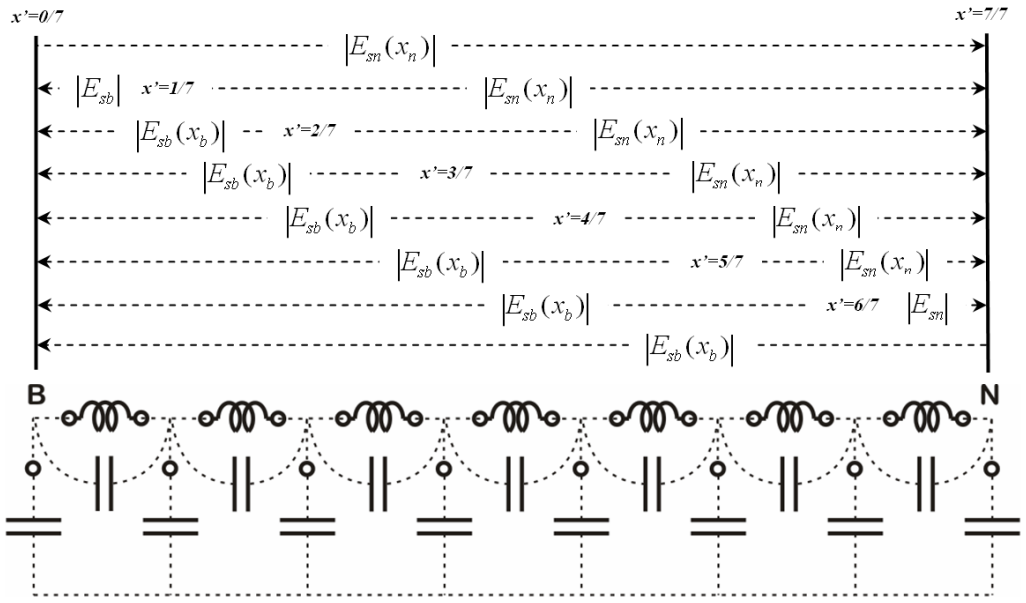

FIGURE 4.10: Transition of amplitude factor equations for different x'

Figures 4.11 and 4.12 show the amplitude distribution along the interleaved winding and plain winding respectively. Both compare the calculated distribution from the model equation and from measurement of a travelling wave generated using a $5V$ infinite rectangular dc signal source for the duration of $450\mu s$ for interleaved winding and $45\mu s$ for plain winding. The patterns show that for waves that travel towards the neutral to ground terminal, there is an accumulation of harmonic amplitude levels that finally decay to zero. However for waves travelling towards the bushing tap point, both simulated and measured amplitudes show increasing accumulated harmonic levels. Note that the results shown in Figures 4.11 and 4.12 only consider the first order of harmonic, which is the most dominant level. The extraction begins with the identification of the first order harmonic frequency in frequency domain from terminal measurements, then a bandpass filter is used to extract the frequency band component and using the inverse Fourier transform to transform it back into the time domain.

Both windings give very similar patterns by means of the amplitude factor and frequency variations. Taking the amplitude factor as a measure of power spectrum density for the first harmonic, the curve of amplitude factor is plotted in Figure 4.13. Both windings have a similar amplitude factor for different discharge source positions. However, at $x = 0$ (the ground connection) both windings show the level of amplitude factor is near constant and lower in magnitude as the injection point is at the same level as the ground connection.

The patterns also show that the interleaved winding has a lower magnitude of amplitude factor (in dB), compared to the plain winding. This is due to the difference of the distribution constants for α and β where in this case the approximate difference is 0.04 for the interleaved winding and 0.44 for the plain winding.

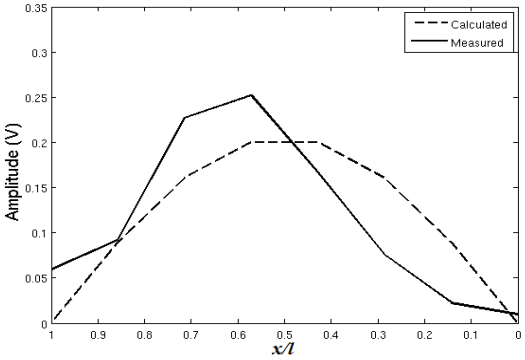

(a) $x' = 7/7$

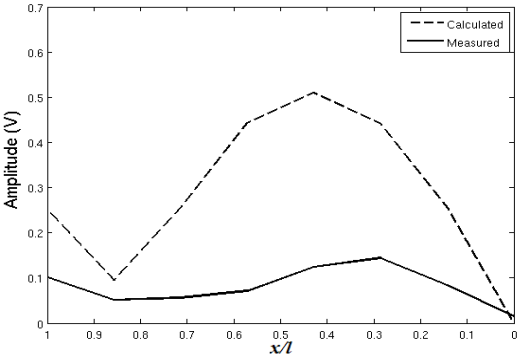

(b) $x' = 6/7$

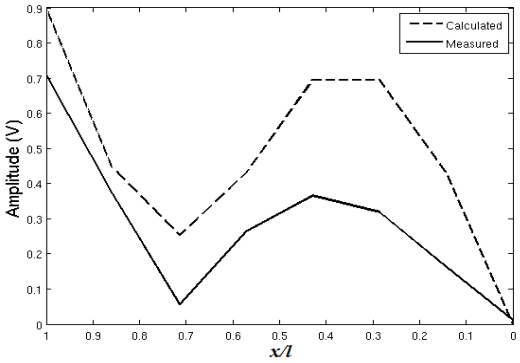

(c) $x' = 5/7$

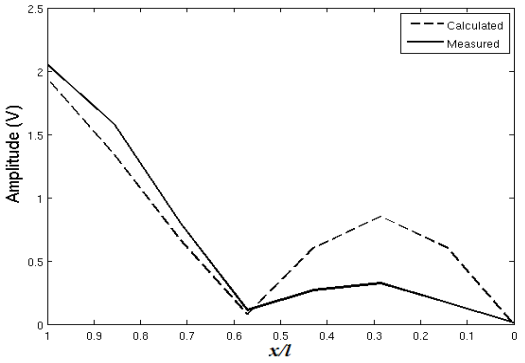

(d) $x' = 4/7$

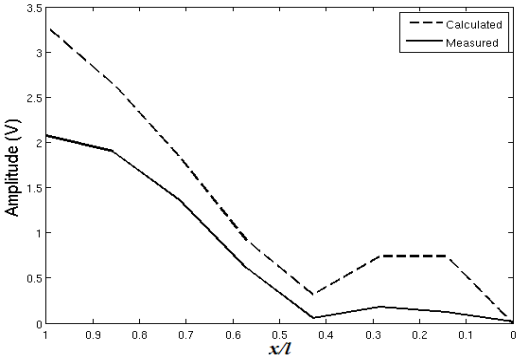

(e) $x' = 3/7$

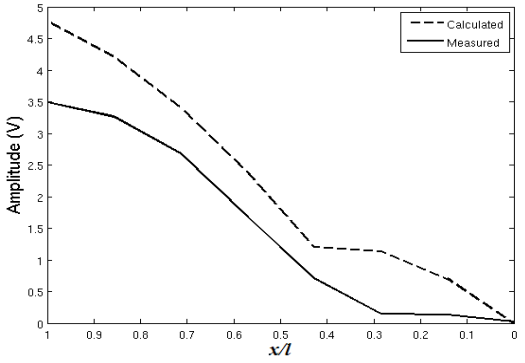

(f) $x' = 2/7$

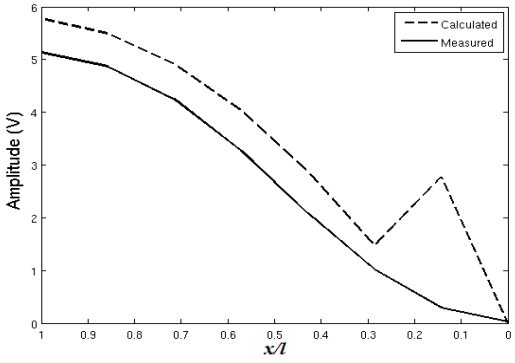

(g) $x' = 1/7$

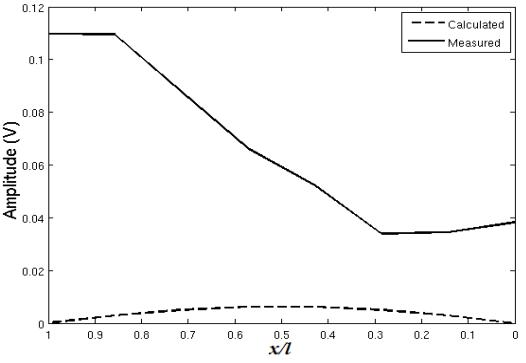

(h) $x' = 0/7$

FIGURE 4.11: Comparison of amplitude distribution between measured and calculated for interleaved winding

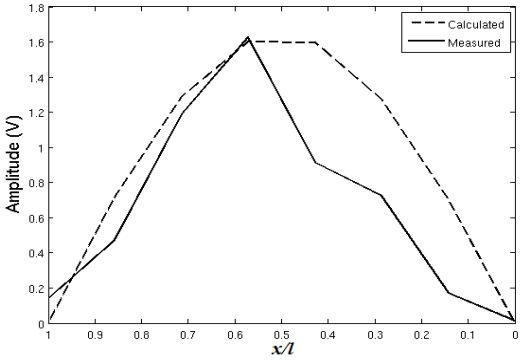

(a) $x' = 7/7$

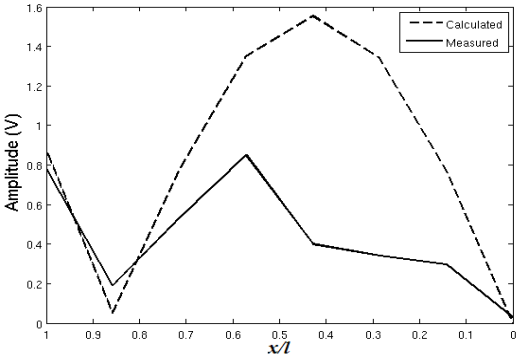

(b) $x' = 6/7$

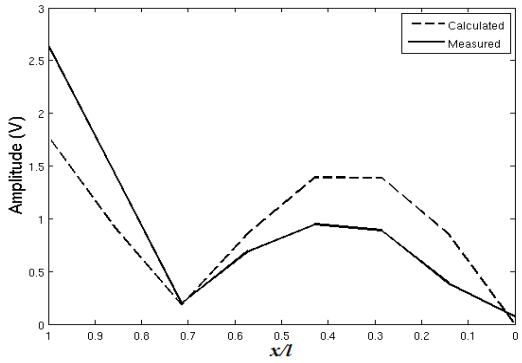

(c) $x' = 5/7$

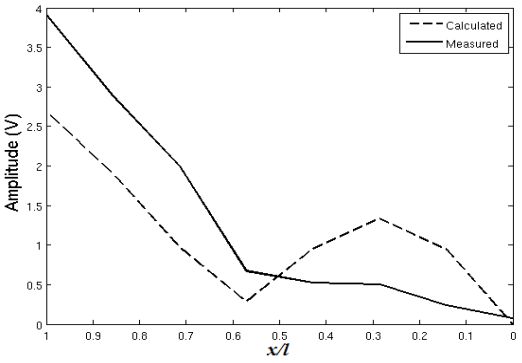

(d) $x' = 4/7$

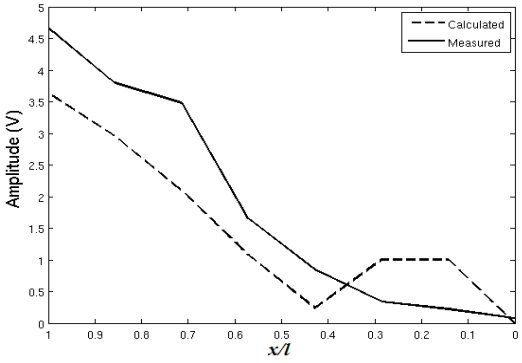

(e) $x' = 3/7$

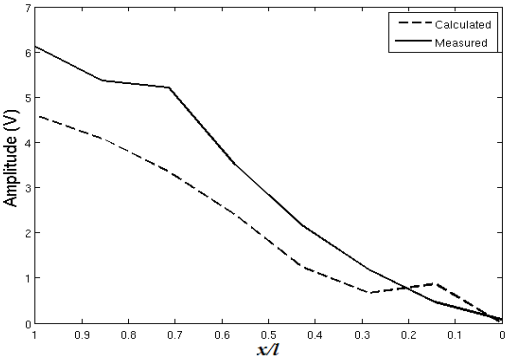

(f) $x' = 2/7$

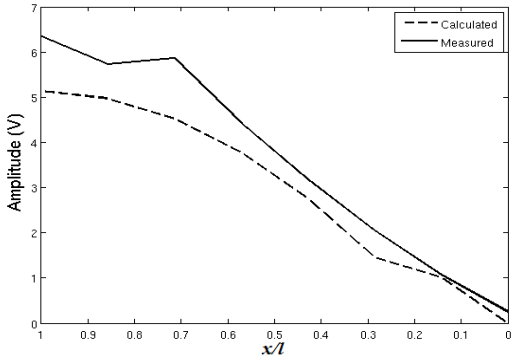

(g) $x' = 1/7$

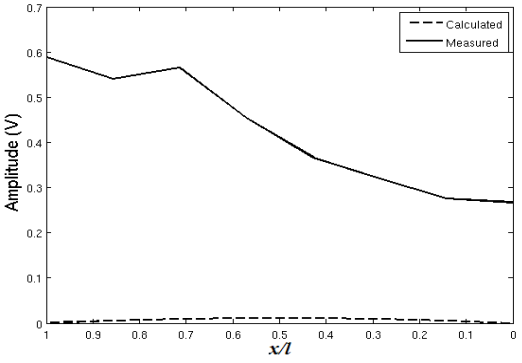

(h) $x' = 0/7$

FIGURE 4.12: Comparison of amplitude distribution between measured and calculated for plain winding

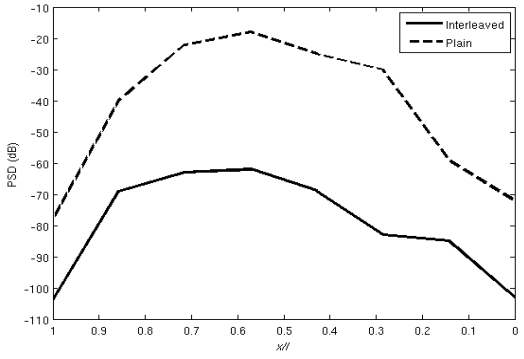

(a) $x' = 7/7$

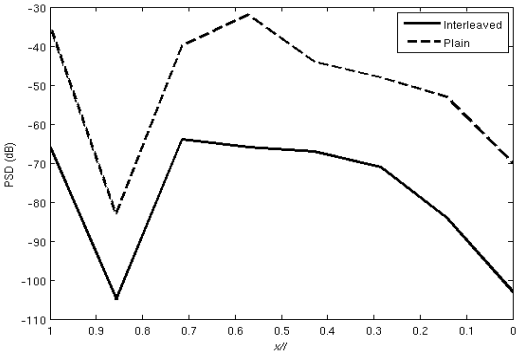

(b) $x' = 6/7$

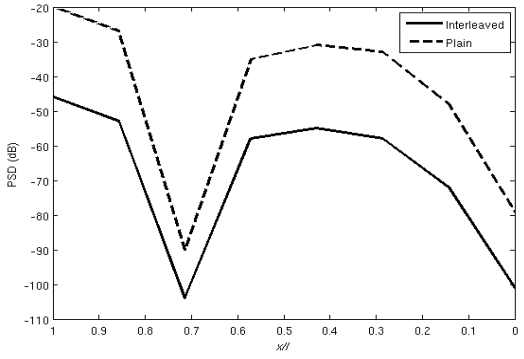

(c) $x' = 5/7$

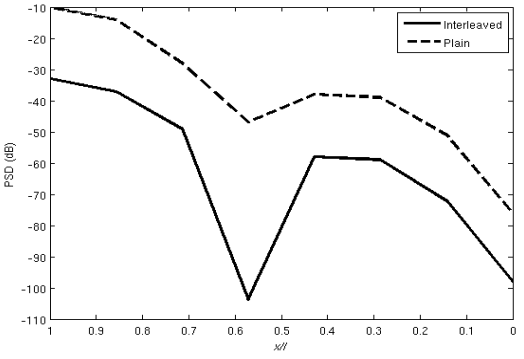

(d) $x' = 4/7$

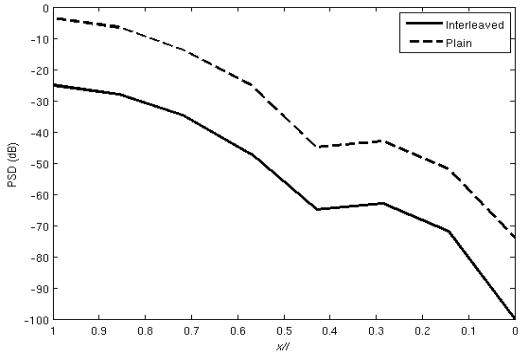

(e) $x' = 3/7$

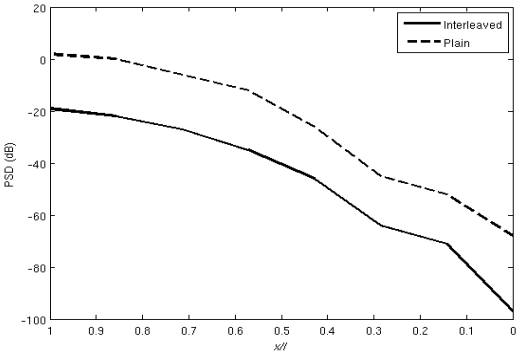

(f) $x' = 2/7$

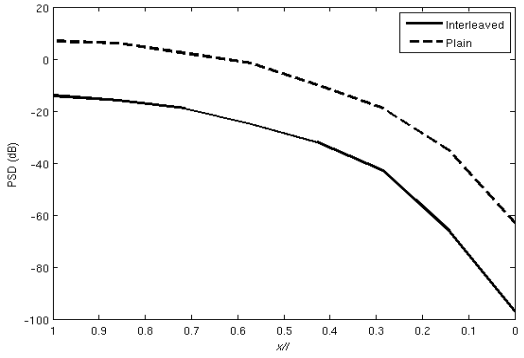

(g) $x' = 1/7$

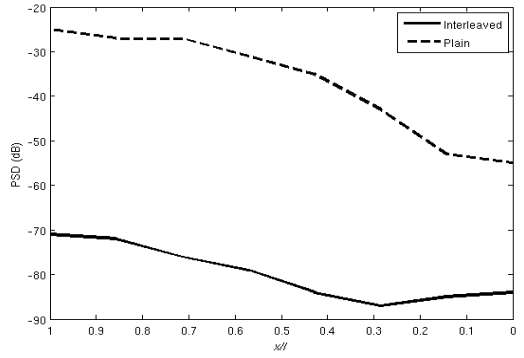

(h) $x' = 0/7$

FIGURE 4.13: Comparison of amplitude distribution between interleaved winding and plain winding

4.3.7 Harmonic Frequency Components

The PDE equation of (4.15) can be written in auxiliary form. Let a and b be the auxiliary contants as follows:

$$a = \frac{\partial v}{\partial x} \qquad and \qquad b = \frac{\partial v}{\partial t} \tag{4.40}$$

The auxiliary format for the PDEs therefore is:

$$LKa^2b^2 - a^2 + LC_g b^2 = 0 \tag{4.41}$$

Now, let $a = \pm j\eta$, and by writing b in terms of η, equation 4.41 becomes:

$$b = \frac{\pm j\eta_b}{\sqrt{LC_g - LK\eta^2}} \tag{4.42a}$$

$$b = \pm j\omega_s \tag{4.42b}$$

Therefore the harmonic frequency of the LCK circuit towards the neutral point is equivalent to

$$\omega_{sn} = \frac{s\pi}{\sqrt{L\left(l^2C_g - Ks^2\pi^2\right)}} \tag{4.43}$$

Similarly for the analysis towards the bushing the harmonic frequency can be written as:

$$\omega_{sb} = \frac{s_o\pi}{\sqrt{L\left(4l^2C_g - Ks_o^2\pi^2\right)}} \tag{4.44}$$

In the case of limited knowledge of the internal parameters of the transformer winding, it is possible to establish the ratio of harmonics for signal responses between the two terminals. Hence, the relationship of the harmonic frequency between the two terminals can be found by

$$\frac{\omega_{sb}}{\omega_{sn}} = \sqrt{\frac{s_o^2(l^2\alpha_n^2 - s^2\pi^2)}{s^2(4l^2\alpha_b^2 - s_o^2\pi^2)}} \tag{4.45}$$

Where α_n and α_b are the corresponding effective initial distribution coefficient towards neutral and bushing respectively. Figure 4.14 shows the frequency distribution of the measured winding response for both type of windings by injecting the infinite rectangular wave at different positions. It is evident that the dominant frequencies of the travelling waves are very similar for signals components travelling towards both ends of the winding.

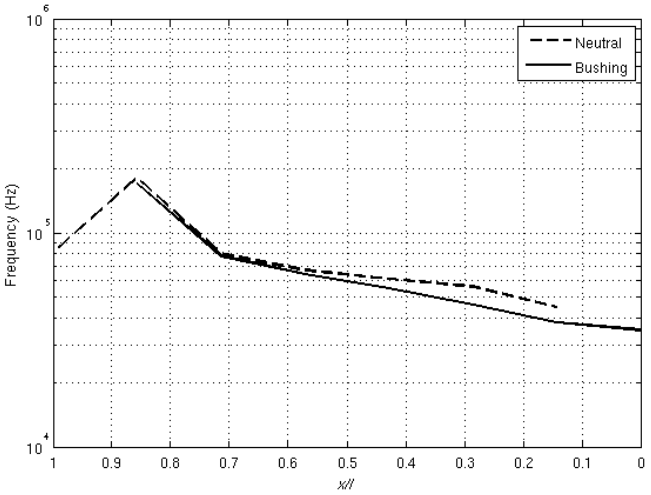

(a) Interleaved Winding

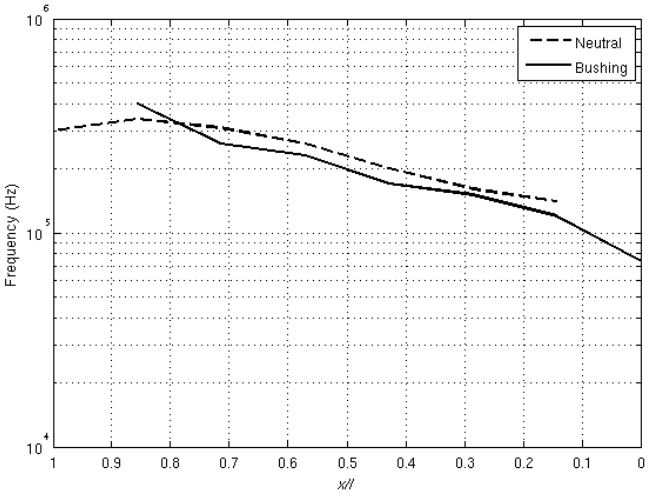

(b) Plain Winding

FIGURE 4.14: Comparison of frequency distributions for travelling waves moving towards bushing and neutral measurement points

4.4 Modelling The Discharge Signal

Practically, the source of signal oscillation due to a partial discharge may occur deep within in a transformer winding. Due to the fact that transformers are sealed in an enclosure with limited access to internal windings, any change in winding structure or signal disruption within the windings will be small and limited in terms of description using physical parameters, electrically and mechanically. Therefore the common way to evaluate the level of signal oscillation within the windings, is by measuring the signals injected at the winding ends.

It is therefore necessary to make several assumptions in order to model the discharge propagation of a signal within the windings. The assumptions are based on the classical aspect of travelling wave theory in a solid medium. It is assumed that the signal propagates away from the source, either towards the bushing or towards neutral lines, where they are then measurable from outside the transformer tank. No winding deformation either due to mechanical stress or electrical stress on the transformer winding is assumed to have occured. This is to ensure that the level of signal measured on both terminal ends is authentic and free of disruption. Finally the signal captured at the windings ends is assumed to originate from inside the transformer, and not from anywhere else outside of the transformer.

By ensuring the above assumptions are met, later analysis is limited to identical conditions. Unlike boundary conditions, the standing waves are bounded between the winding length of $0 < x < l$, which varies and only measurable at boundaries x equal to zero and l. The single condition under consideration for time is zero is known as the Initial Boundary Value Problem (IBVP).

4.4.1 Solution for the IBVP

PD signals originate at a point between the two terminals (bushing end and neutral end). The signal diverges into two different directions opposite to one another; hence the initial boundary value problem can be solved for a one dimensional wave equation. At point of source (on the transformer winding at x') the oscillation of signals is dominantly affected by the ground connection via capacitance, C_g, and series inductance, L. Hence by making K equals to zero the PDE is now [108]:

$$\frac{\partial^2 v}{\partial t^2} = \omega_{x'}^2 \frac{\partial^2 v}{\partial x^2} \tag{4.46}$$

Where

$$\omega_{x'} = \sqrt{\frac{1}{LC_g}} \tag{4.47}$$

The harmonic frequency at the source can be estimated by using the ratio of the harmonic frequency from the source to end terminals. Let $\omega_{x'b}$ and $\omega_{x'n}$ be the corresponding harmonic frequency at point x' towards bushing and neutral respectively. Therefore:

$$\frac{\omega_{x'b}}{\omega_{sb}} = \sqrt{\frac{4l^2}{s_o^2\pi^2} - \frac{1}{\alpha_{beff}^2}} \tag{4.48}$$

and

$$\frac{\omega_{x'n}}{\omega_{sn}} = \sqrt{\frac{l^2}{s^2\pi^2} - \frac{1}{\alpha_{neff}^2}} \tag{4.49}$$

Where α_{beff} and α_{neff} are the effective initial distribution constants towards bushing and neutral respectively. The PDE of equation (4.46) shows that the solution of the original source of the discharge signal can be derived in the xt-plane. This gives a solution that is straight forward. Therefore this thesis introduces a one dimensional solution for the IBVP using the D'Alembert Solution.

4.4.2 The D'Alembert Solution

The objective of D'Alembert solution is to find the solution of the initial value problem. The only conditions that are available and can be derived are the initial conditions at $t = 0$. In addition, the solution has an interesting interpretation in terms of two waves moving in opposite direction that can be solved using the D'Alembert solution as follows:

$$F(x,t) = \frac{1}{2}\big[f(x - \omega_{x'}t) + f(x + \omega_{x'}t)\big] + \frac{1}{2\omega_{x'}}\int_{x-\omega_{x'}t}^{x+\omega_{x'}t} g(x)dx \tag{4.50}$$

Where the initial conditions of the discharge signal at point x' are [108]:

$$\begin{aligned} F(x,0) &= f(x) \\ \frac{dF}{dt}(x,0) &= g(x) = 0 \end{aligned} \tag{4.51}$$

The initial conditions defined in equation (4.51), are the initial conditions of signal propagation. It has been shown that for the solution of signal propagation towards the neutral and bushing tap points, the initial conditions for the D'Alembert solution will

follow the same arguments as used for equations (4.18) and (4.25). Therefore the second term in D'Alembert solution of equation (4.50) can be disregarded to leave only the superposition principle of the following terms:

$$F(x,t) = \frac{1}{2}\Big[f(x-\omega_{x'}t) + f(x+\omega_{x'}t)\Big] \tag{4.52}$$

The equation represents two waves moving in opposite x-directions. However, the application of D'Alembert solution for a lumped circuit parameter model yields two different x transformations in the form of a half range sine series and a quarter range sine series. Figure 4.15 shows the transformation of x-plane to the Fourier range sine series in both directions.

The solution can now be explained in the x-plane for moving waves travelling in different directions. Applying the harmonic decay component to the solution of D'Alembert formula, the moving wave in xt-plane towards the bushing tap point now becomes:

$$\sum_{s_o=1}^{\infty} \frac{8l}{s_o^2\pi^2} sin\frac{s_o\pi}{2}\, e^{-\gamma_s t}\, \zeta_b sin\Big(\frac{s_o\pi x_b^*}{2l}\Big) cos\Big(\frac{s_o\pi x_b^*}{2l} - \omega_{x'b}t\Big) \tag{4.53}$$

and towards neutral is:

$$\sum_{s=1}^{\infty} \frac{2(-1)^s}{s\pi}\, e^{-\gamma_s t}\, \zeta_n sin\Big(\frac{s\pi x_n^*}{l}\Big)\, cos\Big(\frac{s\pi x_n^*}{l} + \omega_{x'n}t\Big) \tag{4.54}$$

Where

$$x_b^* = x_n^* = (1 - x') \tag{4.55}$$

Hence, the solutions for signals travelling toward bushing and neutral of Equations (4.53) and (4.54) respectively, are part of the D'Alembert solution. Applying the solution to the harmonic decay component problems yields the following derived solution:

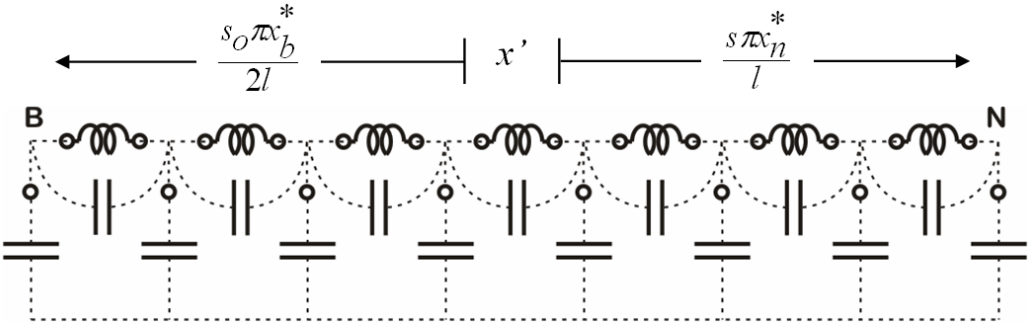

FIGURE 4.15: x-plane transformation into Fourier range sine series

$$F(x',t) = \varphi(x',t) + \sum_{s=1}^{\infty} \frac{(-1)^s}{\pi} e^{-\gamma_s t} \left[\frac{1}{s} \zeta_n sin\Big(\frac{s\pi x_n^*}{l}\Big) cos\Big(\frac{s\pi x_n^*}{l} + \omega_{x'n} t\Big) - \frac{4l}{s_o^2 \pi} \zeta_b sin\Big(\frac{s_o \pi x_b^*}{2l}\Big) cos\Big(\frac{s_o \pi x_b^*}{2l} - \omega_{x'b} t\Big) \right] \tag{4.56}$$

The first $\varphi(x',t)$ term represents the time domain voltage fixed distribution component of the transformer winding at point x'. This component is independant of the direction of the travelling wave, i.e.

$$\varphi(x',t) = \varphi_n(x',t) = \varphi_b(x',t) \quad for \quad 0 < x' < l \tag{4.57}$$

This analytical solution implies that the initial harmonic signal or the signal source can be estimated provided that x' has been identified. The advantage of the solution is that it could provide insight into partial discharge magnitude estimation, using fewer parameters for estimation. As α and β are part of the solution for ζ_b and ζ_n (see Equations (4.21) and (4.28)), therefore α and β are the main parameters that need to be estimated, and can be found using a non-linear least square estimation technique.

Figure 4.16 and Figure 4.17 show the comparison of the simulated results from the model equation using the D'Alembert solution and experimental measurements for the interleaved winding and plain winding respectively. Both results have common patterns of oscillations; the lower the signal is injected from the bushing the more energy in any oscillation, the higher the amplitude of any oscillation and the lower the frequency of oscillation. The interleaved winding also shows a more constant oscillation frequency when compared to the plain winding. The slow change contributes to the phase shift of the source signal as it moves from $x' = 7/7$ to $x' = 0/7$. Analytically it can be shown from equation (4.56) that for the decay component only, this can be rewritten as:

$$\sum_{s=1}^{\infty} \frac{1}{\pi} \left[A_N cos\left(\frac{s\pi x_n^*}{l} + \omega_{x'n} t \right) + A_B cos\left(\frac{(2s-1)\pi x_b^*}{2l} - \omega_{x'b} t \right) \right] \tag{4.58}$$

Where A_N and A_B are amplitude factors towards neutral point and bushing tap-point respectively.

The second finding from this model analysis is, the harmonic frequency of both measured waveforms are lower as the wave injection position moves from $x' = 7/7$ to $x' = 0/7$. This is due to the intermediary inductance at position x', where analytically it can be ex-

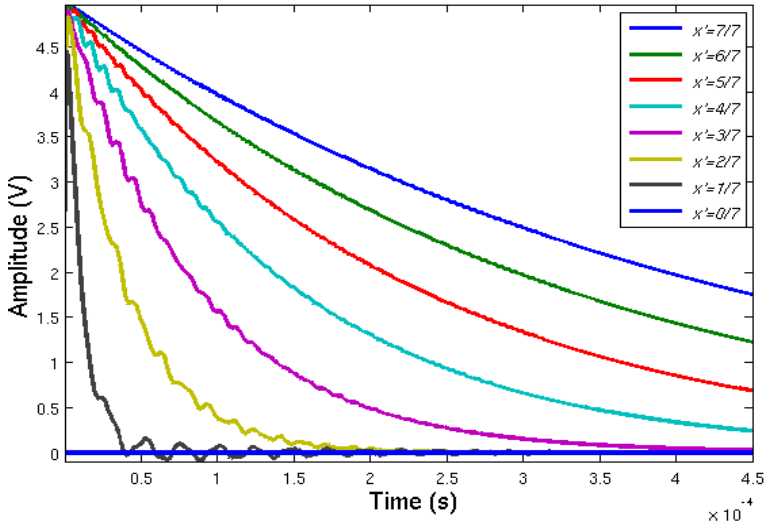

(a) Model simulation

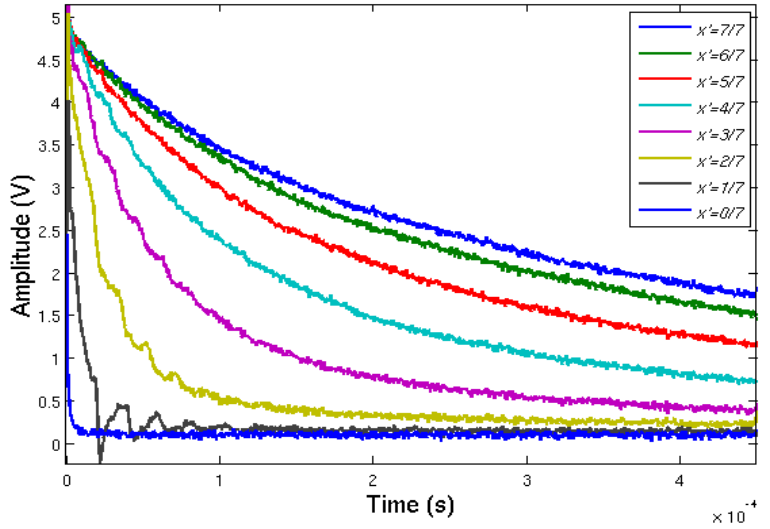

(b) Measured waveforms

FIGURE 4.16: Comparison of discharge signal for interleaved winding between D'Alembert winding model and measured waveform

plained by equation (4.44). In this case the harmonic frequency is inversely proportional to the square root of $L_{dx'}$ and it can be expressed as follows:

$$\omega_{sb} = \frac{c'}{\sqrt{L_{dx'}}} \tag{4.59}$$

Where c' is equivalent to:

$$c' = \frac{s_o \pi}{\left(4l^2 C_g - K s_o^2 \pi^2\right)^2} \tag{4.60}$$

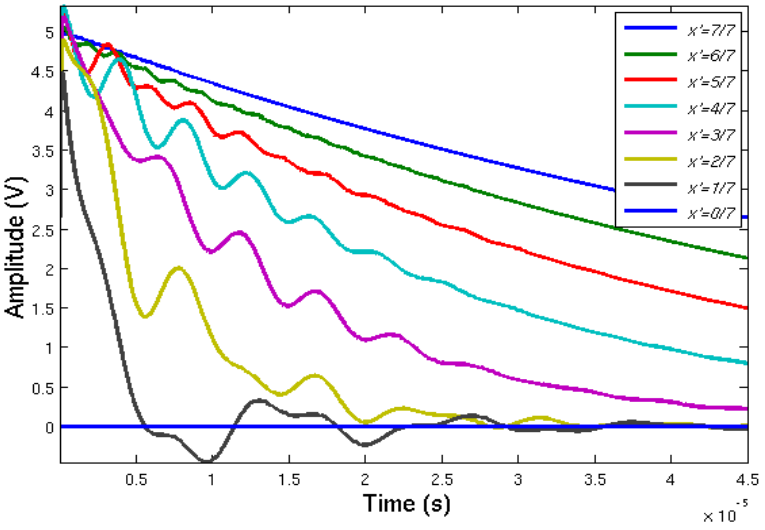

(a) Model simulation

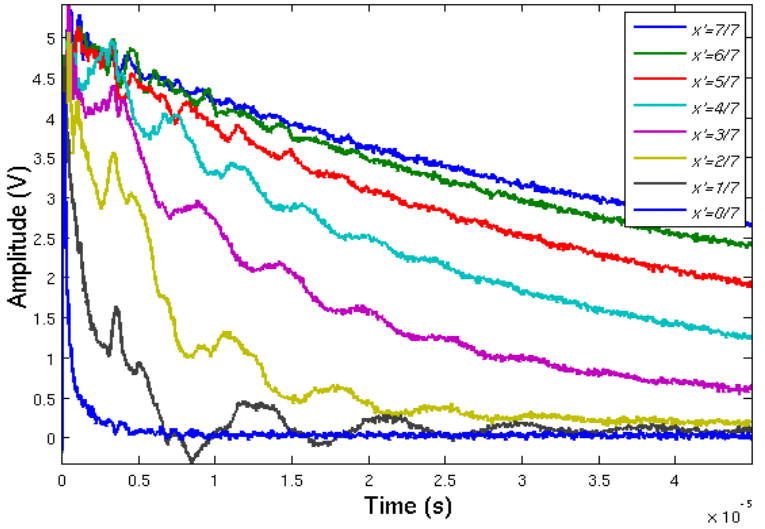

(b) Measured waveforms

FIGURE 4.17: Comparison of discharge signal for plain winding between D'Alembert winding model and measured waveform

4.5 Moving Zeros Analysis

Frequency analysis can be experimentally undertaken by using the same calibrated signal in order to simulate infinite rectangular wave propagation for different location along the winding [75]. This time, the time domain propagated signals are transformed into power spectrum densities (PSD) in its frequency domain. The measured signals at points of source, x', were captured using a DSO and stored digitally. With a sampling rate of 20 mega sample per-second, the total length of the data is 10000 sample. The results clearly indicate the change in zero locations that give information about the location of the signal source along a transformer winding. Moving zeros analysis of the PSD is shown in Figure 4.18 and Figure 4.19 for interleaved winding and plain winding respectively.

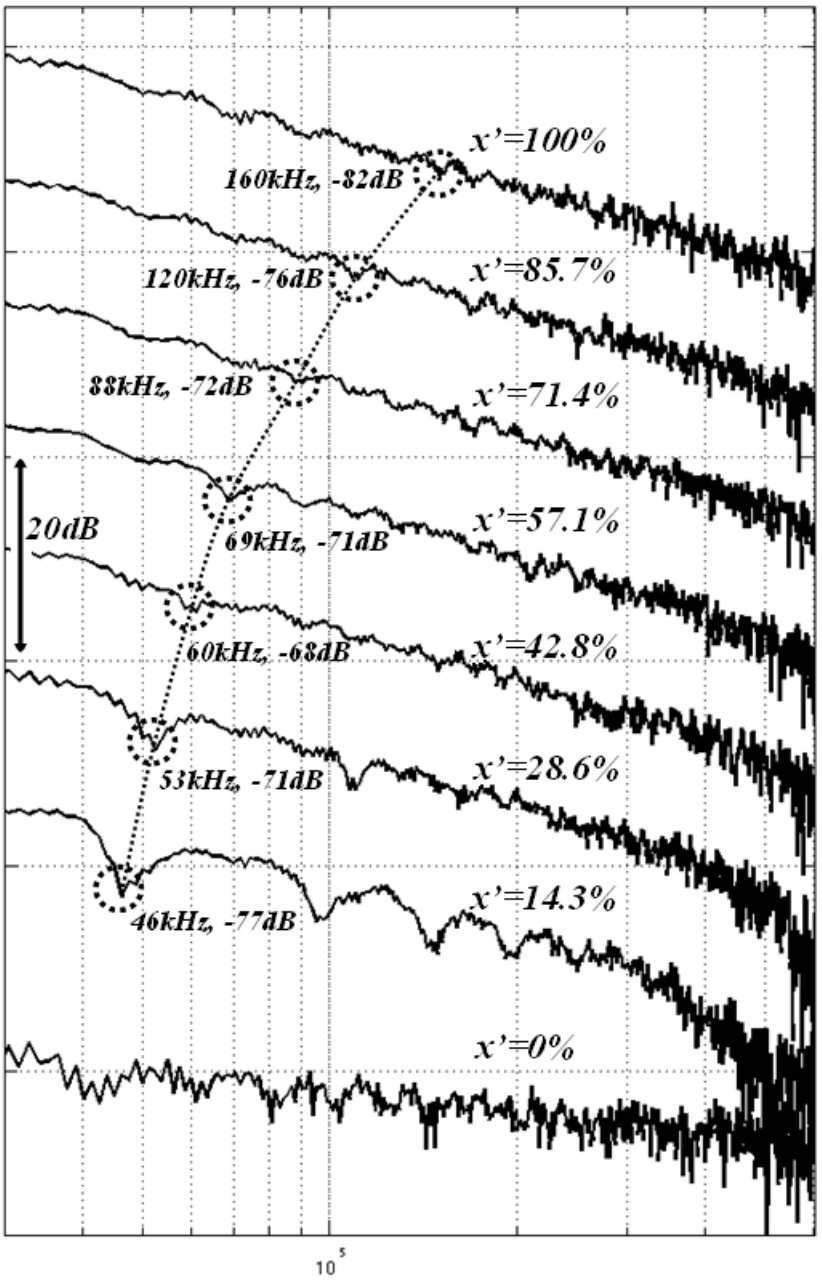

FIGURE 4.18: Moving zeros of interleaved winding, measurements at different x'

Again both windings show a similar pattern in terms of the movement of the first zero, which represents the lowest frequency of oscillation of the propagated signals. The zero magnitudes also show that it has a constant range between -82dB to -68dB and -63dB to -54dB for the interleaved winding and plain winding respectively.

Table 4.1 shows the fundamental frequency for every point of injection. The frequencies were extracted based on the dominant peaks on the PSD that represent the main frequency component of the transformed signals. The fundamental frequency of both windings at $x' = 7/7$ to $x' = 5/7$ is above the range of 1MHz. This is apparently not quite the fundamental frequency of the harmonic decay component, since it is very close

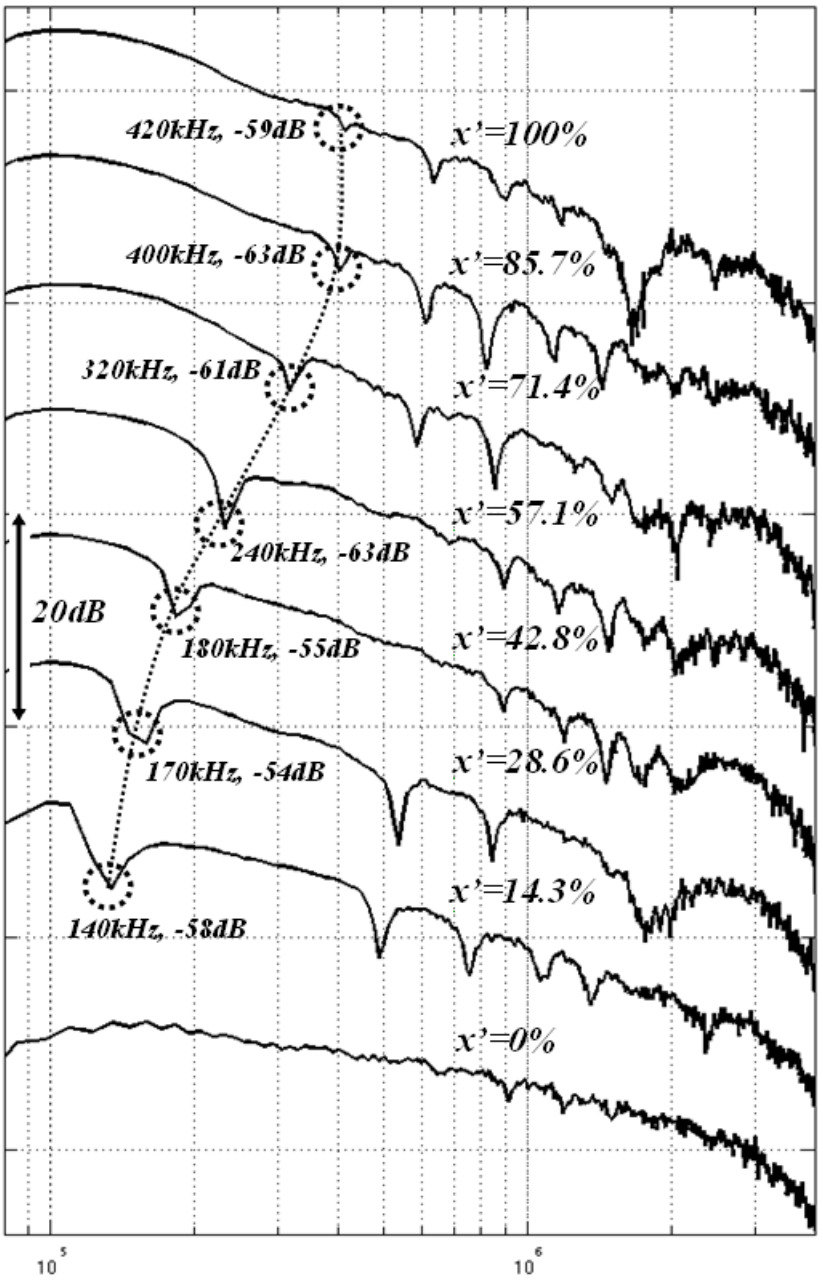

FIGURE 4.19: Moving zeros of plain winding, measurements at different x'

to the noise of the system. However, the fundamental frequencies at these points are very high and low in amplitude and are almost insignificant within the overall response of the harmonic decay component in the time domain. Thus the visible component as from Equation (4.56) now becomes:

$$\psi(x', t) \approx \varphi(x', t) \tag{4.61}$$

which is approximately equivalent to the fixed distribution components.

TABLE 4.1: Fundamental frequency at various point of injection

Winding Sections	**Interleaved Winding**		**Plain Winding**	
x'	$\sim f_o$ (Hz)	$\sim$ dB	$\sim f_o$(Hz)	$\sim$dB
$x' = \frac{7}{7}$:	1.1M	-103	2M	-78
$x' = \frac{6}{7}$:	1.1M	-103	3M	-83
$x' = \frac{5}{7}$:	1.1M	-103	3M	-90
$x' = \frac{4}{7}$:	980k	-104	260k	-47
$x' = \frac{3}{7}$:	70k	-65	240k	-45
$x' = \frac{2}{7}$:	50k	-64	190k	-45
$x' = \frac{1}{7}$:	60k	-66	100k	-35
$x' = \frac{0}{7}$:	20k	-84	50k	-55

However the injection signal at $x' = 0$, do not have a distinct zero for both windings, since the signals are all at the ground connection and have almost zero response along the winding. Therefore as it can be seen from Figures 4.16(a) and 4.17(a), the calculated model simulates results which show insignificant harmonic decay components for signal injection close to the bushing. However a significant change of frequency and amplitude occurs once the injection point is beyond 71.4%. Apart from that, the only difference between the two windings is the amplification factor of the oscillating magnitude which for the plain winding has a higher significant difference of initial distribution constant; α, to final distribution constant; β, as compared to the interleaved winding. This difference analysis has been discussed previously with reference to Figure 4.13.

4.6 Summary

New techniques for simulation of a PD signal propagating along a transformer winding have been derived and presented in this chapter using the concept of standing wave theory. The fundamental principle involved is to solve the initial boundary value problem. The use of split winding analysis has been able to estimate the intermediary level of oscillation along the winding. This involves partitioning the level of equivalent lumped parameter model into two; from the signal source towards the bushing tap point and towards neutral to ground connection.

By using the D'Alembert solution, the problem for describing propagation of an infinite rectangular wave and identification of its source gives good results based on comparison of simulation results with measurements from injected calibrated signals on the model windings. The advantages of this solution are that it provides an estimation without fully knowing the boundary condition and only a few standing wave parameters require definition.

The combination of fixed distribution component and harmonic decay component from analytical model solutions, provides an insight into the oscillation of travelling waves which can be used to estimate the energy level of the oscillation within the windings. Thus the results presented using the PSD technique not only provide the spectrum level of the oscillation but also provide harmonic frequency information by means of analysis of the moving zeros. This also provides the information about the signal source which can be approximated using the D'Alembert solution.

Chapter 5

Arbitrary Waveform Injection into a Transformer Winding

The model description in Chapter 4 is based on homogeneous partial differential equations. The input to the system is a unit step input of infinite rectangular that can be validated experimentally with the injection of calibrated signals into the winding. In reality, the input to the system is a time varying signal, having variable amplitudes, frequencies and decay factors. Unlike rectangular waves, a partial discharge signal may be represented as a high transition front wave signal, that is oscillating and decaying over time.

This chapter presents a solution for time varying function inputs injected into the system represented by a lumped parameter model. Based on the standing wave solution of Chapter 4, the solution for a time varying input is derived using Duhamel's principle. This leads on to a possible way to estimate measured waves at the end terminals of transformer windings based on a restricted information of its physical parameters. Experiments using impulse response measurement and frequency response measurement have been conducted to investigate the capability of applying the developed model and analytical technique.

5.1 Model Description

A time varying input to a system will lead to a time varying output response. Thus in the case of partial discharge events, the problem is treated as a time varying input response of the lumped parameter model system. Figure 5.1 shows the theoretical concept in a simplified diagram and the system description of time varying boundary conditions for the experimental model.

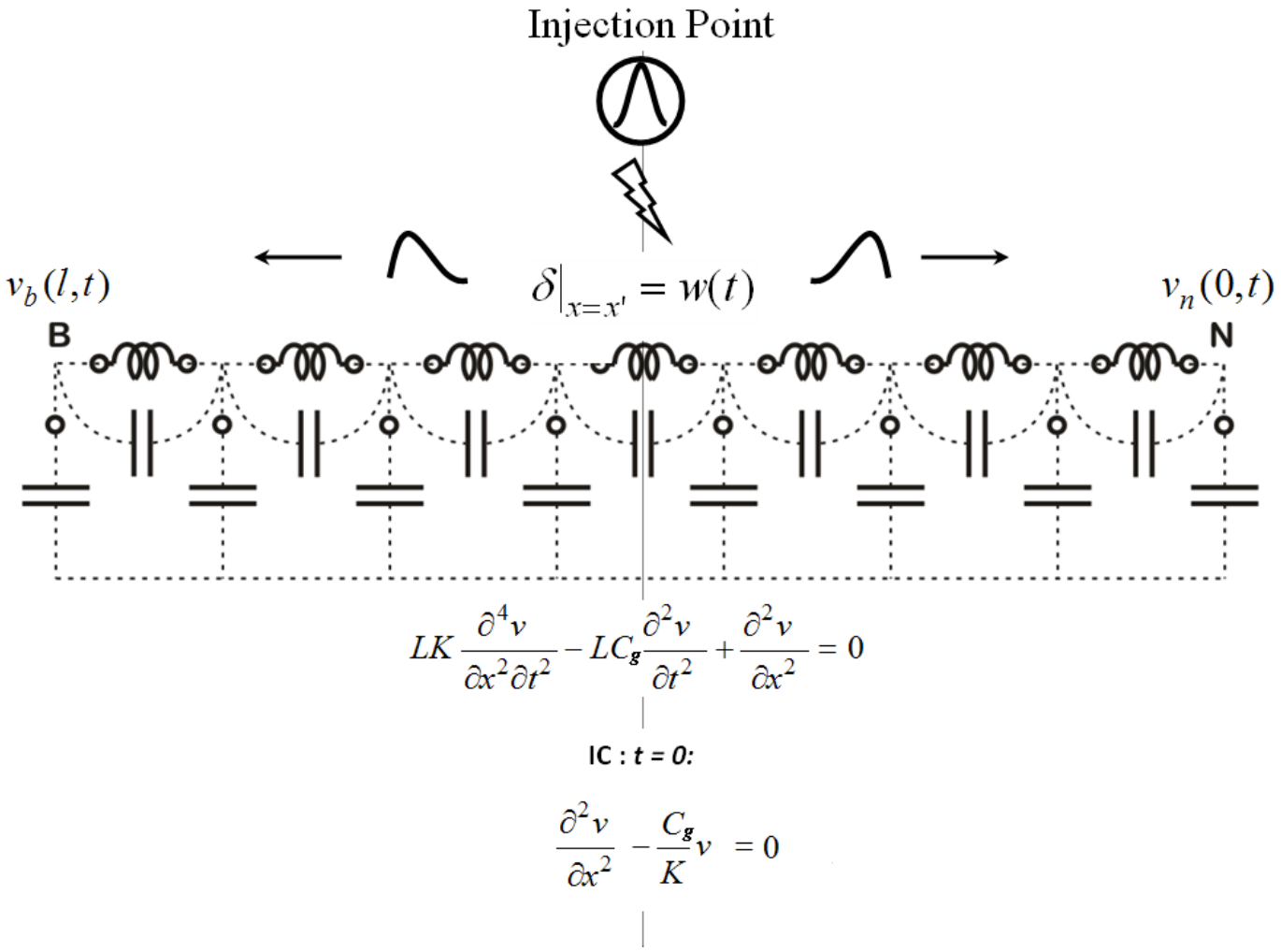

FIGURE 5.1: Model description

Consider a signal injected at distance x' to represent the source $w(x', t)$, and the corresponding time varying response is captured at both ends of the windings, bushing and neutral to ground terminal represented by $V_B(t)$ and $V_N(t)$ respectively. With the same PDE as for Equation (4.15), the following time varying boundary conditions are considered:

$$\begin{aligned} v(0,t) &= V_N(t) \\ v(l,t) &= V_B(t) \end{aligned} \tag{5.1}$$

With following initial condition:

$$\frac{\partial^2 v}{\partial x^2} - \frac{C_g}{K} v = 0 \tag{5.2}$$

To solve the problem of a time varying input signal with time varying boundary conditions, Duhamel's principle is employed by using the constant input solution of the homogeneous system as a fundamental solution [108].

5.1.1 Time Varying Signal Model

Transient analysis is often used to represent the behaviour of a transformer at high frequency. The analytical results as well as experimental measurements can be used to explain the behaviour of a transformer under transient conditions [45]. Experimentally, an impulse response measurement is the best approach to explain transformer behaviour as it excites all of the system responses across the frequency domain. Analytically, the transient signal or impulse signal input can be modelled using an equation, similar to Equation (3.9), based on the principle of superposition,

$$w(t) = E(e^{-at} - e^{-bt}) \tag{5.3}$$

where E, a and b are arbitrary constants. Depending on the value of a and b, the transient input signal can have a different shape and frequency components. Figure 5.2, shows the variation of pulse waveshape for different values of a and b.

The rectangular waveshape of Figure 5.2(a), has a sharp increase of its wavefront from zero to full value and maintained at that value thereafter. Such a wave can become dangerous to any apparatus, since its abrupt changes of its wavefront may cause maximum gradients and its sustained tail will cause maximum oscillation in a winding. For

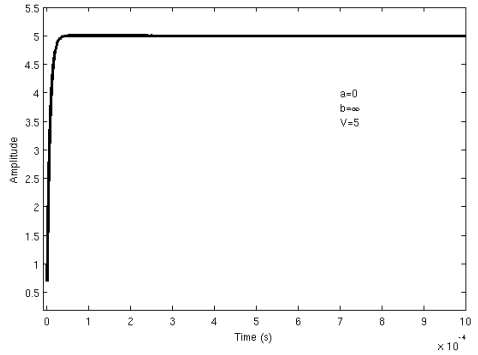

(a) $a = 0$, $b = \infty$, $E = 5$

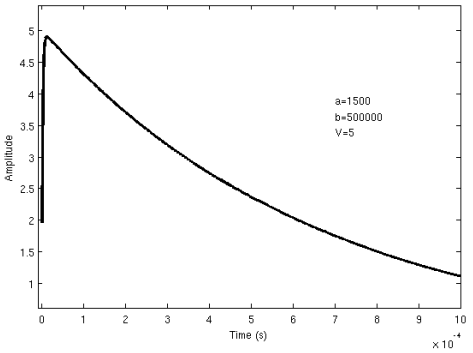

(b) $a = 1.5 \times 10^3$, $b = \infty$, $E = 5$

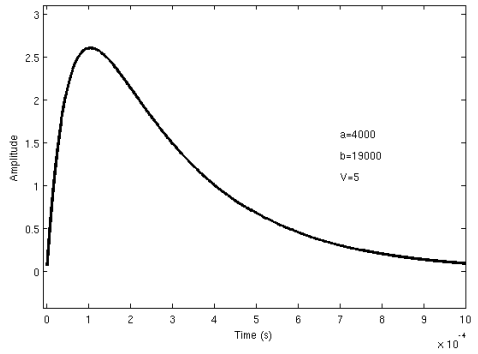

(c) $a = 1.5 \times 10^3$, $b = 5 \times 10^5$, $E = 5$

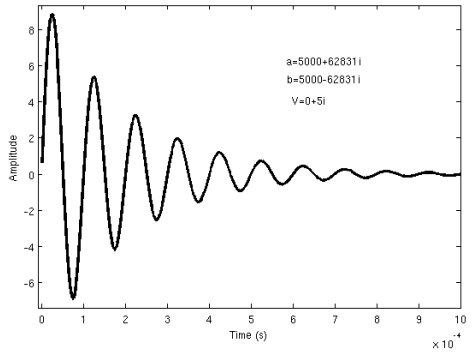

(d) $a = 5 \times 10^3 + 2\pi(1 \times 10^4)i$, $a = 5 \times 10^3 + j2\pi(1 \times 10^4)$, $E = j5$

FIGURE 5.2: Examples of waveshapes approximation using $w(t) = E(e^{-at} - e^{-bt})$

simplicity, $b = \infty$ is used to represent such a high magnitude. The simple exponential wave in Figure 5.2(b), is found by specifying the value of b high enough compared to a.

Figure 5.2(c) is a typical waveshape of impulse response, with a slower high rise transition and faster decay factor compared to 5.2(a) and 5.2(b). This is the typical waveshape that represents an impulse-like input signal. By assigning an imaginary value to the constant, the superposition principle of the transient equation now becomes a hyperbolic function and thus oscillatory. Thus by superposition, a typical waveform may consist of a complex response containing a real sinusoidal decay component. Careful choice of a and b mean that Equation (5.3) can represent a range of possible discharge input signals for the purposes of simulation studies.

5.1.2 Application of Duhamel's Principle

The model presented in Chapter 4 is based on a constant step input generating an incident wave. This is however subject to zero initial conditions of the system response. In the case of a transient incident wave injected along the transformer winding, the system response can be determined using Duhamel's principle [108]. Where Duhamel's principle states that:

" If $F_f(x,t)$ is the response of a linear system with zero initial conditions to a single, constant boundary condition with magnitude of unity (referred to as the fundamental solution), then the response of the same system to a single, time-varying boundary conditions with magnitude $w(t)$ can be obtained from the fundamental solution according to [108]:

$$f(x,t) = \int_0^t F_f(x, t-\tau)\, w(\tau) d\tau \tag{5.4}$$

or using integration by parts:

$$f(x,t) = w(t)F_f(x,0) + \int_0^t F_f(x, t-\tau)\, \frac{dw(\tau)}{d\tau} d\tau \qquad " \tag{5.5}$$

Therefore, applying Duhamel's principle to Equation (5.3) with a non-zero initial conditions as an addition, and using the solution towards the neutral of Equation (4.36) gives;

$$\begin{aligned} f(x,t) = E(t)\Big[V_N(t) + \frac{x}{l}\Big(V_B(t) - V_N(t)\Big)\Big] \\ + \int_0^t \sum_{s=1}^{\infty} A_{sn} sin\left(\frac{s\pi x_n}{l}\right) e^{-\gamma_s t}\, cos\omega_{sn}(t-\tau) \frac{d}{d\tau}\left(E(e^{-a\tau} - e^{-b\tau}\right) d\tau \end{aligned} \tag{5.6}$$

where

$$A_{sn} = \frac{2(-1)^s}{s\pi}\zeta_n \tag{5.7}$$

Solving the equation using integration by parts and considering only second order polynomial expansion, the complete solution for a time varying input impulse like waveshape is:

$$f_n(x,t) = E\Big[V_N(t) + \frac{x}{l}\Big(V_B(t) - V_N(t)\Big)\Big]\Big(e^{-at} - e^{-bt}\Big) + \sum_{s=1}^{\infty} A_{sn}\, E\, e^{-\gamma_s t}\, sin\Big(\frac{s\pi x_n}{l}\Big)\Big(\frac{b-a}{\omega_{sn}} sin\,\omega_{sn}t + \frac{b^2-a^2}{\omega_{sn}^2} cos\,\omega_{sn}t + \frac{a^2e^{-at} - b^2e^{-bt}}{\omega_{sn}^2}\Big) \tag{5.8}$$

and applying the same technique for the solution towards bushing, the arbitrary waveform at any point x is defined as:

$$f_b(x,t) = E\Big[V_N(t) + \frac{x}{l}\Big(V_B(t) - V_N(t)\Big)\Big]\Big(e^{-at} - e^{-bt}\Big) + \sum_{s=1}^{\infty} A_{sb}\, E\, e^{-\gamma_s t}\, sin\Big(\frac{s_o\pi x_b}{2l}\Big)\Big(\frac{b-a}{\omega_{sb}} sin\,\omega_{sb}t + \frac{b^2-a^2}{\omega_{sb}^2} cos\,\omega_{sb}t + \frac{a^2e^{-at} - b^2e^{-bt}}{\omega_{sb}^2}\Big) \tag{5.9}$$

where

$$A_{sb} = -\frac{8l(-1)^s}{s_o^2\pi^2}\zeta_b \tag{5.10}$$

Both solutions of equations (5.8) and (5.9) are subject to the range of distance from the neutral to ground connection as follows:

$$x_n = \frac{x}{x'} - 1 \quad and \quad x_b = x - x' \tag{5.11}$$

5.2 Time Varying Impulse Waveshape

The estimation of the resulting waveform using Duhamel's principle can be achieved in two ways, *superimposition* and *superposition*. Superimposition is by retaining the waveshape of impulse signal at a time range and superimpose another signal on top of the first signal at a different time range. However the superposition technique consists of summation of several harmonic levels using time domain to frequency domain transformations and the inverse Fourier transform to obtain the resultant signal.

Figure 5.3 shows the different type of impulse signal used in the experiment. The pulses are varied in width and rise time. A HP 8082A pulse signal generator with multivarible frequencies and pulse width was used to produce the impulse used in the experiment. The choice of pulses is based on the equipment capability and the response of transformer windings under different pulse transitions.

The pulse transition under consideration in the experiment are:

(a) Pulse Width = $40\mu s$; Rise Time = $30\mu s$.

(b) Pulse Width = $5\mu s$; Rise Time = $2.5\mu s$.

(c) Pulse Width = $1.2\mu s$; Rise Time = $0.5\mu s$.

(d) Pulse Width = $150ns$; Rise Time = $75ns$.

(e) Pulse Width = $100ns$; Rise Time = $30ns$.

(f) Pulse Width = $6ns$; Rise Time = $3ns$.

5.3 Estimation by Superimposition

The test was carried out for different types of impulse waveform transitions, which were injected at different terminals. The propagated signals were then captured at both bushing and neutral terminals, using a Tektronix DPO7254 digital phosphor oscilloscope.

Consider a pulse of width τ second (Figure 5.4) injected into the winding system. Hence the estimation of the system response can be achieved by superimposition of two different waves over the time ranges;

$$\begin{aligned} f(x, 0 < t < \tau) &= w(t) \\ f(x, t > \tau) &= w(t - \tau) \end{aligned} \tag{5.12}$$

hence the superimposition of signal captured at the bushing becomes:

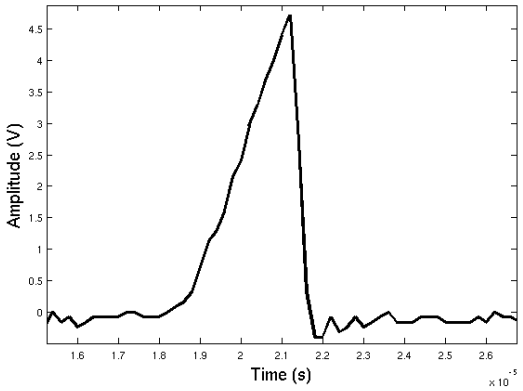

(a) Pulse Width = $40\mu s$; Rise Time = $30\mu s$

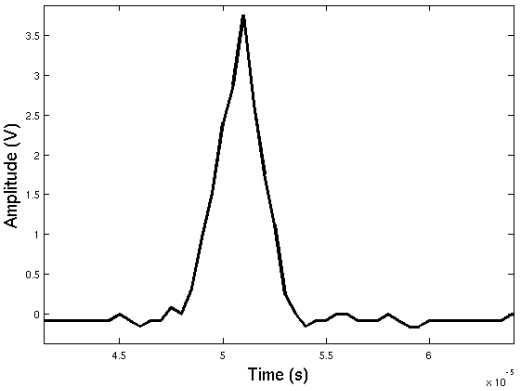

(b) Pulse Width = $5\mu s$; Rise Time = $2.5\mu s$

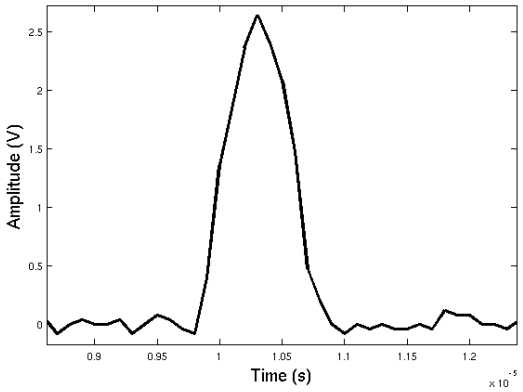

(c) Pulse Width = $1.2\mu s$; Rise Time = $0.5\mu s$

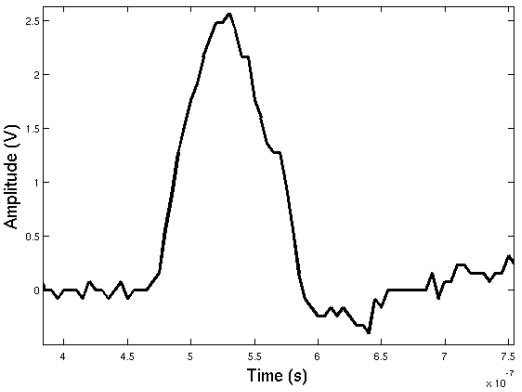

(d) Pulse Width = $150ns$; Rise Time = $75ns$

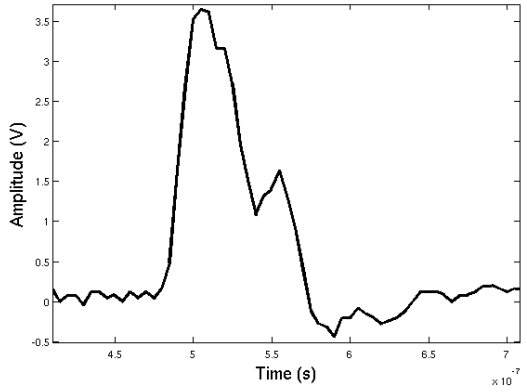

(e) Pulse Width = $100ns$; Rise Time = $30ns$

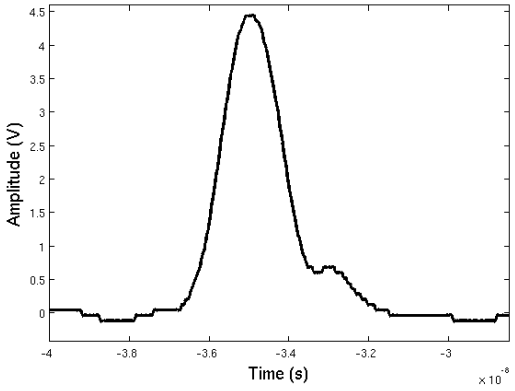

(f) Pulse Width = $6ns$; Rise Time = $3ns$

FIGURE 5.3: Impulse waveshapes with different pulse width and transition

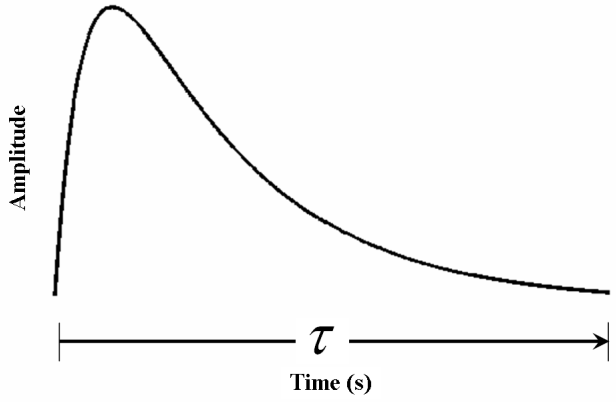

FIGURE 5.4: Pulse with width τ

$$f(x,t>\tau)=\sum_{s=1}^{\infty}A_{sb}\,E\,e^{-\gamma_s(t-\tau)}\,sin\left(\frac{s_o\pi x_b}{2l}\right)\left(\frac{b-a}{\omega_{sb}}sin\,\omega_{sb}(t-\tau)\right.$$
$$\left.+\;\frac{b^2-a^2}{\omega_{sb}^2}cos\,\omega_{sb}(t-\tau)+\frac{a^2e^{-a(t-\tau)}-b^2e^{-b(t-\tau)}}{\omega_{sb}^2}\right) \tag{5.13}$$

However the solution for $f(0<t<\tau)$ is obtained using Equation (5.9), which also represents the general solution for this type of input signal. The τ operator analytically represents the time delay in the time domain signal response, which consequently may vary depending on the width of the injected pulse.

5.3.1 Pulse Width $5\mu s$, Rise Time $2.5\mu s$; Neutral Grounded

Consider an applied wave of $5\mu s$ pulse width and $2.5\mu s$ rise time to the fully grounded interleaved winding. Only six measurements are considered to demonstrate the propagation model within the range inside the transformer winding. Based on the model description with multi-point injection for $l > x' > 0$, the end terminals bushing tap point and neutral point are used as measurement points. Figure 5.5 shows the measured signal at bushing terminal for different position of x's starting from $x' = 6/7$ to $x' = 1/7$. The variation of time domain accumulated wave can be seen clearly from the PSD plot, where the further away the pulse is injected the higher the accumulated wave, for which the injection at $x' = 1/7$ shows the the highest gain of amplitude factor of the first harmonic captured at the bushing terminal.

To demonstrate the superimposition principle, consider the injection point at $x' = 4/7$. Figure 5.6(a) shows the comparison of the experimental results for the end terminal measurements and the source waveform. Table 5.1 shows the estimated parameter calculated based on the derivation of Duhamel's principle from Equations (5.9) and (5.13) where the estimated waveform are shown in Figure 5.6(b).

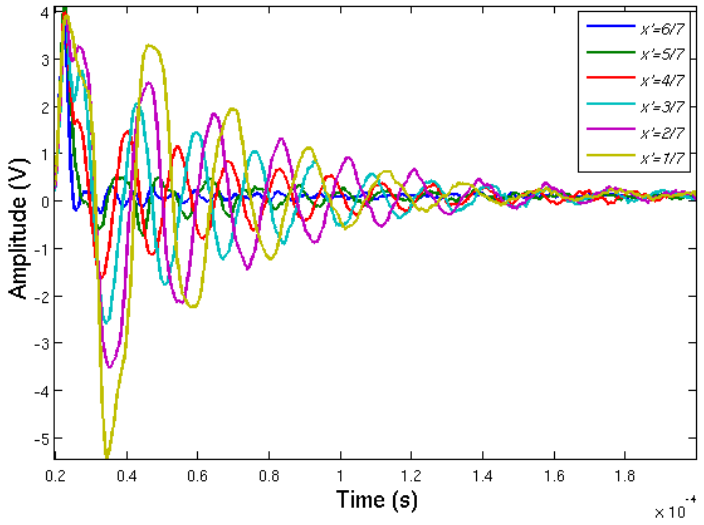

(a) Time domain

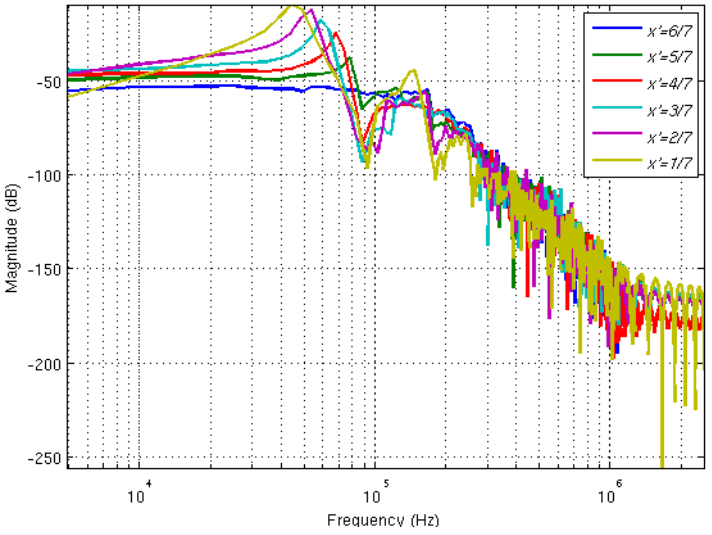

(b) Frequency domain

FIGURE 5.5: Impulse waveshape measured at bushing for interleaved winding, with $5\mu s$ pulse width and $2.5\mu s$ rise time, pulse injected at x'

Note that the signal applied at $x' = 4/7$, still retains its original waveshape with the same τ and this can be seen from the terminal bushing measurement. The captured signal at bushing is therefore divided into two different time ranges, where the source of the original signal is estimated for $t < \tau$.

TABLE 5.1: Calculated parameters based on superimposition principle

$\tau = 26\mu s$	E	α	β	ω_{sb}	a	b	γ_s
$0 < t < \tau$:	$4V$	0.3347	0.31	10kHz	6.9×10^5	1.1×10^6	-2×10^5
$t > \tau$:	$1.5V$	0.3347	0.31	69kHz	7×10^6	9.1×10^6	-2.3×10^4

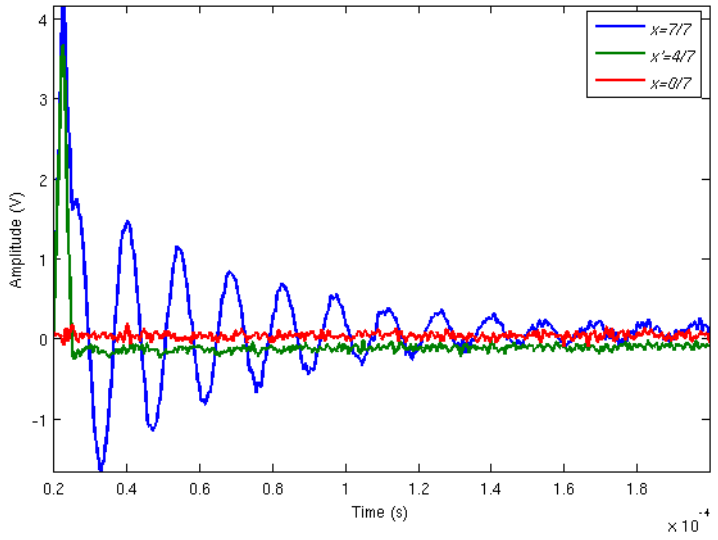

(a) Measurement

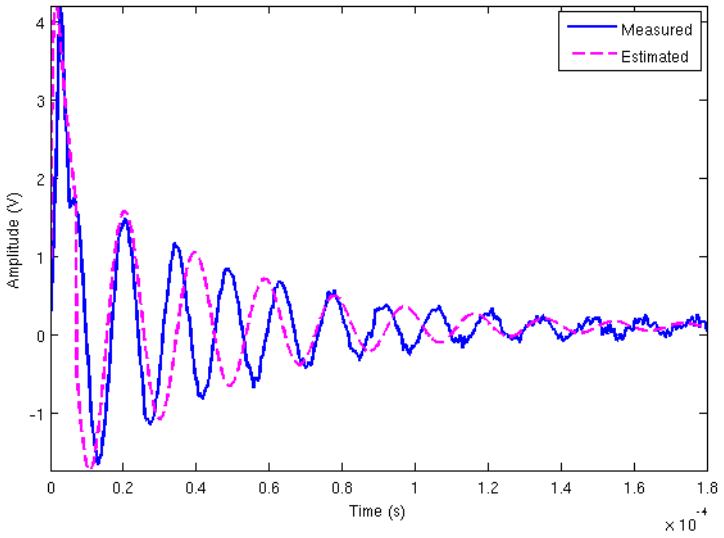

(b) Estimation at $x = 7/7$

FIGURE 5.6: Impulse waveshape, with $5\mu s$ pulse width and $2.5\mu s$ rise time, pulse injected at $x' = 4/7$; $V_B = 0.2V$, $V_N = 0V$

5.3.2 Pulse Width $40\mu s$, Rise Time $30\mu s$; With DC offset on pulse

The plain disc winding is now connected via a 50Ω resistor to ground. The value of $Z(50\Omega)$ provides a mean offset voltage to ground. A pulse with $40\mu s$ pulse width and $30\mu s$ rise time is used to investigate the signal response at the bushing and neutral to ground terminal points. Figure 5.7 shows the measurement results of pulse measurement at bushing terminal point for various point of source x's.

The two diagrams of Figure 5.7(a) and Figure 5.7(b) show the signal propagation behaviour in the time domain and frequency domain respectively. The PSD shows a moving pole, which carries information about the location of the disharge source. Similarly, the

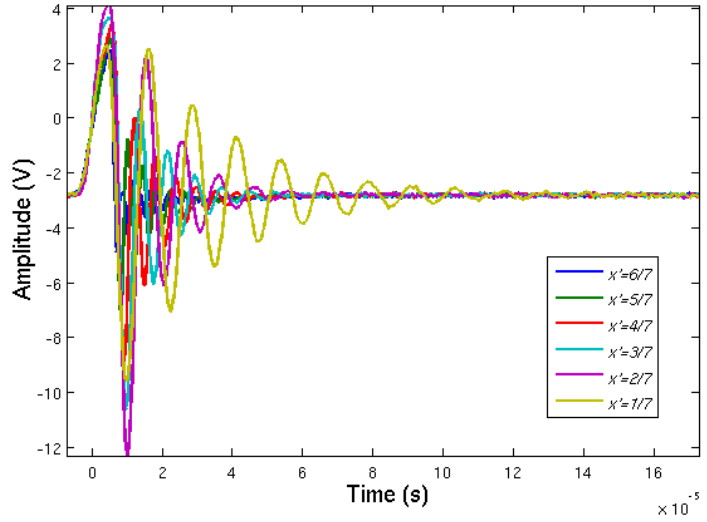

(a) Time domain

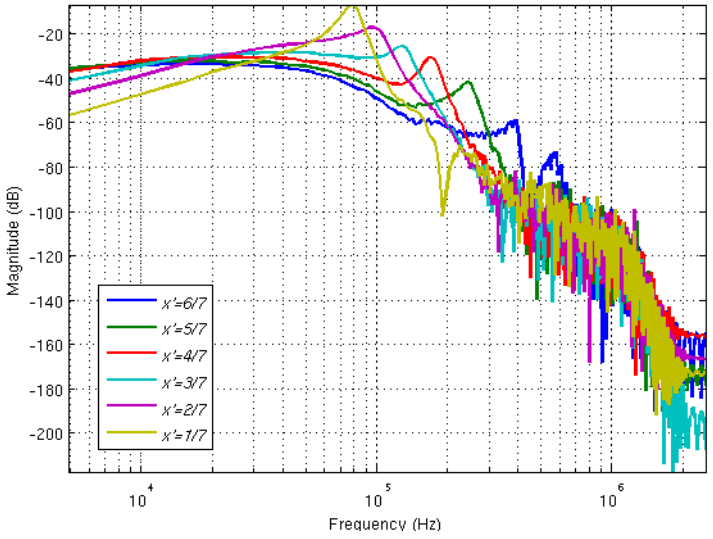

(b) Frequency domain

FIGURE 5.7: Impulse waveshape measured at bushing for plain winding, with $40\mu s$ pulse width and $30\mu s$ rise time, pulse injected at different x'

accumulated harmonic level is highest for the pulse injected at $x' = 1/7$ which is the furthest distance of injection from the bushing. To demonstrate the estimation process, consider the pulse signal measured from the injection point at $x' = 2/7$ with a negative offset voltage of $-2.8V$. Hence the offset level on both terminal ends will have the fixed distribution level at $V_B = -2.8V$ and, $V_N = -2.8V$.

The terminal response at bushing and neutral to ground connections of the pulse injection is shown in Figure 5.8. Having different pulse signals with higher rise times, the response at the terminal ends also shows different forms of response. By comparison with the $2.5\mu s$ pulse rise time, the response at the bushing ($x = 7/7$) of Figure 5.6(a) shows no change from the original waveshape of the source pulse. However, the time domain

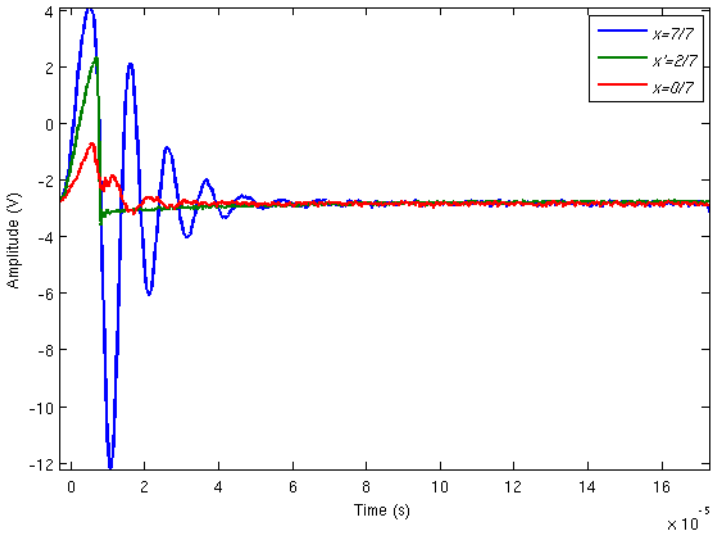

(a) Measurement

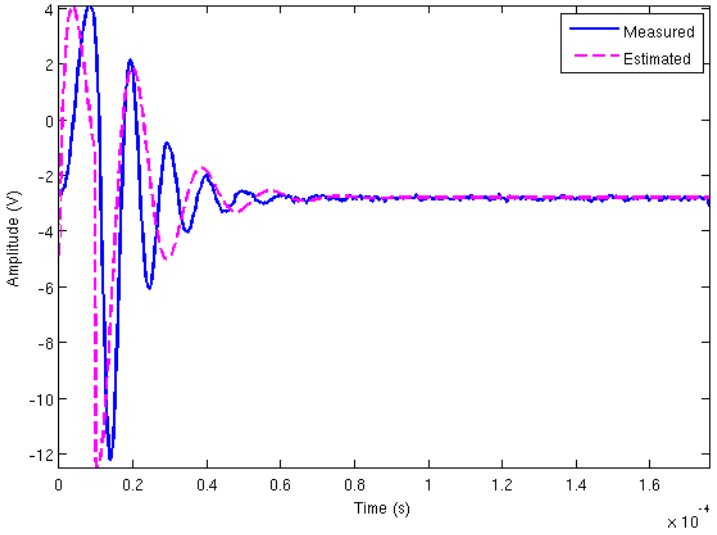

(b) Estimation at $x = 7/7$

FIGURE 5.8: Impulse waveshape, with $40\mu s$ pulse width and $30\mu s$ rise time, pulse injected at $x' = 2/7$; $V_B = -2.8V$, $V_N = -2.8V$

response at the neutral terminal ($x = 0/7$) of Figure 5.8(a) shows a non steady state level compared to the measurement for pulse with $2.5\mu s$ rise time at neutral terminal as shown in Figure 5.6(a).

The pulse estimation using Duhamel's principle is shown in Figure 5.8(b), where the corresponding calculated parameters are tabulated in Table 5.2.

TABLE 5.2: Calculated parameters

$\tau = 6.4\mu s$	E	α	β	ω_{sb}	a	b	γ_s
$0 < t < \tau$:	$4V$	0.6926	0.26	60kHz	10	400	-1.9
$t > \tau$:	$12V$	0.6926	0.26	100kHz	10	49	-1.31

5.4 Estimation by Superposition

In the superposition technique, the signal is transformed into the frequency domain. Using visual inspection or an automated process for detecting the pole peak, the dominant frequency of the captured response can be obtained. Then a clustering technique by segmenting the frequency spectrum is performed in order to obtain the significant waveshape of interest. A bandpass filter is used to cluster the response signals in frequency domain by selecting the frequency of interest. Then an inverse Fourier transform is used to obtain the time domain filtered signal response. The superposition is the summation of the inversed Fourier transform signals within the same time domain.

5.4.1 Zero Phase Filter

A zero phase filter is a special case of a linear filter in which the phase slope is zero. It performs digital filtering by processing the input data in both forward and reverse directions. After performing in the forward direction, it reverses the filtered output sequence and runs it through the filter again. Consequently, it is a filter of double order and removes any phase changes introduced during the first pass of the raw data.

Let $h(n)$ be the impulse response of the recursive filter. Then output to the system in forward direction by a convolution process has

$$v(n) = h(n) * u(n) \tag{5.14}$$

where $u(n)$ is the input signal of sample signal n. In the reverse direction, a flip process occurs by letting the new input be $v(-n)$ which is the reverse order of the first output signal. Hence, applying to the filter again, the response of the second filtering process is:

$$y(n) = h(n) * v(-n) \tag{5.15}$$

where the final output to the filtered signal is in the reverse order of the desired output signal $y(n)$. Hence to obtain the desired output it is necessary to reverse its order, equivalent to:

$$y(-n) = inv\big[h(n) * v(-n)\big] = h(-n) * v(n) \tag{5.16}$$

The zero phase filter employed here is used in Matlab environment, by applying the $filtfilt$ filter command. It also allows the use of various types of filter design.

5.4.2 Pulse Width 1.2μs, Rise Time 0.5μs; Sinusoidal Decay

A 5V peak pulse with narrower pulse width was injected into the fully grounded plain winding at $x' = 2/7$. The time domain response was captured at the bushing tap point and transformed into the frequency domain to access the frequency contents of trasmitted wave. Using visual inspection to detect peak poles, a filtering process is carried out for every extracted centre frequency or corner frequency. The first is to filter and estimate the main frequency of the signal. This is achieved using a second order Butterworth filter with a corner frequency, f_C of 247kHz and the obtained spectrum is shown in Figure 5.9(b). The peak frequency of the spectrum is at 10kHz which is the dominant frequency of the captured response. The inverse transform of the filtered spectrum is shown in Figure 5.9(a).

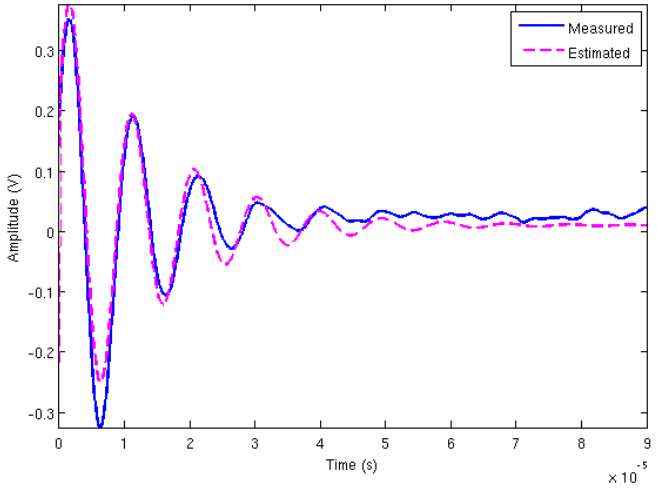

(a) Measured and estimated

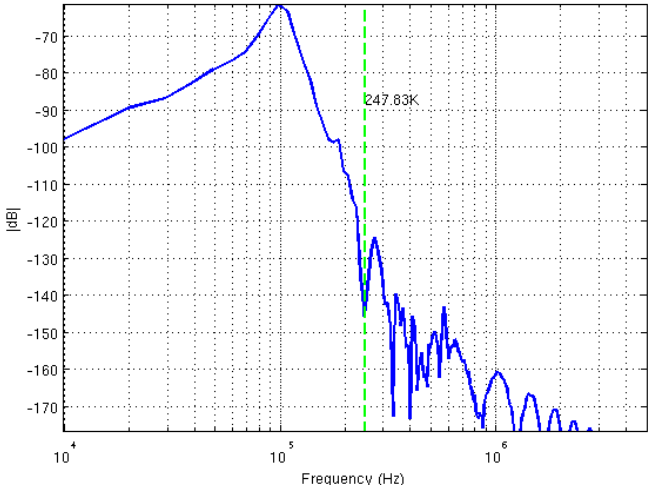

(b) Low pass filter

FIGURE 5.9: Comparison between inverse FFT, and estimated with low pass filter at $f_C = 247$kHz, with 1.2μs pulse width and 0.5μs rise time, pulse injected at $x' = 2/7$;

The estimated signal using Duhamel's principle has also been calculated and plotted on Figure 5.9(a). The sinusoidal decay represented by the main frequency carrier of the system response is also known as the natural frequency of the system. This natural frequency, as can be seen from previous analytical solutions is due to energy storage in the transformer winding inductive elements L, and the decay process is due to the discharging process via the winding capacitances. Where it is simplified by the natural frequency propotional to the inverse square root of LC_g.

Figure 5.10 shows the second estimation process using Duhamel's principle with a higher frequency bandwidth.

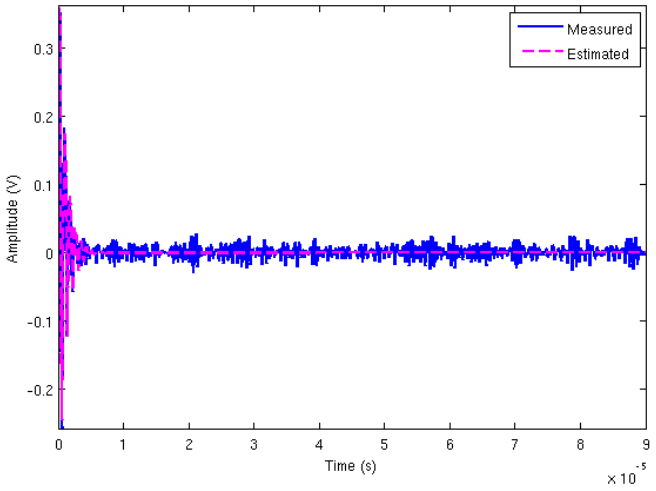

(a) Time domain estimation

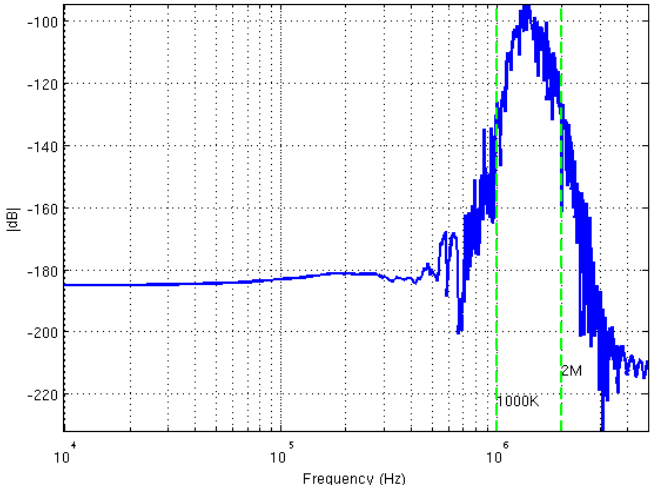

(b) Bandpass filtered spectrum

FIGURE 5.10: Comparison between inverse FFT, and estimated with band pass filter at $f_L = 1$MHz and $f_U = 2$MHz, with $1.2\mu s$ pulse width and $0.5\mu s$ rise time, pulse injected at $x' = 2/7$;

The second filtering process involves capturing the transient decay of the original injected signal from the pulse generator. The signal frequency content is between 1MHz and 2MHz. The peak power spectrum density of Figure 5.10(b) is at 1.5MHz. By inverse transforming the frequency domain spectrum into the time domain, Figure 5.10(a) shows the filtered signal and its estimation. The time domain signal represents the highest frequency component within the captured data and is very similar to the original source signal.

The third process involves the superposition principle and is the summation of the first inversed transform with the second inversed transformed signals. By superpositioning the signal in the time domain, theoretically it builds its original signal from decomposed frequency components. In other word the superposition process is a composition of signals from multi harmonic levels. In this example, the harmonic levels are captured for $f < 247\text{kHz}$ and $1\text{MHz} < f < 2\text{MHz}$. As tabulated in Table 5.3, the superposition principle is demonstrated in Figure 5.11, with a standard sampling rate of $10\text{MS}s^{-1}$. Both frequency ranges have shown no change in the value of α and β, and the harmonic amplitude is simply determined by the range of values of a and b.

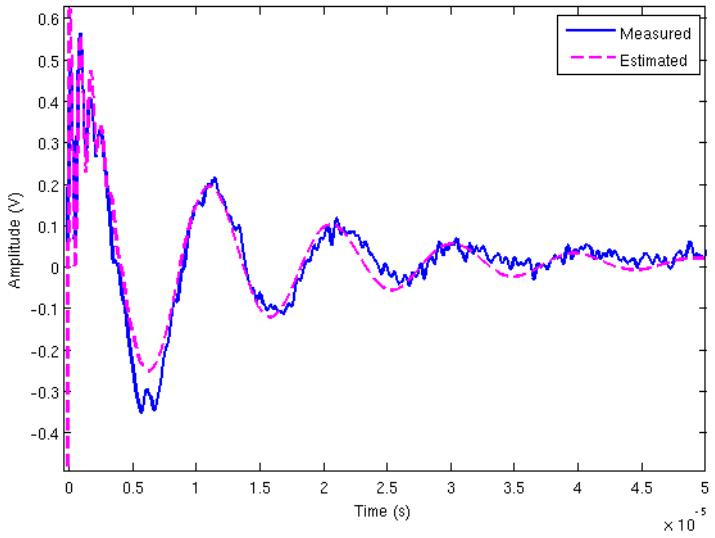

FIGURE 5.11: Superposition result of low pass and band pass, with $1.2\mu s$ pulse width and $0.5\mu s$ rise time, pulse injected at $x' = 2/7$;

TABLE 5.3: Calculated parameters for $1.2\mu s$ pulse width and $0.5\mu s$ rise time

$f_C, f_L \& f_U$	E	α	β	ω_{sb}	a	b	γ_s
$f < 247\text{kHz}$	$0.4V$	0.6926	0.26	196kHz	100	9000	-1.2
$1\text{MHz} < f < 2\text{MHz}$	$0.4V$	0.6926	0.26	2.23MHz	100	1.2×10^5	-15

5.4.3 Pulse Width 150ns, Rise Time 75ns; Sinusoidal Decay

A pulse with 150ns pulse width, 75ns rise time was injected into the fully grounded plain winding. Using a similar analysis as in the previous section, the captured signal at the bushing is transformed into its frequency domain. Identification by visual inspection of the harmonic frequency level is again done in two stages to determine the main natural frequency of the winding and the frequency of the source signal. The main natural frequency is determined by low pass filtering using a second order Butterworth filter, which yields a maximum spectrum level at 176kHz (Figure 5.12(b)). The possible harmonic peaks in the signal is noted as 1^{st}, 2^{nd} and 3^{rd}.

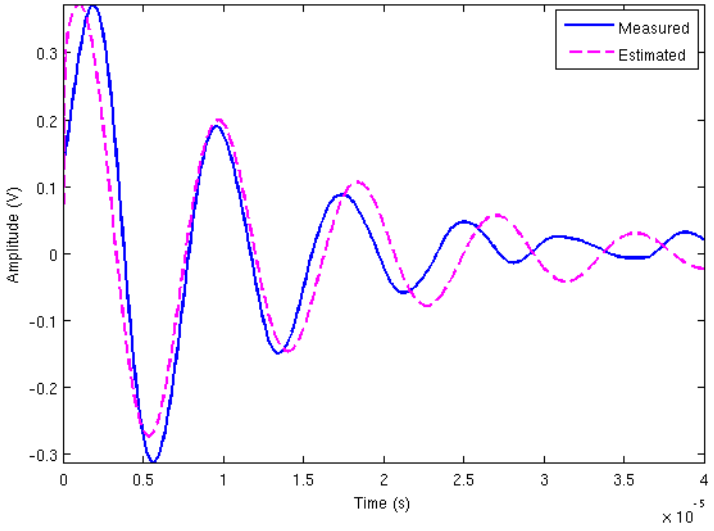

(a) Time domain estimation

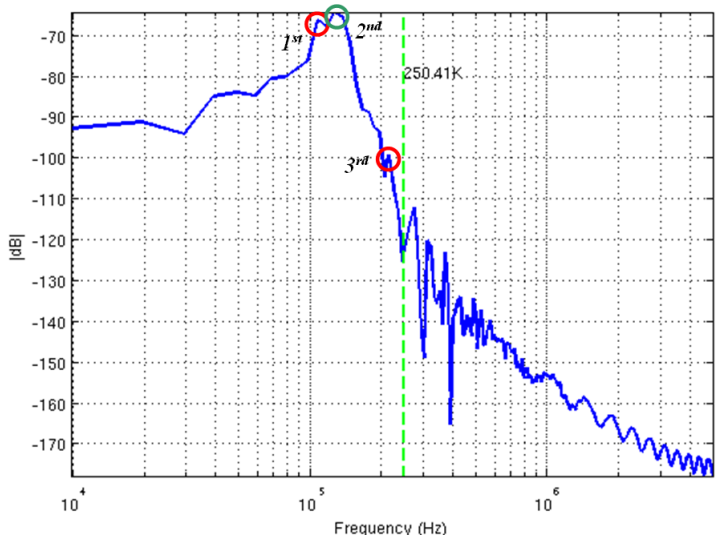

(b) Low pass filtered spectrum with harmonic peaks as 1^{st}, 2^{nd} and 3^{rd}

FIGURE 5.12: Low pass at $f_C = 250$kHz, with 150ns pulse width and 75ns rise time, pulse injected at $x' = 3/7$;

Note that in the first approximation, there are more than one harmonic components in the frequency spectrum represented by more than one peak value. The 1^{st} and 3^{rd} components of the PSD do not appear in the inversed transform (Figure 5.12(a)). However, the wavetail of the time based transformation and the estimated sinusoidal decay, shows significant phase shift. This may be due to different levels of frequency component within the signal. The second level of filtering technique, identifies the original frequency of the source. It can be determined by looking at the peak level of its PSD, using a band pass filter and inverse transformation. This was achieved using a second order of bandpass filter and the filtered signal is shown in Figure 5.13.

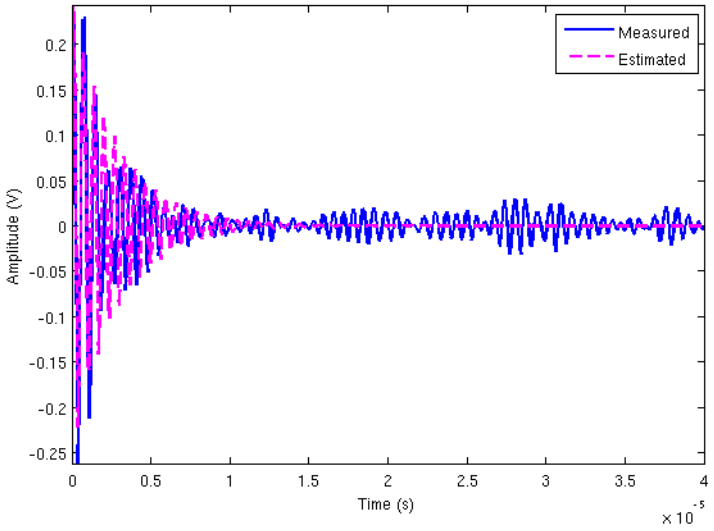

(a) Time domain estimation

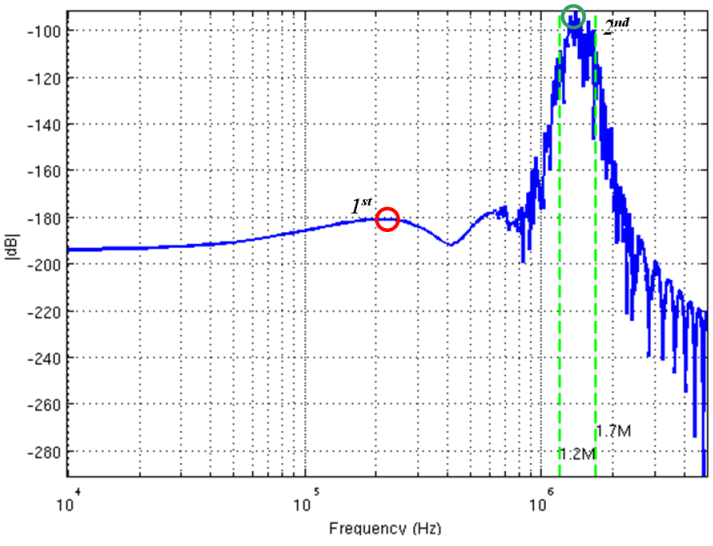

(b) Band pass filtered spectrum with harmonic peaks as 1^{st} and 2^{nd}

FIGURE 5.13: Band pass at $f_L = 1.2$MHz and $f_U = 1.7$MHz, with $150ns$ pulse width and $75ns$ rise time, pulse injected at $x' = 3/7$;

Here, the level of harmonic frequency varies as it has more than one peak in its frequency response. In Figure 5.13(b) the lower peak harmonic level represents the lower frequency component of the inverse time domain response. It can be seen quite clearly in the measured signal after $15\mu s$ (Figure 5.13(a)). Whereas the remaining higher frequency level denoted as 2^{nd} in Figure 5.13(b), represents the main frequency component which can also be clearly seen in the time domain measurement. It is therefore, a process of frequency segmentation and refining that is required to achieve the best approximation. This will give different levels of harmonic frequency that represent the main frequency components of the signal response.

As can be seen from Figure 5.14, the superposition technique is performed as a final stage in order to obtain the approximate waveform. Both the approximations are performed using Duhamel's principle, where the estimation of standing wave parameters are tabulated in Table 5.4. Similarly the value of fixed distribution constants of α and β, are constant. The harmonic frequency ω_{sb} varies according to the peak level of its PSD of the overall estimated signal. Parameters E, a and b are changed according to the level of signal peak amplitude in the time domain.

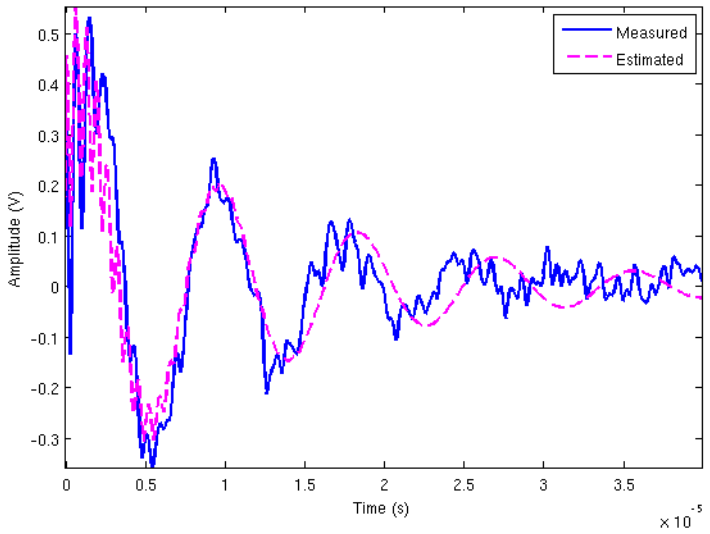

FIGURE 5.14: Superposition result of low pass and band pass, with $150ns$ pulse width and $75ns$ rise time, pulse injected at $x' = 3/7$;

TABLE 5.4: Calculated parameters for $0.5\mu s$ pulse width and $0.5\mu s$ transition

$f_C, f_L \& f_U$	E	α	β	ω_{sb}	a	b	γ_s
f <250kHz	$0.4V$	0.6926	0.26	176kHz	1000	1.2×10^4	-1.2
1.2MHz< f <1.7MHz	$0.25V$	0.6926	0.26	2.35MHz	100	1.4×10^5	-5.8

5.5 Current and Voltage Relationship

As a wave travels from its source, it will obey the laws of electromagnetism. Refering to Figure 5.15, associated with the transmitted voltage pulse is an electrostatic flux Ψ. The transmitted current wave has an electromagnetic flux, Φ, so for each change of distance x in lumped parameter model;

$$d\Phi = i'' L\, dx \tag{5.17}$$

$$d\Psi = v'' C_g\, dx \tag{5.18}$$

Initially, the voltage and current pulses have the same shape, at the start of discharge initiation. But as they travel the waves will experience losses and attenuation. At the points of measurement it is likely that there will be dissimilarity in their waveshapes, which will have become distorted. Distortion and attenuation are caused by energy losses and also by variations in inductance and capacitance along the winding.

Based on travelling wave theory and with reference to Figure 5.15, the voltage drop in the positive direction of x for each element of dx due to $d\Phi$ can be described as

$$-dv'' = -\frac{\partial v''}{\partial x} dx = i'' r\, dx + \frac{\partial}{\partial t}(d\Phi) = \left(R + L\frac{\partial}{\partial t}\right) i''\, dx \tag{5.19}$$

Similarly, the corresponding total in the transmitted current in the element dx is the sum of leakage current and the charging current:

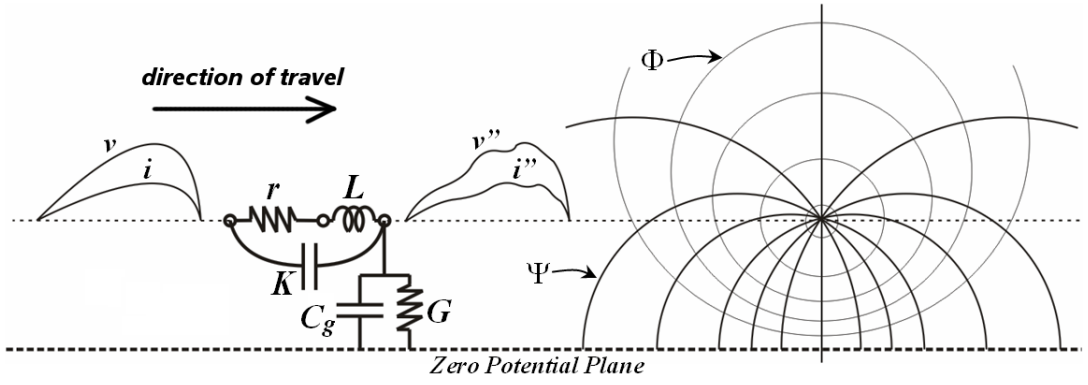

FIGURE 5.15: Lumped parameter circuit as transmission lines model

$$-di'' = -\frac{\partial i''}{\partial x}dx = v''Gdx + \frac{\partial}{\partial t}(d\Psi) = \left(G + C_g\frac{\partial}{\partial t}\right)v''dx \tag{5.20}$$

By cancelling the differential operator dx on both side of Equations (5.19) and (5.20), the change of voltage and current with respect to x are:

$$-\frac{\partial v''}{\partial x} = \left(R + L\frac{\partial}{\partial t}\right)i'' \tag{5.21}$$

$$-\frac{\partial i''}{\partial x} = \left(G + C_g\frac{\partial}{\partial t}\right)v'' \tag{5.22}$$

According to Equations (5.21) and (5.22), voltage and current are both affected by the change of inductance and capacitance respectively over the change of distance x. In the lumped parameter model, both parameters experienced changes with the small changes in the position of signal source. It is therefore of interest to investigate any dissimilarities and consider their potential consequences.

5.5.1 Total Current

According to Equations (4.12) the total current is:

$$(i_K + i_L) = \left(C_g\frac{\partial}{\partial t}\right)\int v\,\partial x \tag{5.23}$$

Obtaining the solution towards neutral, the general equation may begin with the derivation for the homogeneous solution of infinite rectangular wave. Let z_s be the surge impedance of harmonic oscillation that is defined as;

$$z_s = \frac{v_s}{i_s} \tag{5.24}$$

where v_s and i_s are the corresponding harmonic voltage and harmonic current respectively. By considering the solution of Equation (4.36) the harmonic voltage is:

$$v_{sn}(x,t) = \sum_{s=1}^{\infty} A_{sn}\, e^{-\gamma_s t}\, sin\Big(\frac{s\pi x_n}{l}\Big)\, cos(\omega_{sn}t) \tag{5.25}$$

where

$$A_{sn} = \frac{2(-1)^s}{s\pi}\zeta_n \tag{5.26}$$

Applying the fundamental relationship of Equation (5.23), the corresponding total harmonic current therefore is:

$$i_{sn}(x,t) = \sum_{s=1}^{\infty} \frac{A_{sn}C_g l\omega_{sn}}{s\pi}\, e^{-\gamma_s t}\, cos\Big(\frac{s\pi x_n}{l}\Big)\, sin(\omega_{sn}t) \tag{5.27}$$

Hence the surge impedance towards neutral according to (5.24) is

$$z_{sn} = \frac{s\pi}{\omega_{sn}C_g l} \tag{5.28}$$

For an arbitrary waveshape injection, the harmonic current towards the neutral applying Duhamel's principle becomes:

$$\begin{aligned} i_{sn}(x,t) = \sum_{s=1}^{\infty} \frac{EA_{sn}C_g l}{s\pi}\, e^{-\gamma_s t}\, cos\left(\frac{s\pi x_n}{l}\right)\Bigg[(b-a)cos\,\omega_{sn}t \\ + \frac{a^2-b^2}{\omega_{sn}} sin\,\omega_{sn}t + \frac{b^3e^{-bt} - a^3e^{-at}}{\omega_{sn}^2}\Bigg] \end{aligned} \tag{5.29}$$

Using similar analysis for solution for the currents travelling towards the bushing, the harmonic voltage according to Equation (4.37) becomes

$$v_{sb}(x,t) = \sum_{s_o=1}^{\infty} A_{sb}\, e^{-\gamma_s t}\, sin\Big(\frac{s_o\pi x_b}{2l}\Big) cos(\omega_{sb}t) \tag{5.30}$$

where

$$A_{sb} = \frac{8l}{s_o^2\pi^2}\, sin\frac{s_o\pi}{2}\, \zeta_b \tag{5.31}$$

Similarly, the corresponding total harmonic current using equation (5.23) is

$$i_{sb}(x,t) = \sum_{s_o=1}^{\infty} \frac{2A_{sb}C_g l\omega_{sb}}{s_o\pi}\, e^{-\gamma_s t}\, cos\Big(\frac{s_o\pi x_b}{2l}\Big) sin(\omega_{sb}t) \tag{5.32}$$

with surge impedance:

$$z_{sb} = \frac{s_o \pi}{2\omega_{sb} C_g l} \tag{5.33}$$

Thus the solution for the total harmonic current travelling towards the bushing, applying Duhamel's principle using Equation (5.23) becomes

$$\begin{aligned} i_{sb}(x,t) = \sum_{s=1}^{\infty} \frac{2EA_{sb}C_g l}{s_o \pi}\, e^{-\gamma_s t}\, cos\left(\frac{s_o \pi x_b}{2l}\right) \Bigg[(b-a) cos\, \omega_{sb} t \\ + \frac{a^2 - b^2}{\omega_{sb}} sin\, \omega_{sb} t + \frac{b^3 e^{-bt} - a^3 e^{-at}}{\omega_{sb}^2} \Bigg] \end{aligned} \tag{5.34}$$

Figure 5.16 shows the amplitude factor versus distribution constant α of current in transformer winding. The amplitude growth is for the solution of:

$$\frac{2EA_{sb}C_g l}{s_o \pi} \quad or \quad \frac{EA_{sn}C_g l}{s\pi} \tag{5.35}$$

At the point where $\alpha = \beta$ the amplification factor is zero, where this is analytically solved by the solution of ζ_n and ζ_b. For values of α greater than 2 there is not much change in the envelope of oscillations.

5.5.2 Current and Voltage Measurement

To measure current propagation in high voltage transformer, two current transformers (CT) are used. The CT is a typical ring type toroidal current transformer with a useful maximum bandwidth of 200MHz. Figure 5.17 shows the experimental arrangement for current and voltage measurement. The CTs are placed close to bushing terminal via a ground connected wire, and close to neutral terminal to ground connection. To increase the gain the primary of the CTs were wrapped three times around the conductors to earth in the direction so as to respond to positive current travel. A pulse generator with selectable pulse width and transition was used to generate a suitable pulse.

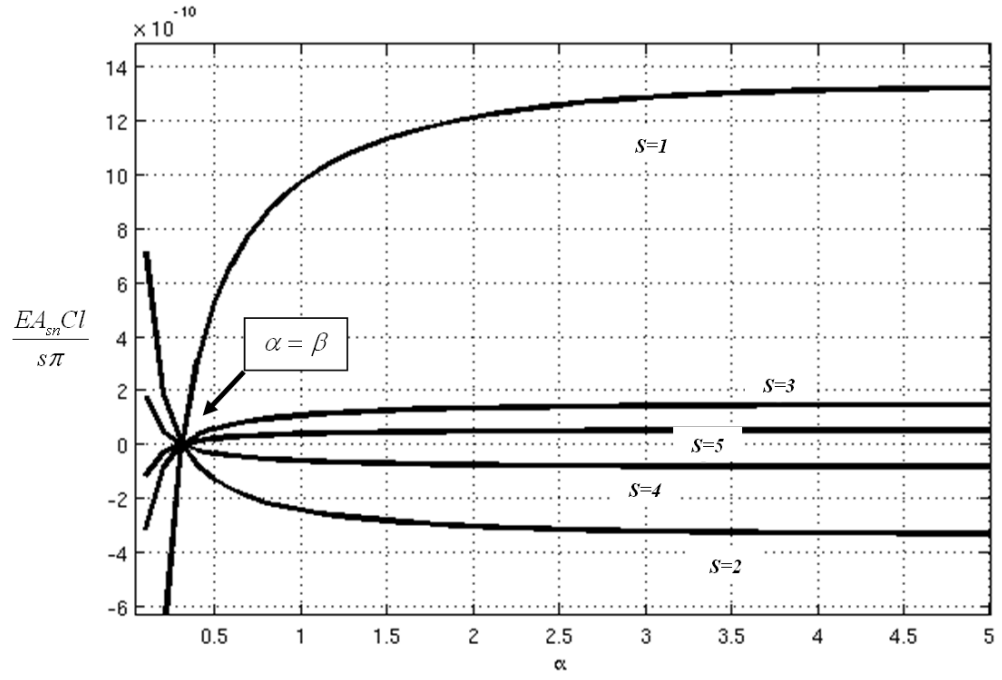

FIGURE 5.16: Current amplitude of transformer winding

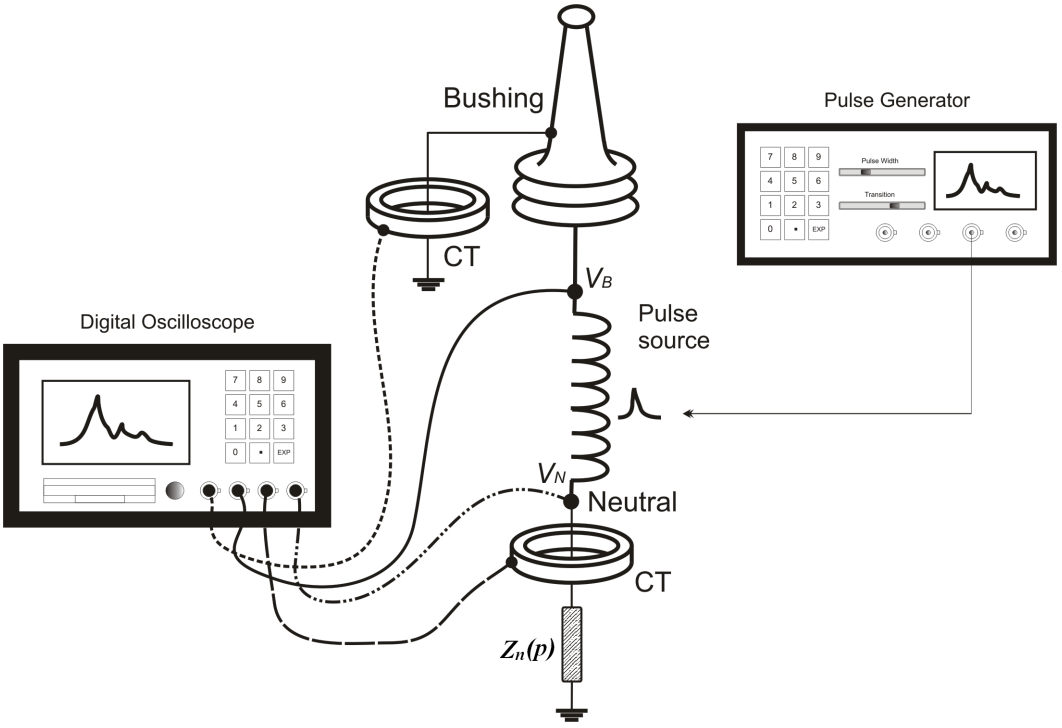

FIGURE 5.17: Current measurement via current transformer

The injection of pulses is measured and captured using a digital storage oscilloscope at the point of injection (representing the source) and at the end of winding, neutral terminal and bushing tap point. Both current and voltage are simultaneously measured and compared. The measured voltages and currents on the two terminals are represented by the transmitted waves of Figure 5.15, by v'' and i'' respectively.

A 50Ω resistor is used as the termination impedance end, $Z_n(p)$, neutral to ground connection and it is used to determine and calibrate the current flowing through the CTs. The calibration process involves capturing the voltage signal at both the bushing and neutral ends, and dividing it by $Z_n(p)$. This resulting waveform is equivalent to the current flowing relative to the measured voltage assuming that there is no distortion and that the 50Ω termination is purely resistive. The apparent charge of travelling wave is then calculated by:

$$Q = \int \frac{v''}{Z_n(p)} dt \tag{5.36}$$

where Q is the apparent charge in Coulombs.

At wideband frequencies of an impulse event, a high frequency current transformer has a response that is the time derivative of the current flowing in the main system. This derivative corresponds to the high transitions of the impulse signal or any high frequency signal transition with respect to time t. Therefore, current measurement using wideband toroidal CTs, will analytically have no offset and the output will oscillate with a steady state zero level.

5.5.3 Current and Voltage Dissimilarities

A signal of pulse width $1.2\mu s$ and rise time of $0.5\mu s$ was injected at Terminal 2 ($x' = 6/7$) of the interleaved winding. Both voltage and current measurements were recorded using a digital signal oscilloscope where the plots are enhanced and superimposed on the same time frame. The captured signals were then filtered using the zero phase low pass filter with a 4MHz corner frequency. Figure 5.18 shows a comparison of applied voltage and current meaurements of both end terminals.

Using the inverse Laplace transform, the time domain of the filtered signal at the bushing tap point is shown in Figure 5.18(a) and at the neutral terminal in Figure 5.18(b). Current measurements using high frequency current CTs are calibrated using the 50Ω resistor.

Based on the measured signal characteristics of Table 5.5, the signals have common measurement parameters of record length, sample interval, trigger point, trigger time

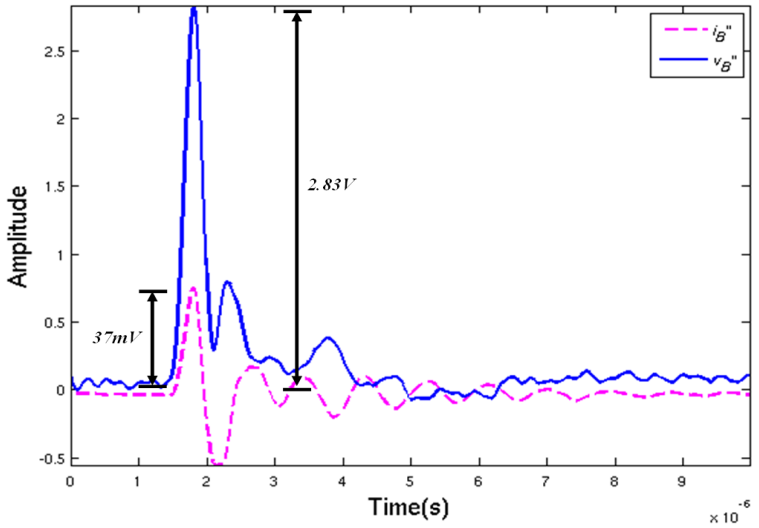

(a) Voltage and current at bushing

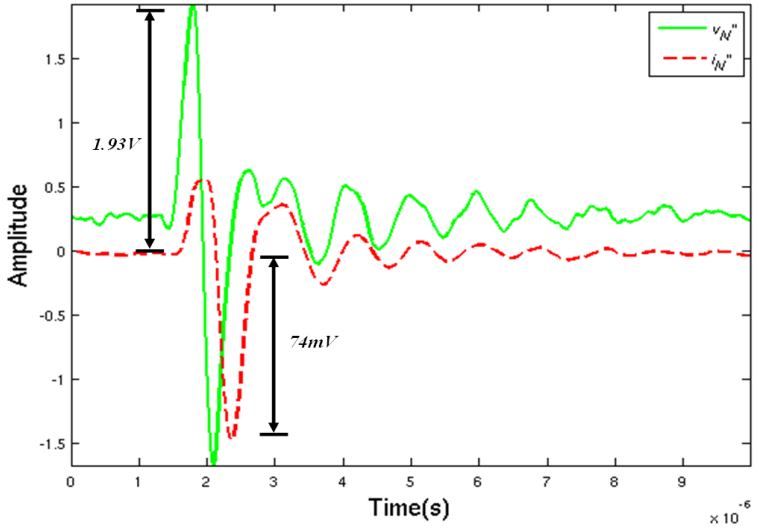

(b) Voltage and current at neutral

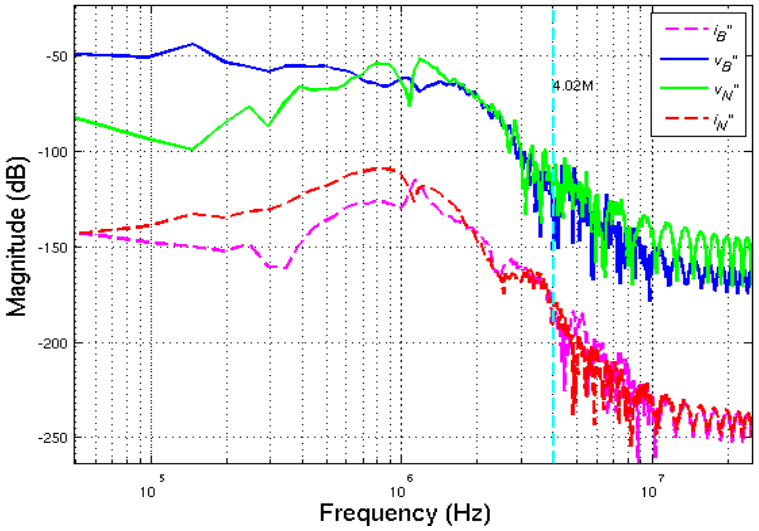

(c) PSD plot

FIGURE 5.18: Voltage and current measurement for $x' = 6/7$ on interleaved winding

TABLE 5.5: Measured signal characteristic for $1.2\mu s$ pulse width and $0.5\mu s$ rise time, and $x' = 6/7$ on interleaved winding

Current @ Voltage	Record Length	Sample Interval	Trigger Point	Trigger Time	Horizontal Offset	Peak Absolute Value
i''_B	1000	2×10^{-8} S/s	100S	7×10^{-9}s	-2×10^{-6}	37.4mV
v''_B	1000	2×10^{-8} S/s	100S	7×10^{-9}s	-2×10^{-6}	2.83V
i''_N	1000	2×10^{-8} S/s	100S	7×10^{-9}s	-2×10^{-6}	73.9mV
v''_N	1000	2×10^{-8} S/s	100S	7×10^{-9}s	-2×10^{-6}	1.93V

and horizontal offset. Thus the signals can be calibrated using the same parameter, i.e. the temination impedance at the neutral end.

Calibration of current is achieved by considering the voltage measurement v''_N, divided by the termination impedance and intergrated over time t. However, the measurement unit for the CTs are in mV. Therefore using a proportional ratio calibration technique, the calculated current is calibrated at $74mV$ (measurement from CT) and is equivalent to a 770pC charge magnitude.

From the filtered time domain inverse Fourier transform plots (Figure 5.18), both current and voltage measurements are disimilar at the terminals. The current responses however start at almost the same time. Initially, the voltage and current have the same polarities and this is analytically due to the intergration of current distribution over the domain of x_n and x_b as described in Equation (5.23).

From the frequency domain comparison of Figure 5.18(c), the gain magnitude of the signals change significantly between 1MHz to 2MHz. Note the pattern of the voltage and current frequencies measured at both terminals. At the bushing terminal, the polarity of peak responses of each spectrum are opposite to each other, however at the neutral terminal both spectra show a similar zero position.

Using similar analysis as for interleaved winding, a $100ns$ pulse width and $30ns$ rise time impulse (Figure 5.3(e)) is injected at $x' = 6/7$ on plain winding. The low pass zero phase filter with corner frequency 2.56MHz is applied to all the measured signals. After noise reduction the peak charge magnitudes were calculated and calibrated. The measured signal characteristics are tabulated in Table 5.6

The calculation of charge magnitude is estimated based on the amount of current flowing to the ground through the termination impedance at the neutral to ground connection. By considering only the peak value of the time domain waveform, calibration assumes that there is only a small change in sample time interval with respect to the period of the dominant measured frequency. The maximum charge is chosen rather than accumulated charge over a time period, since it is due to the function of the accumulative amplitude factor over the harmonic levels as described in Equations (5.29) and (5.34). Therefore, by using the same termination impedance of 50Ω, the calibrated current at the Neutral

is $i''_N = 5.8mV$ and is equivalent to a charge of 310pC. This gives 404pC at the bushing tap point. The calculated peak charge however does not represent the total current flowing out of the winding, where a full integration of the time period of $0 < t < 500ms$ is required.

Looking at the waveshape of the measured waveforms for both terminals of Figure 5.19(a) and 5.19(b), the current polarity is initially the same to the voltage polarity for the first few cycles and oscillates thereafter. Comparatively, the current waveforms are very dissimilar to the voltage waveforms. However observation of the frequency domain shown in Figure 5.19(c) reveals that the current response at bushing and neutral terminals have similar frequency characteristics. The voltage frequency responses are also very similar.

The dissimilarities of the time-based waveforms are also explained by considering the phase of the frequency responses. Figure 5.20 shows the phase plot of interleaved winding over the frequency range between 600kHz to 2.2MHz. Whereas Figure 5.21 shows the voltage and current phase plot of the plain winding between 300kHz to 2.0MHz. The change of phase due to zeros peaks and pole peaks is seen between 1MHz to 1.5MHz range and 700kHz to 1MHz for the plain winding. The pattern also shows that the phase of the voltages at the bushing and neutral terminals are very similar.

It is however, the phase plots for the current measurements at the neutral and bushing terminals that are significantly different. Consider Equations (4.54) and (4.53), if θ_n and θ_b are the corresponding phase angles towards the neutral and bushing tap point on xt-plane respectively, then the phase angles in both directions are defined as;

TABLE 5.6: Measured signal characteristic for $100ns$ pulse width and $30ns$ rise time, and $x' = 6/7$ on plain winding

Current @ Voltage	Record Length	Sample Interval	Trigger Point	Trigger Time	Horizontal Offset	Peak Absolute Value
i''_B	1000	5×10^{-8} S/s	110S	2.8×10^{-9}s	-5.5×10^{-6}	7.5mV
v''_B	1000	5×10^{-8} S/s	110S	2.8×10^{-9}s	-5.5×10^{-6}	0.41V
i''_N	1000	5×10^{-8} S/s	110S	2.8×10^{-9}s	-5.5×10^{-6}	5.8mV
v''_N	1000	5×10^{-8} S/s	110S	2.8×10^{-9}s	-5.5×10^{-6}	0.32V

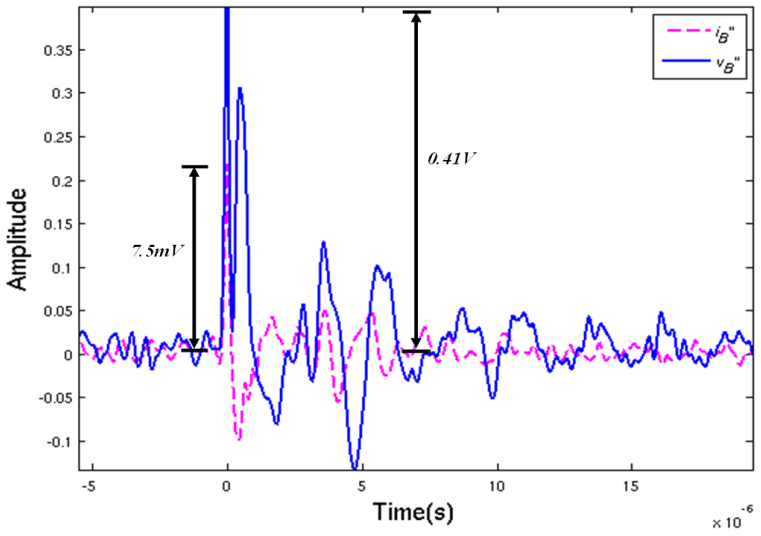

(a) Voltage and current at bushing

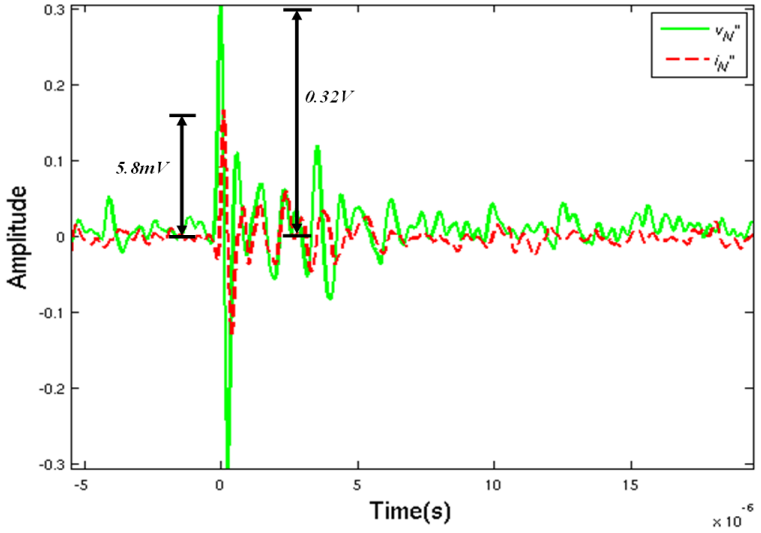

(b) Voltage and current at neutral

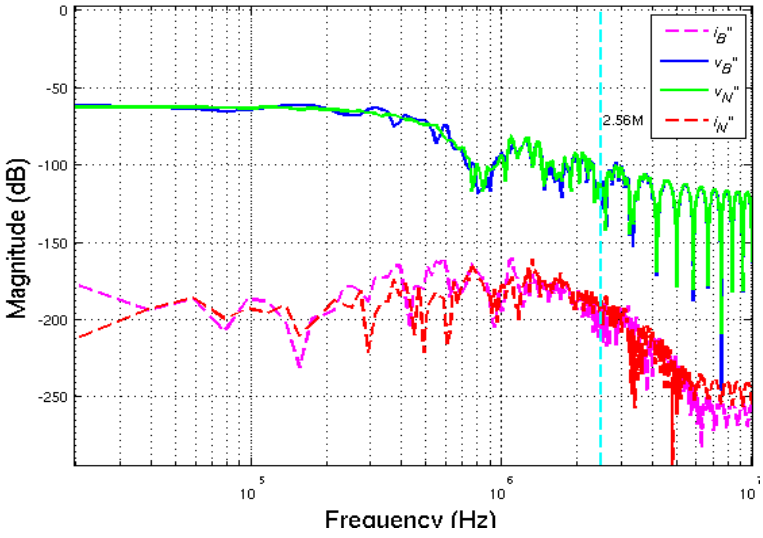

(c) PSD plot

FIGURE 5.19: Voltage and current measurement for $x' = 6/7$ on plain winding

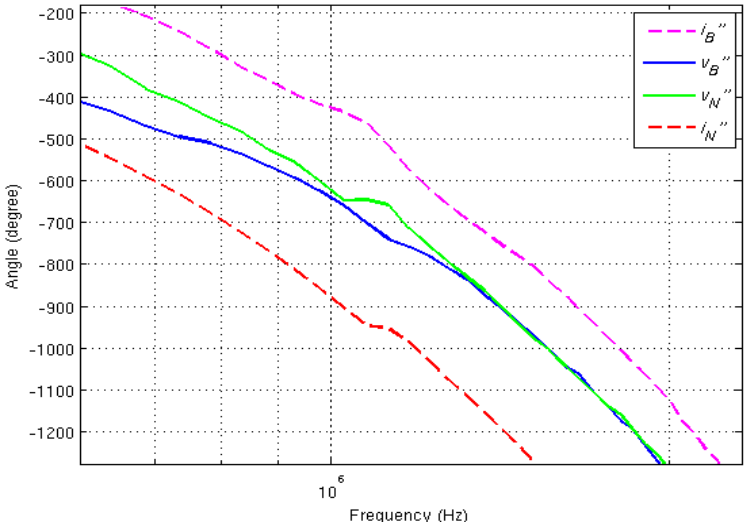

FIGURE 5.20: Voltage and current measurement phase angle for $x' = 6/7$ on interleaved winding

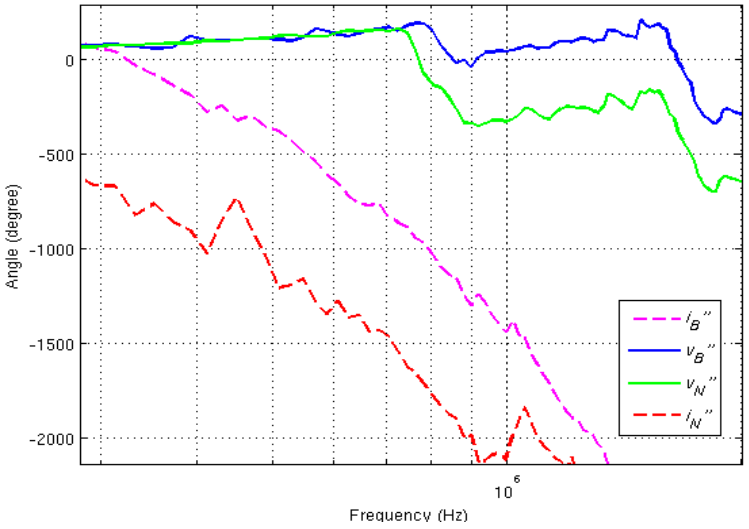

FIGURE 5.21: Voltage and current measurement phase angle for $x' = 6/7$ on plain winding

towards the neutral point

$$cos\Big(\frac{s\pi x_n}{l} + \omega_{x'n}t + \theta_n\Big) \tag{5.37}$$

and towards the bushing tap-point

$$cos\Big(\frac{s_o\pi x_b}{2l} - \omega_{x'b}t - \theta_n\Big) \tag{5.38}$$

5.6 Impulse Response vs Frequency Response

Theoretically if a linear plant input is defined as a dirac delta function, then the corresponding output fully characterises the frequency response of the plant. Experimentally, the determination of an impulse response provides a good estimate of the frequency response of the linear system. From a theoretical point of view, when a system is injected with a unit impulse of $\delta(t)$, it is equivalent to:

$$U(j\omega) = 1 \qquad \forall\omega \tag{5.39}$$

The equation implies that an impulse response will excite all the system frequencies and the output response from that system is equivalent to the system excitement of the plant. Figure 5.22 shows the conceptual frequency response for an injected unit pulse with $\delta(t)$ that represents an impulse, where the transformation of its time domain output response into Fourier coefficients represents the frequency response of the system.

A pulse with narrower pulse width and shorter transition time is used in this measurement, which will represent the nearest possible practical form of dirac delta function $\delta(t)$. A wider transition time however will only excite a certain frequency range, where the system excitement is explained by the Duhamel's principle. It is therefore necessary to investigate the response for higher system frequencies using steeper pulse wavefronts and narrower widths in order to model the high frequency signal propagation behaviour.

An impulse reponse measurement is carried out the same way as for the arbitrary waveform experimental setup of Figure 5.17. The injection point is terminal 1 ($x = 7/7$) of the transformer windings and the time domain response is captured consecutively at different distance from $x = 6/7$ to $x = 0/7$. The winding configuration is connected to ground for all measurements. It is also possible to reverse the polarity of current propagation due to an injected impulse, where the injection is near the neutral point and the corresponding response is captured at different terminals towards the bushing tap point.

Measurement of the frequency responses of the transformer windings was also obtained using a network analyzer, Agilent 4395A. During the test the measurement frequency range was set from 100Hz to 500MHz, with a sample bandwidth of 30Hz. It is necessary to measure the frequency response over the largest range possible in order to represent the total system response. To improve the measurement data quality the response was measured many times and resampled to further refine the complete frequency response which has a total length of 1400 sample points.

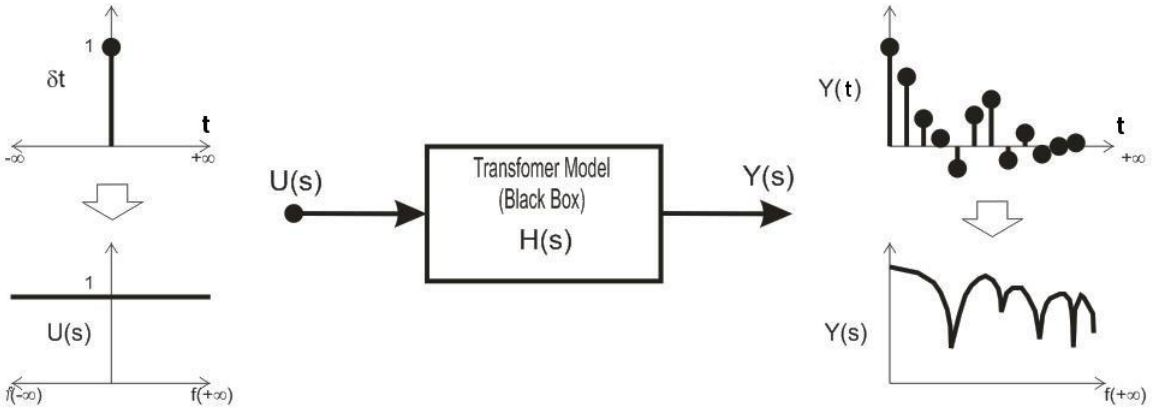

FIGURE 5.22: An illustration of impulse response

5.6.1 Response on Interleaved Winding

The transformer has many frequency dependant parameters such as, capacitance, mutual inductance, conductance and resistance. These parameters will change as a function of frequency [33] and the lumped parameter impedance hence changes. Therefore it is necessary to ensure that the frequencies excited are high enough in order to account for the possible characteristics of wave propagation along the windings. The circuit for the interleaved winding frequency response measurement is shown in Figure 5.23. To avoid error due to flux interlinkages between the adjacent winding, all terminal measurement points of the plain winding are short circuited and grounded.

Measurements were also taken for the ungrounded winding, where $Z_n(p)$ now becomes $Z_n(\infty)$. A sweep variable signal frequency was set and injected at terminal 1 ($x = 7/7$), and the corresponding reponses were captured at different distance towards Neutral for $x = 6/7$ to $x = 0/7$.

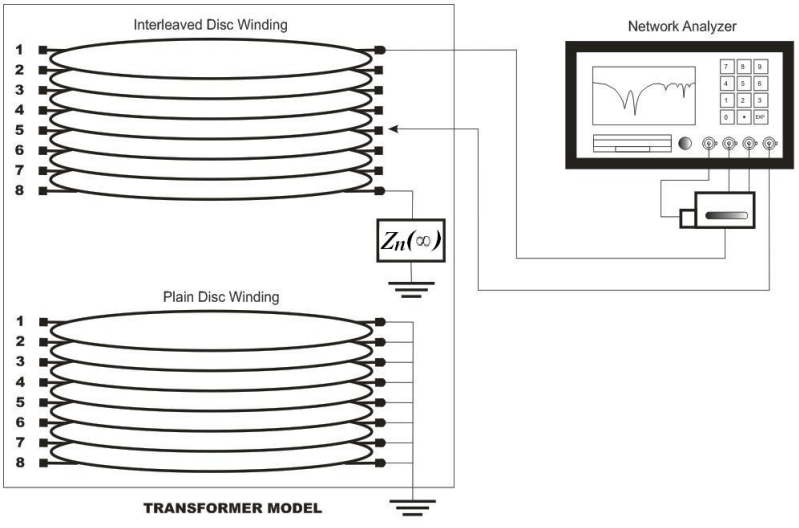

FIGURE 5.23: Measurement setup for interleaved windings

The captured frequency response is in the form of a complex coefficient, which is then used to calculate the response in terms of dB gain and phase angle. Figure 5.24 shows the measured frequency response data in dB magnitude and its corresponding phase response in degrees.

Every measurement of the frequency response on interleaved winding represents the response of the winding disc pairs, where every sequence of decrement of distance x is equivalent to the frequency response of several disc pairs from the top winding. Note the formation of poles and zeros from the dB magnitude plot. As the wave sweeps from the lower frequency to the higher frequency the signal experiences a decrease in magnitude caused by a zero-pair that is followed almost immediately by a resonance caused by a pole-pair.

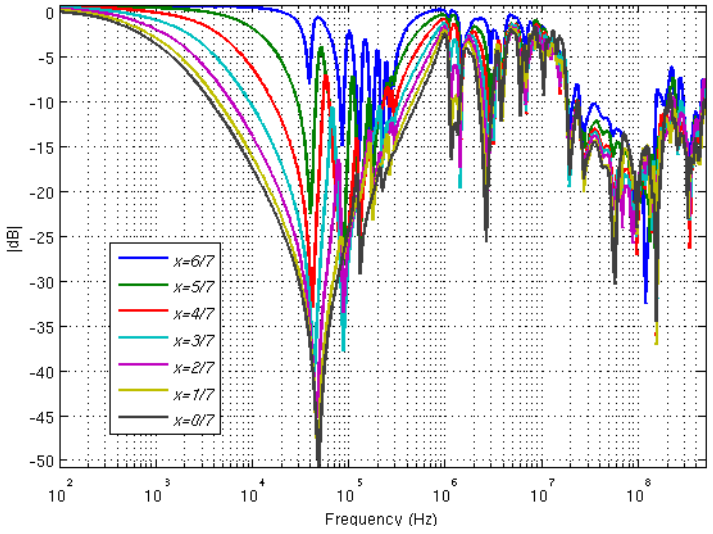

(a) Frequency response measurement

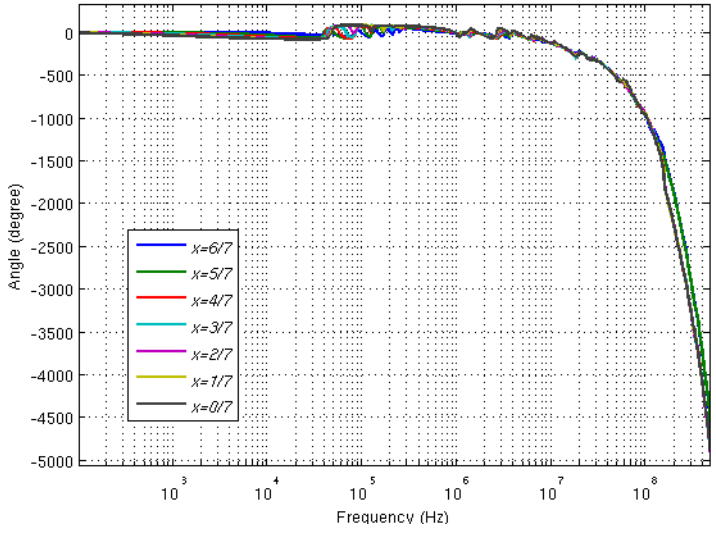

(b) Phase response measurement

FIGURE 5.24: Frequency response and phase response of interleaved winding using network analyser

The process is continued thereafter alternating between poles and zeros, where the poles and zeros are the resonant and anti-resonance frequencies of the system represented by the passive components of L and C. The position of the anti-resonant zeros from the frequency response measurement are plotted in Figure 5.25. The plot was extracted from Figure 5.24(a) for every zeros of its dB magnitudes and frequencies. The alternating oscillation between poles and zeros continues and behaves similarly for all disc coils up to a frequency of approximately 4MHz.

The alternating of poles and zeros also can be explained from the phase response measurement. The phases are caused to lead and lag alternately depending on the formation between poles and zeros. The negative sign of phases shows a lagging process where the system operates in the more inductive region. As the gain changes due to poles the system response gain increases due capacitive elements which causes positive changes in the system phase.

As shown in Figure 5.25, the zeros positions are fairly static for all frequencies below 4MHz except for the first low frequency zero pair between 30kHz to 60kHz. The gain of the zeros differ by an offset level between consecutive coils. This offset was analytically explained in the chapter, where the signal is applied to a lumped parameter model based on the LCK components. The solution is represented by a general solution defined as the sum of a fixed distribution component and the total harmonic decay component.

The solution represents the separation of the lumped parameter circuit where the fixed distribution component represents the model in predominantly capacitive elements, and the harmonic decay component represents predominantly inductive elements. Using Duhamel's principle to model arbitrary waveform injections, the general solution still holds a similar form where the solution of the source is embedded in the output response at the terminal ends.

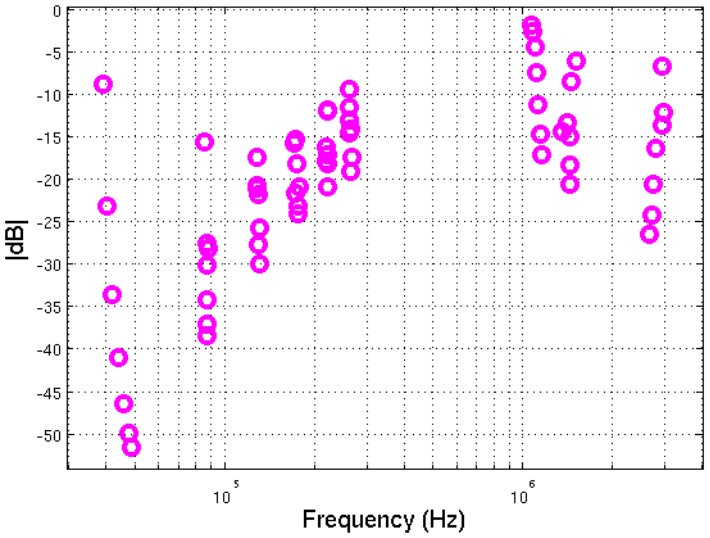

FIGURE 5.25: Zeros position of interleaved winding from frequency response measurement

A comparison between impulse response and frequency response measurements has been undertaken. Here a shorter transition time pulse, a $100ns$ pulse width and $30ns$ rise time (Figure 5.3(e)) impulse signal is used. The pulse is injected at terminal 1 ($x = 7/7$), and the subsequent response is captured for the fully grounded winding and plotted in Figure 5.26. The time domain injected signal response, Figure 5.26(a), experiences oscillations and highly damped losses over the time interval t. Due to the high energy of the transient and its higher frequency oscillation, along the length of transformer winding, the signal propagation waveshape retains its waveshape and shows a small voltage offset between each disc pair. Figure 5.26(b) shows the peak amplitude at different sampling times of the impulse response. The peak amplitudes were chosen because it represent the magnitude of oscillation of the signals. It shows a linear amplitude distribution over the range $0 < x < l$ for each time instant.

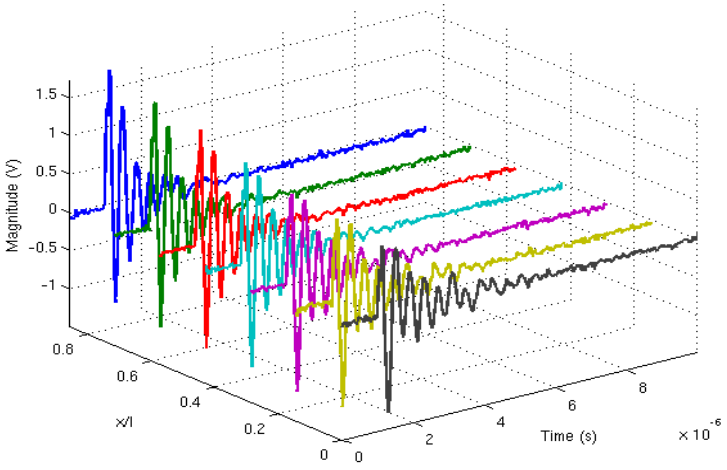

(a) Impulse response

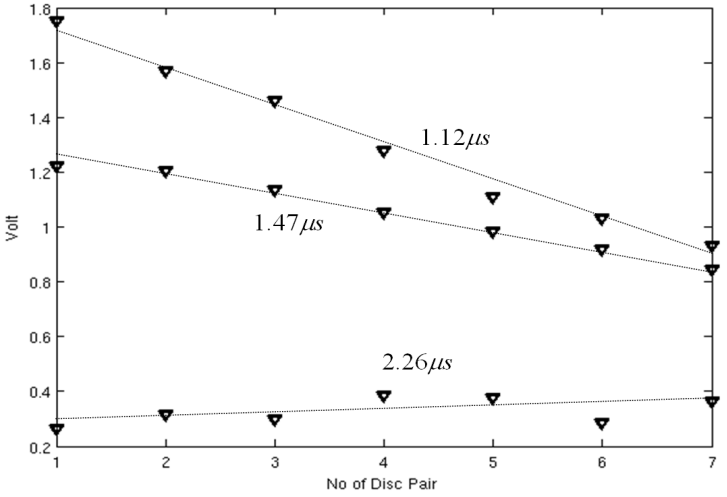

(b) Amplitude distribution

FIGURE 5.26: Impulse response measurement of interleaved winding with $100ns$ pulse width, $30ns$ rise time

Figure 5.27 shows a comparison of impulse response measurement and frequency response measurement over the frequency range 100kHz to 4MHz. The range is selected based on the theoretical principle of standing wave theory for the transmission line model. The impulse response measurement is transformed into its power spectrum density from its time domain response, using a sampling rate of $100\mu s$. The horizontal offset DC level of the impulse in the time domain is set at the lowest possible value of zero level with a trigger time of $1\mu s$.

At an initial frequency of 100kHz, both response of Figures 5.27(a) and Figure 5.27(b) show a damped level due to the predominantly inductive frequency region. But as the wave moves from $x = 6/7$ of disc 1 to $x = 0/7$ of disc 7, the offset level is lower.

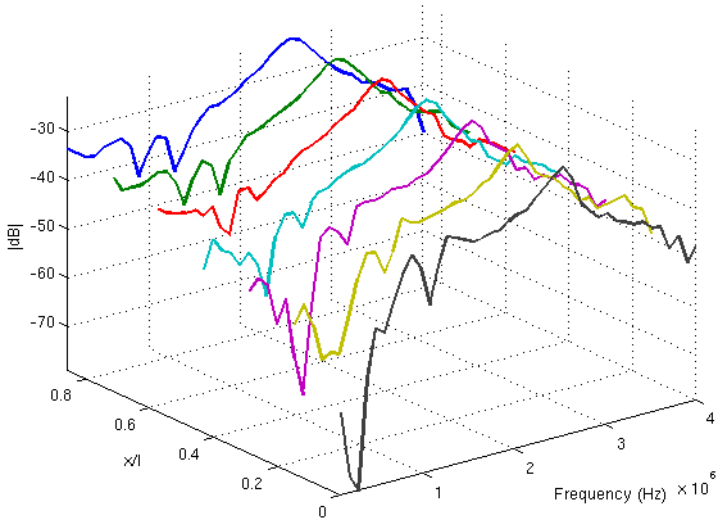

(a) Fourier transform of impulse response

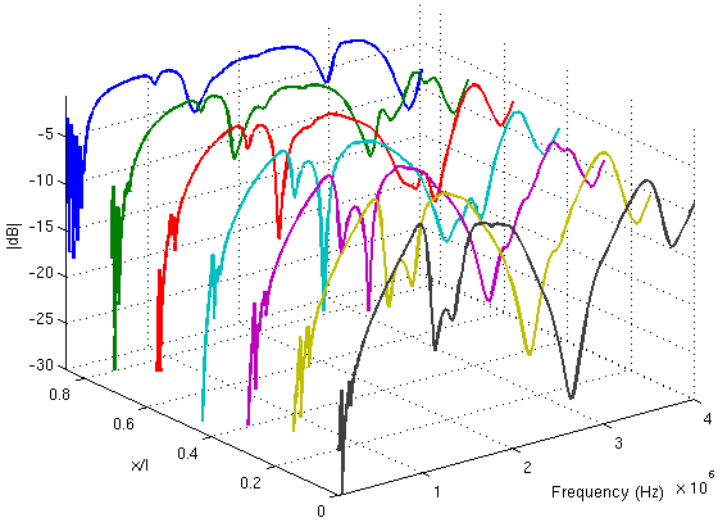

(b) Frequency response from network analyser

FIGURE 5.27: Comparison of impulse response and frequency response of interleaved winding for 100kHz to 4MHz frequency range

Similarly for the range frequency of 1MHz to 2MHz the offset level of the zeros is lower as the wave moves from the bushing tap-point to the neutral terminal. However different zeros exist in the frequency response measurement between 2.5MHz to 3MHz, whereas the power spectrum density of the impulse response shows a pole peak with a magnitude of -23dB to -24dB.

5.6.2 Response of the Plain Winding

The plain disc winding has the same geometrical size as the interleaved winding. The difference between them is the arrangement of the connections between each disc. This reduces the inter-disc capacitance (K_r) compared to the interleaved disc winding. Consequently, the frequency response of the plain disc winding is different from the interleaved disc winding. The same measurement setup is still applied for the plain disc winding (Figure 5.28), except now the interleaved winding is shorted and grounded.

The sweep frequency for frequency response measurement starts at 100Hz to a maximum frequency of 500MHz. The termination impedance was left unconnected to provide an infinite termination impedance. As shown in Chapter 3, the effect of a ground connection on the interleaved winding will certainly damp the transmitted signal v'', and affect the level of distribution.

Unlike the impulse response, the sweep variation of the frequency response measurement is a slow process, which is due to the low sampling frequency bandwidth. This however gives more accurate measurement of each frequency increment of the transformer response. In order to validate the accuracy and the offset level of gain measurement, it is necessary to perform self calibration of the analyser. Using an impedance reflector, a self response calibration is performed in transmission and reflection mode.

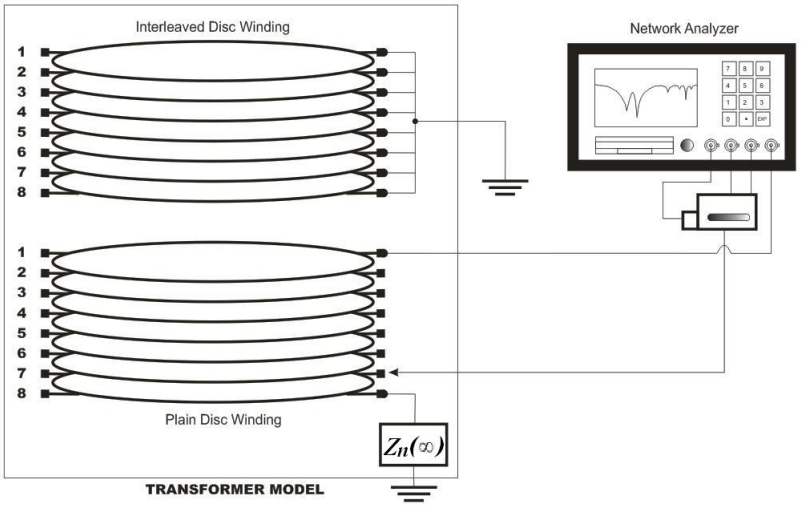

FIGURE 5.28: Measurement setup for plain disc winding

Table 5.7 shows the typical setting for frequency response measurement and self calibration. Figure 5.29 shows the frequency response plot and phase response plot of the plain winding. The offset reference for measurement is set at a steady state level of the first disc pair of the transformer coil with the value of 6.42dB. It is then calibrated for the remaining offset level of every disc pair measurement to have zero gain at the begining of the frequency sweep by using the same offset value.

Due to different connections between each disc pair, the poles and zeros exist above 100kHz. Similar to the interleaved winding, Figure 5.29(a) shows the obtained frequency response for the plain winding. Analytically, the passive resonant frequency of an LC lumped parameter is equivalent to

$$\omega_r = \frac{1}{\sqrt{L_{dx}C_{dx}}} \tag{5.40}$$

where ω_r is the resonance frequency, L_{dx} and C_{dx} are the respective effective inductance and effective capacitance from neutral to ground terminal. The solution of peak resonance is dependant on the position of the disc winding with respect to the distance from neutral to ground connection. This is in turn will result in the moving zero for a lower energy transition and lower fundamental frequency of transmitted signal. As tabulated in Table 3.2, lowering the value of the effective inductance will influence the values of the poles and zeros according to the solution of Equation (5.40).

Figure 5.30 shows the positions of the zeros for the plain winding over 100kHz to 1MHz. The position of the zeros along the frequency axis shows that the lowest frequencies of zeros are the most shifted in frequency. These move between 150kHz to 400kHz, which is a significantly wider bandwidth compared to the interleaved winding. It is believed to be due to the non-uniform inter-section capacitance between the disc pairs. As the frequency gets higher the zeros positions are more consistent.

To see the significant effect of pulse propagation at higher frequencies, a pulse with $6ns$ pulse width and $3ns$ rise time (Figure 5.3(f)) was used for impulse response measurements of a grounded plain winding. Figure 5.31 shows the impulse response measurement measured at different disc pairs and the corresponding amplitude levels for different sampling instants.

TABLE 5.7: Parameter setting for frequency response measurement

Channel	Measure Type	Format Type	Number of Points
1	B/R	$POLAR$	600
Sweep Time	Sweep Type	Source Power	IF Bandwidth
00 : 01 : 10	$LOG\,FREQ$	0 dBm	30 Hz

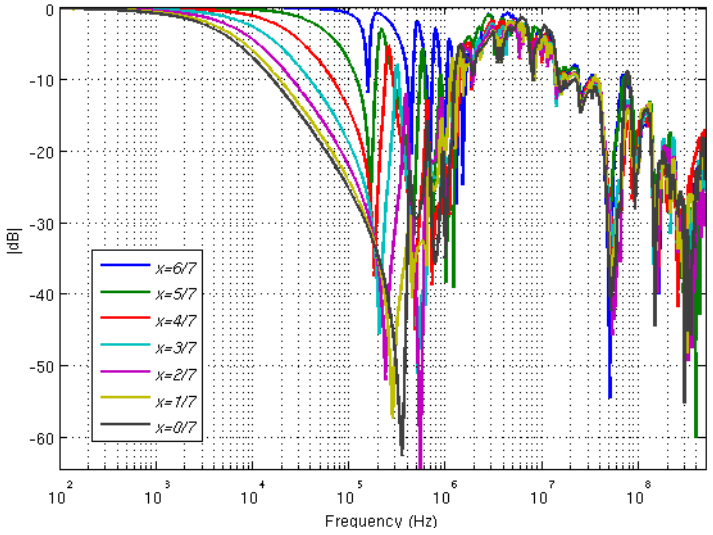

(a) Frequency response measurement

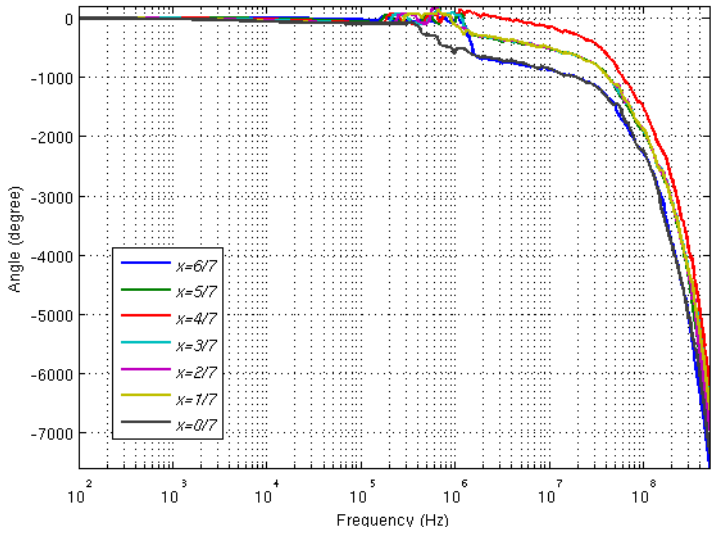

(b) Phase response measurement

FIGURE 5.29: Frequency response and phase response of plain winding using network analyser

Figure 5.26(b) and Figure 5.31(b) show the effect of a very high frequency signal propagating in the interleaved winding and plain winding respectively, there is a linear relationship of the measured peak magnitudes between the bushing tap point and neutral terminals. The magnitudes are for different sampling times.

By looking at the Fourier coefficients of the impulse response measurement, Figure 5.32(a) shows the power spectrum density of the impulse response captured for every disc pair of grounded plain winding for frequency range of 3MHz to 100Mhz. Figure 5.32(b) shows the same frequency range of the measured frequency response but for the ungrounded winding.

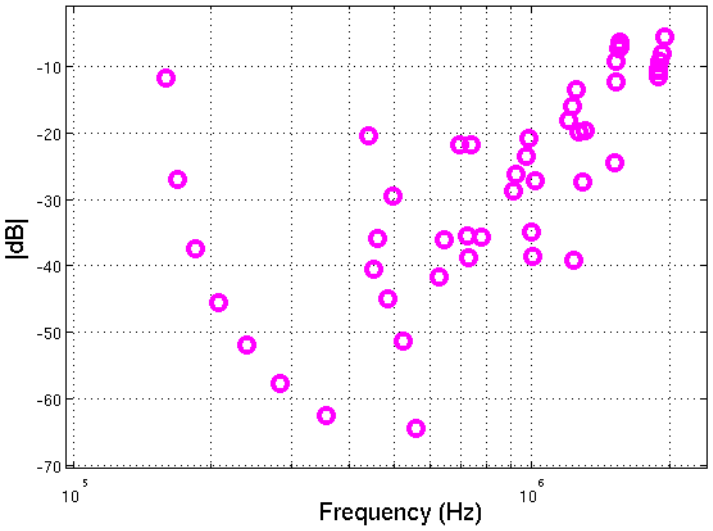

FIGURE 5.30: Zeros position of plain winding from frequency response measurement

The response from the impulse measurement reveals zeros at the same frequency and with the same magnitude of offset between the disc coils. Three main level magnitudes of zeros occured at 30MHz, 58MHz and 90MHz, with gains of -92dB, -107dB and -110dB respectively. By employing a bandpass zero phase filter at the specific frequencies, the zeros represent the harmonic decay of sinusoidal signals. This can be modeled using the solution of the harmonic decay as in Equation (5.8) with the known x' and the harmonic frequency ω_{sn}. The offset amplitude of the harmonic signals is however very small having a maximum value of up to 0.04V. This is quite insignificant in order to determine the source of a signal with a small offset margin. In frequency response measurements, the main zeros are located at the same frequencies but have significant difference in terms of offset magnitudes. Similar to the impulse response, the level of gain between adjacent disc coils are about the same, and have the same pattern for all zeros.

With this analysis, it shows that at very high frequency, the response of the winding for every disc coil for both the grounded and ungrounded winding configurations are the same. As the frequency gets higher both types of winding show very similar behaviour.

5.7 Summary

A model representing a transformer winding based on a time varying boundary conditions system has been presented in this Chapter. By using the solution of the homogeneous model in Chapter 4, the solution for injection of an arbitrary waveshape is derived using Duhamel's principle. Duhamel's principle is based on the derivation of the initial condition at $t = 0$ which represents the fixed distribution solution and also the final condition at $t = \infty$ that represents the harmonic decay component with losses. It also provides a solution that contains information of the original source waveform.

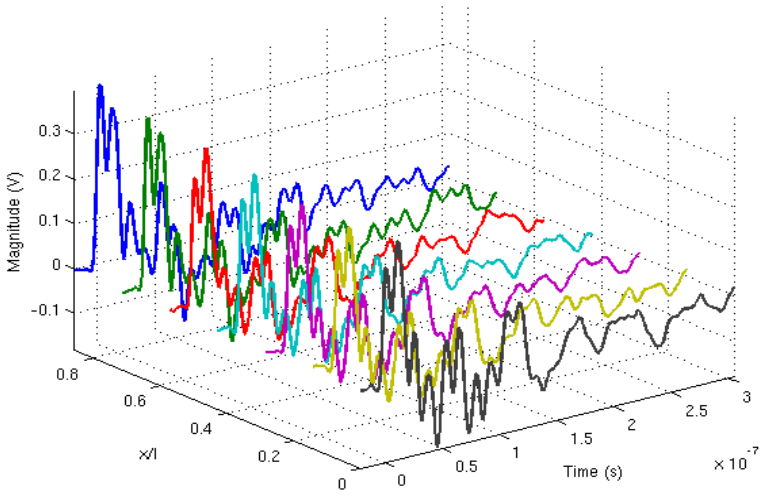

(a) Impulse response

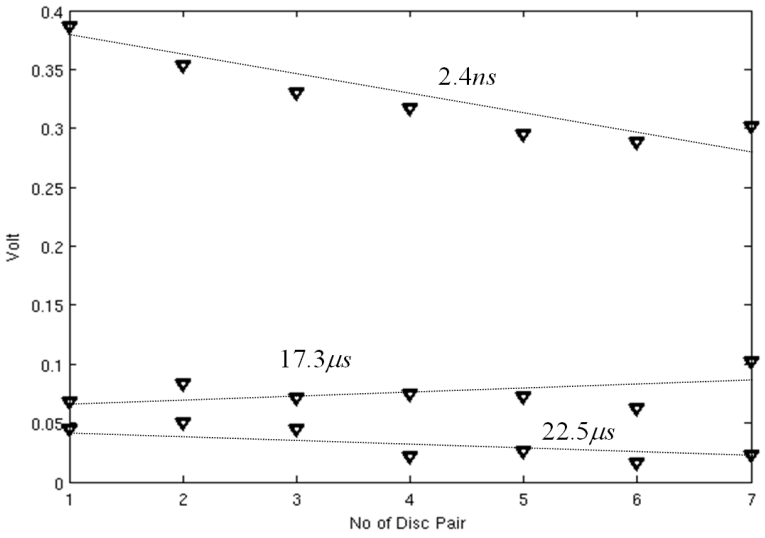

(b) Amplitude distribution

FIGURE 5.31: Impulse response measurement of plain winding with $6ns$ pulse width, $3ns$ rise time

Two techniques of wave estimation are presented; the *superimposition* and *superposition* techniques to provide a solution using Duhamel's principle. Determination of pulse width τ is needed for superimposition technique, where τ is equivalent to the pulse width of the waveshape of the source pulse. However, the superimposition technique is superceded by the superposition technique by means of identifying the harmonic content of the accumulated wave and the original source harmonic pulse. Without determining the time width τ, processing using superposition technique is more robust requiring a zero phase filter which requires a frequency transformation. Moreover, the harmonic pulse is represented by poles peaks and is more easier to identify in the frequency domain.

Due to limited access to the internal structure of the transformer windings, current transformers are used to measure the current propagation within the transformer windings.

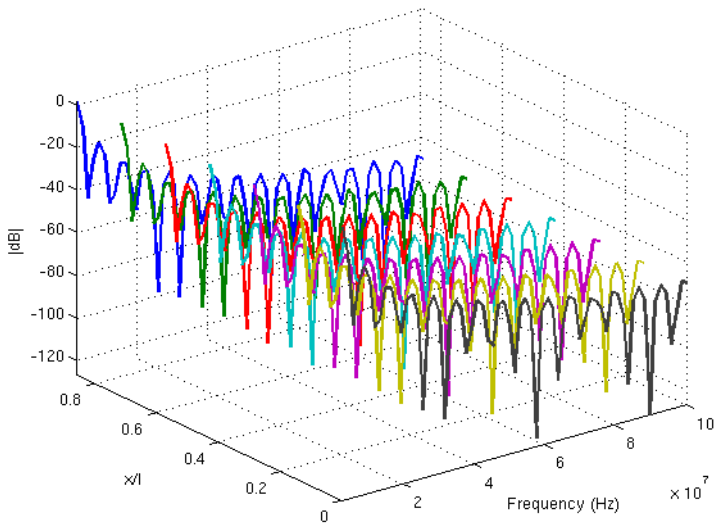

(a) Fourier transform of impulse response

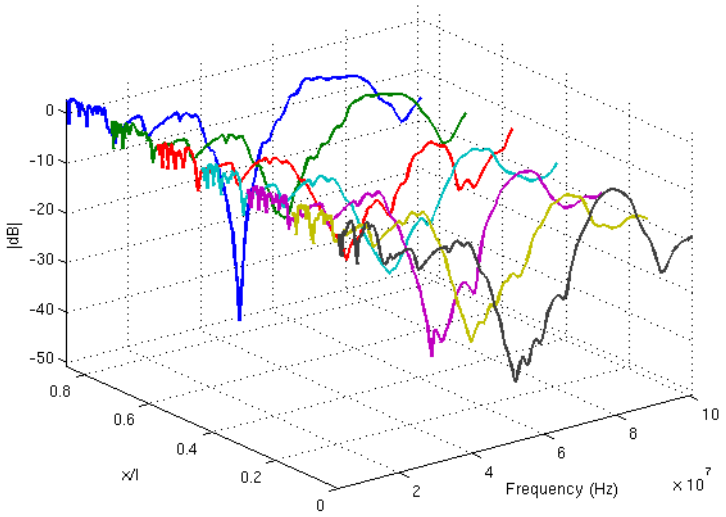

(b) Frequency response from network analyser

FIGURE 5.32: Comparison of impulse response and frequency response of plain winding for 3MHz to 100MHz frequency range

The current transformers are placed at the bushing tap and neutral terminal points. In section 5.5 an analytical model equation for the current and voltage dissimilarities is presented. The use of a terminating impedance $Z_n(50\Omega)$, equivalent to the characteristic impedance of coaxial cable is for calibration purposes to determine the charge current measured by the current transformer.

For real PD measurements, the PD signals can sometimes contain components of hundreds of Mega Hertz. Thus, impulse response measurements and frequency response measurements were conducted to investigate propagation behaviour at very high frequencies. Two types of pulse were considered for impulse response, $100ns$ pulse width, $30ns$ rise time and with $6ns$ pulse width, $3ns$ rise time. For different winding configura-

tions, grounded for impulse responses and ungrounded for frequency responses, at low frequencies both impulse and frequency response measurements show similar analysis in terms of poles and zeros. At this region of frequency the lumped parameter model is operating according to transmission line theory and provides a standing wave solution.

However it is found that, from both types of measurement beyond 4MHz, the transformer model winding is predominantly capacitive in nature. The results have shown that the level of amplitude in time domain and gain in the frequency domain have a linear relationship. According to Duhamel's principle of Equation 5.5, the predominantly capacitive region is defined by the initial condition of $t = 0$, where in this case the inductance current is negligible ($i_L \approx 0$).

By considering the solution towards Neutral, the total current in Equation 5.23 now becomes:

$$i_K = \left(C_g \frac{\partial}{\partial t} \right) \int v \, \partial x_n \tag{5.41}$$

Therefore, the solution for current towards neutral with a very high frequency has a similar form in its time domain:

$$\frac{\partial i_K}{\partial x} = C_g \frac{\partial F(t)}{\partial t} = i_C \tag{5.42}$$

where $F(t)$ is the high frequency time domain response at any point x.

Chapter 6

Parameter Estimation

Even with limited information from terminal measurements it is possible to estimate the original waveform and hence identify source location. In addition this process gives an indication of the transient behaviour of the transformer. An estimation of a signal can be undertaken in either the time domain or the frequency domain using a range of techniques described in this chapter. The overall objective is to estimate the propagation of a partial discharge signal along the winding of a transformer. This then assists in determining the source of the partial discharge within the winding itself.

Standing wave solutions are used for parameter estimation in time domain. The advantage of using standing wave solutions is that only a limited knowledge of the internal physical parameters of the transformer is required. The parameters under consideration are based on known equations that contain arbitrary parameter constants. It has been demonstrated that the physical parameters of a transformer in terms of RLC components can be represented using fixed distribution constants of α and β.

At high frequency, the transformer operates in its capacitive domain, which infers the propagation or attenuation relationship between the bushing and neutral terminals is linear. This is the case when the system operates with negligible inductive current. Therefore, any high frequency oscillation of a transmitted signal consists of elements of a fixed distribution component plus a small factor of decay harmonic components. To separate these components, a Hilbert Huang Transform (HHT) based on Empirical Mode Decomposition (EMD) can be employed.

It was shown in Chapter 5 that for higher frequency signal propagation, use of the frequency domain is required in order to estimate any specific frequency of interest that may contain original information about the source signal. Therefore, an estimation of the signal in the frequency domain is necessary as this can provide coefficients for a transfer function model describing signal propagation.

6.1 Non-Linear Least Square Estimation (NLSE)

The NLSE technique can be used to estimate standing wave parameters and fixed distribution parameters along a transformer winding [57]. These parameters are used in estimating the wave propagation and voltage level using known equations. However the relationship of these parameters to the output response is nonlinear. Therefore the choice of parameters is such that it must meet the requirement of providing a linear combination equation. This can be achieved by reconstructing the matrix of parameters in the form of a linear equation.

To solve this problem, the nonlinear least squares estimation technique models a nonlinear set of unknown parameters, say a_k, where $k = 1, 2, ..., \mathcal{M}$ to a predicted model having a known equation. The model predicts a functional relationship between the measured independent and dependant variables, i.e

$$y(x) = y(x : a_1, a_2, a_3, \cdots, \mathcal{M}) \tag{6.1}$$

where the dependence on the parameters is indicated explicitly on the right hand side. The objective of the technique is to minimize Equation 6.2,

$$\sum_{i=1}^{\mathcal{N}} [y_i - y(x_i : a_1, a_2, a_3, \cdots, \mathcal{M})] \tag{6.2}$$

6.1.1 NLSE by Chi-Square Estimation

In nonlinear systems, the estimation must be undertaken using an iterative procedure. The function to estimate in this case must reach a minimum point or close to zero, then the procedures will finally stop. The Chi-Square, χ^2, function places the problem procedure in a quadratic from, which can be written as:

$$\chi^2(\boldsymbol{a}) \approx \gamma - \boldsymbol{d.a} + \frac{1}{2}\boldsymbol{a.D.a} \tag{6.3}$$

where $\boldsymbol{d}$ is an $\mathcal{M}$-vector and $\boldsymbol{D}$ is an $\mathcal{M} \times \mathcal{M}$ matrix. The minimization approach is to iterate until $\boldsymbol{a_{min}}$ is reached based on current parameter values $\boldsymbol{a_{cur}}$. Where $\boldsymbol{a_{min}}$ is;

$$\boldsymbol{a_{min}} = \boldsymbol{a_{cur}} + \boldsymbol{D^{-1}}.\left[- \bigtriangledown \chi^2(\boldsymbol{a_{cur}}) \right] \tag{6.4}$$

In order to achieve the minimum value, a negative gradient descent of the current value must be approximated. This is done by using a constant variable; c, that can be updated

according to the previous value or gradient value. Modifying equation (6.4) the new negative gradient descent is:

$$\boldsymbol{a_{next}} = \boldsymbol{a_{cur}} - c \times \left[\bigtriangledown \chi^2(\boldsymbol{a_{cur}}) \right] \tag{6.5}$$

where c is small enough to update the iterative gradient smoothly.

By using the χ^2 function, the minimization of the known model can be achieved. Assume that the model to be fitted is described using the equation model of multivariables as shown in Equation (6.1). Therefore the χ^2 function can be constructed as follows:

$$\chi^2(a_1, \cdots, a_{\mathcal{M}}) = \sum_{i=1}^{\mathcal{N}} \frac{y_i - y(x_i; a_1, \cdots, a_{\mathcal{M}})^2}{\sigma^2} \tag{6.6}$$

By taking the first derivative of the function, it becomes a gradient function of χ^2 with respect to $a_k \cdots a_M$ that has components:

$$\frac{\partial \chi^2}{\partial a_k} = -2 \sum_{i=1}^{\mathcal{N}} \frac{[y_i - y(x_i; a_1, \cdots, a_{\mathcal{M}})]}{\sigma_i} \frac{\partial y(x_i; a_i, \cdots, a_{\mathcal{M}})}{\partial a_k} \tag{6.7}$$

Then the second derivative is derived as follows:

$$\begin{aligned} \frac{\partial^2 \chi^2}{\partial a_k \partial a_l} = 2 \sum_{i=1}^{\mathcal{N}} \frac{1}{\sigma_i^2} \left[\frac{y_i - y(x_i; a_1, \cdots, a_{\mathcal{M}})}{\partial a_k} \frac{\partial y(x_i; a_i, \cdots, a_{\mathcal{M}})}{\partial a_l} \right] \\ - [y_i - y(x_i; a_1, \cdots, a_{\mathcal{M}})] \frac{\partial^2 y(x_i; a_1, \cdots, a_{\mathcal{M}})}{\partial a_l \partial a_k} \end{aligned} \tag{6.8}$$

The second derivative is known as the Hessian matrix. It has symmetrical properties, with an equivalent second order derivative in its diagonal. Expressed in square matrix form, the Hessian matrix is;

$$\begin{bmatrix} \frac{\partial^2 f}{\partial x_1^2} & \frac{\partial^2 f}{\partial x_1 \partial x_2} & \cdots & \frac{\partial^2 f}{\partial x_1 \partial x_{\mathcal{N}}} \\ \frac{\partial^2 f}{\partial x_2 \partial x_1} & \frac{\partial^2 f}{\partial x_2^2} & \cdots & \frac{\partial^2 f}{\partial x_2 \partial x_{\mathcal{N}}} \\ \vdots & \vdots & \ddots & \vdots \\ \frac{\partial^2 f}{\partial x_{\mathcal{N}} \partial x_1} & \frac{\partial^2 f}{\partial x_{\mathcal{N}} \partial x_2} & \cdots & \frac{\partial^2 f}{\partial x_{\mathcal{N}}^2} \end{bmatrix} \tag{6.9}$$

Rewriting the first derivative and the second derivative as follows:

$$\begin{aligned} \eta_k &= -\frac{1}{2}\frac{\partial \chi^2}{\partial a_k} \\ \vartheta_{kl} &= \frac{1}{2}\frac{\partial^2 \chi^2}{\partial a_k \partial a_l} \end{aligned} \tag{6.10}$$

Allows a set of linear equations to be constructed to model the fitting technique:

$$\sum_{i=1}^{\mathcal{N}} \vartheta_{kl}\delta_{al} \;=\; \eta_k \tag{6.11}$$

From which by using the minimization process it is possible to estimate the value of parameter a_k by using equation:

$$a_{min} \;=\; a_{cur} \;+\; \delta_{al}[-\bigtriangledown \chi^2(a_{cur})] \tag{6.12}$$

6.1.2 The Levenberg-Marquardt Method

The Levenberg-Marquardt method makes the minimization technique more robust and efficient through the use of a fast gradient descent technique [86]. The technique introduces a variable learning rate. If λ is defined as a constant learning rate such that:

$$\delta_{al} = \frac{1}{\lambda \vartheta_{ll}}\eta_l \tag{6.13}$$

by letting the new diagonal parameter be:

$$\vartheta'_{jj} = \vartheta_{jj}(1+\lambda) \tag{6.14}$$

and the non-diagonal parameters are defined as;

$$\vartheta'_{jk} = \vartheta_{jk} \qquad j \neq k \tag{6.15}$$

To estimate parameters using Lavenberq-Marquardt algorithm, it is necessary to know the solution to the problem undertaken. The solution becomes the basis of the function with paramaters $\boldsymbol{a}$. These parameters are arranged in a single row matrix form as follows:

$$\boldsymbol{a} = \begin{bmatrix} a_1 & a_2 & a_3 & \cdots & a_{\mathcal{M}} \end{bmatrix} \tag{6.16}$$

The parameters are estimated in an iterative loop, where $\boldsymbol{a}$ becomes $\boldsymbol{a_{new}}$ and are updated during the process. During the process, λ is also updated with a small variable change so as to accelerate the process to meet an end stoppage criteria. When λ gets very large the matrix of Equation (6.9) is forced into a state of diagonally dominance with large λ, hence the process will come to a state of large error with positive gradient descent.

Given an initial value for the set of matrix $\boldsymbol{a}$, the recommended update process is as follows; First compute the $\chi^2(\boldsymbol{a})$ which becomes the first criteria to calculate for the gradient. Then set a low value for λ so that the learning step will result in better accuracy of the updated $\boldsymbol{a_{new}}$. Solve the linear Equation (6.11) for $\delta\boldsymbol{a}$, hence evaluate $\chi^2(\boldsymbol{a}+\delta\boldsymbol{a})$ which then will update $\boldsymbol{a_{new}}$. For the new solution of $f(\boldsymbol{a_{new}})$ obtain its Mean Square Error (MSE) value. If $\chi^2(\boldsymbol{a}+\delta\boldsymbol{a}) \geq \chi^2\boldsymbol{a}$, multiply λ by a factor 10. However if $\chi^2(\boldsymbol{a}+\delta\boldsymbol{a}) < \chi^2\boldsymbol{a}$ then decrease λ by a factor 10. Finally, update the trial solution for $\boldsymbol{a}+\delta\boldsymbol{a}$.

The iteration process will continue until either the maximum number of epochs is reached, or performance has been achieved with respect to the goal, or the maximum amount of time has been exceeded, or the performance gradient falls below the minimum gradient, or λ exceeds λ_{max}.

6.1.3 Steady State Fixed Distribution Solution

Analysis of the model shown in Chapter 3 produced the fixed distribution equation for currents travelling to the Neutral and Bushing tap points. The solution derived yields a steady state solution as α gets very small. From a theoretical point of view, the distribution of voltage along a transformer can come to a state of pseudofinal distribution for a certain frequency of any incident pulse [45]. Where the distribution can osillate along the transformer winding between two fixed points of voltage level V_B representing the Bushing voltage and V_N representing the Neutral voltage. Figure 6.1 shows an illustration of a steady state level using a fixed distribution solution along the transformer winding.

Let α_{bep} and α_{nep} be the fixed distribution constant of α towards bushing and neutral respectively. Hence, considering the model solution of the fixed distribution described in Equations 3.19 to 3.30, with the effect of end plates and a pseudofinal distribution [45], the solution used to estimate the value of α is:

$$v_n = \varphi_n(x) + \sum_{1}^{\infty} sin\left(\frac{s\pi x}{l}\right) \tag{6.17}$$

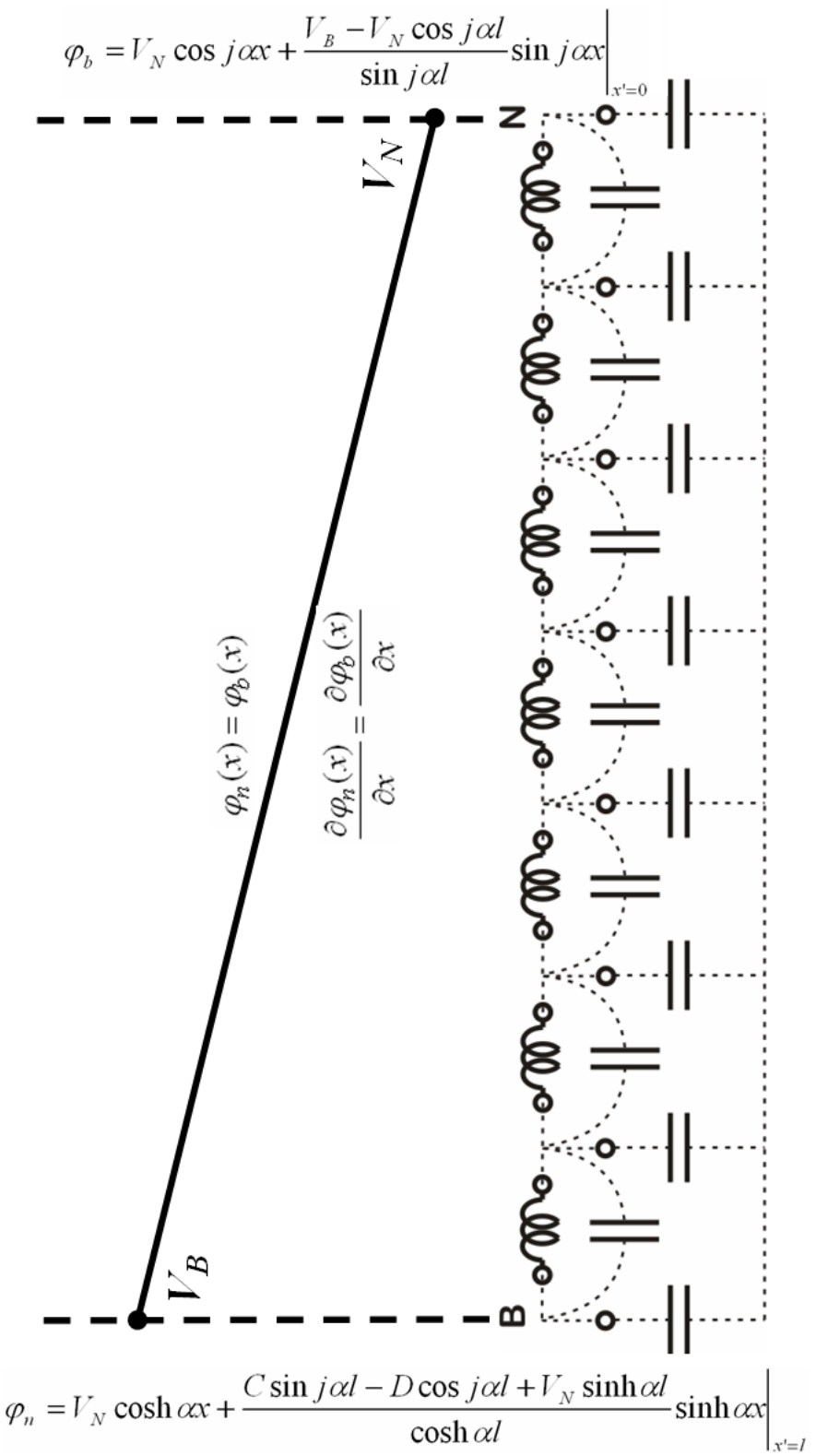

FIGURE 6.1: Steady state level with fixed distribution solution

where $\varphi_n(x)$ is the fixed distribution solution towards the neutral with α_{nep}. The second term of the equation is known as orthogonality function which derived from half range Fourier sine series, where the property of the orthogonolity function is shown in Figure 6.2 [108].

6.1.4 Estimation of α using the Fixed Distribution Solution

The type of distribution level to determine α_{bep} and α_{nep} for multiple points of pulse injection has been illustrated in Figures 3.20 and 3.22. A practical way to obtain the fixed distribution voltage level is by considering an infinite rectangular wave as the source signal. This will give a response with a short rise time that is similar in property to $\delta(t)$.

The time domain output response of signals are filtered using the zero phase filtering technique, at a corner frequency, f_c, where the corner frequency can be determined from its frequency domain of the PSD plot. Figure 6.3 shows the extraction of fixed distribution level at a time close to the wavefront of the output response of the interleaved disc winding. A set of parameters for the NLSE technique were determined to achieve a goal. The target MSE of the process is set to 5×10^{-3}; the maximum number of iterations or epochs is equal to 70; the learning rate is $\lambda = 0.001$ and the minimum gradient of descending process is -1×10^{-3}.

Figures 6.4 to 6.10 show the estimation process using the NLSE technique. The initial parameter of α_{bep} and α_{nep} is set to a suitable value so that the estimation process will converge. The second plot in the figure is the plot of χ^2 which shows the update process with its negative gradient versus the iteration number.

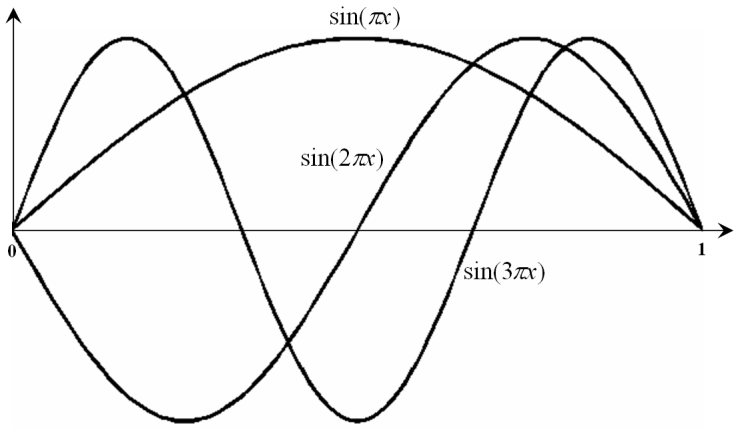

FIGURE 6.2: Orthogonolity function properties

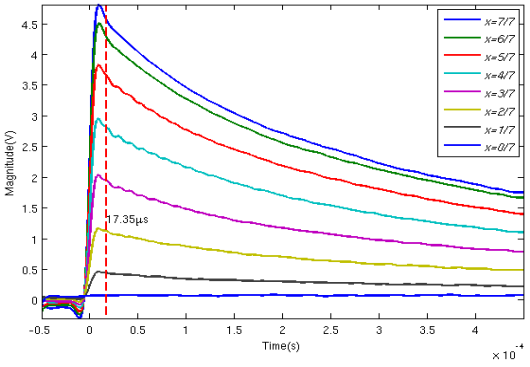

(a) $x' = 7/7$, $f_c = 50.04$kHz

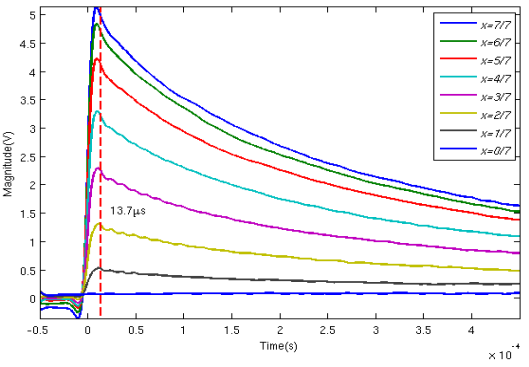

(b) $x' = 6/7$, $f_c = 50.04$kHz

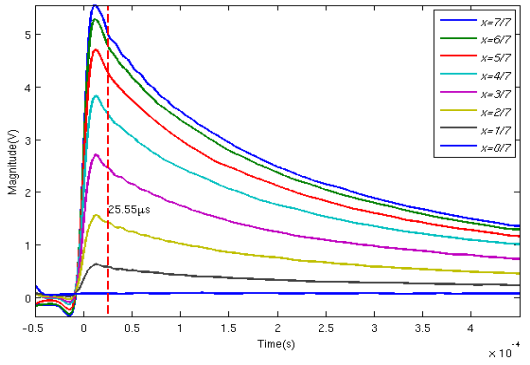

(c) $x' = 5/7$, $f_c = 35.56$kHz

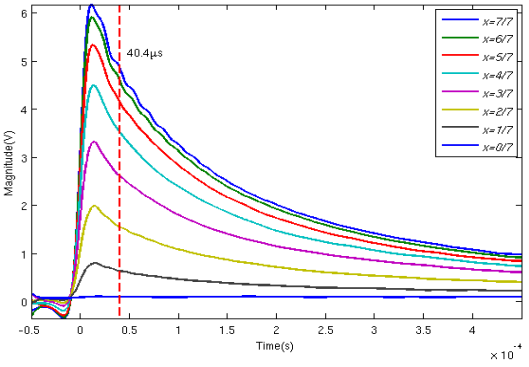

(d) $x' = 4/7$, $f_c = 30.50$kHz

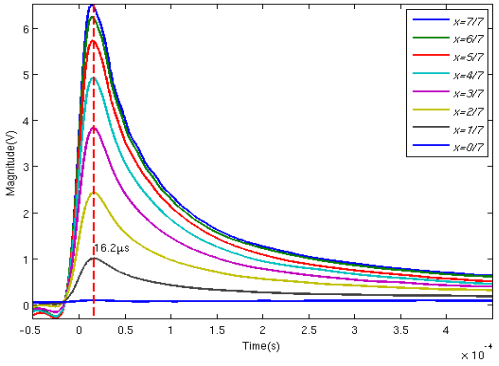

(e) $x' = 3/7$, $f_c = 23.00$kHz

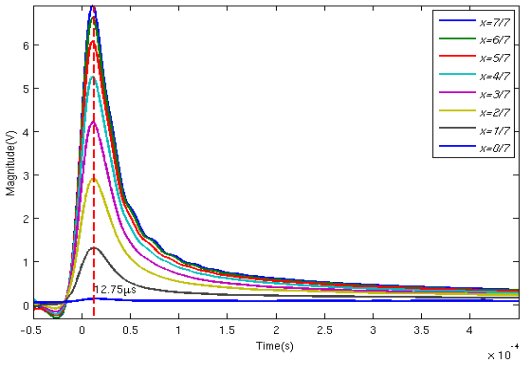

(f) $x' = 2/7$, $f_c = 20.11$kHz

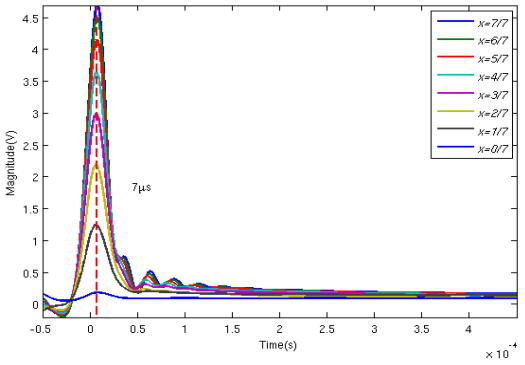

(g) $x' = 1/7$, $f_c = 20.41$kHz

FIGURE 6.3: Interleaved winding time domain extraction at peak magnitudes (at time $t\,\mu s$, to represent the predominantly capacitive distribution)

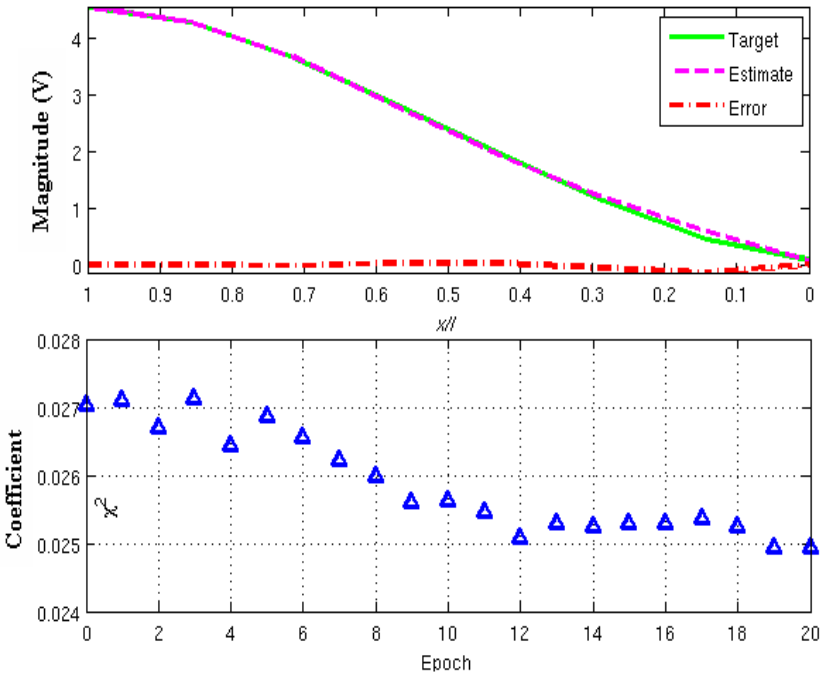

FIGURE 6.4: Interleaved winding parameter estimation, $t = 17.35\mu s$, $x' = 7/7$

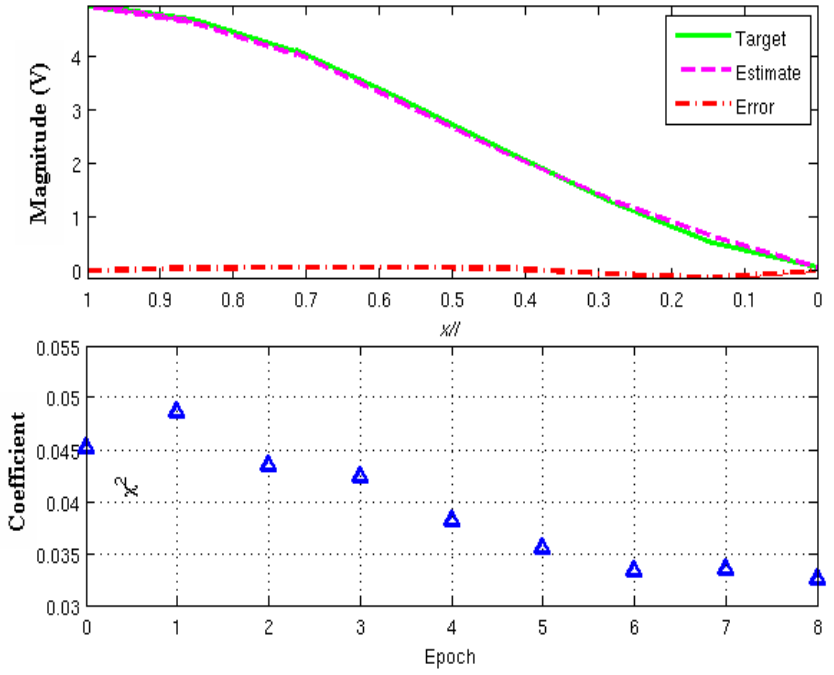

FIGURE 6.5: Interleaved winding parameter estimation, $t = 13.7\mu s$, $x' = 6/7$

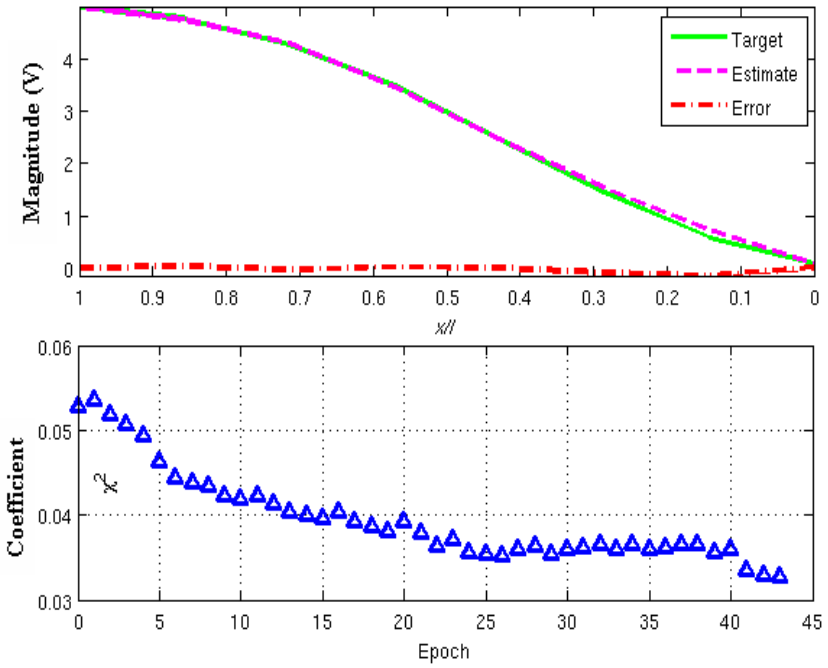

FIGURE 6.6: Interleaved winding parameter estimation, $t = 25.55\mu s$, $x' = 5/7$

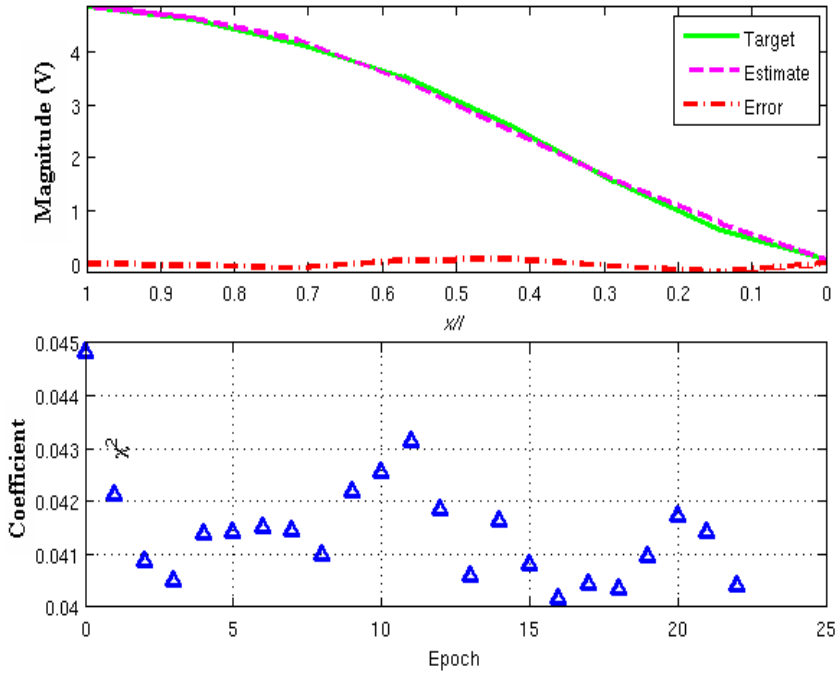

FIGURE 6.7: Interleaved winding parameter estimation, $t = 40.4\mu s$, $x' = 4/7$

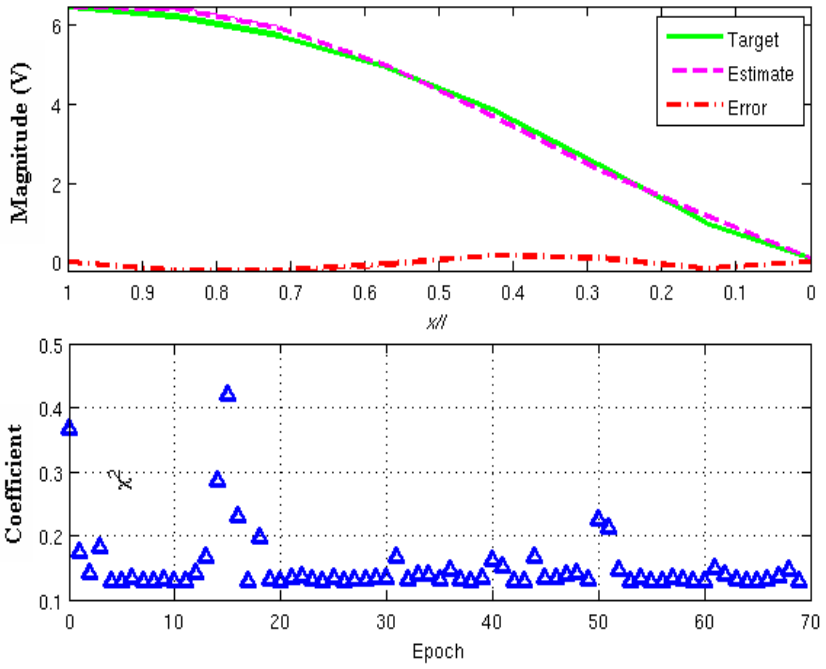

FIGURE 6.8: Interleaved winding parameter estimation, $t = 16.2\mu s$, $x' = 3/7$

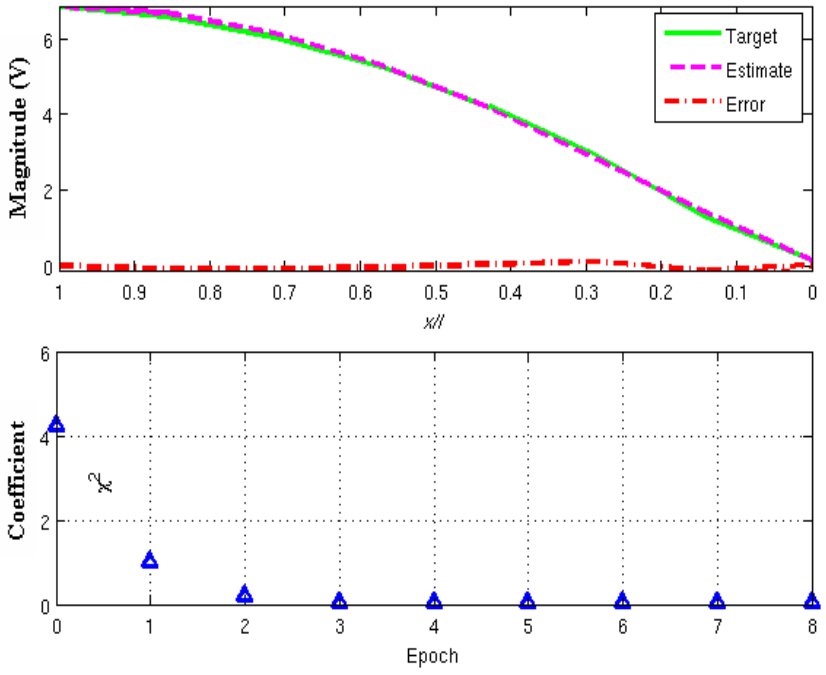

FIGURE 6.9: Interleaved winding parameter estimation, $t = 12.75\mu s$, $x' = 2/7$

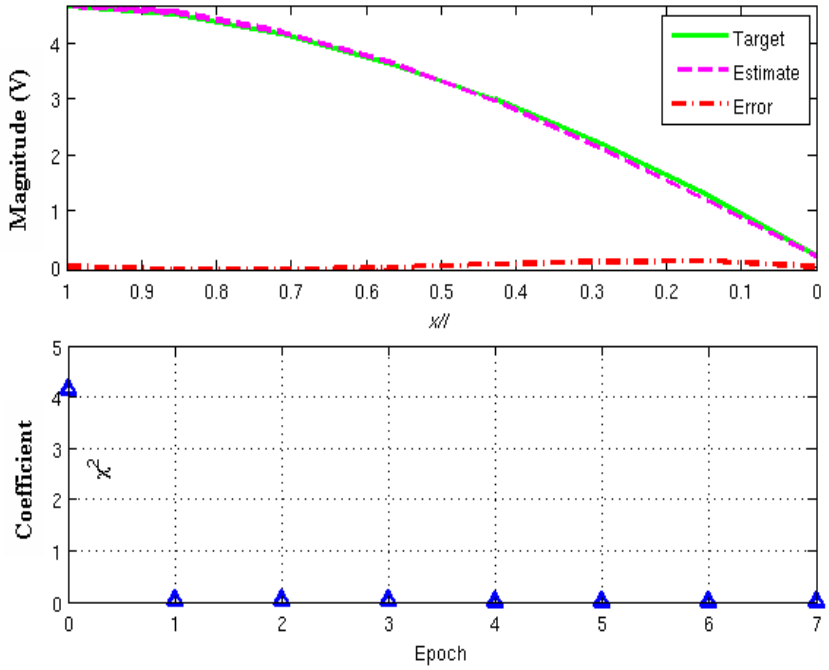

FIGURE 6.10: Interleaved winding parameter estimation, $t = 7\mu s$, $x' = 1/7$

Table 6.1 shows all the NLSE parameters that correspond to every process of α estimation at different point of x'. The value of α_{bep} and α_{nep} are considered, where α_{bep} is for 50% of the total length towards bushing, which is close to the end plate, and α_{nep} is for the remaining length of 50% towards neutral. Note that the distribution of the winding at $x' = 0/7$ is not considered in the estimation process, as it has a very low voltage response near zero volt, that will lead to a false estimation in the iteration procedure with a very low MSE value.

The estimation of α for the plain winding is done in the same way as for the interleaved winding. Figure 6.11 shows the time domain extraction near the wavefront of plain winding distribution level. The set of parameters for the initial value of NLSE has 5×10^{-3} for the MSE; maximum epoch is 70, learning rate $\lambda = 0.0001$; and the minimum gradient descent is -1×10^{-3}.

TABLE 6.1: Estimated parameter, α, for interleaved winding

x'	**MSE**	$\triangle\chi^2$	Epoch	Initial α	Estimated α
7/7	0.0031	-1.39×10^{-4}	20	4.5	$\alpha_{bep} = 4.57$
6/7	0.004	-9.04×10^{-4}	8	4.5	$\alpha_{bep} = 4.31$
5/7	0.004	-9.47×10^{-4}	43	4.5	$\alpha_{bep} = 4.81$
4/7	0.005	-7.19×10^{-4}	22	4.5	$\alpha_{bep} = 4.32$
3/7	0.016	-16.9×10^{-3}	70	2.0	$\alpha_{nep} = 1.89$
2/7	0.0056	-1.9×10^{-3}	8	2.0	$\alpha_{nep} = 1.6$
1/7	0.0029	-5.78×10^{-4}	7	2.0	$\alpha_{nep} = 1.52$

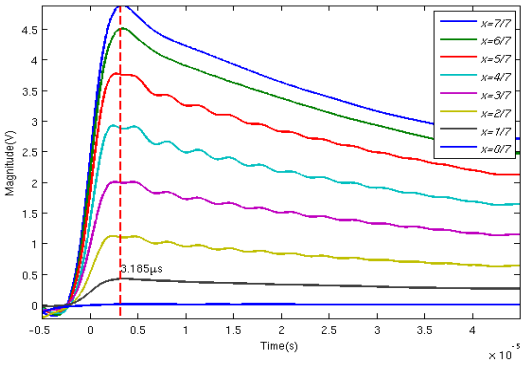

(a) $x' = 7/7,\ f_c = 138.4\text{kHz}$

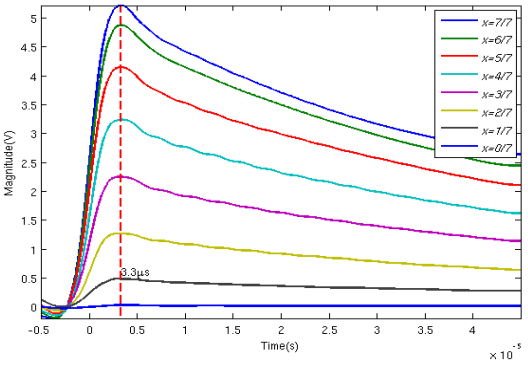

(b) $x' = 6/7,\ f_c = 153.70\text{kHz}$

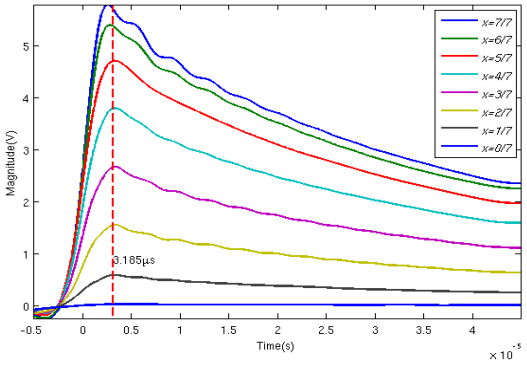

(c) $x' = 5/7,\ f_c = 132.3\text{kHz}$

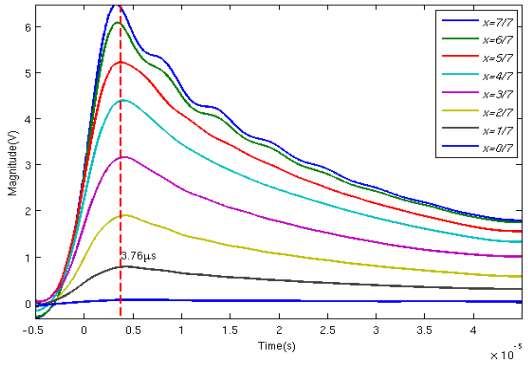

(d) $x' = 4/7,\ f_c = 96.71\text{kHz}$

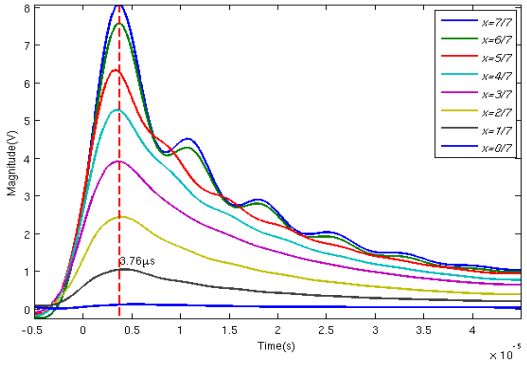

(e) $x' = 3/7,\ f_c = 101.15\text{kHz}$

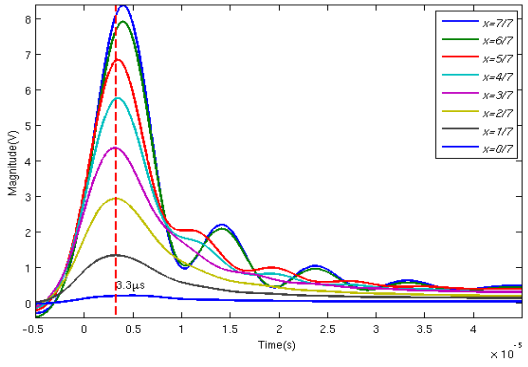

(f) $x' = 2/7,\ f_c = 85.81\text{kHz}$

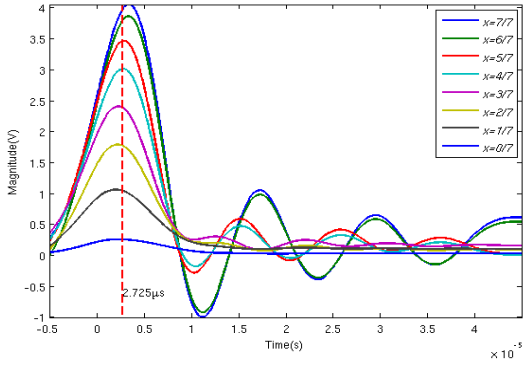

(g) $x' = 1/7,\ f_c = 59.09\text{kHz}$

FIGURE 6.11: Plain winding time domain extraction at peak magnitudes (at time $t\,\mu s$, represent the predominantly capacitive distribution)

The extracted distribution of the voltage levels and the corresponding estimation process are plotted in Figures 6.12 to 6.18. For each estimation process, the parameters α_{bep} and α_{nep} are updated for a small change of $\delta\boldsymbol{\alpha} = 1 \times 10^{-15}$ using a finite difference technique, where finite difference technique is a numerical technique of differenting a known equation with a small change of signal parameters.

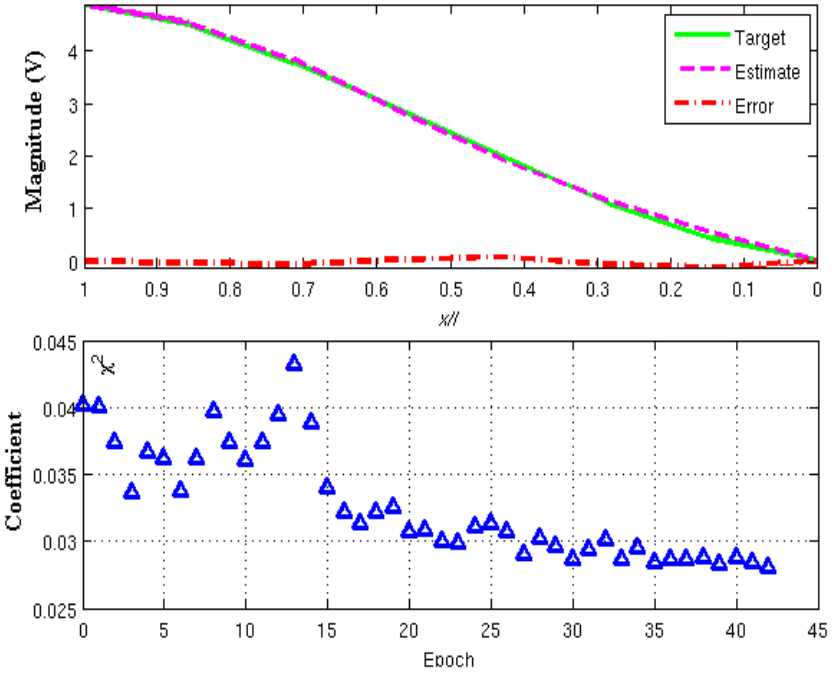

FIGURE 6.12: Plain winding parameter estimation, $t = 17.35\mu s$, $x' = 7/7$

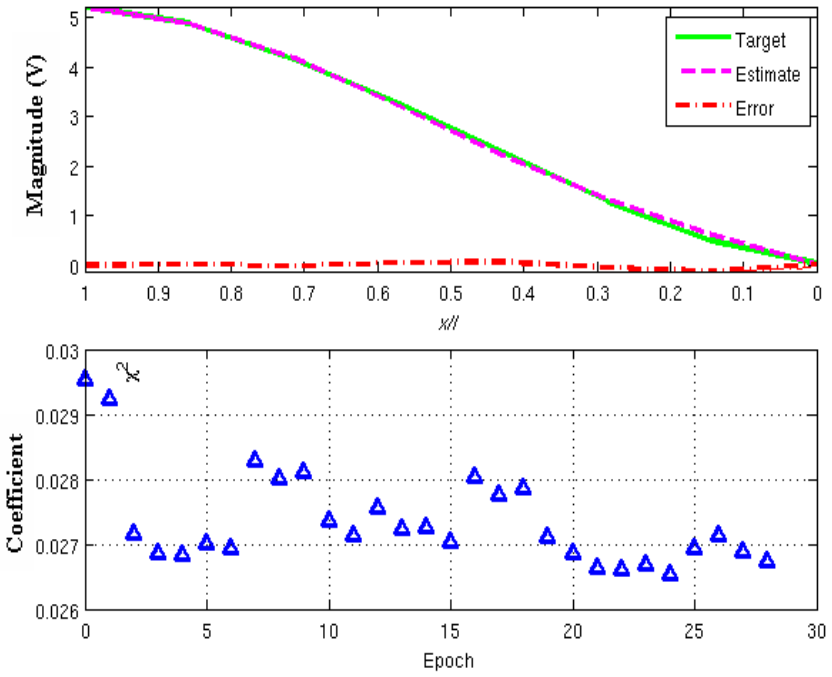

FIGURE 6.13: Plain winding parameter estimation, $t = 13.7\mu s$, $x' = 6/7$

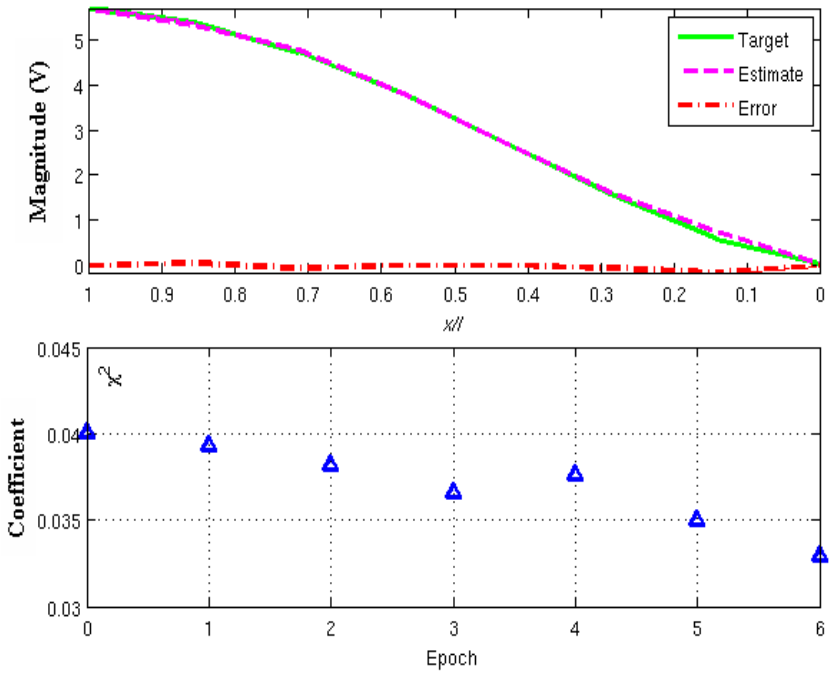

FIGURE 6.14: Plain winding parameter estimation, $t = 25.55\mu s$, $x' = 5/7$

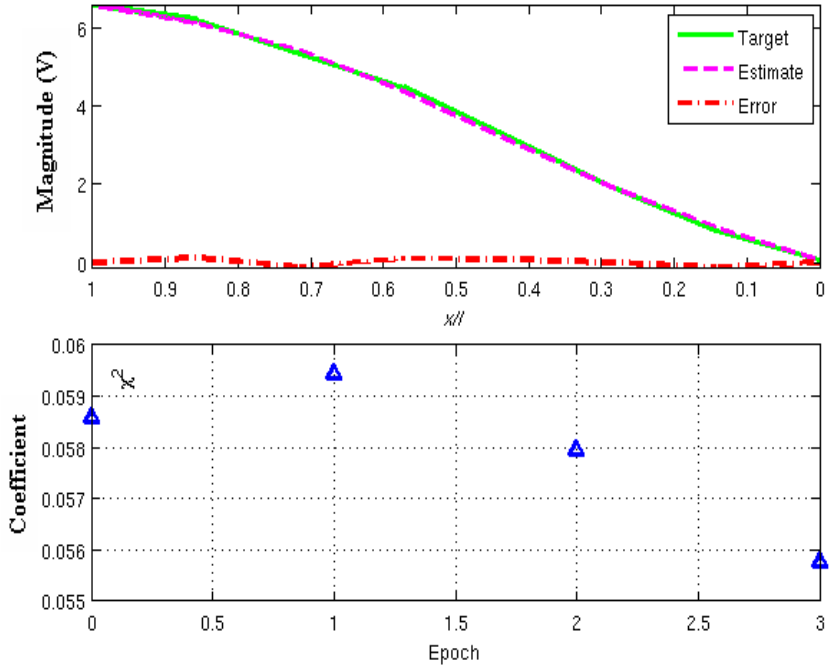

FIGURE 6.15: Plain winding parameter estimation, $t = 40.4\mu s$, $x' = 4/7$

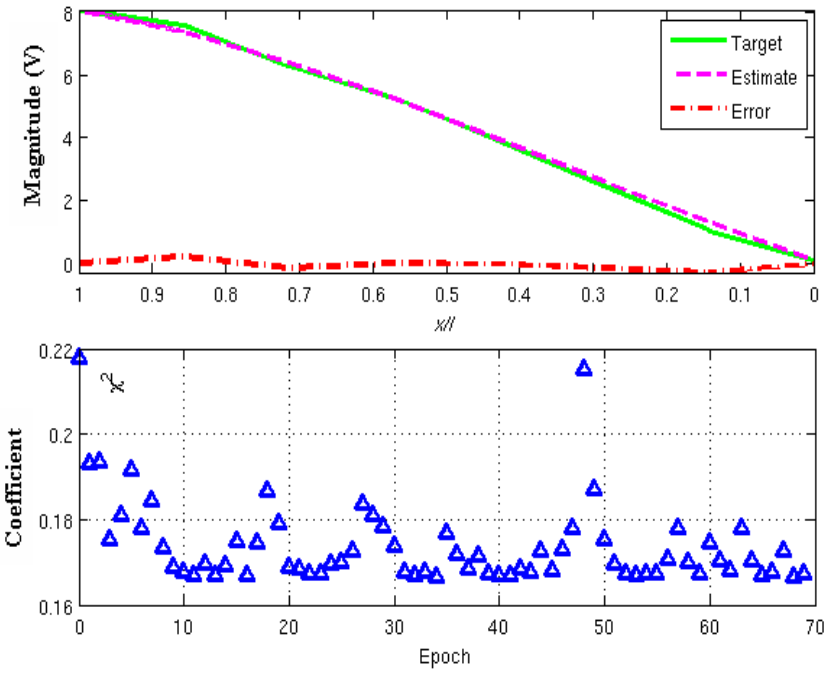

FIGURE 6.16: Plain winding parameter estimation, $t = 16.2\mu s$, $x' = 3/7$

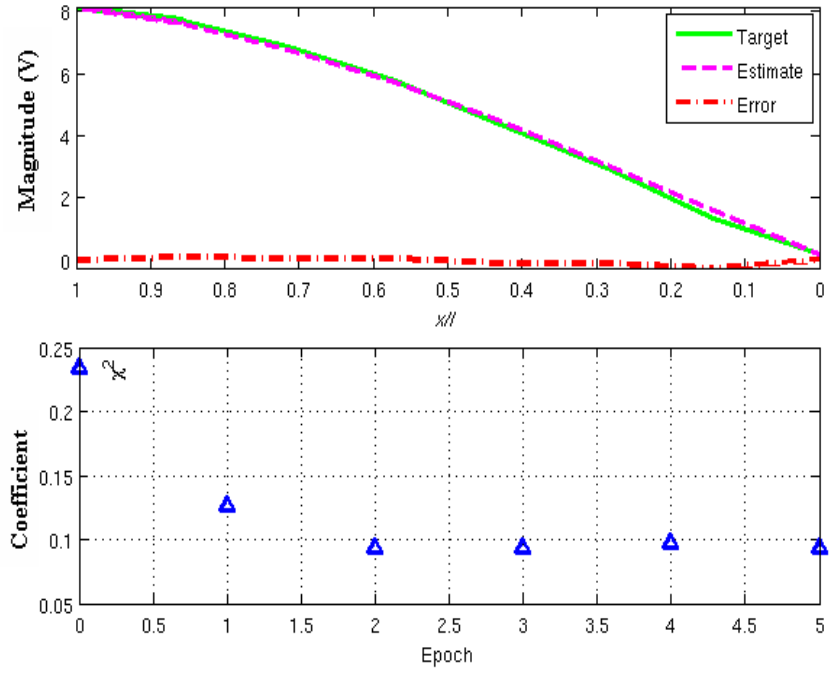

FIGURE 6.17: Plain winding parameter estimation, $t = 12.75\mu s$, $x' = 2/7$

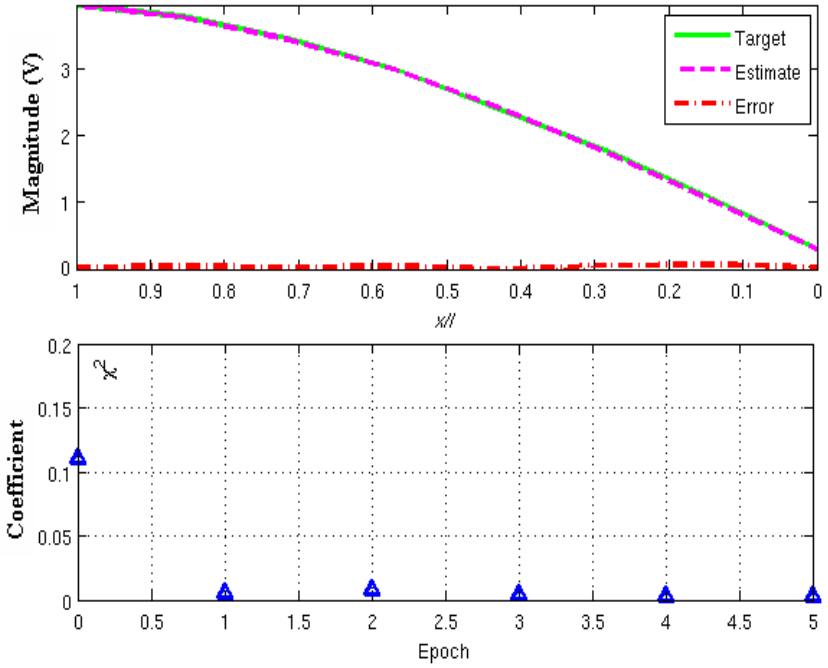

FIGURE 6.18: Plain winding parameter estimation, $t = 7\mu s$, $x' = 1/7$

The process of updating the value of α_{bep} and α_{nep} requires a low value of the diagnonal Hessian matrix. As seen from the iteration process of all the estimated results for interleaved winding and plain winding, the values of χ^2 often jump to higher positive gradients. They are then forced back to a negative gradient to minimize the error. Hence it is therefore necessary to set an appropriate initial value of α, to avoid for positive χ^2 gradient.

Table 6.2 shows the NLSE parameter after iteration process and the estimated value of α_{bep} and α_{nep} for the plain winding. Again the estimation of α_{bep} and α_{nep} are based on the analysis near the winding end for 50% upper and 50% lower length respectively. As seen from both results of interleaved winding and plain winding, the estimated value of α_{bep} is higher compared to α_{nep}. This is due to the different solution analysis of the winding with the effect of an end plate as shown in Equation (3.43).

TABLE 6.2: Estimated parameter, α, for plain winding

x'	**MSE**	$\triangle\chi^2$	Epoch	Initial α	Estimated α
7/7	0.0035	-1.55×10^{-4}	42	4.5	$\alpha_{bep} = 4.74$
6/7	0.0033	-6.37×10^{-4}	28	4.6	$\alpha_{bep} = 4.48$
5/7	0.0042	-8.68×10^{-4}	6	4.6	$\alpha_{bep} = 4.70$
4/7	0.0069	-1.81×10^{-4}	4	4.0	$\alpha_{bep} = 3.9$
3/7	0.02	-7.75×10^{-4}	70	1.1	$\alpha_{nep} = 1.26$
2/7	0.011	-4.94×10^{-5}	6	1.2	$\alpha_{nep} = 1.33$
1/7	3.99×10^{-4}	-3.60×10^{-4}	6	1.2	$\alpha_{nep} = 1.37$

6.2 Hilbert Huang Transform

The Hilbert Huang Transform (HHT) [109] can describe any nonlinear and linear distorted signal, and eliminates any nonstationary elements. The HHT consists of two parts; Empirical Mode Decomposition (EMD), and Hilbert spectral analysis.

The key element of the algorithm is the assumption that a signal can be decomposed into a finite number of Intrinsic Mode Functions (IMF) [109]. An IMF is defined as a function having the same number of zero-crossing and extrema, and also having symmetric envelopes defined by local maxima and minima.

The procedure starts with finding the upper and lower envelopes of a signal. The mean of the upper and the lower envelopes must be equal to zero. The signal is decomposed into these functions using a sifting technique. The upper and lower envelopes are developed by finding local maxima and local minima respectively, and are connected with a cubic spline to form the envelope. The mean of these envelopes, m_1 is calculated and the first component $h_1(t)$ is obtained by subtracting the mean from the original signal such that,

$$h_1(t) = x(t) - m_1 \tag{6.18}$$

After the first subtraction, a decomposed $h_1(t)$ is treated as data for the next subsequent sifting processes up to k times to become $h_{1k}(t)$, as follows:

$$h_{1k}(t) = h_{1(k-1)}(t) - m_{1k} \tag{6.19}$$

then, it is designated as

$$c_1(t) = h_{1k}(t) \tag{6.20}$$

where $c_1(t)$ becomes the first IMF.

The first shifting process extracts the highest frequency oscillation. The following sifting will produce the next highest frequency of oscillation. The process is finished when $c_n(t)$ becomes monotonic or is too small. A stoppage criterion after the k_{th} sifting process is determined by a Cauchy type of convergence process described by,

$$SD_k = \sum_{t=0}^{T} \frac{|h_{k-1}(t) - h_k(t)|^2}{h_{k-1}^2} \leq S_{min} \tag{6.21}$$

On convergence, after n IMFs then residue can be found by:

$$r_{n-1}(t) - c_n = r_n(t) \tag{6.22}$$

S_{min} is chosen so that any variation in $r_n(t)$ is minimized, and can be disregarded in further analysis. The original signal can be composed by summing up all the IMFs and the residue,

$$x(t) = \sum_{i=1}^{n} c_i(t) + r_n(t) \tag{6.23}$$

6.2.1 Application of HHT

The EMD technique used with a repetitive procedure is suitable for the application to a distorted signal. Using infinite rectangular wave and finite rectangular wave to both types of model windings, the application of HHT is demonstrated in Figures 6.19 and 6.20. The test on interleaved winding is by injecting the rectangular wave at $x' = 7/7$ and measured the response at $x = 0/7$ for ungrounded winding and $x = 3/7$ for grounded winding. Note that all the responses of the injected waves in Figures 6.19(a) and 6.19(c) show that an oscillatory response on the wavetail of infinite rectangular wave and finite rectangular wave. Except that the finite rectangular wave response shows both oscillation at trigger time $t = 0s$ and at $\tau = 8ms$. By applying the HHT for the oscillatory waves response Figure 6.19(b) and 6.19(d) show the reduction in the oscillatory waveform, which results in a less oscillatory signal.

The application of HHT on the plain winding is shown in Figure 6.20. This time the injection of rectangular wave is at $x' = 3/7$ and measured at $x = 7/7$, at the bushing tap point. Similar to the application on the interleaved winding the time domain response of finite and infinite rectangular wave at the bushing tap point show an oscillatory waveform response. By applying HHT on the output response, the measured signals are smoother and have similar shape to the original injected waveforms.

Therefore from the simple test procedures, the use of HHT on an oscillatory waveform response, is capable of isolating the osillatory waveform from the measured response. It is also has the ability to match the original source signal injected at x'.

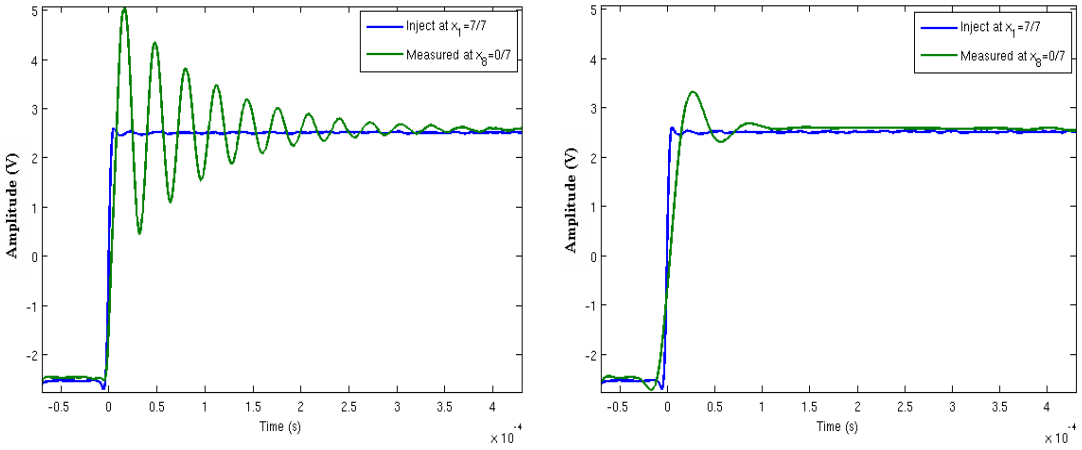

(a) Before HHT

(b) After HHT

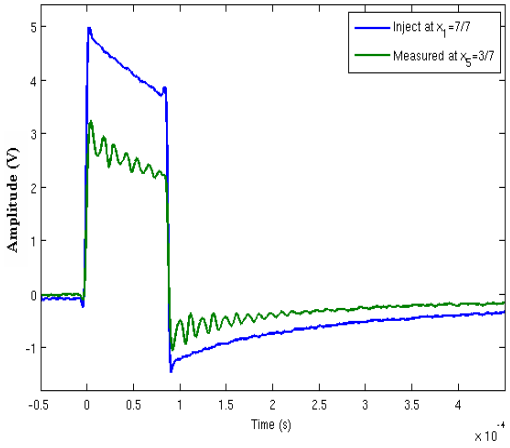

(c) Before HHT

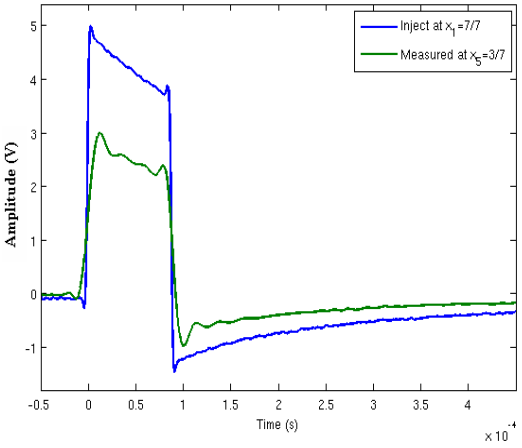

(d) After HHT

FIGURE 6.19: Infinite rectangular response for ungrounded and infinite rectangular response for grounded interleaved winding before and after HHT

6.3 Estimation Using Principle of Superimposition

The application of HHT can be used to estimate the original source of the pulse signal. Suppose an impulse oscillatory waveform is used to investigate the application of the HHT and the NLSE to identify and estimate the source of original PD signal in a transformer winding. Figure 6.21 shows the application of HHT to split the harmonic decay component, denoted by the term $\sum_{i=1}^{n} c_i(t)$, and the fixed distribution component, denoted by the residual $r_n(t)$, for empirical mode decomposition of a pulse signal captured at neutral point. It has been shown that the IMF signal has a symmetrical property and thus can be solved by the harmonic decay function of Equation (5.8). The spectrum level of the EMD is shown in Figure 6.21(b). The spectrum was extracted for 50 levels of signal decomposition until a minimum criterion of S_{min} is met. The spectrum was plotted in Matlab environment using *image* command file. The EMD spectrum shows that the higher the level of EMD the signal becomes more flatter and level to zero, which

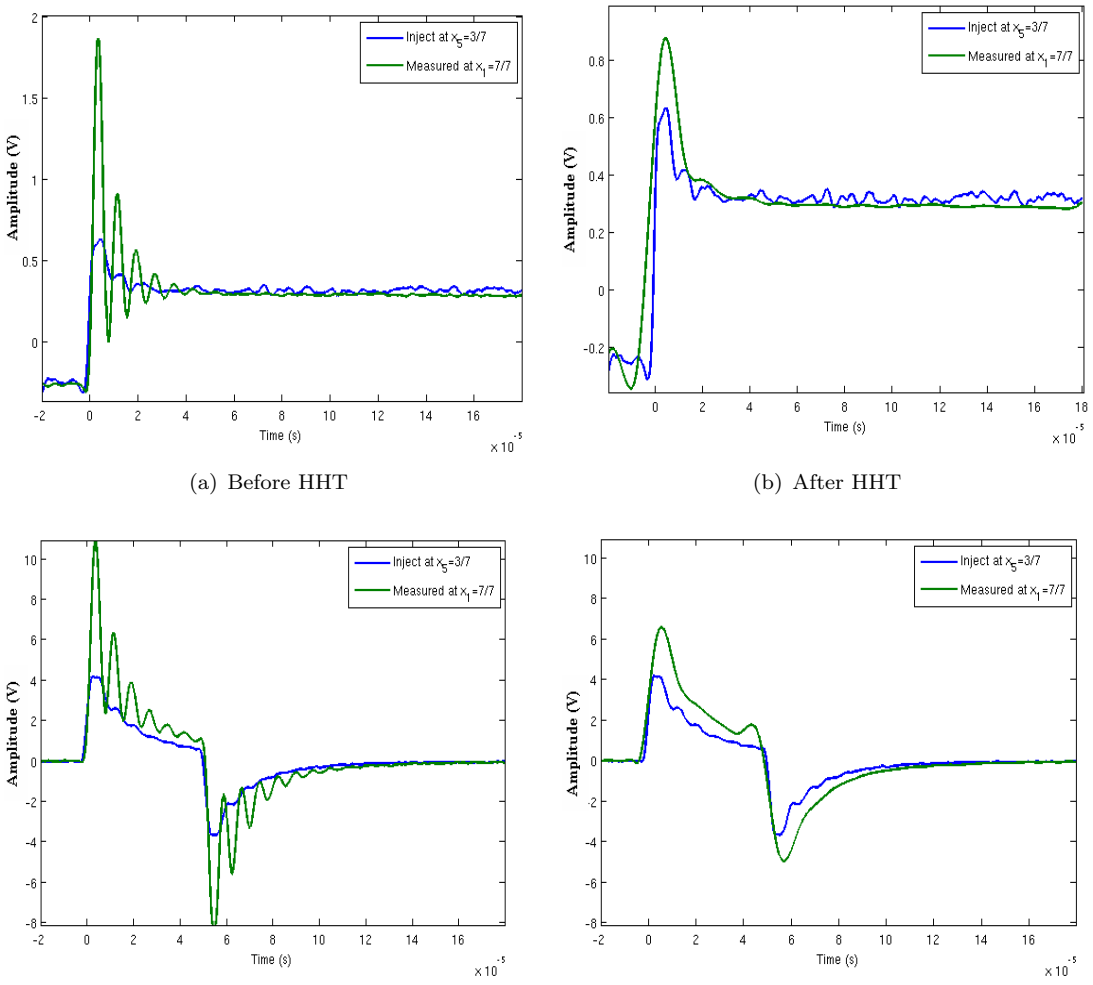

(a) Before HHT

(b) After HHT

(c) Before HHT

(d) After HHT

FIGURE 6.20: Infinite rectangular response for ungrounded and infinite rectangular response for grounded plain winding before and after HHT

is close to achieving S_{min} from Equation (6.21).

The experimental investigation of the partial discharge propagation started by injecting a single pulse signal at Bushing tap point to interleaved winding. The signal captured at the Neutral point is used for the analysis using HHT and parameter estimation using the NLSE technique. Figure 6.22 shows the step procedures for the investigation to determine the signal oscillation along the transformer winding. The first Figure (a) shows the pulse signal injected at Bushing tap point, and (b) shows the corresponding response at the Neutral to earth connection. T1 and T2 indicate the time range where the oscillation occurs along the transformer winding. For the purpose of analysis and estimation of the domain of interest, it is clearly seen from captured signal at the Neutral, that a signal oscillation develops between T1 and T2 compared to the original source signal.

A Zero phase filter is used to remove noise and HHT is employed to remove the fixed

distribution components leaving only harmonic decay component. Note the symmetrical property as a result of HHT for the built up oscillation between T1 and T2 as shown. Finally, a nonlinear least square estimation using the Levenberg Marquardt algorithm is used to estimate the standing wave parameters of the harmonic decay component using Equation (5.8).

Figure 6.23 shows the comparison of estimated signals of the oscillations within the transformer winding with the measured signal between the time range of T1 to T2. The injected pulse signal, at $x' = 7/7$, and the measured neutral signal at $x = 0/7$, is the only available terminal for real transformer measurements. Therefore, the estimation process is only for the intermediary winding length between $x = 1/7$ to $6/7$.

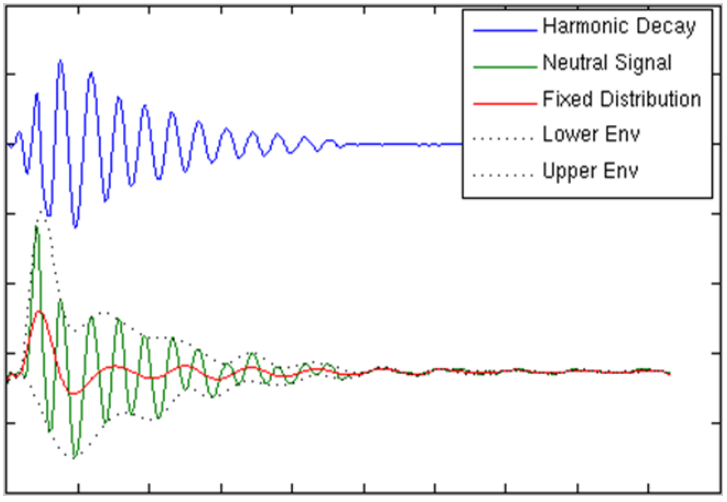

(a) Hilbert spectral

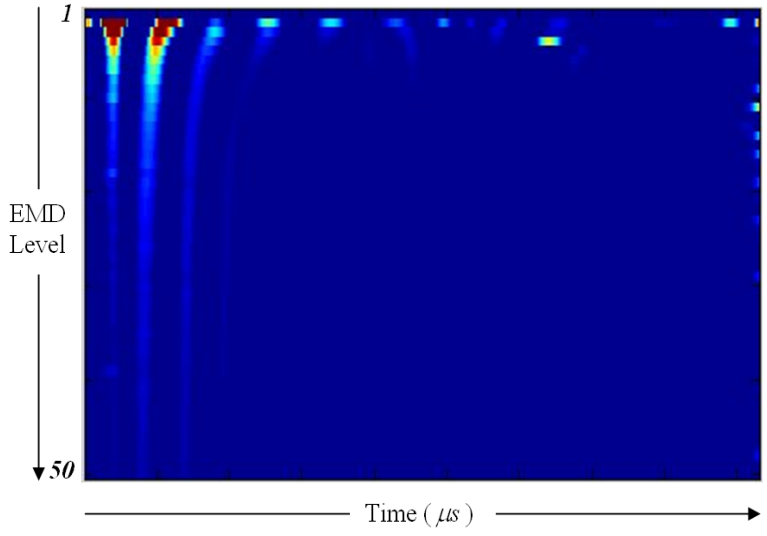

(b) Empirical Mode Decomposition spectrum

FIGURE 6.21: Application of Hilbert Huang transform with empirical mode decomposition

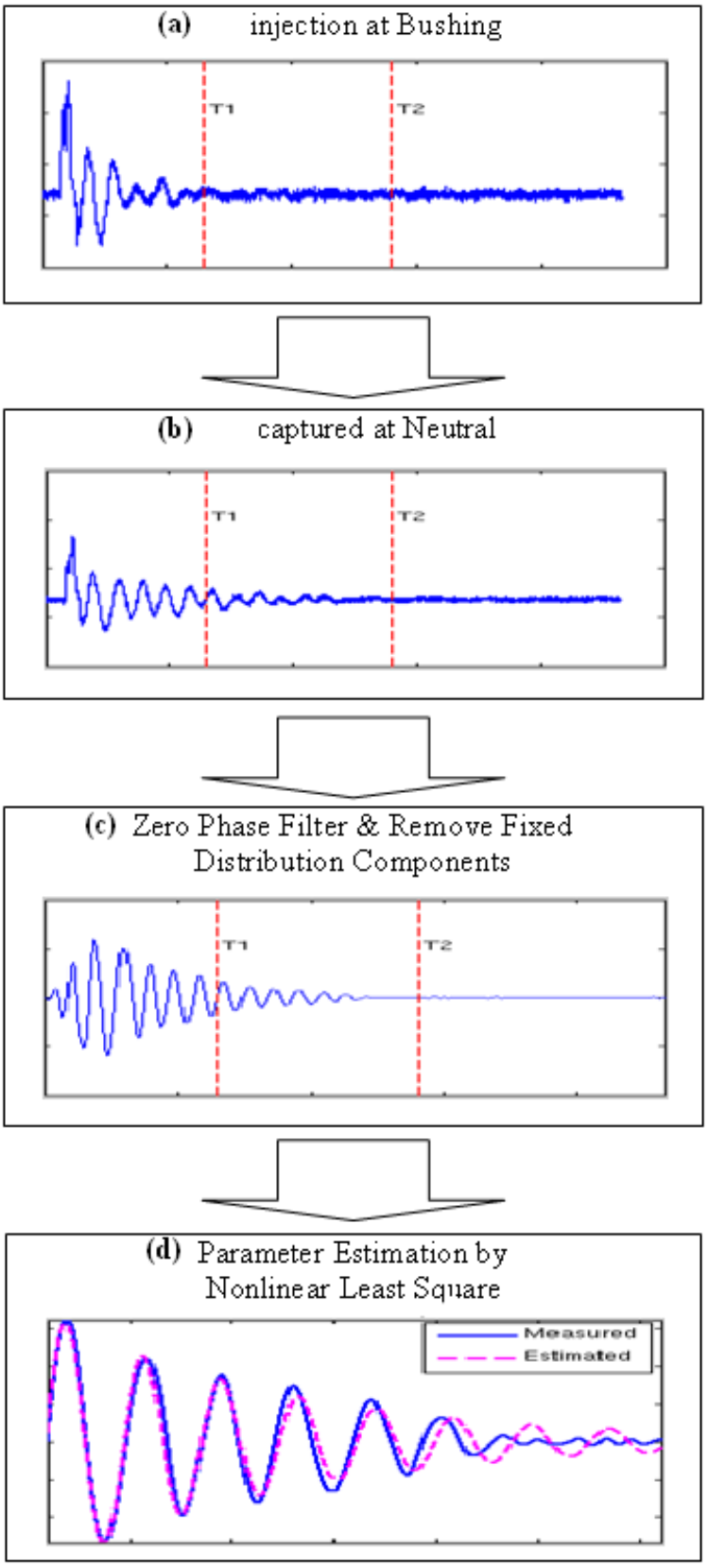

FIGURE 6.22: Step procedure of pulse estimation

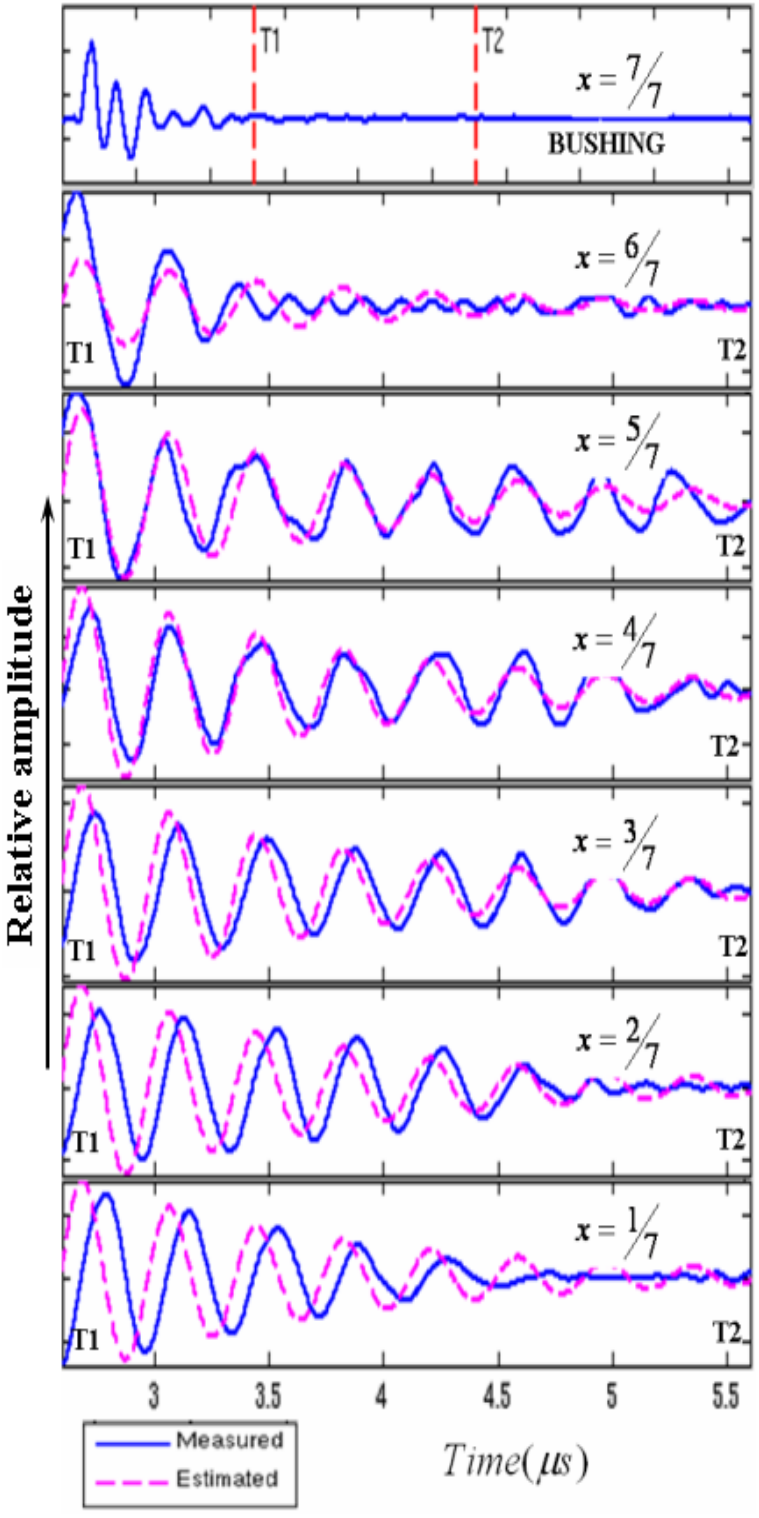

FIGURE 6.23: Estimation at different points along winding

6.4 Transfer Function Model

Without reference to the internal windings of transformer structure, the complicated frequency response can be expressed in general form as a fractional polynomial function. This is based on the assumption that the transformer characteristic is linear time-invariant in the frequency domain [32]. The Laplace operator, $\mathfrak{s}$, is used to express the problem, with the assumption that $\mathfrak{s} = jw$. The complex transfer function form can be shown in equations (6.24) and (6.25) [102].

$$G(\mathfrak{s}) = \frac{Z(\mathfrak{s})}{P(\mathfrak{s})} = \frac{\prod_{i=1}^{n_1} Z_i(\mathfrak{s}) \prod_{i=1}^{n_2} Z_i(\mathfrak{s}) e^{-\mathfrak{s}T}}{\prod_{i=1}^{m_1} P_j(\mathfrak{s}) \prod_{i=1}^{m_2} P_j(\mathfrak{s})} \tag{6.24}$$

$$G(\mathfrak{s}) = \frac{\mathcal{G}_{\mathfrak{s}} \prod_{i=1}^{n_1} (\mathfrak{s} + w_{1i}) \prod_{i=1}^{n_2} (\mathfrak{s}^2 + \xi_1 w_{2i} \mathfrak{s} + w_{2i}^2) e^{-\mathfrak{s}T}}{\prod_{i=1}^{m_1} (\mathfrak{s} + w_{1j}) \prod_{i=1}^{m_2} (\mathfrak{s}^2 + \xi_1 w_{2j} \mathfrak{s} + w_{2j}^2)} \tag{6.25}$$

The constant $\mathcal{G}_{\mathfrak{s}}$ is the system gain, and w_i are the break frequencies of the zeros and poles, and $e^{-\mathfrak{s}T}$ allows the effect of time delay. The symbol ξ represents the damping factor or the damping ratio. The value of the time delay can be determined by plotting phase against frequency, and measuring the negative slope of the resulting straight line.

Knowing the complexity of transformer structure, Equation (6.25) can be simplified and expressed in the form of Equation (6.26) [110].

$$G(\mathfrak{s}) = Y(\mathfrak{s}) = \frac{1}{(\mathfrak{s}^2 + 2\xi w_n \mathfrak{s} + w_n^2)^{\mathfrak{r}}} \tag{6.26}$$

Where $\mathfrak{r}$ is the order of poles and zeros, denoting the order of estimated transfer function of the transformer. It can be identified that if $\mathfrak{r}$ is negative value $Y(\mathfrak{s})$ consists of zeros coefficients, and if $\mathfrak{r}$ is positive $Y(\mathfrak{s})$ consists of poles coefficients. By simplifying Equation (6.26) the new equation becomes;

$$Y(\mathfrak{s}) = \frac{w_n}{\left[\frac{\mathfrak{s}^2}{w_n^2} + \frac{2\xi\mathfrak{s}}{w_n} + 1\right]^{\mathfrak{r}}} \tag{6.27}$$

By substituting $\mathfrak{s} = jw$ a complex transfer function can be obtained as shown in Equation (6.28)

$$Y(jw) = \frac{w_n}{\left[1 - \frac{w^2}{w_n^2} + j\frac{2\xi w}{w_n}\right]^{\mathfrak{r}}} \tag{6.28}$$

Hence, the frequency response and the phase response of the transformer can be obtained as follows:

$$|Y(jw)| = 20log|w_n| - 10log\left[\left(1 - \frac{w^2}{w_n^2}\right)^2 + \frac{4\xi^2 w^2}{w_n^2}\right] \tag{6.29}$$

$$\phi(w) = -\mathfrak{r}\tan^{-1}\left(\frac{2\xi\frac{w}{w_n}}{1 - \frac{w}{w_n}}\right) \tag{6.30}$$

6.5 Transfer Function Estimation

The identification of a transformer transfer function and parameter estimation from frequency response data involves complex mathematical derivations and is a time consuming iterative process. However, in this thesis it is intended to elaborate only the typical techniques and available tools to solve the problem. The first technique is the Frequency Response Test [110] and the second is using Matlab Signal Processing Toolbox based on Non-linear Least Square Estimation Techinque (NLSE) [92] and finally using a Vector Fitting technique [97].

6.5.1 The Frequency Response Test

The Frequency Response test is the traditional technique of obtaining a transfer function. It begins from the measured results - a sinusoidal signal of varying frequency is applied to the system input (the transformer model) and the corresponding system output is measured in term of magnitude and phase relative to the input of every individual eight terminals (Network Analyzer). The results of the response are normally plotted as Bode diagram in logarithmic scale. The system gain can now be calculated from the response by looking at the lower frequency region and calculated using Equation (6.31).

$$\mathcal{G}_{\mathfrak{s}} = 10^{\frac{F(\mathfrak{s}_1)}{20}} \tag{6.31}$$

Where $F(\mathfrak{s}_1)$ is the first sampling unit in frequency domain. The following procedures refer to the simple approach appropriate in determining the transfer function of a system and can be written in the rule based form:

- The frequencies are determined at which the gradient of the asymptotic diagram changes and denoted as w_n.
- If the gradient becomes more negative by 20dB/decade, there is a $(1+\mathfrak{s}/w_n)$ term in the denominator of the transfer function.
- If the gradient becomes more positive by 20dB/decade, there is a $(1+\mathfrak{s}/w_n)$ in the numerator of the transfer function.
- If the gradient becomes more negative by 40dB/decade, there is a $(\mathfrak{s}^2+2\xi w_c\mathfrak{s}+w_n^2)$ term in the denominator of the transfer function.
- If the gradient becomes more positive by 40dB/decade, there is a $(\mathfrak{s}^2+2\xi w_c\mathfrak{s}+w_n^2)$ term in the numerator of the transfer function.

6.5.2 Estimation by NLSE

The non-linear least square estimation technique can be invoked using Matlab routine *invfreqs*. It is able to find continuous time transfer function that corresponds to the complex frequency response. Analytically, the function is useful in converting magnitude and phase data into a transfer function. It returns the real numerator and denominator coefficients of the transfer function in the form of Equation (6.32).

$$H(\mathfrak{s}) = \frac{B(\mathfrak{s})}{A(\mathfrak{s})} = \frac{b_1\mathfrak{s}^{nb} + b_2\mathfrak{s}^{nb-1} + ... + b_{nb+1}}{a_1\mathfrak{s}^{na} + a_2\mathfrak{s}^{na-1} + ... + a_{na+1}} \tag{6.32}$$

in which the complex frequency response is derived from Equation (6.28). $B(\mathfrak{s})$ and $A(\mathfrak{s})$ represent the numerator and denominator respectively, and scalar nb and na specify the desired orders of both numerator and denominator polynomials.

The *invfreqs* function uses a least square estimation technique to find the equation error in Equation (6.33) of b and a in a least square sense

$$\min_{a,b} \sum_{k=1}^{\mathfrak{n}} wt_k |h_k A(w_k) - B(w_k)|^2 \tag{6.33}$$

by solving the system as a linear equation. Here $A(w(k))$ and $B(w(k))$ are the Fourier transforms of the polynomials a and b, respectively at the frequency $w(k)$, and $\mathfrak{n}$ is the number of frequency points. *invfreqs* also uses the damped Gauss-Newton method for fast convergence. It solves the direct problem in minimizing the weighted sum of the squares between the actual and the desired frequency response as in Equation (6.34).

$$\min_{a,b} \sum_{k=1}^{\mathfrak{n}} wt_k \left| h_k - \frac{B(w_k)}{A(w_k)} \right|^2 \tag{6.34}$$

6.5.3 Vector Fitting

Vector fitting is another technique for estimating the transfer function parameter using a least square estimation technique. The name itself describes the process, of which the measured response from the frequency analyser will be fitted with a new approximation equation. However, typical techniques for modelling the transfer function use a typical polynomial transfer function in the form of:

$$f(\mathfrak{s}) = \frac{a_0 + a_1\mathfrak{s} + a_2{\mathfrak{s}}^2 + ... + a_{\mathfrak{R}}{\mathfrak{s}}^{\mathfrak{R}}}{b_0 + b_1\mathfrak{s} + b_2{\mathfrak{s}}^2 + ... + b_{\mathfrak{R}}{\mathfrak{s}}^{\mathfrak{R}}} \tag{6.35}$$

Equation (6.35) is a nonlinear equation in terms of the unknown coefficients a and b. The equation can be written as a linear problem of type $Ax = b$ by multiplying both sides by common denominator [32]. However the technique often causes poor scaling especially for higher frequency ranges. Vector fitting has the ability to solve this problem. The process starts by modeling a system in state space standard form:

$$\dot{x} = \mathbf{Ax} + \mathbf{Bu} \tag{6.36a}$$

$$y = \mathbf{Cx} + \mathbf{Du} \tag{6.36b}$$

where **A**, **B**, **C** and **D** are the state matrices for linear parts of the dynamic system. Hence in the case of a high voltage transformer, the state equation can be used as it is a linear system in its range of linear frequency. In all cases, the information available is in the frequency domain, as it is much more convinient for characterising transient behaviour in the higher frequency region.

The frequency domain transfer function $H(\mathfrak{s})$ where $\mathfrak{s} = j\omega$, can be obtained either by computation or measurement. Thus $H(\mathfrak{s})$ can be explained in nonrational form as:

$$H(\mathfrak{s}) = \mathbf{C}(\mathfrak{s}I - \mathbf{A})^{-1}\mathbf{B} + \mathbf{D} \tag{6.37}$$

The matrix $\mathbf{D}$ is normally the model for system noise, however for simplicity and to reduce computational burden $\mathbf{D}$ is often neglected in (6.36) and (6.37). Hence $H(\mathfrak{s})$ is a rational transfer function with common poles contained in $\mathbf{A}$, denoted as a_n, and $\mathbf{B}$ corresponds to system excitation (all one to excite the whole system) and $\mathbf{C}$ corresponds to its residual matrix denoted as c_n. Therefore the above system can be written in rational transfer function form as:.

$$h(\mathfrak{s}) = \sum_{n=1}^{\mathfrak{R}} \frac{c_n}{\mathfrak{s} - a_n} + d \tag{6.38}$$

6.5.4 Vector Fitting by Pole Relocation

The vector fitting approach starts by considering the transfer function equation in partial fraction form:

$$h(\mathfrak{s}) = \sum_{n=1}^{\mathfrak{R}} \frac{c_n}{\mathfrak{s} - a_n} + d + \mathfrak{s}h \tag{6.39}$$

The equation consists of residues c_n and poles a_n that can either come in real quantities or in complex conjugate pairs. The technique developed by [97, 98] is by fitting the vector function $h(\mathfrak{s})$ using a least squares approximation technique and to estimate the c_n and a_n coefficients that appears in the numerator and denominator respectively.

This is a nonlinear problem in terms of the unknown parameters that need to be approximated. To solve the problem, a set of initial values of $\bar{a}_n$ is introduced. $\bar{a}_n$ is updated iteratively by using a pole relocation technique over an interval of frequencies.

The pole relocation technique starts by setting the initial values of poles $\bar{a}_n$ as either a complex conjugate pair or real quantities and multiply Equation (6.39) with an unknown function $\sigma(\mathfrak{s})$. Here, $\sigma(\mathfrak{s})$ is a rational transfer function such that:

$$\sigma(\mathfrak{s})h(\mathfrak{s}) = \sum_{n=1}^{\mathfrak{R}} \frac{c_n}{\mathfrak{s} - \bar{a}_n} + d + \mathfrak{s}h \tag{6.40a}$$

$$\sigma(\mathfrak{s}) = \sum_{n=1}^{\mathfrak{R}} \frac{\tilde{c}}{\mathfrak{s} - \bar{a}_n} + 1 \tag{6.40b}$$

In Equation (6.40), both function $\sigma(\mathfrak{s})h(\mathfrak{s})$ and $\sigma(\mathfrak{s})$ have the same poles as denominator. By solving Equation (6.40), yields the following relationship which in the form of $\mathbf{A}\breve{x} = b$:

$$(\sum_{n=1}^{\mathfrak{R}} \frac{c_n}{\mathfrak{s} - \bar{a}_n} + d + \mathfrak{s}h) = (\sum_{n=1}^{\mathfrak{R}} \frac{\tilde{c}_n}{\mathfrak{s} - \bar{a}_n} + 1)h(\mathfrak{s}) \tag{6.41}$$

The above relationship also can be simplified to further understand the fitting problem as follows:

$$(\sigma f)_{fit}(\mathfrak{s}) \approx \sigma_{fit}(\mathfrak{s})f(\mathfrak{s}) \tag{6.42}$$

Equation (6.41) is linear in its unknowns c_n, d, h, and $\tilde{c}_n$, and can be written in the form of $\mathbf{A}\breve{x} = b$ where the unknowns are in the solution $\breve{x}$. Equation (6.42) can be solved using least squares estimation techniques.

6.5.5 Zeros Calculation

The zeros can be calculated using the vector fitting technique from the calculated poles when $\sigma(\mathfrak{s})$ is rational scalar function in the form:

$$\sigma(\mathfrak{s}) = \frac{y(\mathfrak{s})}{u(\mathfrak{s})} = \sum_{m} \frac{c_m}{\mathfrak{s} - a_m} + 1 = \frac{\prod(\mathfrak{s} - z_m)}{\prod(\mathfrak{s} - a_m)} \tag{6.43}$$

Deriving Equation (6.43) as $1/\sigma(\mathfrak{s})$, yields:

$$\frac{1}{\sigma(\mathfrak{s})} = \sum_{m} \frac{\mathfrak{s} - a_m}{c_m + (\mathfrak{s} - a_m)} = \frac{\prod(\mathfrak{s} - z_m)}{\prod(\mathfrak{s} - a_m)} \tag{6.44}$$

Therefore, it is evident that the zeros of $\sigma(\mathfrak{s})$ are equal to the poles $1/\sigma(\mathfrak{s})$. This is also known as the inverse of $\sigma(\mathfrak{s})$ and can be found by interchanging the input (u) with output (y) of a system. Consider a state space domain of the form:

$$\dot{x} = \mathbf{A}\mathbf{x} + \mathbf{B}\mathbf{u} \tag{6.45a}$$

$$y = \mathbf{C}\mathbf{x} + \mathbf{D}\mathbf{u} \tag{6.45b}$$

where $\mathbf{A}$ is a diagonal matrix holding the elements a_m, $\mathbf{C}$ is a row vector consists the elements c_m, $\mathbf{D}$ is unity, and $\mathbf{B}$ is a column of ones (whole system excitation). And from Equation (6.45b)

$$\mathbf{u} = \mathbf{D}^{-1}(y - \mathbf{C}\mathbf{x}) \tag{6.46}$$

$$\dot{x} = \mathbf{A}\mathbf{x} + \mathbf{B}\mathbf{D}^{-1}(y - \mathbf{C}\mathbf{x}) = (\mathbf{A} - \mathbf{B}\mathbf{D}^{-1}\mathbf{C})\mathbf{x} \tag{6.47}$$

Since $\mathbf{D} = 1$ the new state becomes:

$$\dot{x} = (\mathbf{A} - \mathbf{B}\mathbf{C})\mathbf{x} \tag{6.48}$$

Therefore the zeros of $\sigma(\mathfrak{s})$ are equal to the eigenvalues of $(\mathbf{A} - \mathbf{B}\mathbf{C})$.

$$zeros = eig(\mathbf{A} - \mathbf{B}\mathbf{C}) \tag{6.49}$$

6.5.6 Transfer Function Estimation Using Vector Fitting

To demonstrate the estimation technique, the transfer function was estimated for the whole winding measurement. A measurement was taken between terminal 1 to terminal 8 for an ungrounded configuration. Figure 6.24 and 6.25 show the estimation of frequency response measurement for the whole seven sections of the interleaved winding and plain winding respectively. The estimation of winding transfer function was up to $\mathfrak{R} = 110$, where $\mathfrak{R}$ represents the order of the transfer function. The result shows that the estimation of the transfer function using vector fitting technique results with very low MSE error below 0.0068p.u. Whereas the calculated poles, residues and zeros are shown in Figure 6.26 and 6.27. Note both the pattern of Zero, Poles and Residue (ZPR) coefficients for each winding has a unique pattern coefficient.

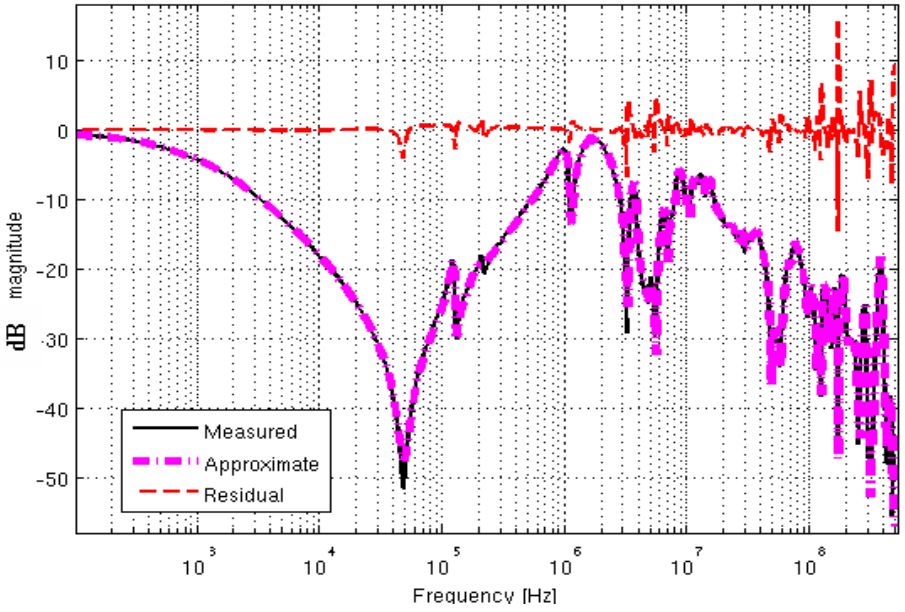

(a) Transfer function estimation

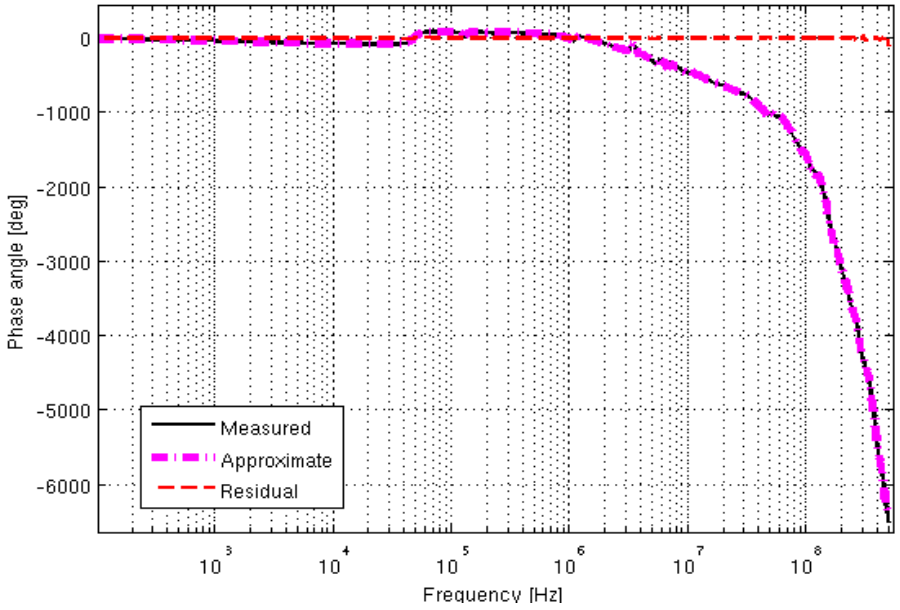

(b) Phase response estimation

FIGURE 6.24: Transfer function estimation of interleaved winding using vector fitting technique

The accuracy of estimation can be improved by varying the number of orders as well as the iteration number. However the iteration number can be fixed and the process stopped if the target error is achieved. Therefore the choice of number of orders was considered in this study. To demonstrate this, a frequency response measurement has been taken for an interleaved winding between terminals 1 and 8. There are four different sets of data over frequency ranges starting from 100Hz up to maximum frequency of 500MHz. The frequency of interest is intended to study the variation of all possible transient behaviour that can happen inside a transformer starting from low harmonic orders up

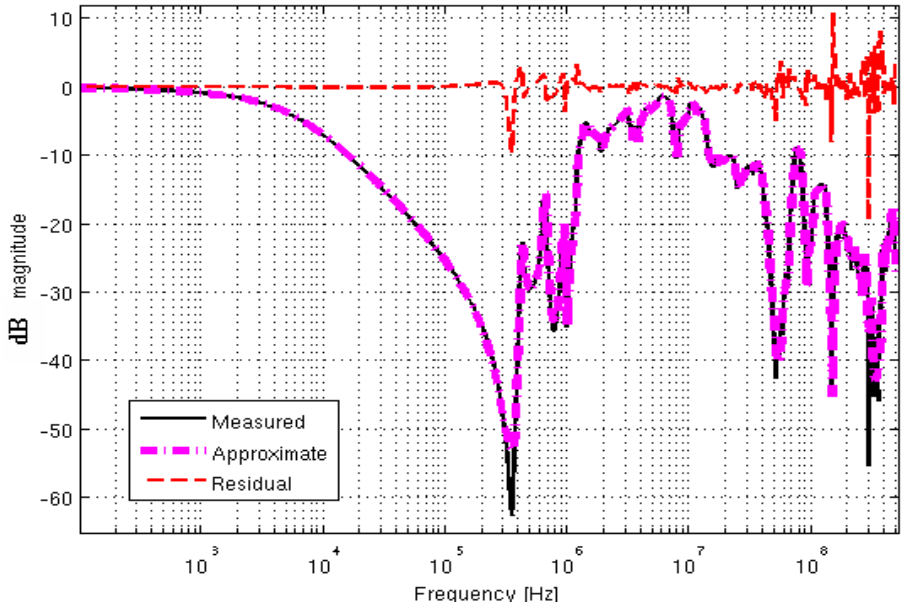

(a) Transfer function estimation

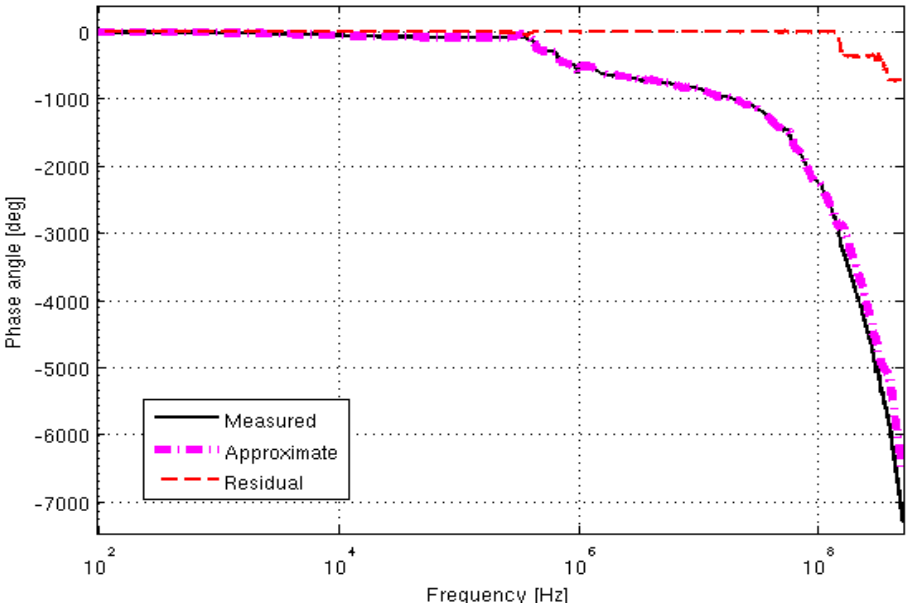

(b) Phase response estimation

FIGURE 6.25: Transfer function estimation of plain winding using vector fitting technique

to frequencies excited by transient effects like partial discharge. It is also important to take into account the model for any sensor device, for example a current transformer may have frequency response up to 200MHz frequency range. The sensor model can then be subtracted from the transformer real model to isolate the processing complexity and hence improve accuracy.

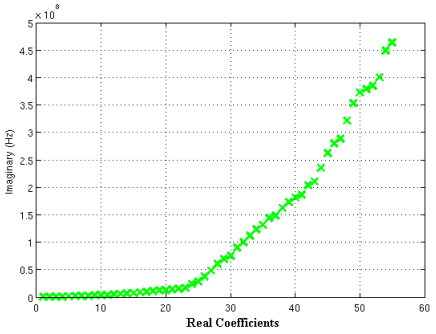

(a) Calculated poles

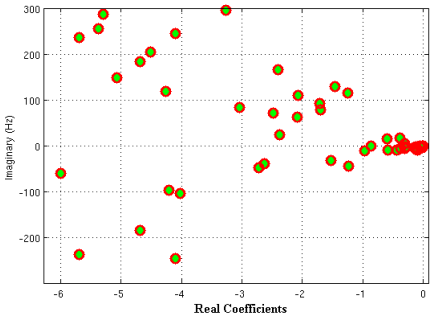

(b) Calculated zeros

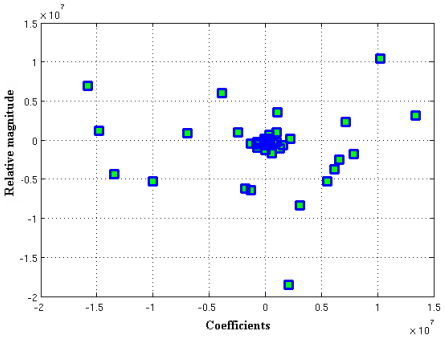

(c) Calculated residue

FIGURE 6.26: Calculated poles, residue and zeros of interleaved winding from vector fitting technique

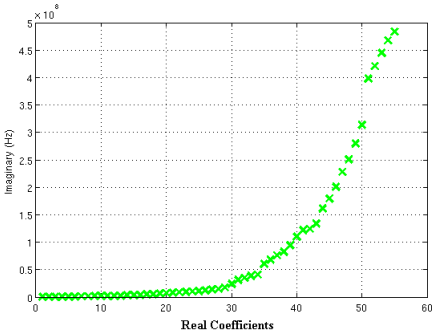

(a) Calculated poles

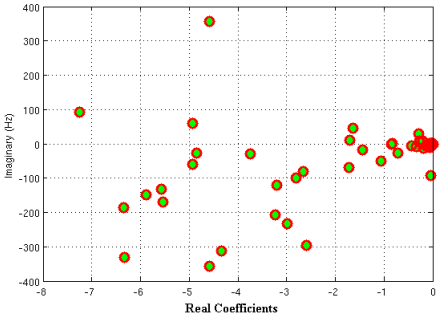

(b) Calculated zeros

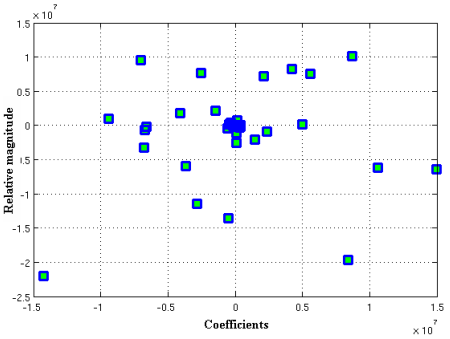

(c) Calculated residue

FIGURE 6.27: Calculated poles, residue and zeros of plain winding from vector fitting technique

The transfer function $h(\mathfrak{s})$ of the frequency response was estimated using the vector fitting technique as shown in Figures 6.24(a) and 6.25(a). Table 6.3, shows the resulting transfer function estimation using vector fitting for different sets of frequency range. Note that the selected order of transfer function (noted as asterisk) is based on the lowest absolute value of highest error in dB and lower rms value.

TABLE 6.3: Effect of number of order with RMS accuracy

Frequency range	No of orders ($\mathfrak{R}$)	R.M.S (p.u)	Highest error (dB)
100Hz-500MHz	70	0.0112	15.9374
	80	0.0081	-13.1712
	90*	0.0060*	-12.3314*
	100	0.0050	-12.6078
	110	0.0036	-14.3219
	120	0.0031	-14.4404
100Hz-100MHz	60	0.0057	5.6189
	70*	0.0049*	-4.6258*
	80	0.0044	-4.6429
	90	0.0029	-4.8744
100Hz-10MHz	30	0.0094	7.5233
	40*	0.0028*	-4.5332*
	50	0.0016	-4.6177
	60	0.0014	-4.5999
100Hz-1MHz	10	0.0061	-5.8721
	15*	0.0017*	-2.4997*
	20	0.0012	-2.5627
	25	0.0011	-2.5706

6.6 Estimation Using Principle of Superposition

Estimation based on superposition principles can be achieved with transformation from the time domain to the frequency domain. There are two techniques used to estimate the impulse like waveform. The first is based on the estimation of the standing wave solution with the use of a zero phase filter, and the second is to use the inverse laplace transform from the estimated vector fitting algorithm.

6.6.1 Standing Wave Parameter Estimation

Consider only the harmonic decay equation of the response to an infinite rectangular wave input for the ungrounded winding configuration, and also accounting for the delay time constant, t_d, of a multiharmonic wave, the general equation becomes:

$$h(t) = \sum A_s e^{-\gamma_s(t-t_d)} cos\, \omega_s(t-t_d)\, sin\left(\frac{s\pi x}{2l}\right) \tag{6.50}$$

To illustrate the estimation process using the superposition principle, consider an impulse response filtered between 100Hz to 100MHz. The estimation is carried out using the NLSE technique. Figure 6.28 shows the two step estimation of the signal response with estimated parameters in time domain. A_s is a measurement of the amplitude factor and can be obtained graphically, ω_s is the harmonic frequency that can also be determined from the frequency domain, and γ_s is the damping factor. The value of x and l are zero and one respectively, because the measurement of frequency response is for the whole winding length. The total harmonic estimation of the impulse response is equivalent to the summation of first estimation and second estimation. This is shown in Figure 6.28(c). The estimated parameters are tabulated in Figure 6.4.

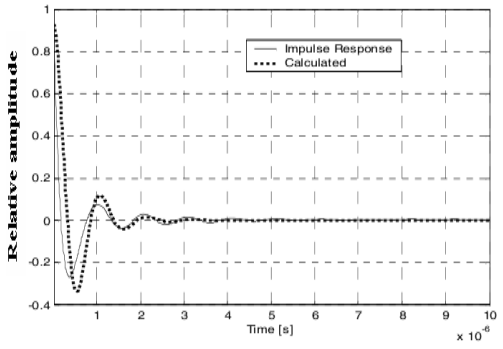

(a) First estimation

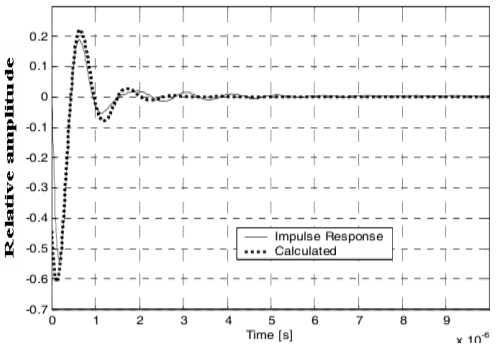

(b) Second estimation

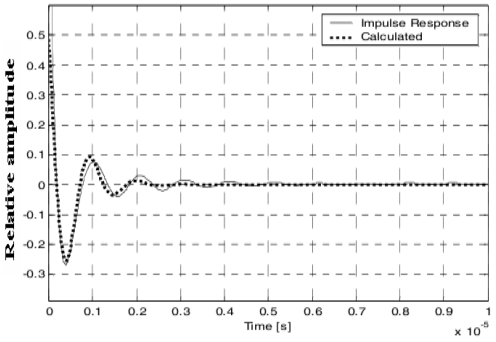

(c) First + Second estimation

FIGURE 6.28: Estimation of inverse Laplace transform waveform using NLSE technique for 100Hz to 1MHz

TABLE 6.4: Estimated parameter value

Parameter	1^{st}	2^{nd}
A_s	1	0.7935
ω_s	$2 \times \pi \times 4.8449 \times 10^4$	$2 \times \pi \times 4.8449 \times 10^4$
γ_s	-1.9×10^6	-1.9×10^6
t_d	$6.5 \times 10^{-8} s$	$7.0 \times 10^{-7} s$

6.6.2 Vector Fitting and the Principle of Superposition

The transformation from time domain to frequency domain reveals winding transfer function information which is useful in determining the winding level gain. The analysis in this section shows transformation from the frequency domain to the time domain and illustrates the usefulness of frequency response measurements for time domain parameter estimation.

Using the frequency response measurement from Section 5.6 the estimation of the transfer function is found using the vector fitting technique in Section 6.5.6. The estimation of the transfer function from frequency response measurements was carried out for a frequency range similar to the impulse response frequency range. Mathematically, the impulse waveform can be represented by $\delta(t)$ function, where $\delta(t)$ has the following:

$$\delta(t) = \begin{cases} +\infty & \text{for } t = 0 \\ 0 & \text{for } t \neq 0 \end{cases}$$

which equivalent to

$$\int_{-\infty}^{+\infty} \delta(\mathfrak{s}) d\mathfrak{s} = 1 \tag{6.51}$$

in frequency domain, for the range of $-\infty$ to $+\infty$ frequencies. Hence, the analysis for transformation of frequency response data to its time domain begins by estimating its transfer function. Consider the rational transfer function in the Laplace domain as shown in the following equation:

$$h(\mathfrak{s}) = \sum_{n=1}^{\mathfrak{R}} \frac{c_n}{\mathfrak{s} - a_n} \tag{6.52}$$

by taking the inverse Laplace transform, the time domain equation becomes:

$$h(t) = \sum_{n=1}^{\mathfrak{R}} c_n e^{-a_n t} \tag{6.53}$$

Equation (6.53) is very similar to Equation (5.3), where it represents as a typical impulse like waveform equation based on the principle of superposition. Therefore, the inverse Laplace transform of frequency response data can be used to model the impulse response measurement. Figures 6.29 and 6.30 show the estimated frequency response using vector fitting technique and the corresponding inverse waveform using Equation (6.53) for interleaved winding and plain winding respectively over the frequency range 100Hz to 500MHz.

6.7 Summary

Based on the model solution of current divergence to estimate the level of voltage distribution along a transformer winding, the estimation of α using the NLSE technique is divided into two. Firstly, due to the end plate at the bushing the estimation corresponds to α_{bep} and secondly due to the end plate at the neutral point the estimation corresponds to α_{nep}. This is however only applicable to short stacks and wide disc coils windings. With reference to Figure 3.13 the dimension of the windings has disc coils of q m in diameter, and a total length of l m. As included in Appendix A the ratio of q/l of both windings is equivalent to 1.43. This shows that, both model windings are wide, with short stacks, where $q > l$ and are suitable for this estimation technique.

The application of a non-linear least square estimation technique has the capability to estimate the parameters of standing wave equations. With limited knowledge of the internal physical parameters (RLC) of the transformer windings, parameters from standing wave equations allow estimation of the source of partial discharge. By transforming the non-linear relationship to a linear relationship between the output response and the parameters of interest the NLSE technique with the Lavenberg-Marquardt algorithm managed to speed up the convergence process to achieve a suitably accurate estimation.

The application of Hilbert Huang Transform and NLSE techniques have demonstrated the possibility of estimating signal propagation levels based on impulse response measurements. This can be done using a superimposition technique, whereby a range in the time domain needs to be specified for the development of a harmonic signal that corresponds to the natural frequency of oscillation of the transformer. The estimation technique is then achieved by specifying the distance x from the neutral to ground connection.

The applicability of a superposition technique with the application of NLSE has been demonstrated. Firstly the NLSE technique with χ^2 convergence algorithm has been shown to provide standing wave solutions. The propagated wave is filtered at different frequencies, decomposed and the summation performed in the time domain. Alternatively, using vector fitting techniques, the transformation of the partial fraction of its transfer function using an inverse Laplace transform yields a superposition solution in the time domain. This is very significant when considering the higher frequency range required for partial discharge estimation. Both the Hilbert Huang Transform and vector fitting have therefore been used in this research.

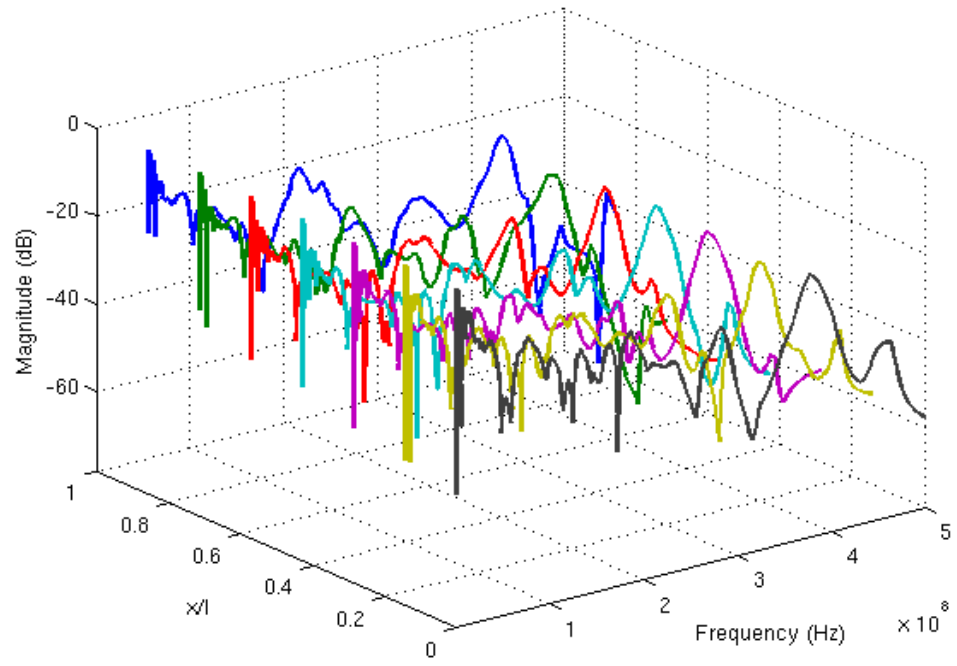

(a) Estimated transfer function using vector fitting

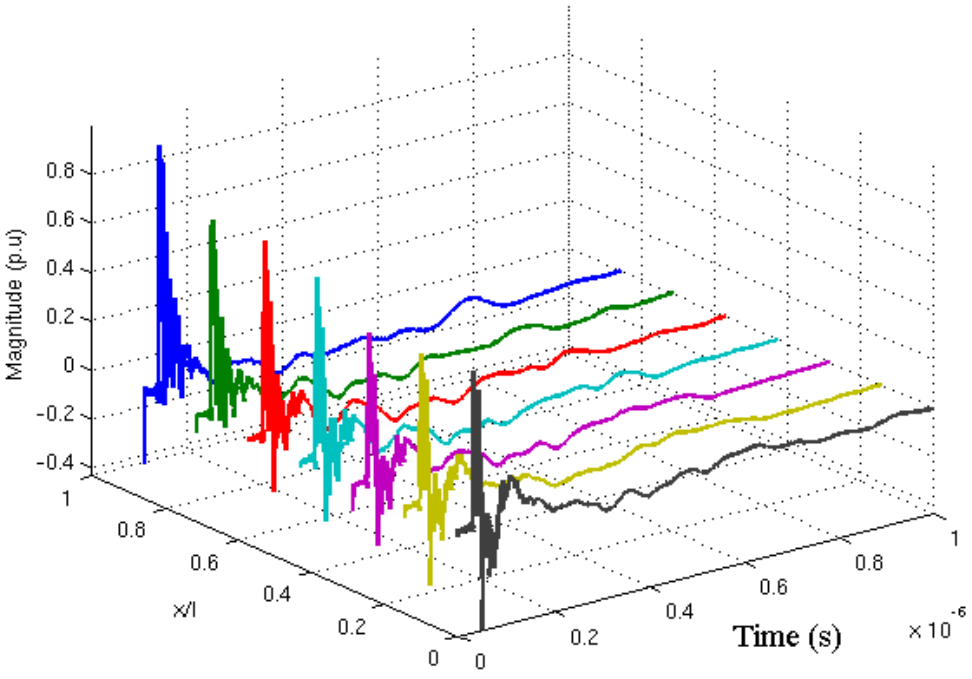

(b) Estimated impulse response using inverse Laplace transform

FIGURE 6.29: Estimated transfer function and inverse Laplace transform using vector fitting from frequency response measurement of interleaved disc winding

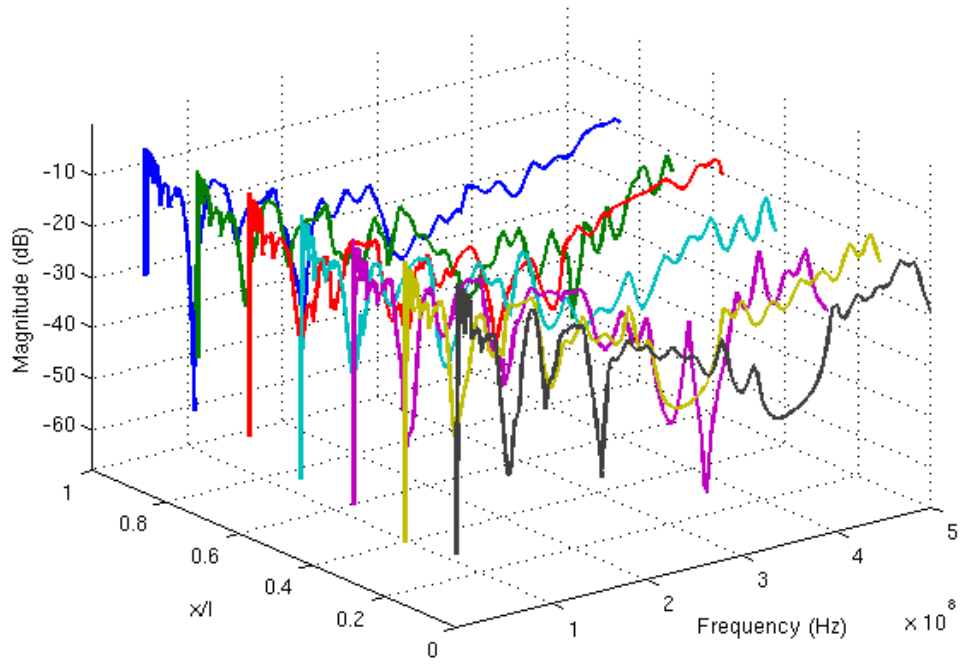

(a) Estimated transfer function using vector fitting

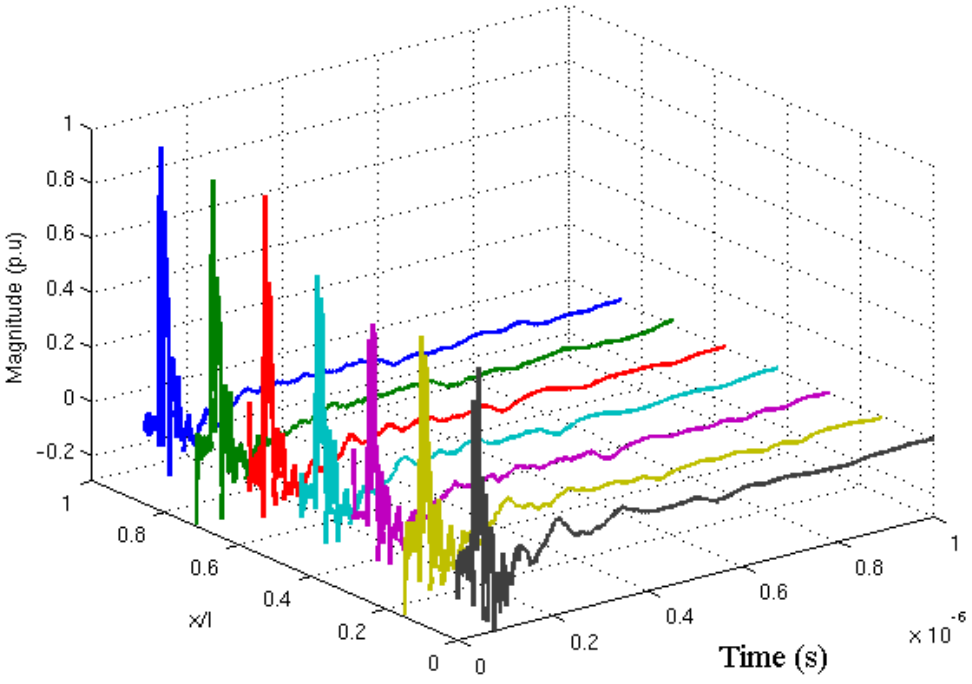

(b) Estimated impulse response using inverse Laplace transform

FIGURE 6.30: Estimated transfer function and inverse Laplace transform using vector fitting from frequency response measurement of plain disc winding

Chapter 7

Partial Discharge Experiments

As demonstrated in Chapter 5, analysis of the propagation of a high frequency transition signal can be divided into two, by considering the transmission line operating region and capacitive operating region. The transmission line operating region is characterised by creating an accumulated harmonic waveform that travels from the source to the terminal winding ends, and the capacitive operating mode is characterised for higher frequency regions by the linear attenuation relationship between bushing and neutral ends of the winding.

This chapter describes experiments undertaken to investigate PD propagation within a transformer winding. The developed experimental procedures considered the way the winding responses have been modelled and derived. Two types of PD source were used, namely surface discharge sources and a void source.

7.1 Partial Discharge Experiment

The use of an RFCT has been demonstrated to be able to capture high frequency transition signals that are proportional to the time derivative of current in a conductor. Hence the RFCT is an ideal sensor to monitor discharge currents at the bushing tap point and neutral to earth point. Thus a technique to extract PD data from the RFCT which has a wide band frequency response is necessary and this approach must be validated experimentally.

7.1.1 PD samples

Figure 7.1 shows three types of PD source used for the test of PD propagation within high voltage transformer windings. Surface discharge in air is simply achieved using a dielectric block on top of the earthed plane electrode. With a polymeric dielectric

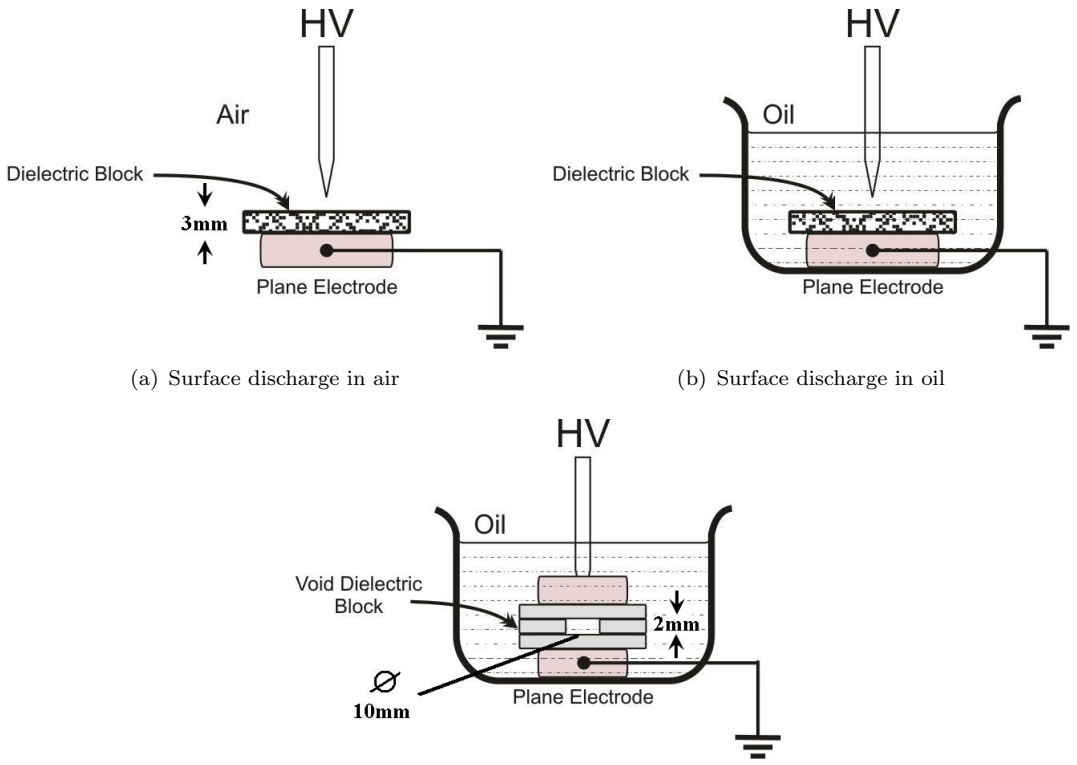

(a) Surface discharge in air

(b) Surface discharge in oil

(c) Partial discharge in void

FIGURE 7.1: PD source from surface discharge and void

material of 3mm thickness, the inception voltage of surface disharge in air is about 5kV. Similarly for surface discharge in oil, using the same material, the inception voltage is 16kV. It was deliberately chosen to produce PDs with a high inception voltage so that the signal to noise ratio (SNR) is very high. A cylindrical void of 10mm diameter and 2mm thickness was made from low-density polyethylene (LDPE) sheet. This was glued to two similar sized sheets to make a void. The PD inception in oil of this type of void was found to be 12kV.

A simple PD experiment is shown in Figure 7.2 using an RFCT and a commercial PD detector. During the test the 200MHz bandwidth RFCT was wrapped with three turns of the earth conductor to improve measurement gain [102]. Digital measurement units were used to display discharges, data storing and analyse collected data. A PD detector unit from OMICRON MTronix with a MPD600 acquisition unit was used to detect PD and to provide calibration measurement of the apparent charge and obtain the original PD pattern. The raw data of the PD pattern from the OMICRON MTronix equipment was stored in binary format, where the PD magnitudes are stored in 32bit format and the time of PD occurence is stored in 64bit format.

Figure 7.3 shows the $\phi - q - n$ pattern of the partial discharge using PD detector for 50 applied cycles. For surface discharge in air the applied voltage was set to 6kV. As can be seen from the Figures, surface discharge in air shows the highest magnitude of

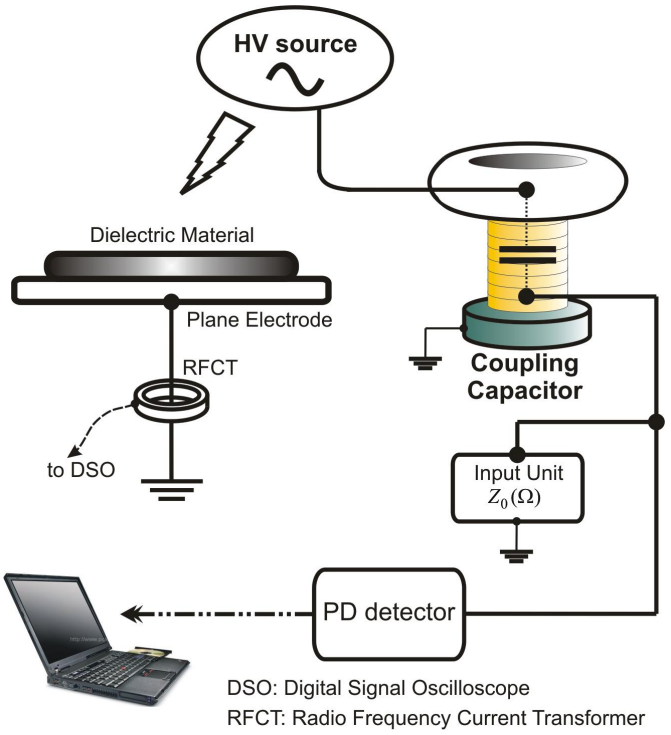

FIGURE 7.2: PD measurement with RFCT

discharges in the positive half cycle. It also shows that the number of PD events is higher for the negative half cycle compared to its positive cycle. As the sample is immersed in transformer oil, the surface discharge is significantly reduced in magnitude and the inception voltage increases to 16kV.

Figures 7.3(c) shows the $\phi - q - n$ pattern for for the 10mm diameter cyclindrical void discharge. The PD pattern is more symmetrical although there are more PD events during the negative half cycle.

7.1.2 PD data extraction from RFCT measurements

The RFCT output was measured using high sampling frequency of 200MS/s (mega sample per second) to ensure good resolution of the signal in the time domain. Due to limitations of the digital monitoring device, the data stored from the monitoring device is limited to 50 cycles for two measurements. This gives a total of 4M data points per cycle. Analysis of the measurement data reveals an average noise level of 1mV peak to peak. Figure 7.4 shows the ground noise level measured by RFCT with its average value shown as a dotted line.

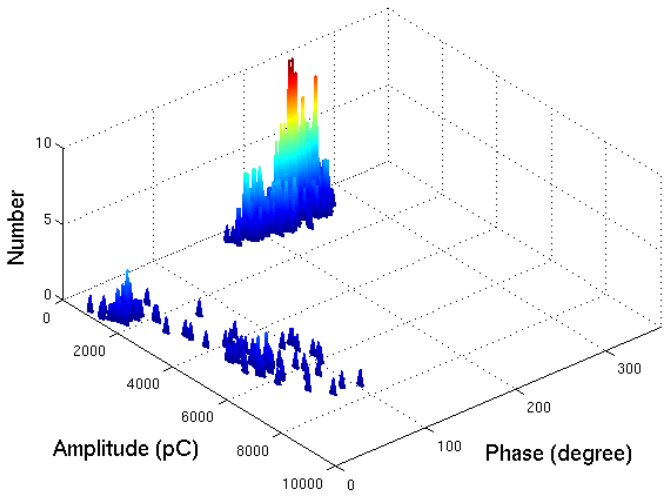

(a) Surface discharge in air

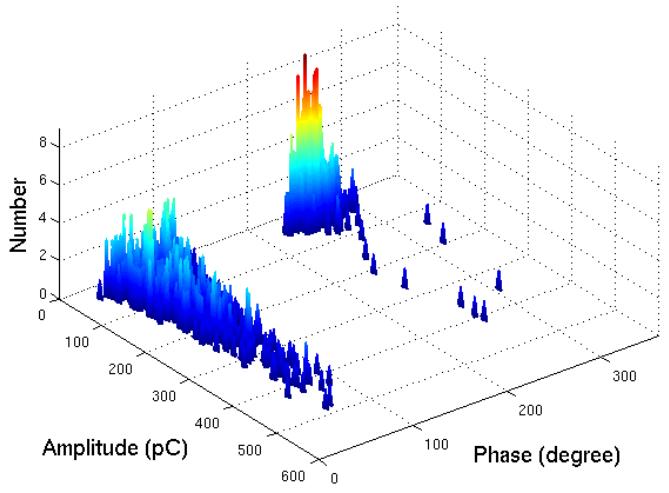

(b) Surface discharge in oil

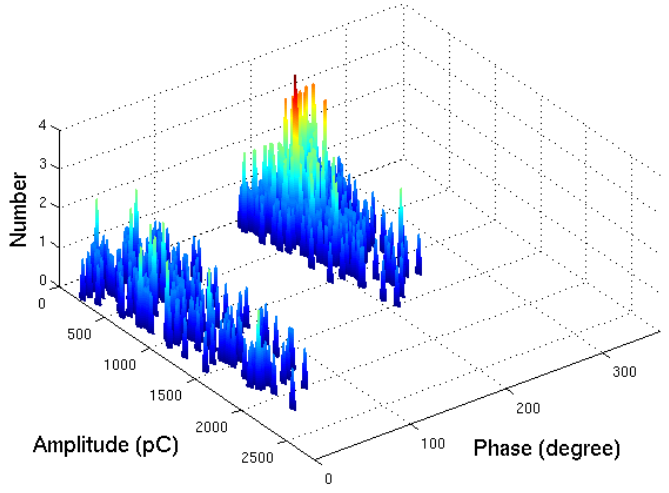

(c) Partial discharge in void

FIGURE 7.3: $\phi - q - n$ pattern of partial discharge using PD detector for over one second period

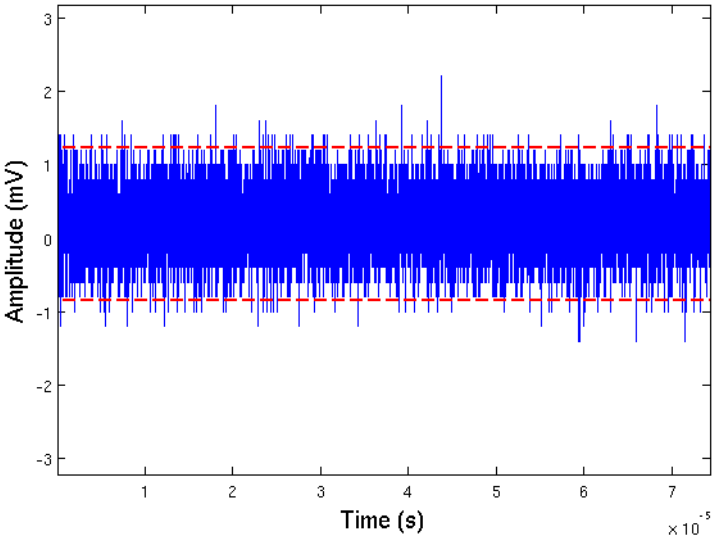

FIGURE 7.4: Noise level measured by RFCT

The key element in PD extraction is the estimate of τ, which is the time duration of the PD occurence. To extract PD signals from the time domain representation a threshold level is set. The threshold is set at $1 \times 10^{-4}\, V^2$. Which then gives the centre of signal energy represented by its maximum level, hence τ is estimated for each PD magnitude above the absolute average line. Figures 7.5 to 7.7 show the result of signal extraction of PD signals from the RFCT measurement data.

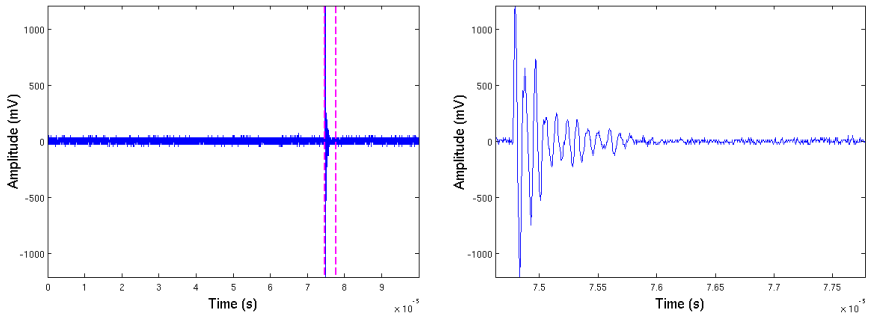

(a) Time domain

(b) Extracted PD

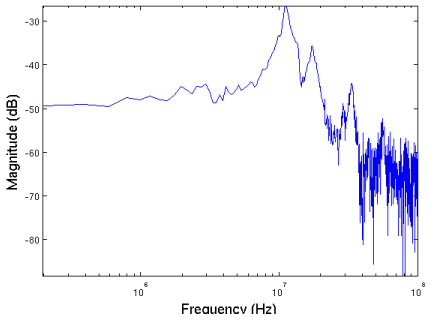

(c) Spectral density plot diagram

FIGURE 7.5: PD extraction and spectral density plot diagram from surface discharge in air

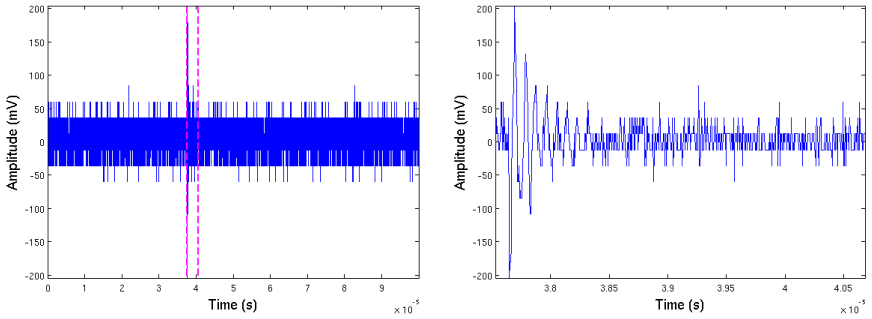

(a) Time domain (b) Extracted PD

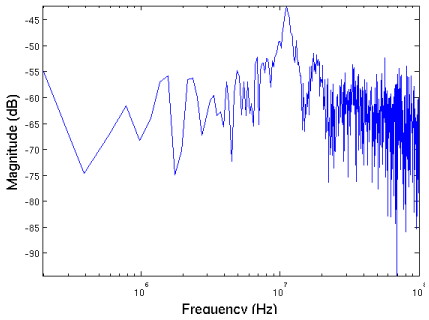

(c) Spectral density plot diagram

FIGURE 7.6: PD extraction and spectral density plot diagram from surface discharge in oil

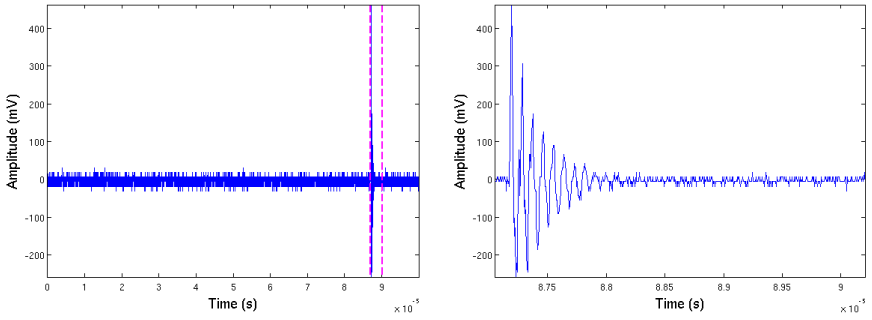

(a) Time domain (b) Extracted PD

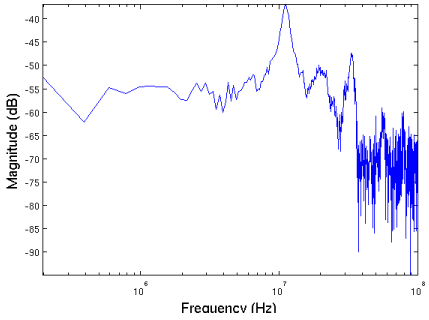

(c) Spectral density plot diagram

FIGURE 7.7: Signal extraction and spectral density plot diagram from PD in void

7.2 PD measurement on transformer

This section investigates different configurations to measure PDs on the transformer model winding with current calibration from the RFCT for real charge calculation. There are two types of PD measurements for charge calculation, current calibration by shunt resistors and current calibration using a comercial PD detector. The main sensor under investigation is the RFCT which has a bandwidth up to 200MHz [102]. The circuit configurations are based on the analytical model derived in Chapter 3 and Chapter 4 for winding distribution and the split winding analysis respectively.

7.2.1 Current calibration by shunt resistor

Figure 7.8 shows the circuit arrangement for current calibration using a shunt resistor. Every line of current measurement is connected via an impedance $Z_b(p)$, $Z_{x'}(p)$ and $Z_n(p)$ where these impedances are used to calibrate for current flowing through the RFCTs. The circuit configuration for the impedance current measurement on the low voltage side is shown in Figure 7.9

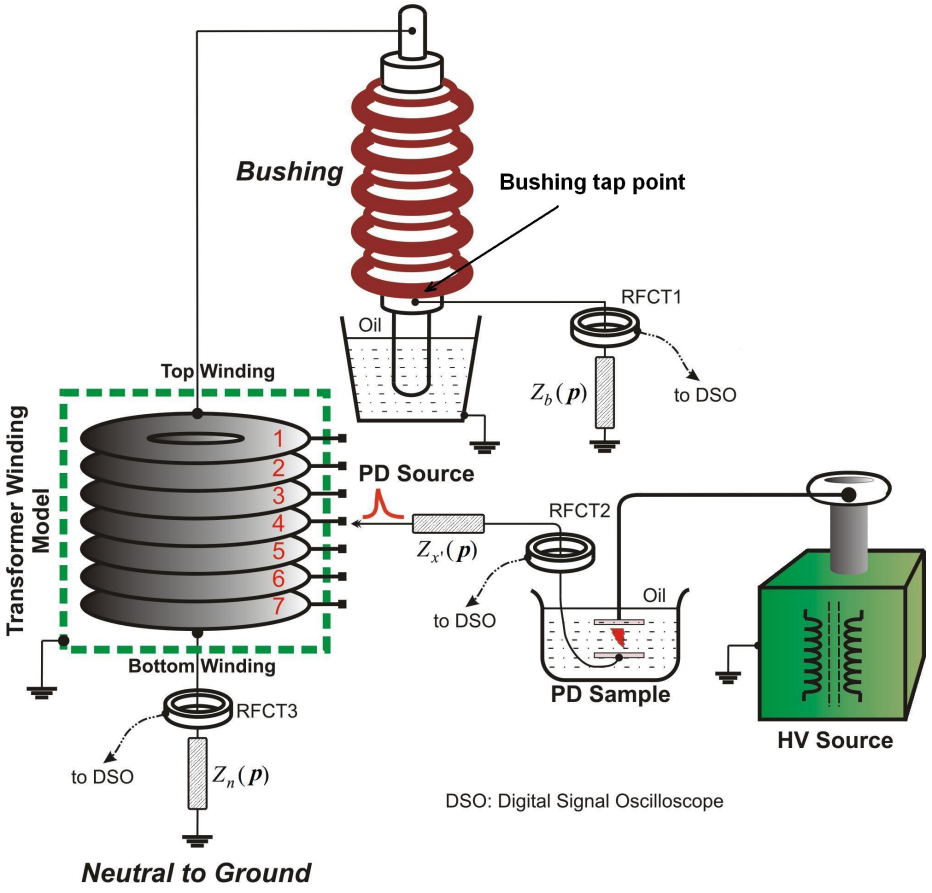

FIGURE 7.8: Partial discharge measurement and current calibration using impedance measurement

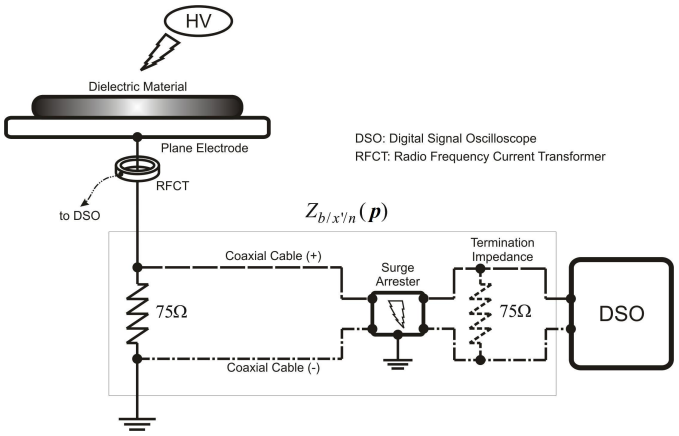

FIGURE 7.9: Schematic diagram for current calibration using $Z_{b/x'/n}(p)$

A 75Ω resistor is used to match the characteristic impedance of the coaxial cable. As discharges occur on or within the dielectric material under test, the PD current will flow through the RFCT and 75Ω resistor. This will create a potential difference between the Coaxial Cable (+) and the Coaxial Cable (-). Thus a potential difference can be measured using the digital signal oscilloscope (DSO). The amount of current that flows in the resistor is determined using Ohm's law and therefore the total charge that flows in the resistor is the same as the total charge flowing through the RFCT secondary circuit. Where total charge can be calculated by:

$$Q = \int_{-\infty}^{\infty} I\,dt \tag{7.1}$$

The 75Ω termination impedance is an optional choice of impedance that can be placed near the DSO. It is used to reduce the reflection of signals from the ground level through coaxial cable (-) to the DSO for current measurement.

With reference to Figure 7.8, during a test, a 50Hz a.c voltage is applied to the PD sample via the high voltage side electrode. When the test voltage rises to a certain value (less than 20kV), a partial discharge occurs on or within the dielectric material. Consequently the discharge signal travels to the low voltage plane electrode, via RFCT2 and into the transformer winding model. The signal then divides heading towards the neutral to ground connection and towards the bushing tap point. At the bushing tap point the discharge signal is transfered to the bushing core bar and the high frequency components of the discharge signals pass through the bushing to reach the bushing tap point. Figures 7.10 to 7.25 show examples of PD voltage waveforms across the shunt resistors and the PD current waveforms through the RFCTs for the PD injection onto the plain winding. The PD current is then calibrated into its equivalent charge using the shunt resistor measurement, where it is found that 10pC is approximately equivalent to 5mV from RFCT.

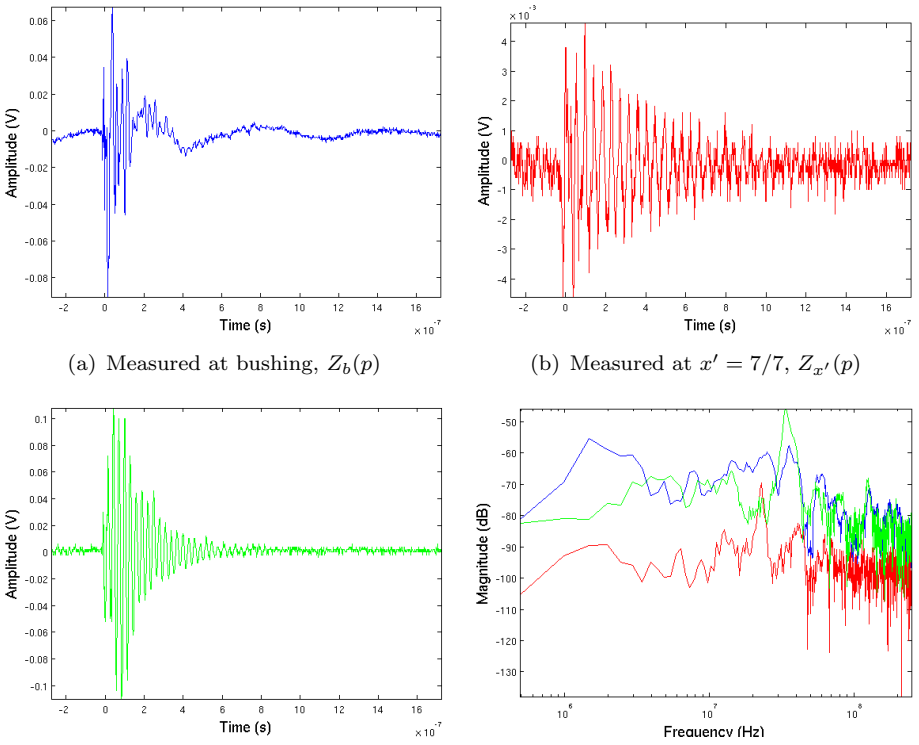

(a) Measured at bushing, $Z_b(p)$ (b) Measured at $x' = 7/7$, $Z_{x'}(p)$

(c) Measured at neutral, $Z_n(p)$ (d) Spectral density plot diagram

FIGURE 7.10: Voltage signal extraction across the shunt resistor and spectral density plot from surface discharge in oil injected at $x' = 7/7$

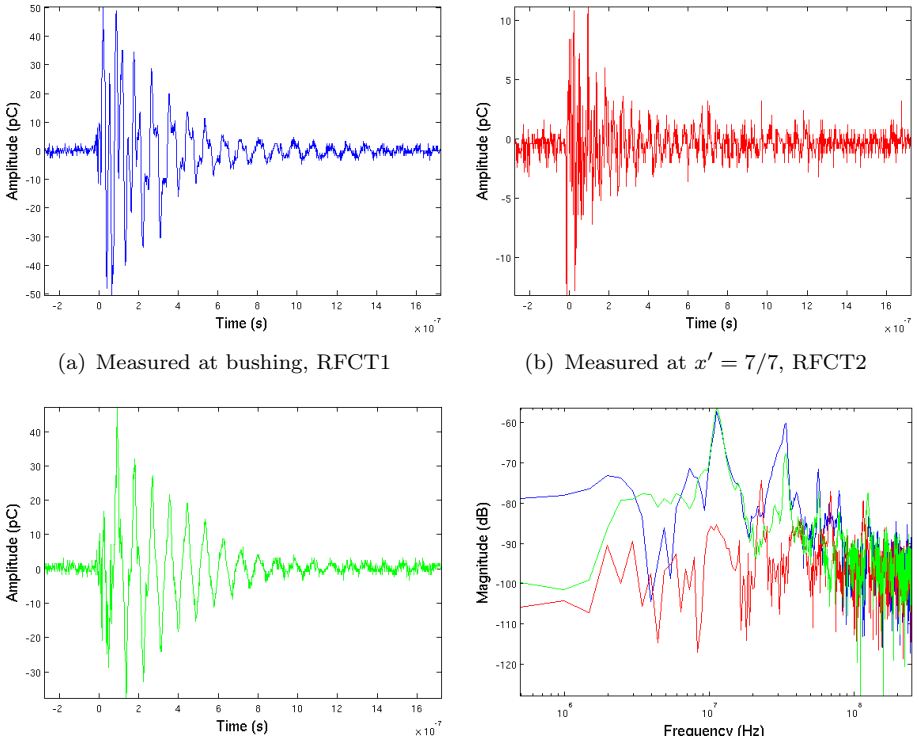

(a) Measured at bushing, RFCT1 (b) Measured at $x' = 7/7$, RFCT2

(c) Measured at neutral, RFCT3 (d) Spectral density plot diagram

FIGURE 7.11: Current signal extraction measured using RFCTs and spectral density plot from surface discharge in oil injected at $x' = 7/7$, with 5mV equals to 10pC

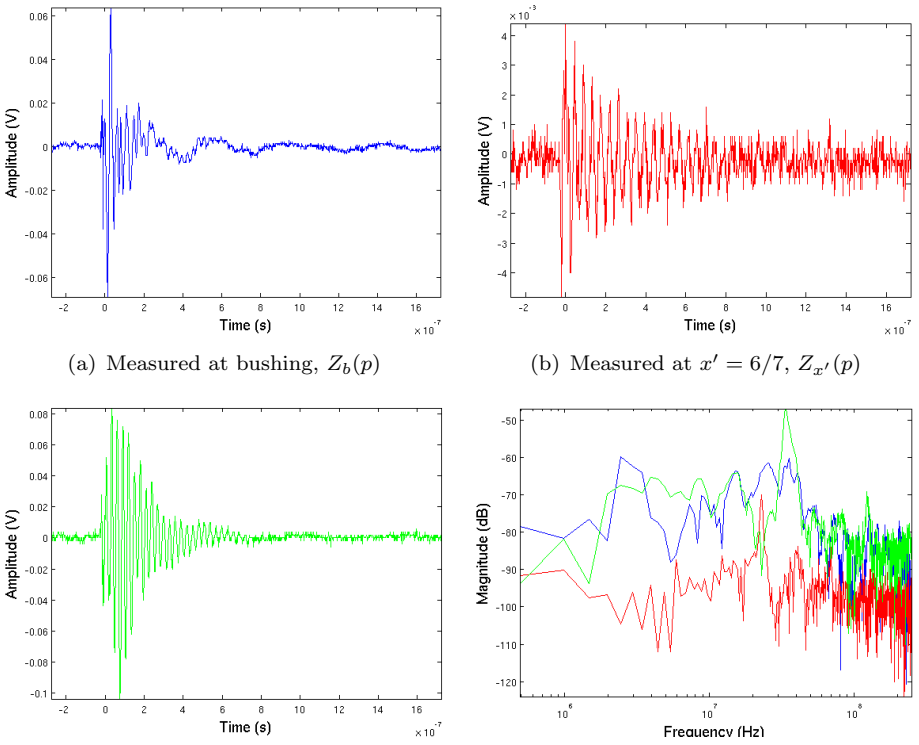

(a) Measured at bushing, $Z_b(p)$ (b) Measured at $x' = 6/7$, $Z_{x'}(p)$

(c) Measured at neutral, $Z_n(p)$ (d) Spectral density plot diagram

FIGURE 7.12: Voltage signal extraction across the shunt resistor and spectral density plot from surface discharge in oil injected at $x' = 6/7$

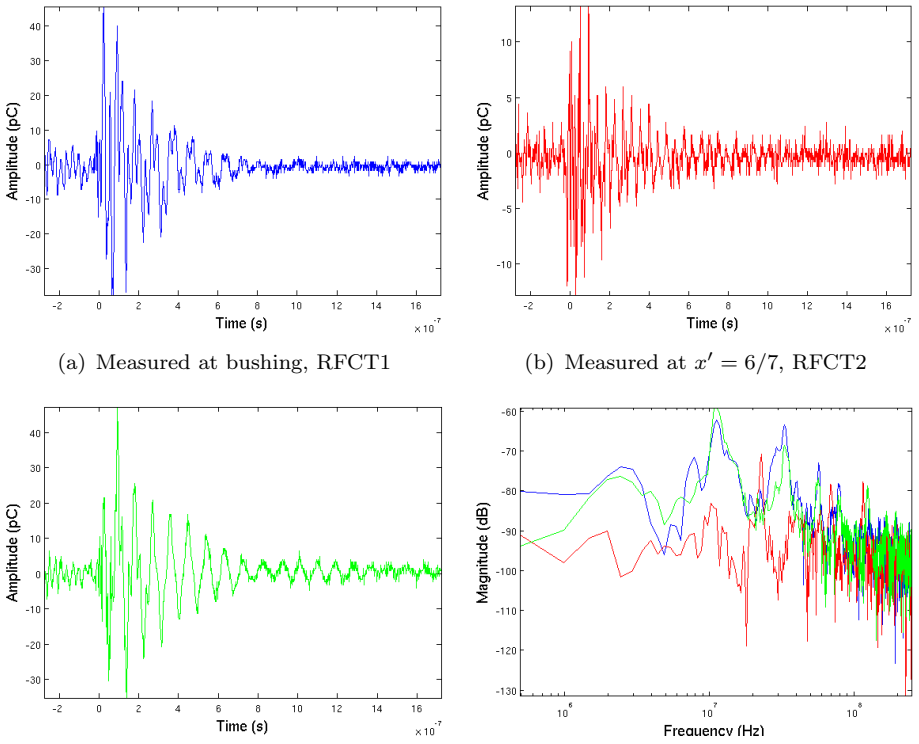

(a) Measured at bushing, RFCT1 (b) Measured at $x' = 6/7$, RFCT2

(c) Measured at neutral, RFCT3 (d) Spectral density plot diagram

FIGURE 7.13: Current signal extraction measured using RFCTs and spectral density plot from surface discharge in oil injected at $x' = 6/7$, with 5mV equals to 10pC

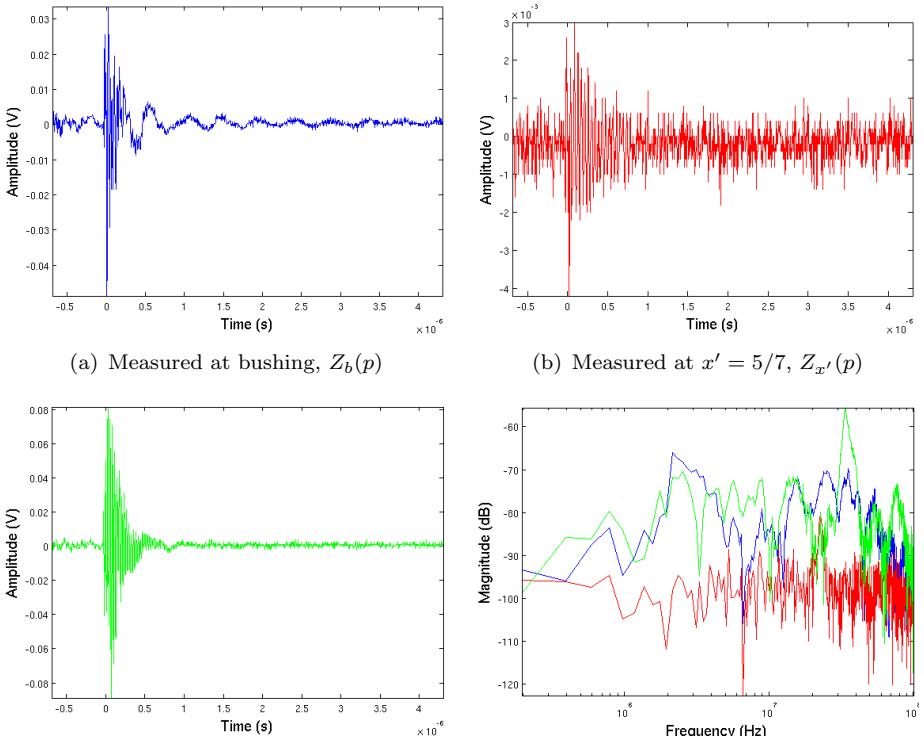

(a) Measured at bushing, $Z_b(p)$ (b) Measured at $x' = 5/7$, $Z_{x'}(p)$

(c) Measured at neutral, $Z_n(p)$ (d) Spectral density plot diagram

FIGURE 7.14: Voltage signal extraction across the shunt resistor and spectral density plot from surface discharge in oil injected at $x' = 5/7$

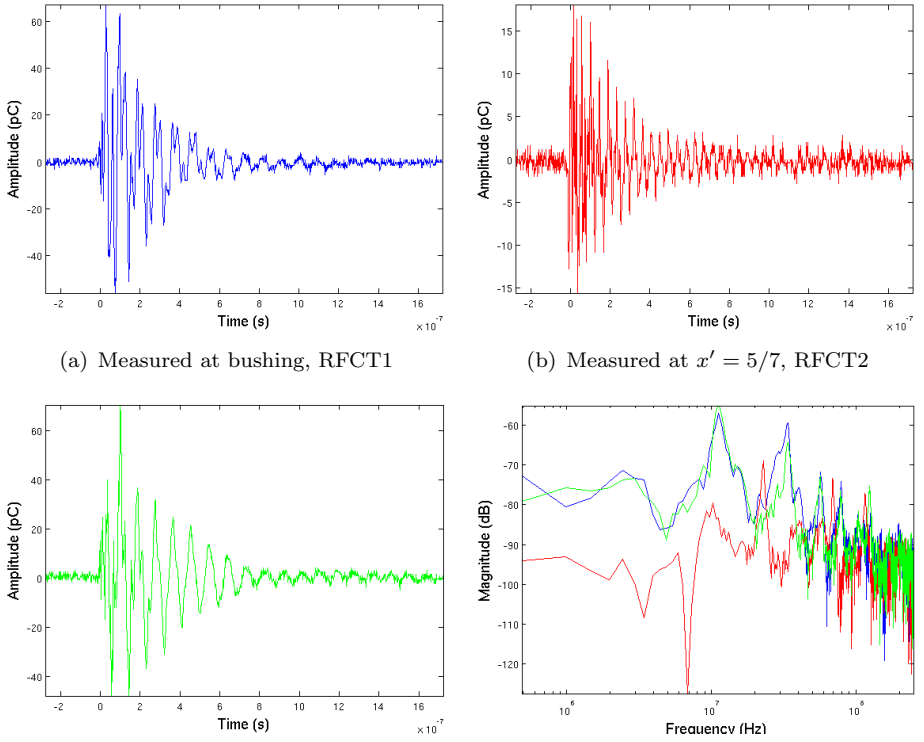

(a) Measured at bushing, RFCT1 (b) Measured at $x' = 5/7$, RFCT2

(c) Measured at neutral, RFCT3 (d) Spectral density plot diagram

FIGURE 7.15: Current signal extraction measured using RFCTs and spectral density plot from surface discharge in oil injected at $x' = 5/7$, with 5mV equals to 10pC

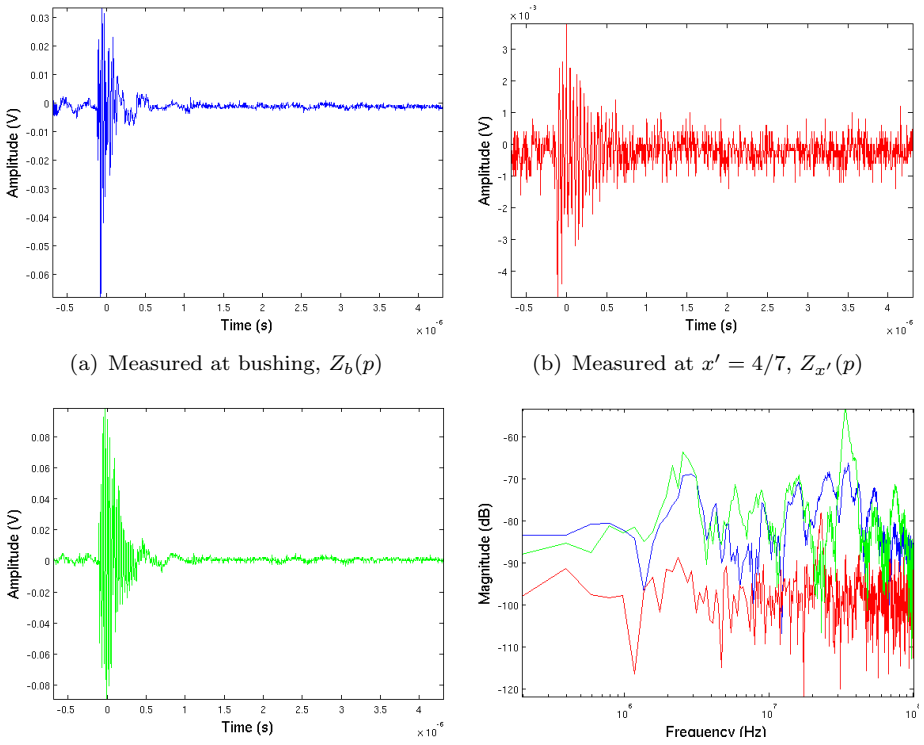

(a) Measured at bushing, $Z_b(p)$ (b) Measured at $x' = 4/7$, $Z_{x'}(p)$

(c) Measured at neutral, $Z_n(p)$ (d) Spectral density plot diagram

FIGURE 7.16: Voltage signal extraction across the shunt resistor and spectral density plot from surface discharge in oil injected at $x' = 4/7$

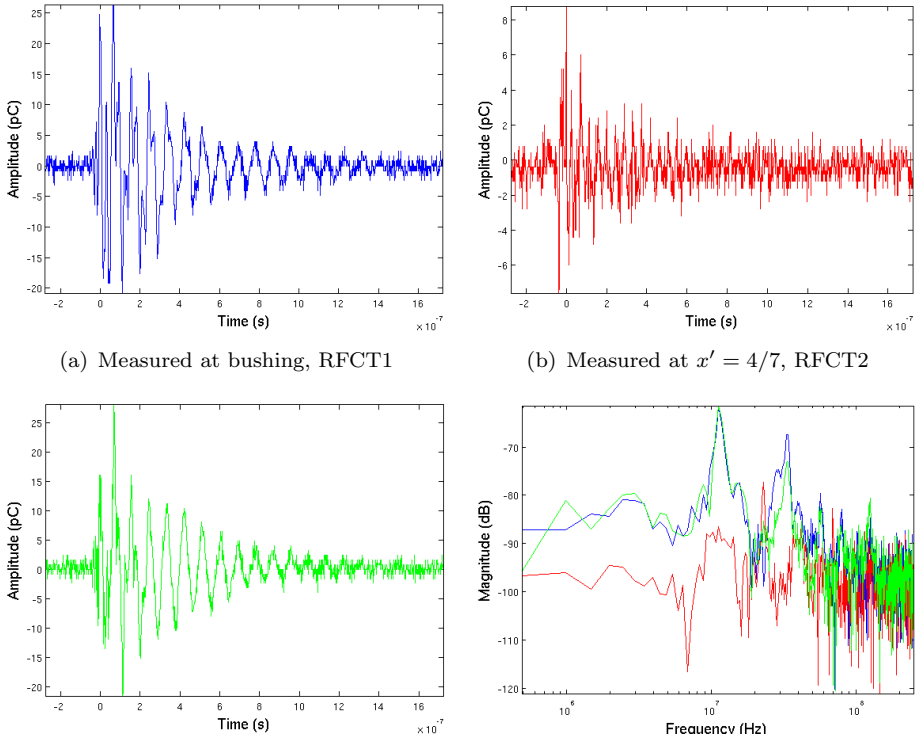

(a) Measured at bushing, RFCT1 (b) Measured at $x' = 4/7$, RFCT2

(c) Measured at neutral, RFCT3 (d) Spectral density plot diagram

FIGURE 7.17: Current signal extraction measured using RFCTs and spectral density plot from surface discharge in oil injected at $x' = 4/7$, with 5mV equals to 10pC

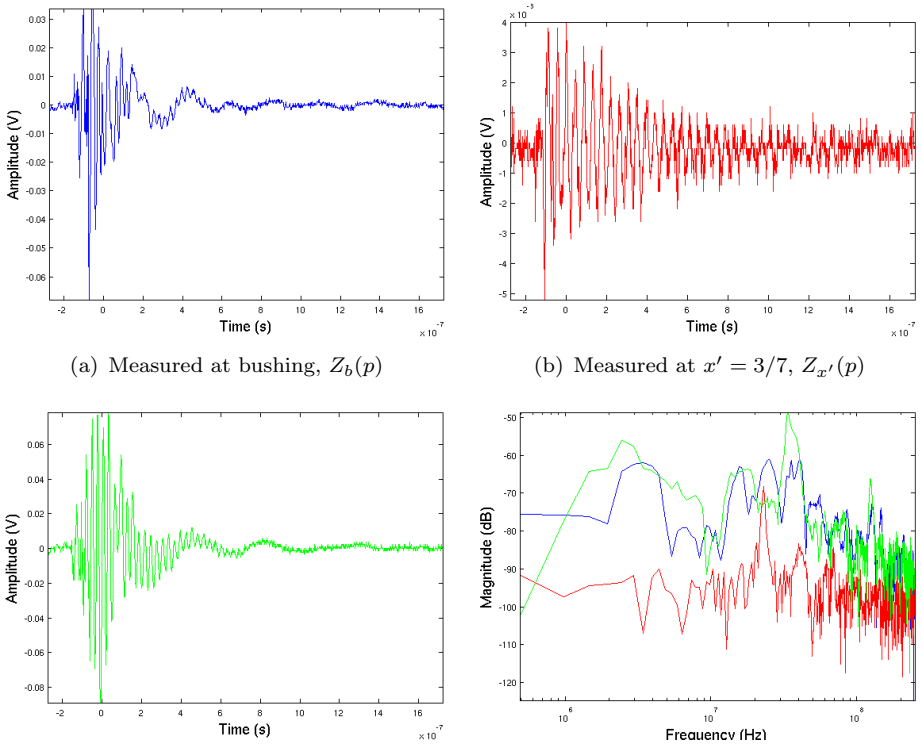

(a) Measured at bushing, $Z_b(p)$ (b) Measured at $x' = 3/7$, $Z_{x'}(p)$

(c) Measured at neutral, $Z_n(p)$ (d) Spectral density plot diagram

FIGURE 7.18: Voltage signal extraction across the shunt resistor and spectral density plot from surface discharge in oil injected at $x' = 3/7$

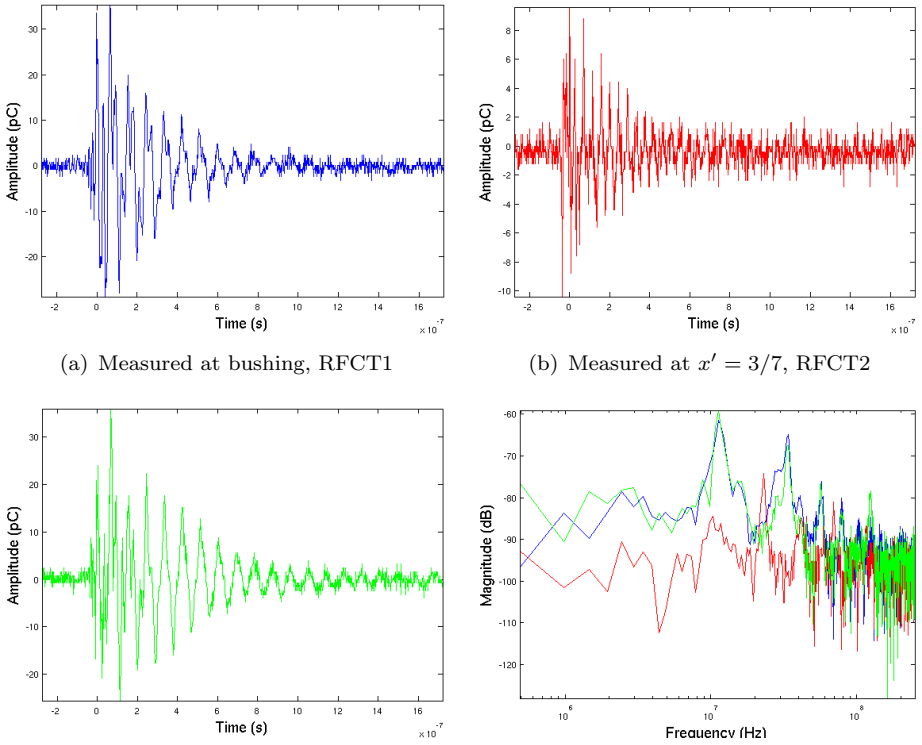

(a) Measured at bushing, RFCT1 (b) Measured at $x' = 3/7$, RFCT2

(c) Measured at neutral, RFCT3 (d) Spectral density plot diagram

FIGURE 7.19: Current signal extraction measured using RFCTs and spectral density plot from surface discharge in oil injected at $x' = 3/7$, with 5mV equals to 10pC

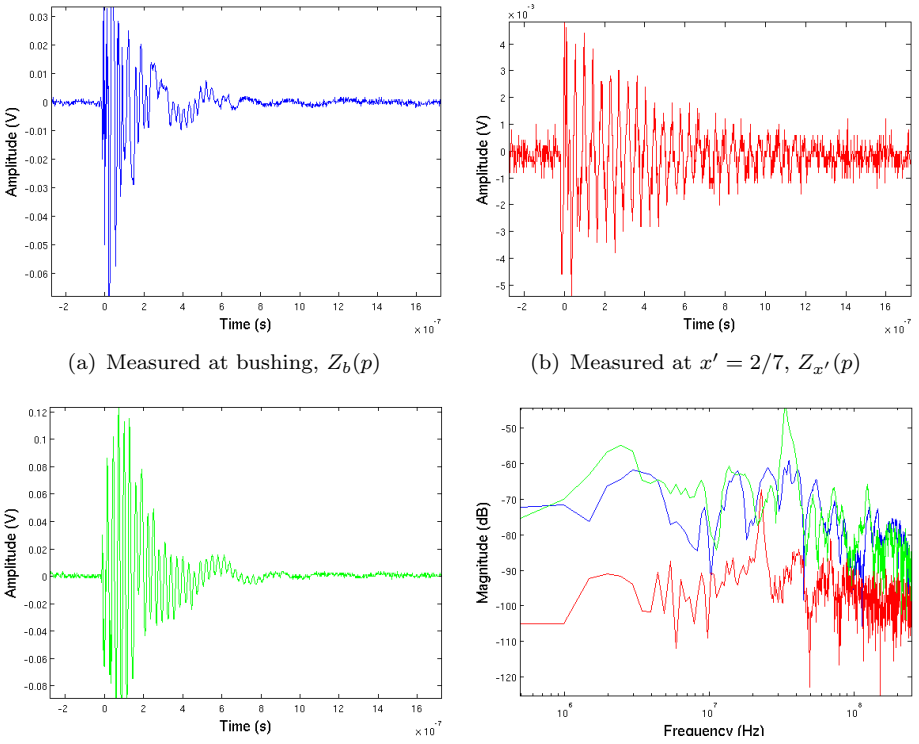

(a) Measured at bushing, $Z_b(p)$

(b) Measured at $x' = 2/7$, $Z_{x'}(p)$

(c) Measured at neutral, $Z_n(p)$

(d) Spectral density plot diagram

FIGURE 7.20: Voltage signal extraction across the shunt resistor and spectral density plot from surface discharge in oil injected at $x' = 2/7$

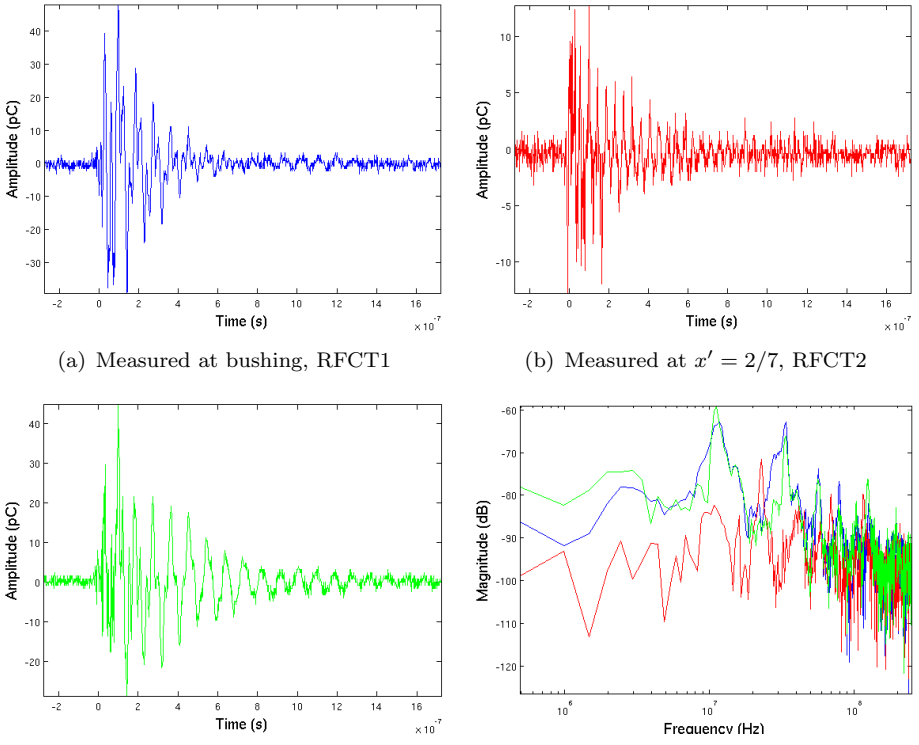

(a) Measured at bushing, RFCT1

(b) Measured at $x' = 2/7$, RFCT2

(c) Measured at neutral, RFCT3

(d) Spectral density plot diagram

FIGURE 7.21: Current signal extraction measured using RFCTs and spectral density plot from surface discharge in oil injected at $x' = 2/7$, with 5mV equals to 10pC

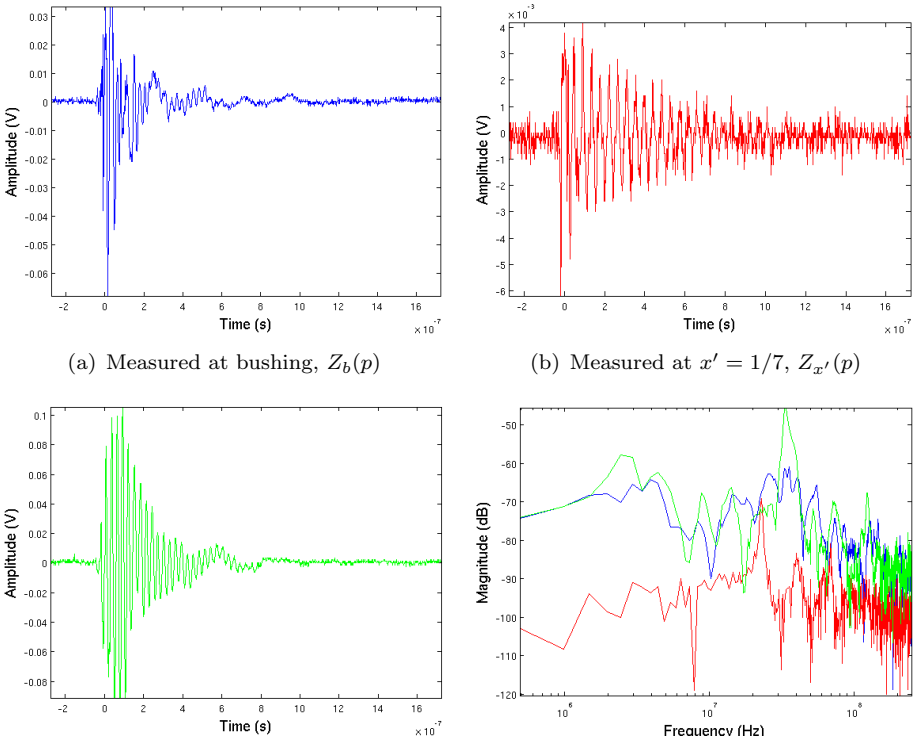

(a) Measured at bushing, $Z_b(p)$ (b) Measured at $x' = 1/7$, $Z_{x'}(p)$

(c) Measured at neutral, $Z_n(p)$ (d) Spectral density plot diagram

FIGURE 7.22: Voltage signal extraction across the shunt resistor and spectral density plot from surface discharge in oil injected at $x' = 1/7$

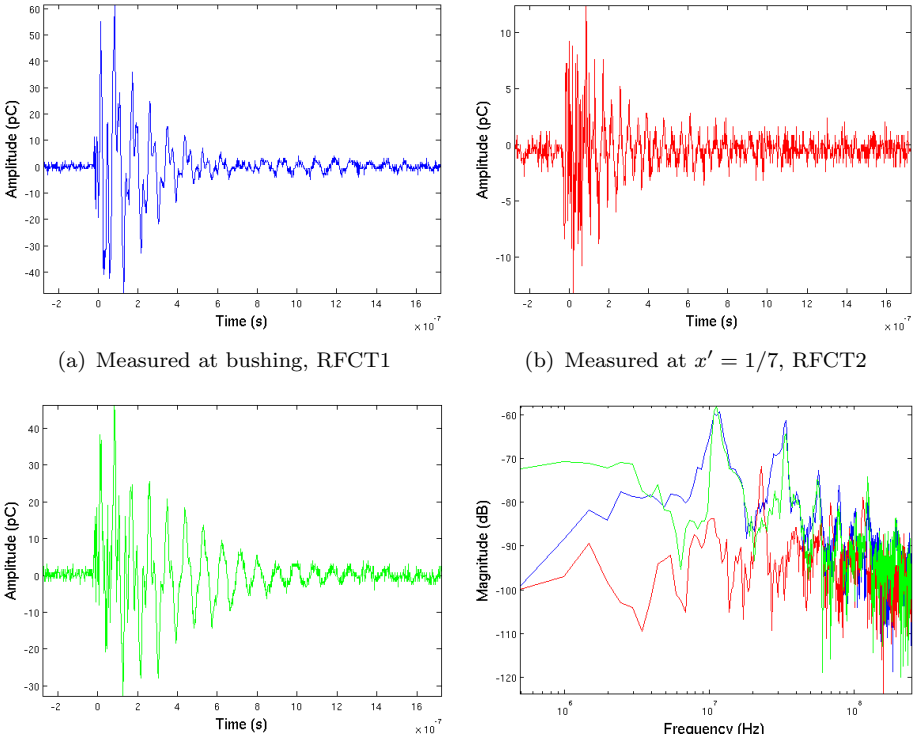

(a) Measured at bushing, RFCT1 (b) Measured at $x' = 1/7$, RFCT2

(c) Measured at neutral, RFCT3 (d) Spectral density plot diagram

FIGURE 7.23: Current signal extraction measured using RFCTs and spectral density plot from surface discharge in oil injected at $x' = 1/7$, with 5mV equals to 10pC

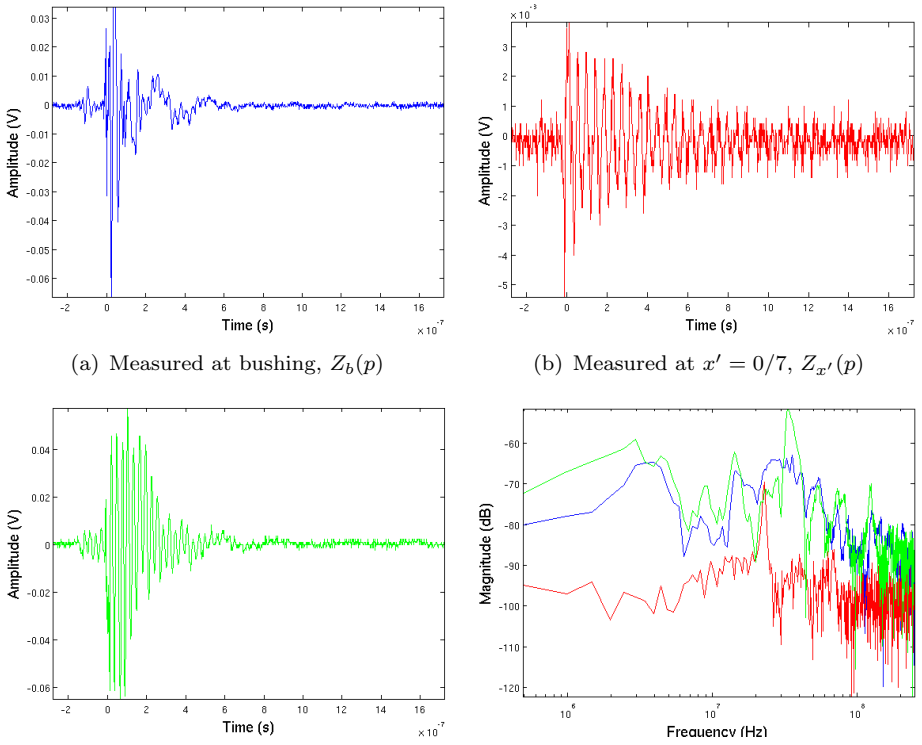

(a) Measured at bushing, $Z_b(p)$ (b) Measured at $x' = 0/7$, $Z_{x'}(p)$

(c) Measured at neutral, $Z_n(p)$ (d) Spectral density plot diagram

FIGURE 7.24: Voltage signal extraction across the shunt resistor and spectral density plot from surface discharge in oil injected at $x' = 0/7$

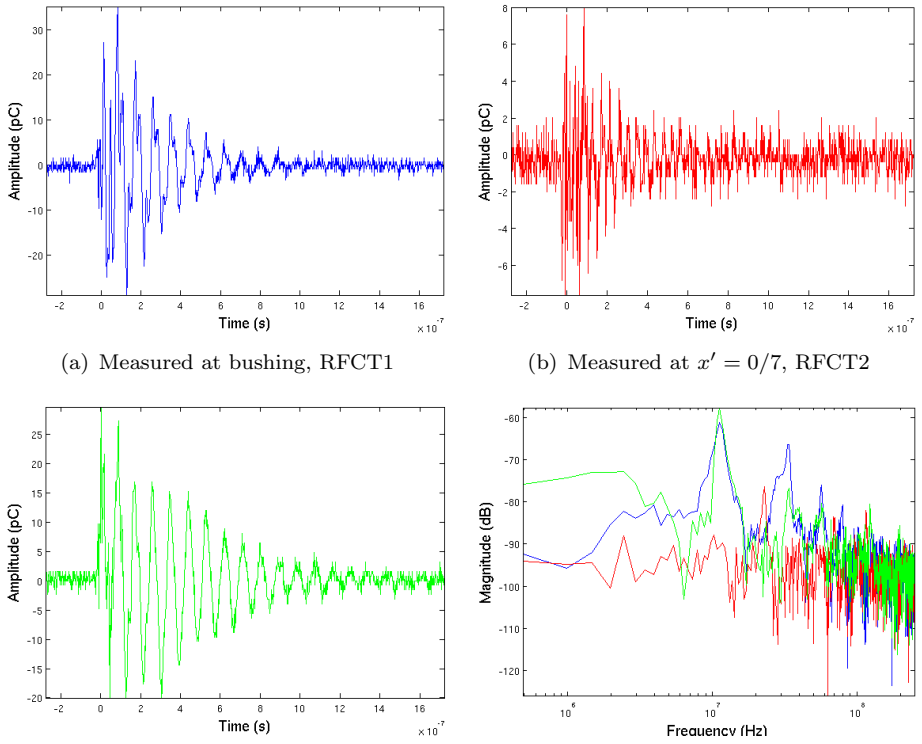

(a) Measured at bushing, RFCT1 (b) Measured at $x' = 0/7$, RFCT2

(c) Measured at neutral, RFCT3 (d) Spectral density plot diagram

FIGURE 7.25: Current signal extraction measured using RFCTs and spectral density plot from surface discharge in oil injected at $x' = 0/7$, with 5mV equals to 10pC

7.2.2 Current calibration by PD detector

The circuit configuration of Figure 7.8 is a suitable arrangement for PD injection from a PD sample into the transformer winding. Without using the shunt resistor the calculation of current is possible and may also be better, through using a commercial PD detector with an arrangement as shown in Figure 7.2. To further investigate PD propagation along a transformer winding, Figure 7.26 shows PD measurement on a high voltage transformer model using five RFCTs. The only difference from the earlier circuit configuration is an additional current wire to ground connection from point of source x' through RFCT4. The reason for this ground connection is to measure a current due to the influence of the winding configuration at the source point x'. However before setting up the experimental arrangement, a frequency response measurement of the bushing and the RFCTs were undertaken in order to investigate the responses at high frequency. Figure 7.27 shows the frequency response of the five RFCTs with the secondary conductor wrapped three times around the RFCT core. The Figure shows that the RFCTs are very similar and have a close frequency response up to 200MHz. Figure 7.28 shows the frequency response of the 60kV bushing the winding with and without RFCT1.

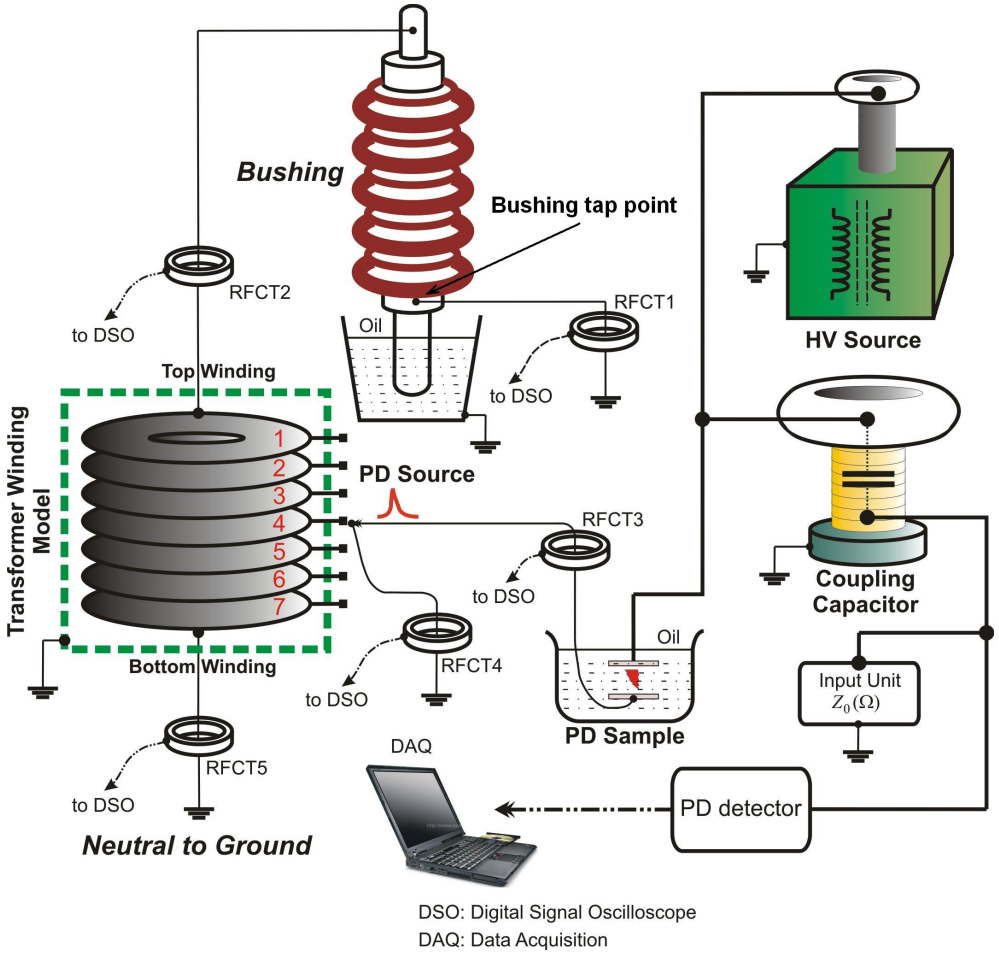

FIGURE 7.26: Schematic diagram for PD measurement with five RFCTs

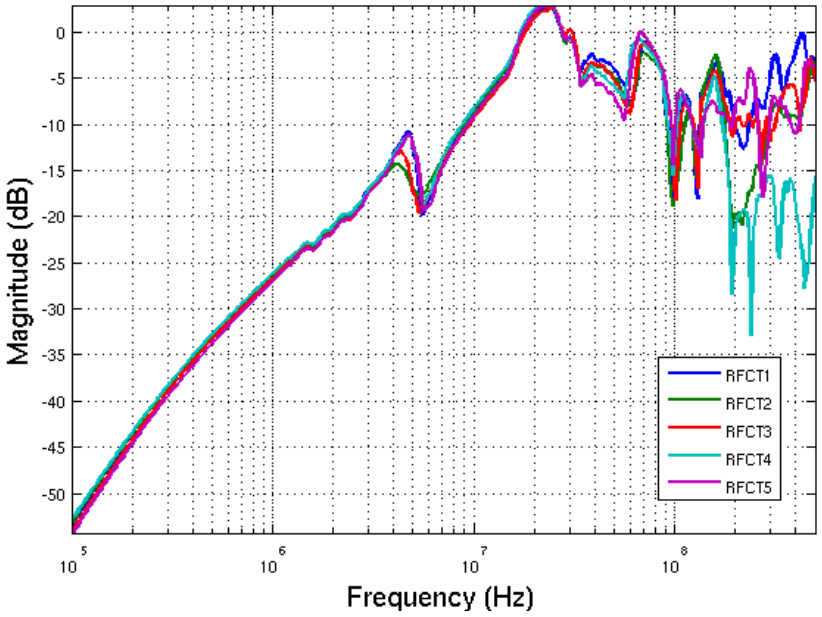

FIGURE 7.27: RFCTs and their frequency response

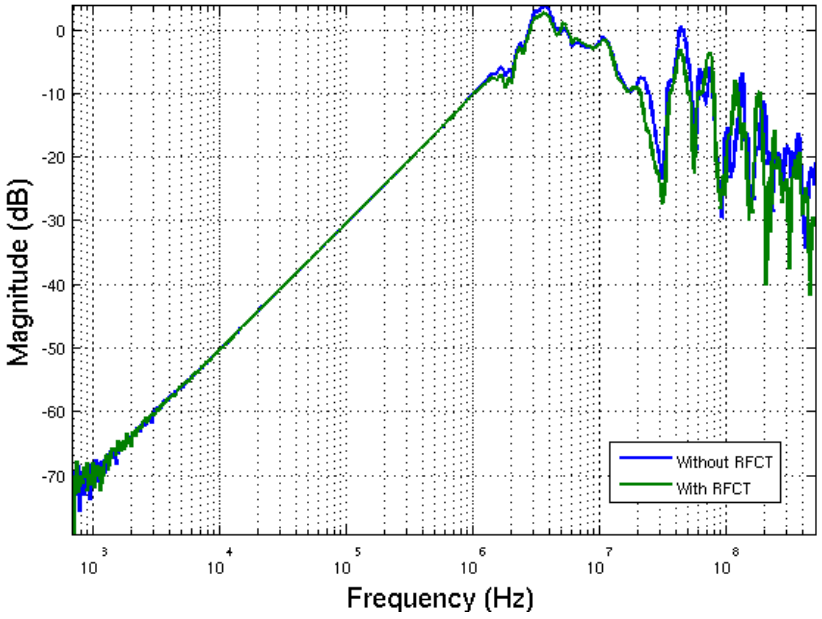

FIGURE 7.28: 60kV bushing and its frequency response with and without RFCT1

The response of the bushing also shows a similar pattern acting as a high pass filter and its response is similar to the response of the RFCT. The comparison of bushing frequency response with and without RFCT shows minimal effect on the overall response at high frequency. This indicates that the presence of the RFCT will not change high frequency signal propagation through the bushing and these frequency components can be detected by RFCT1. In addition, prior to the PD experiment, the bushing was tested by applying a 45kV, 50Hz, high voltage supply to verify that the bushing is PD free at the voltages used in this experiment.

The calibration of the PD from the RFCT measurement was achieved by comparing the magnitude measurement from the PD detector and RFCT3. RFCT3 was chosen because it is monitoring the discharge current that flows before entering the transformer winding. To investigate the calibration process a circuit arrangement without the source connection at x' to the ground (no RFCT4) was carried out for PD injection into the transformer winding using PDs from surface discharge in air and PD from void discharge. Figure 7.29 shows an example of PD comparison measured by PD detector and RFCT3 of surface discharge applied at $x' = 3/7$ onto the plain winding. The ratio for calibration has found from the noise 'floor' at 3mV to be approximately equivalent to 9pC.

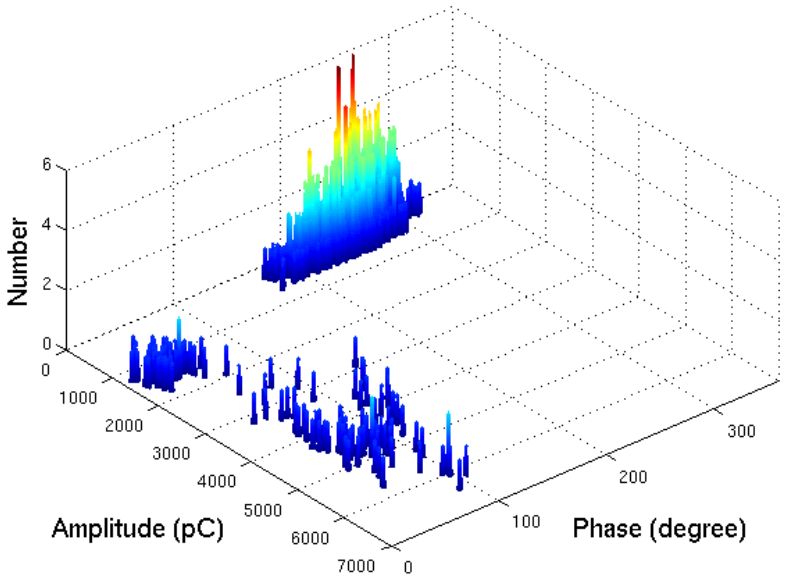

(a) Measured by PD detector

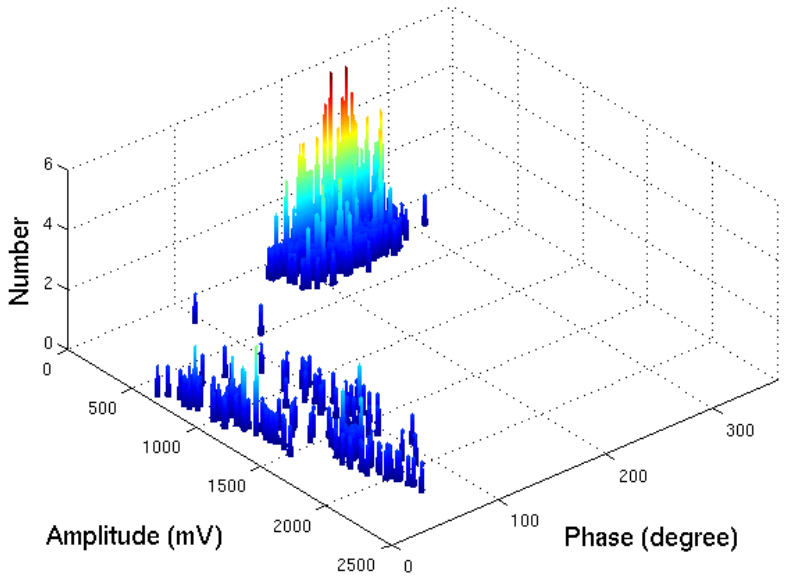

(b) Measured by RFCT3

FIGURE 7.29: Surface discharge calibration with PD detector, injection at $x' = 3/7$ on plain winding: 3mV $\approx$ 9pC, 50 applied cycles

Figure 7.30 shows an example of PD calibration using the PD detector for a void partial discharge injected into the interleaved winding. By applying the PD at $x' = 3/7$ the PD calibration on RFCT3 was found to be 5mV to 20pC.

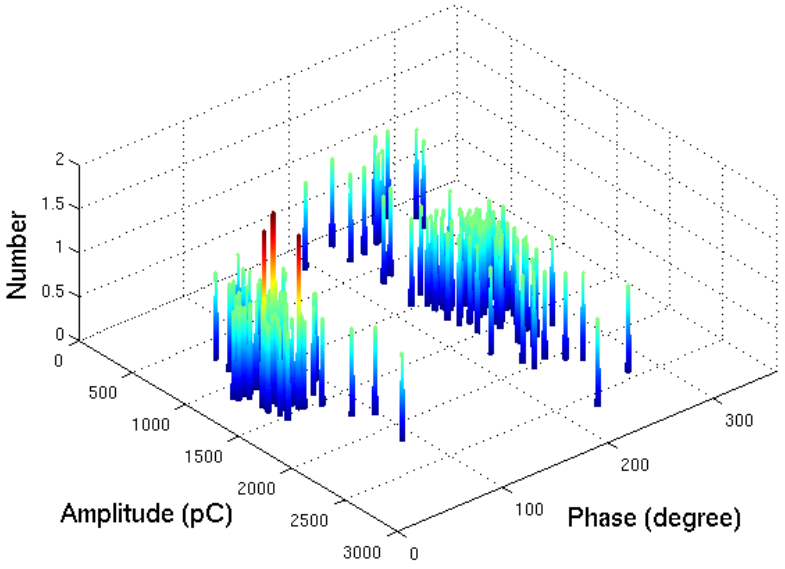

(a) Measured by PD detector

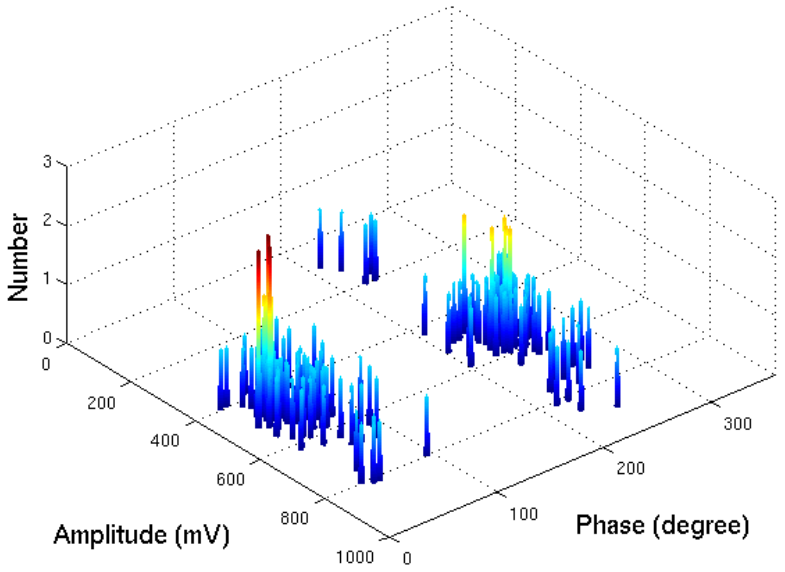

(b) Measured by RFCT3

FIGURE 7.30: Partial discharge in void calibrated with PD detector, injection at $x' = 3/7$ on interleaved winding: 5mV $\approx$ 20pC, 50 applied cycles

7.3 Comparison of Terminal Measurements

Comparison of terminal measurements for the circuit arrangement of Figure 7.26 are essential in order to estimate the PD levels at the source position within the winding. PDs from surface discharge in air are used to investigate the level of PD at different positions. Figure 7.31 shows a measurement of surface discharge based on $\phi - q - n$ pattern measured at the top of the plain winding from RFCT1, RFCT2 and RFCT4 for PD injection at $x' = 7/7$.

All three RFCTs were triggered on the oscilloscope with a zero crossing detector circuit attached to the high voltage source. Comparing the three, RFCT1 shows the lowest magnitude measured at the bushing with a maximum value of 100mV during its positive half cycle. As the PD current flows through RFCT2 and is detected by RFCT1 at the bushing, most of the measured PD magnitudes are attenuated to a lower value. This is due to the property of the bushing as shown in Figure 7.28 which allows the high frequency signals components to pass through it to the tap point. This can be clearly seen in Figure 7.32(b) for a single PD spectrum level in frequecy domain measured by RFCT1 and RFCT2. The level of gain from 300kHz to 2MHz shows a close agreement in gain magnitude between RFCT1 and RFCT2, however at 3MHz to 30MHz frequency range shows that the gain of RFCT2 is much higher compared to RFCT1.

The level of PDs measured using RFCT2 and RFCT4 shows almost the same level of magnitude. Where the range of PD magnitude detected is between 50mV to 250mV in its positive cycle and 5mV to 50mV in its negative cycle. The similar range is due to the position of PD injection at $x' = 7/7$ (at the top of winding). Examining the frequency domains as shown in Figure 7.32(c) reveals that the gain level measured by RFCT2 and RFCT4 is very similar especially at higher frequencies.

A comparison of the PD signal measured at the top of the transformer winding, the source and neutral to ground connection is shown in Figure 7.33. A surface discharge in air signal was injected at terminal $x' = 4/7$ on the plain winding. The PD magnitudes are compared for the measurement at RFCT2, RFCT4 and RFCT5. RFCT4 is the level of PD under the influence of the local ground connection at the source. By comparing the three measurments, the measurement at the source to ground shows the highest magnitudes of PD. However, the patterns of measured PD at the terminal ends ($x = 7/7$ and $x = 0/7$) shows almost the same level of PD.

Figure 7.34 shows two measurements of PD signals from RFCT3 and RFCT4. There is a large difference in magnitude between the two RFCTs measuring the same source at $x' = 3/7$. Due to the influence of the circuit configuration, RFCT4 measured magnitudes are approximately half the values of PDs detected by RFCT3. This can be clearly seen in the frequency domain as Figure 7.35 shows that at high frequencies above 10MHz, the PD signal measured by RFCT3 has a higher magnitudes compared to the PD source

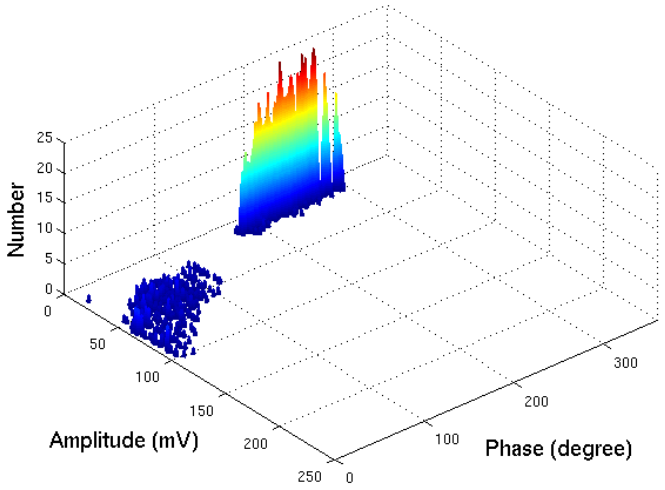

(a) RFCT1: Measurement at bushing

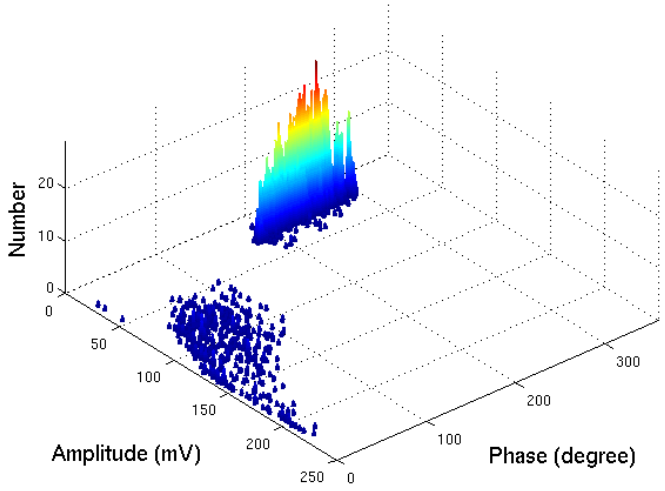

(b) RFCT2: Measurement at bushing tap point

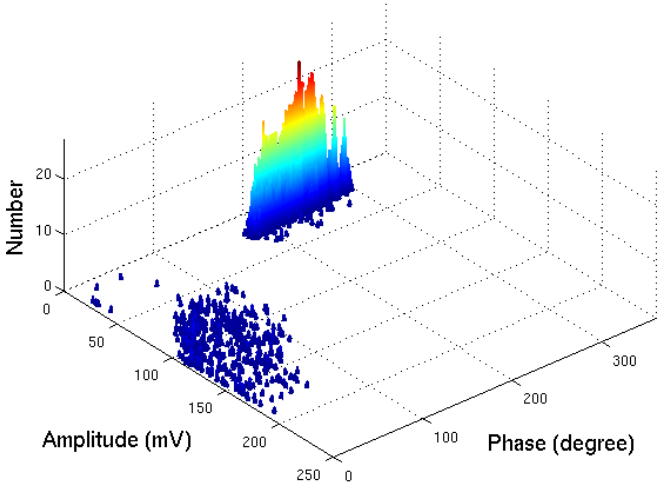

(c) RFCT4: Source to ground

FIGURE 7.31: Surface discharge in air measured at RFCT1, RFCT2 and RFCT4. PD injection at $x' = 7/7$ on plain winding measured over 50 cycles

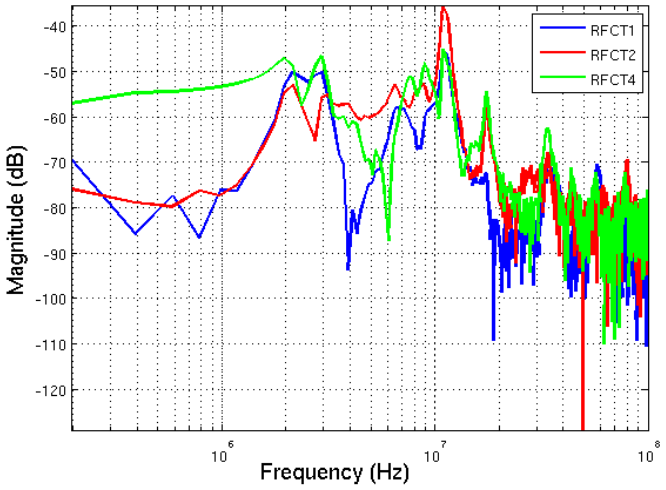

(a) RFCT1, RFCT2 and RFCT4

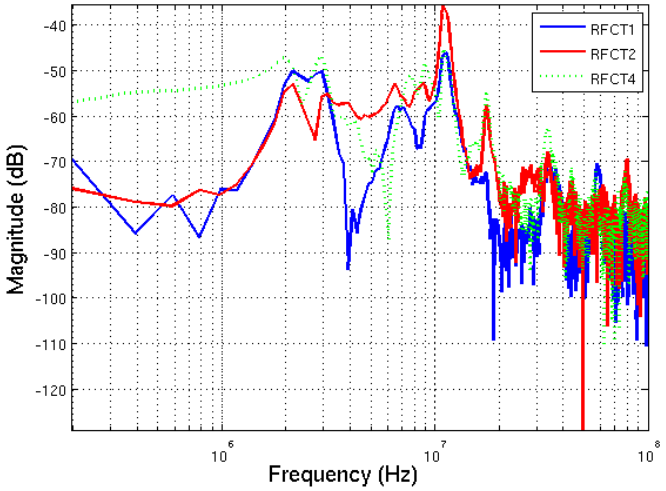

(b) RFCT1 and RFCT2

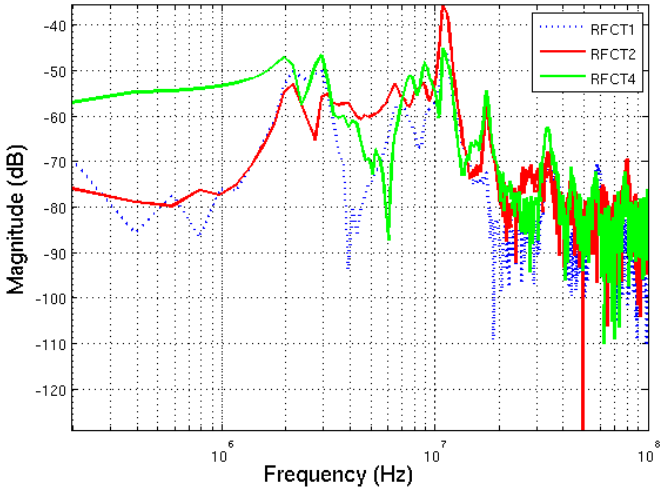

(c) RFCT2 and RFCT4

FIGURE 7.32: Frequency content of surface discharge in air measured at RFCT1, RFCT2 and RFCT4. PD injection at $x' = 7/7$ on plain winding

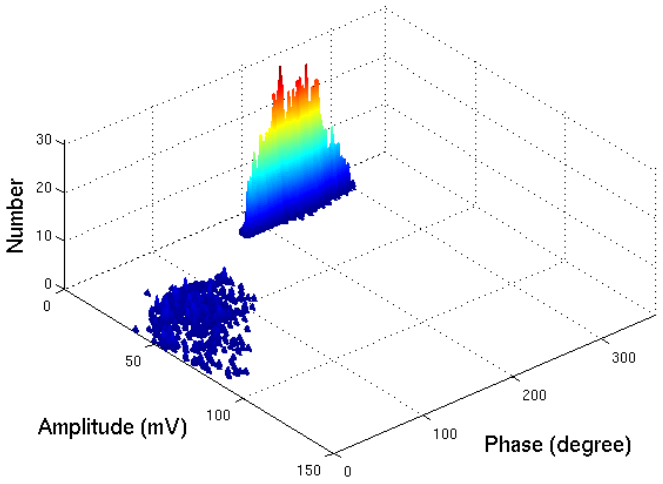

(a) RFCT2: Measurement at bushing tap point

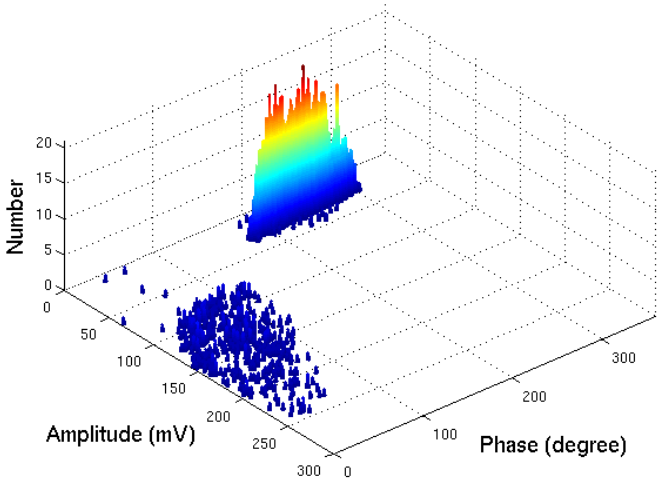

(b) RFCT4: Source to ground

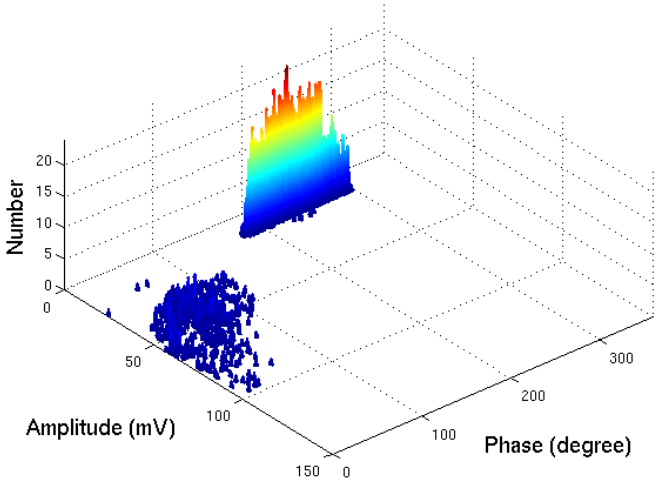

(c) RFCT5: Neutral to ground connection

FIGURE 7.33: Surface discharge in air measured at RFCT2, RFCT4 and RFCT5. PD injection at $x' = 4/7$ on plain winding measured over 50 cycles

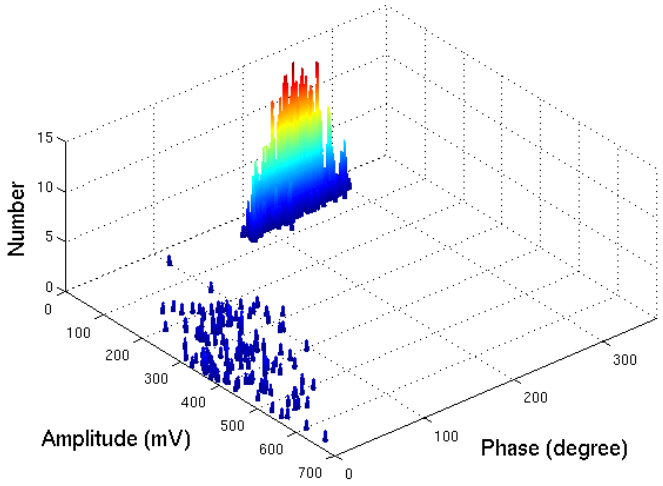

(a) RFCT3: Measurement at $x' = 3/7$

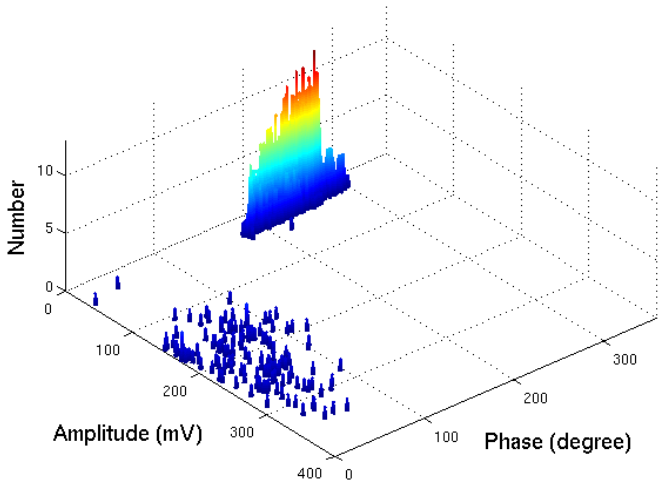

(b) RFCT4: Source to ground $x' = 3/7$

FIGURE 7.34: Surface discharge in air measured at RFCT3 and RFCT4. PD injection at $x' = 3/7$ on plain winding measured over 50 cycles

signal measured by RFCT4. This is due to the high frequency attenuation of the winding as RFCT4 is measuring the transmitted current wave, i'', after the transition point at $x' = 3/7$ and RFCT3 is measuring the incident current wave, i, before the transition point $x' = 3/7$.

A similar analysis can be used to investigate PD signal propagation within the interleaved winding. Figure 7.36 shows surface discharge signal measurements from RFCT3, RFCT4 and RFCT5 for an injection point at $x' = 0/7$. Again, the source measurement from RFCT3 shows a significant higher PD signal magnitudes up to maximum of 450mV (positive half cycle) at the point where the incident current wave, i, enters the transformer winding. As the current reaches the winding, with the effect of the ground connection via RFCT4, RFCT5 shows a smaller magnitude response with lower PD signal magnitudes in the range between 50mV to 150mV over the positive half cycle.

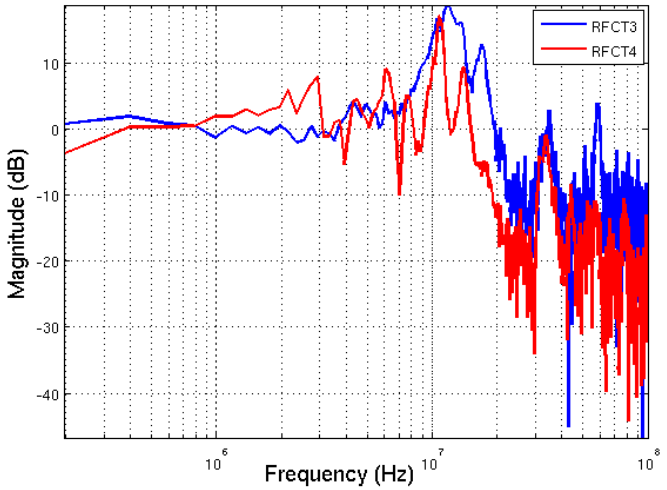

FIGURE 7.35: Frequency content of surface discharge in air measured at RFCT3 and RFCT4. PD injection at $x' = 3/7$ on plain winding

At the point $x' = 0/7$, the measured signals of RFCT4 and RFCT5 have similar magnitudes of the transmitted current wave, i''. By looking at the signal frequency content, Figure 7.37 shows the frequency spectrum of the three RFCTs for signal injection at $x' = 0/7$. It shows that, at the neutral to ground connection, the incident current wave and the transmitted current waves have similar response patterns. The transmitted current waves measured by RFCT4 and RFCT5, however, have lower magnitudes compared to the incident current wave measured by RFCT3.

7.4 Summary

Two experimental procedures have been used to investigate PD signal propagation within transformer windings. Current calibration based on a shunt resistor technique provides both voltage and current information. With this technique as the current is proportional to the voltage across the shunt resistor, then the PD charge can be calculated by integration. The shunt circuit arrangement takes into account of the equivalent characteristic impedance of the connection to the digital storage oscilloscope.

The circuit arrangement for current calibration using a shunt resistor of Figure 7.8 also allows study of the relationship between induced voltages and currents caused by a partial discharge event. It has been shown that from the calibrated waveform of Figure 7.10 to Figure 7.25, the current waveforms at source $x' = 7/7$ to $x' = 0/7$ measured by RFCT are similar to the voltage waveform at source $x' = 7/7$ to $x' = 0/7$ measured via a shunt resistor. However, as the current divides to travel towards the end windings, the measured voltage waveforms and the current waveforms were very dissimilar in terms of their waveshape. However, this is in agreement with the derived results using the model described in Section 5.5.3.

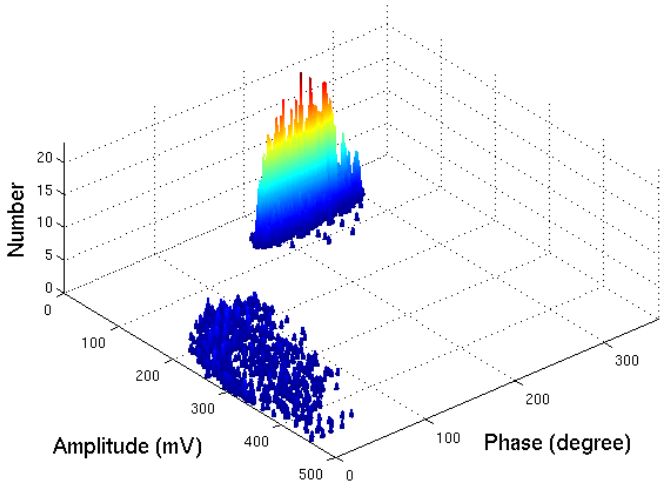

(a) RFCT3: Measurement at $x' = 0/7$

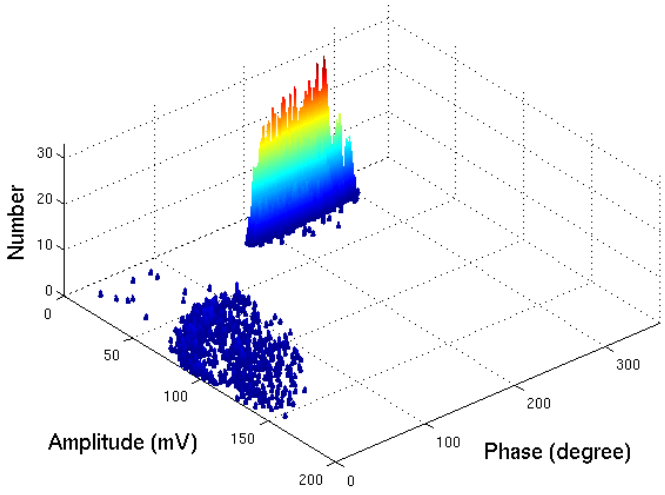

(b) RFCT4: Source to ground $x' = 0/7$

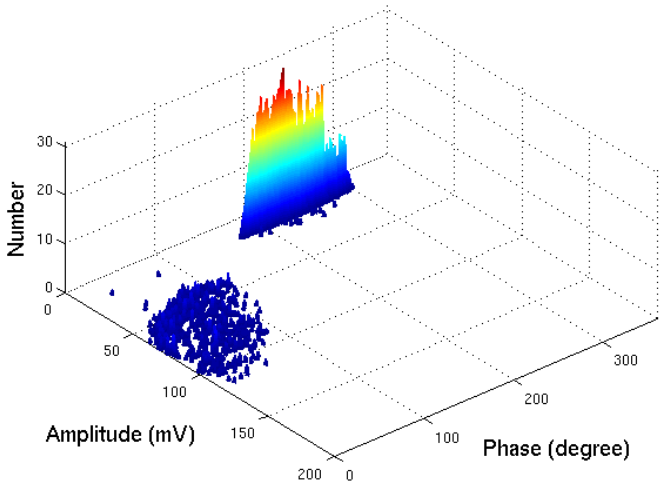

(c) RFCT5: Neutral to ground connection

FIGURE 7.36: Surface discharge in air measured at RFCT3, RFCT4 and RFCT5. PD injection at $x' = 0/7$ on interleaved winding measured over 50 cycles

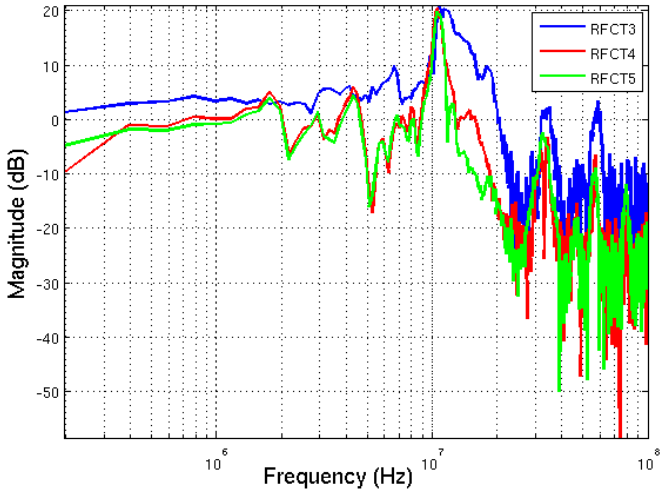

FIGURE 7.37: Frequency content of surface discharge in air measured at RFCT3, RFCT4 and RFCT5. PD injection at $x' = 0/7$ on interleaved winding

Current calibration by commercial PD detector is a common technique and requires simultaneous measurement for better accuracy. The inaccuracy of PD calibration using an RFCT is due to different triggering times, which give different patterns in terms of the number of PD events and amount of charge calculated. Five RFCTs were used for an investigation of PDs propagation in a transformer winding. It has been shown that, the PD magnitude at source point x' will have different magnitudes before the PD current flows through the transformer winding (known as incident current wave, i) and after entering the transformer winding (known as transmitted current wave, i''). It has also been shown that the ground effect of the winding at the point of source to ground connection (RFCT4), will have almost the same level of PD signal magnitudes recorded at both ends of the winding.

Chapter 8

Partial Discharge Location

The models presented in Chapter 4 and Chapter 5 are necessary for estimating transient waveforms and are therefore applicable for simulation of PD propagation within a transformer winding. The distribution and the signals oscillation can be estimated provided the source location of the PD has been identified. It is therefore necessary to first locate the source of PDs within a transformer winding so that a prediction of health and the selection of suitable maintenance or replacement strategies can be identified. However, the techniques of estimating PD location can result in errors because of the complexity of the transformer and the routes by which signals propagate from the source to the measurement point.

This chapter presents a technique for locating PDs along a transformer winding using its mathematical model solutions. The model solution involves consideration of the amplification factor of the derived model equation using Duhamel's principle. An accumulated harmonic waveform factor is considered in order to calculate the error at the windings terminal ends. This introduces a simple terminal ends error calculation between the measurements and the model distribution with respect to the amplification factor of the split winding analysis.

8.1 Accumulative Amplitude Distribution

Chapter 5 has demonstrated the used of Duhamel's principle in deriving a solution for time varying boundary conditions problem. The implication is that, any signal described using the impulse equation (based on principle of superposition) will create a signal consisting of a harmonic decay component plus original components of the source signal. The source waveform of the injected pulse can therefore be determined by means of superimposition and superposition techniques.

The solution provided based on the derivation of Equations (5.6) to (5.9), states that

all the solutions for incident arbitrary waveforms will consist of a standard form of solution, containing fixed distribution components plus harmonic decay components. As demonstrated in the same Chapter, injection of a pulse signal with high rise time and certain pulse width will develop an accumulated harmonic waveform at a different time τ as well as the response to the high frequency incident signal. This can be solved by using the superimposition technique.

Secondly, it is also means that the same derived solutions will contain a response signal where the accumulated harmonic waveform is embedded in the original source waveform that is in the fixed distribution component, which has higher frequency components than the original source signal. As demonstrated in Chapter 6 the application of HHT results in the approximation of the waveshape of the source waveform. Using a zero phase filter, then a superposition technique can be employed to identify the source.

Based on this analysis and the solutions provided, it is therefore necessary to investigate the harmonic decay component as a tool to identify source location of a partial discharge. The results shown in Section 4.3.6 of Figures 4.11 to 4.13 have demonstrated that the distribution of harmonic amplitude either in time domain or frequency domain has a considerable information of location of the source signal. Hence this Chapter will introduce a technique to identify source location of a partial discharge based on the analysis of the accumulative amplitude distribution of harmonic components.

8.1.1 The Effect of Pulse Transition

The investigation of pulse transition by means of different rise time and decay time is necessary to study the effect of the transformer response for different frequencies of incident waves. This is achieved by injecting pulses with different incident angles and different wavetails. Using a pulse generator two types of test were conducted on the plain disc winding model. First by injecting pulses with a fixed rise time and varying the decay time, and secondly injecting pulses with varying rise time and fixed decay time. Due to the limitation of the device four types of transitions are considered and Figure 8.1 shows the type of pulses used during the experiment.

Considering a plain disc winding for the experimental procedure, the pulses were injected at terminal 1 ($x' = 7/7$) and the time domain responses were captured at terminal 8 ($x = 0/7$). The test was carried out for the ground winding connection via a 50Ω shunt resistor. This will give an offset level at the measurement point, where it was then compensated by calibrating its fixed distribution level using a digital signal oscilloscope.

The analysis undertaken is by measuring the whole time domain response with sampling rate at 1GHz and signal captured between $-10\mu s$ to $90\mu s$ with respect to the trigger point. The width of the pulses are compared between the source of the injection and the captured response. By this method τ has been identified. It was found that every signal

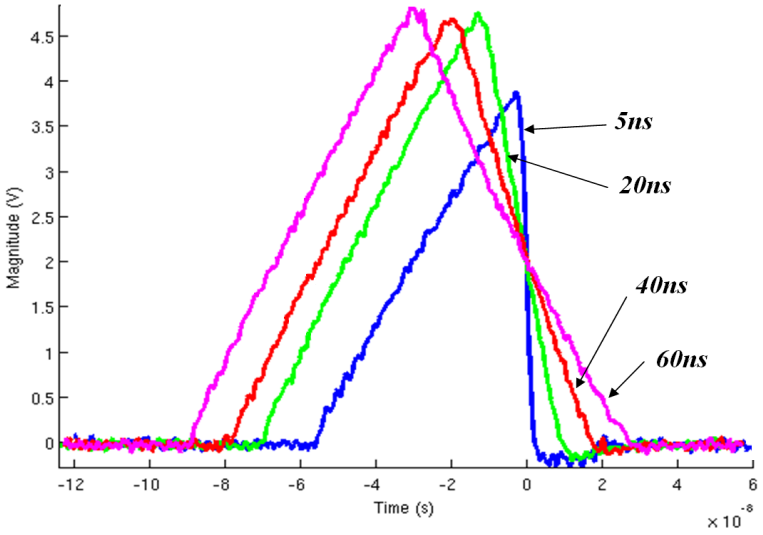

(a) Pulses with fixed rise time of 60ns and variable decay time

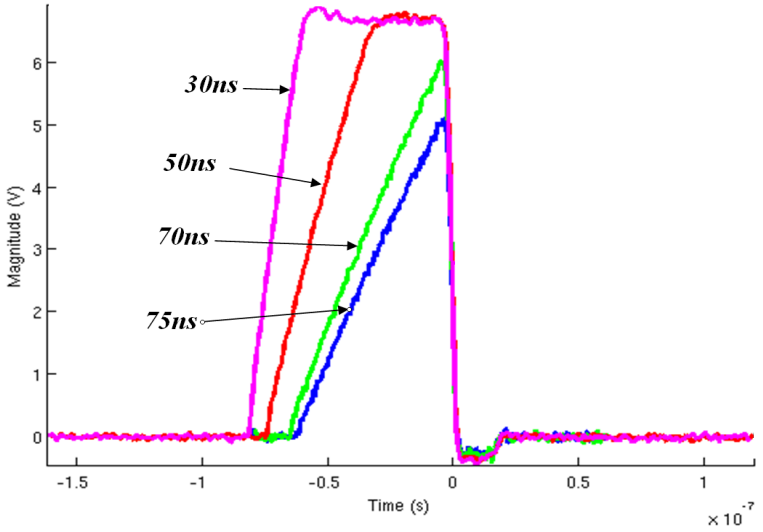

(b) Pulses with fixed decay time of 5ns and variable rise time

FIGURE 8.1: Pulses with variable high rise time and variable decay time

measurement has an extra oscillation after $t = \tau$ due to excited resonant frequencies of the transformer winding. This is the accumulated harmonic waveform.

Based on superimposition, the accumulated harmonic waveforms for $t > \tau$ can be analysed separately to assess the variation of different signal transitions. Figure 8.2 shows the variation of waveform oscillation as a function of different signal rise time and decay time. The response of the signals measured at the Neutral point shows that, the injected pulse will excite the natural frequencies of oscillation of the system.

The amplitudes shown from Figure 8.2 are the maximum amplitudes of the accumulated harmonic signal and can be used for calibration purposes. With reference to Figure 8.2(a), the injected pulse causes a higher accumulated amplitude as the decay time increases. However, Figure 8.2(b) shows a shorter rise time, and a higher accumulated

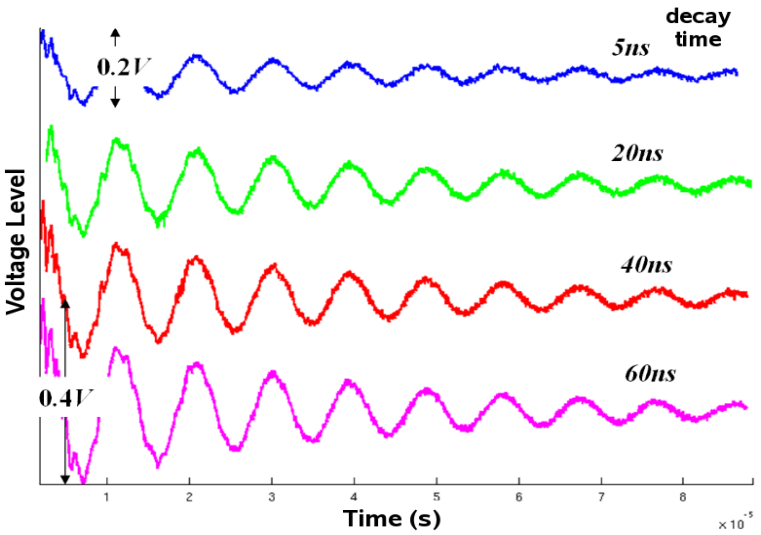

(a) Accumulated harmonic waveform with fixed rise time at $60ns$

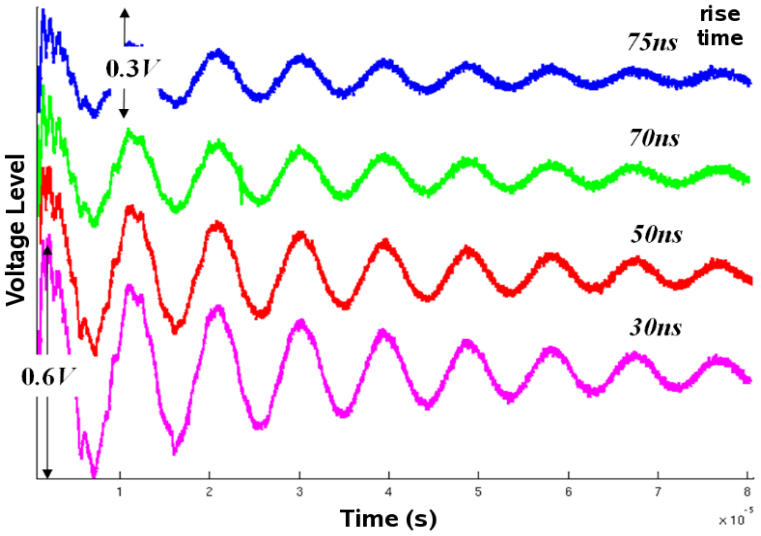

(b) Accumulated harmonic waveform with fixed decay time at $5ns$

FIGURE 8.2: Accumulated harmonic waveform with variable high rise and decay time

harmonic amplitude. This is because the shorter the rise time, the steeper the incident wavefront, and the greater the range of resonant frequencies of the winding that are excited. Whereas for shorter decay times the amplitude of the winding resonant response reduces as the energy of the injected pulse reduces.

From an analytical point of view, not only will certain high transition signals cause oscillations of resonant frequencies for $t > \tau$ but also signal injection at different positions along a transformer winding (with reference to Section 5.3) will excite different responses that give information of the source signal by means of analysing the moving poles. The accumulated harmonic waveform contains the first harmonic peak and can be identified easily in terms of its resonant pole position in the frequency domain.

8.2 The Model Equation

Analysis of accumulated harmonic voltage distribution in Chapter 4, showed that the measurement at the bushing tap point represents an open circuited winding configuration whereas at the neutral point the measured voltages are at the ground level (Figures 4.11 to 4.13). From Chapter 5 it also has been concluded that the amplification factor of harmonic current will be the same for situations represented by transmission line model ($i_L \neq 0$) and where the transient response is within the winding's capacitive region ($i_L = 0$). Hence, the solution for the accumulated harmonic waveform will be the same under both operating conditions.

This section considers the current accumulated harmonic waveform measured by current transformers at the bushing tap point and neutral to earth connection. The model equation is adapted from the current equation model based on the Duhamel's principle (Section 5.5). The distribution of the current is represented by the half range sine series and the quarter range sine series in the solutions towards the neutral and bushing tap points respectively. Rewriting the equation of harmonic amplitude factor for current towards neutral from Equation (5.29) in the range of x_n, gives;

$$A_{isn} = \sum_{s=1}^{\infty} \frac{EA_{sn}C_g l}{s\pi} \, cos \frac{s\pi x_n}{l} \tag{8.1}$$

Dividing this equation by the surge impedance of the model equation, defined as;

$$z_{isn} = \frac{s\pi}{EC_g l} \tag{8.2}$$

Gives the current harmonic amplification factor for currents flowing towards the neutral:

$$\widehat{A_{isn}} = \sum_{s=1}^{\infty} A_{sn} \, cos \frac{s\pi x_n}{l} \tag{8.3}$$

Using a similar approach for the harmonic amplitude factor for currents flowing towards the bushing, from Equation (5.34);

$$A_{isb} = \sum_{s=1}^{\infty} \frac{2EA_{sb}C_g l}{s_o\pi} \, cos \frac{s_o\pi x_b}{2l} \tag{8.4}$$

Dividing this by the surge impedance defined in this case as:

$$z_{isn} = \frac{s_o\pi}{2EC_g l} \tag{8.5}$$

gives the current harmonic amplification factor for currents flowing towards the bushing

tap point:

$$\widehat{A_{isb}} = \sum_{s=1}^{\infty} A_{sb}\, cos \frac{s_o \pi x_b}{2l} \tag{8.6}$$

where the definition of A_{sn} and A_{sb} are using the same as for Equations (5.26) and (5.31) respectively. The domain distribution of $\widehat{A_{isn}}$ and $\widehat{A_{isb}}$ are for ranges of x_n and x_b defined as:

$$x_n = \frac{x}{x'} - 1 \qquad and \qquad x_b = x - x' \tag{8.7}$$

respectively. Figures 8.3 and 8.4 show a simulation of the distribution model of current amplification factor and absolute distribution respectively along a transformer winding.

The parameters under consideration are derived by making several assumptions. First, it is assumed that the harmonic components are embedded in travelling waves that experience no losses, since γ_s is neglected in the distribution model. Therefore, the accumulated harmonic signals captured at both the bushing and neutral point are due to the natural frequencies of the system that are proportional to $1/\sqrt{LC_g}$ which in turn infers that β is equivalent to zero.

Secondly, as current measurements are obtained using current transformers, the offset level of the current is very low. As A_{sb} and A_{sn} are dependant on the variables of A, B, C, and D from Equations (B.8) to (B.12), the offset level of voltages V_B and V_N are now current offsets of I_{Boff} and I_{Noff} respectively. In any case for the grounded winding V_B is always higher than V_N, and V_N can be assumed to be zero volts. However due to using RFCTs for current measurement I_{Boff} and I_{Noff} will vary with respect to the location of the PD source and can be estimated by trial and error technique. Thus the simulation of Figure 8.4 is assumes the value of α to be equivalent to 1.6, I_{Boff} and I_{Noff} vary accordingly, where the absolute value of current at the bushing and neutral points can be extracted as shown in Figure 8.5. The absolute values at the end terminals show that as the source x' moves from the bushing towards the neutral, the amplitude at the bushing becomes lower whilst the amplitude at the neutral increases.

Thirdly, the first harmonic component is the most dominant harmonic signal to be measured at the Bushing and Neutral points. Analytically the solution is obtained by setting the harmonic coefficient, s, equivalent to one. The first harmonic component can be obtained from the transformation of the time domain waveform into its frequency domain. At the point where the pulse is injected at x', the level of the amplitudes are the same and can be found by appropriate selection of the offset current I_{Boff} and I_{Noff}. Since the domain length for the accumulated model equation is for the ranges of x_n and x_b, at the point x' the half range series and the quarter range sine series will be the same when s is equivalent to one.

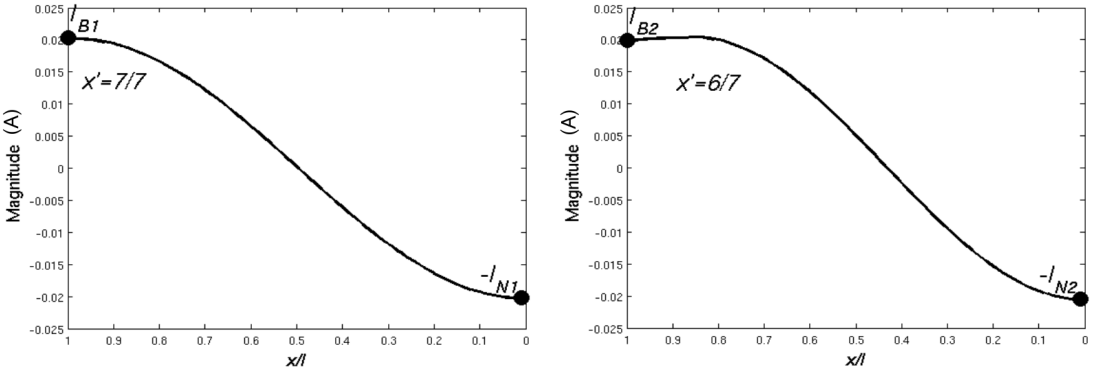

(a) $x' = 7/7$

(b) $x' = 6/7$

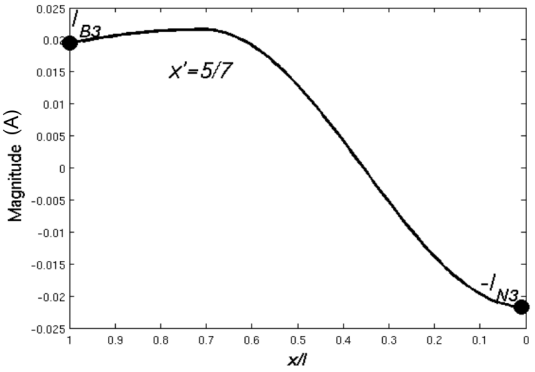

(c) $x' = 5/7$

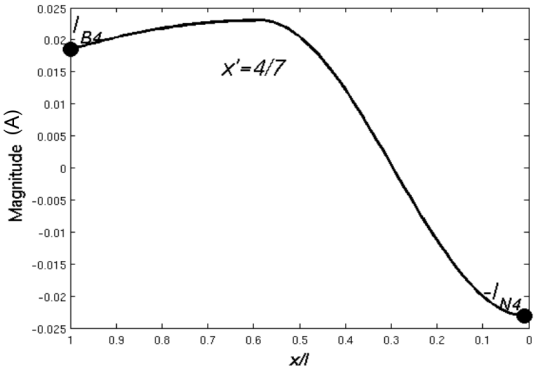

(d) $x' = 4/7$

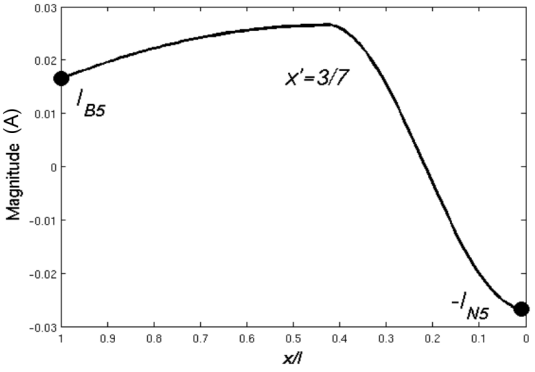

(e) $x' = 3/7$

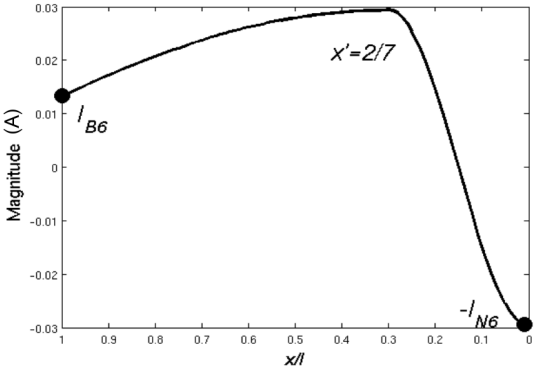

(f) $x' = 2/7$

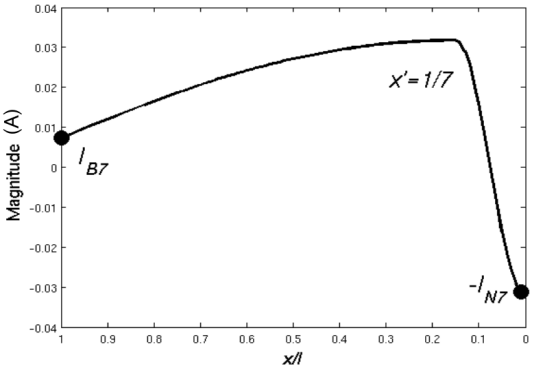

(g) $x' = 1/7$

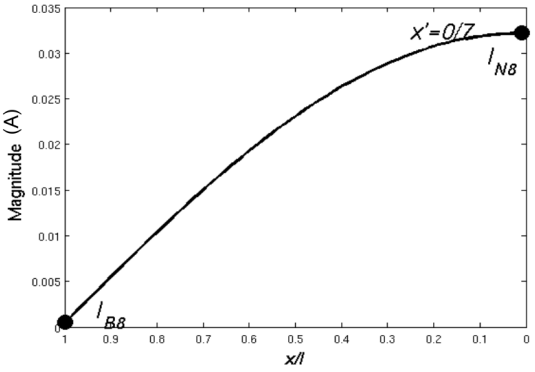

(h) $x' = 0/7$

FIGURE 8.3: Simulation of variation of current amplification factors as a function of source signal injection point

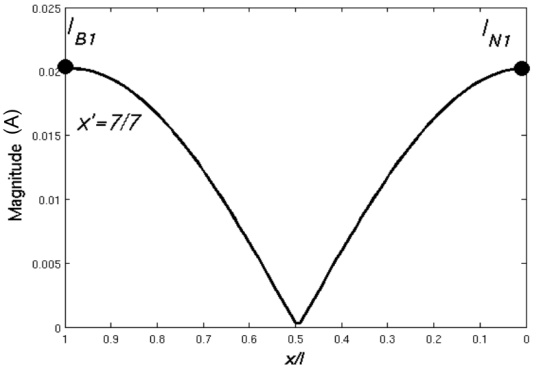

(a) $I_{Boff} = 0.1$; $I_{Noff} = 0.0149$

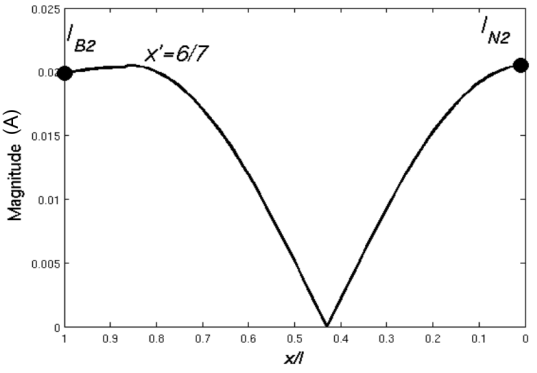

(b) $I_{Boff} = 0.097$; $I_{Noff} = 0.02180$

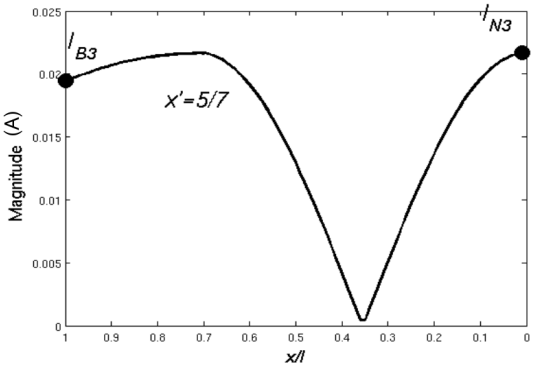

(c) $I_{Boff} = 0.091$; $I_{Noff} = 0.037$

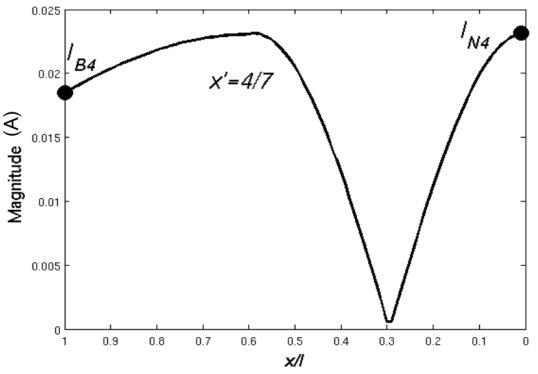

(d) $I_{Boff} = 0.085$; $I_{Noff} = 0.0620$

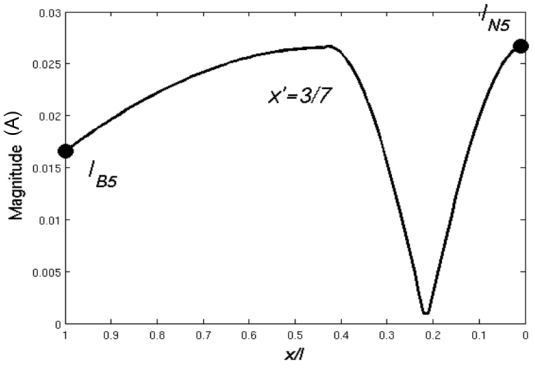

(e) $I_{Boff} = 0.080$; $I_{Noff} = 0.1689$

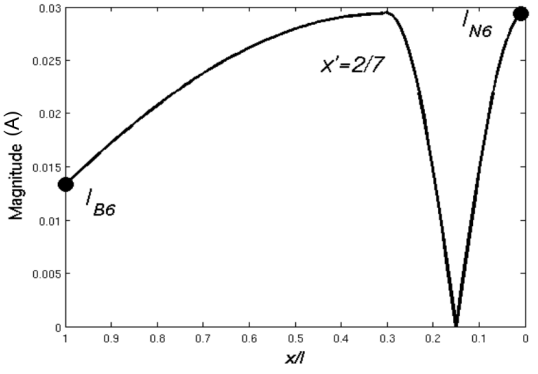

(f) $I_{Boff} = 0.075$; $I_{Noff} = 0.73$

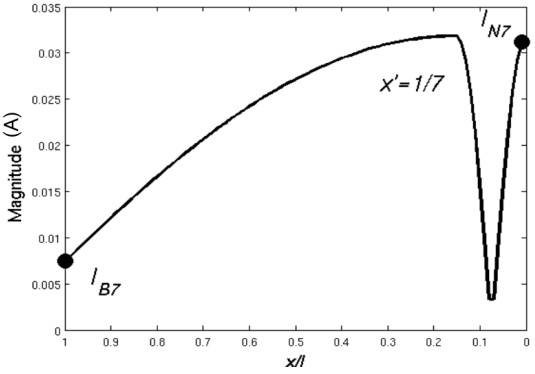

(g) $I_{Boff} = 0.070$; $I_{Noff} = 1.20$

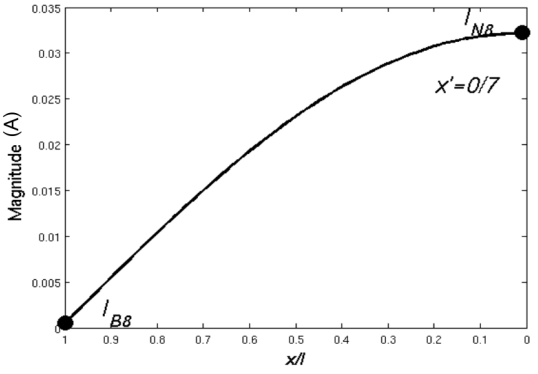

(h) $I_{Boff} = 0.067$; $I_{Noff} = 0.85$

FIGURE 8.4: Simulation of distribution of absolute accumulated harmonic waveform based on the model equation (8.3) and (8.6) as a function of source signal injection point.

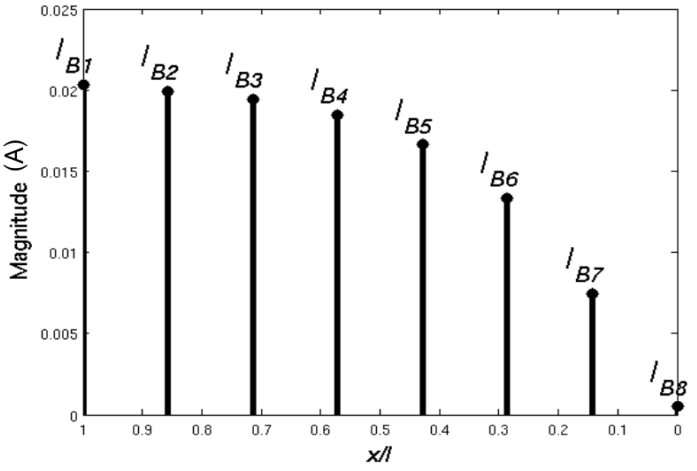

(a) Simulated at Bushing point

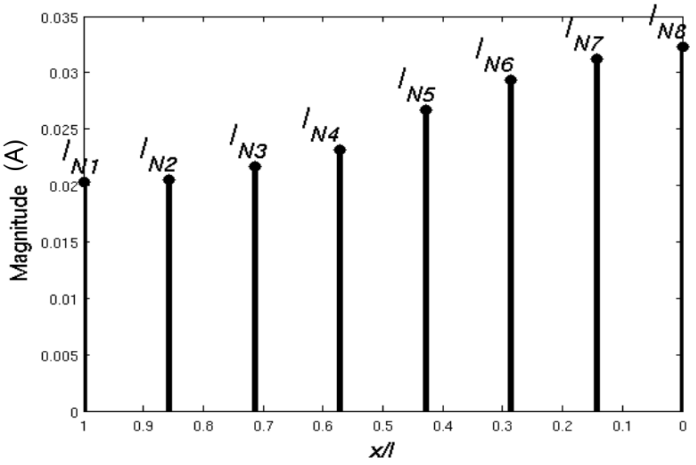

(b) Simulated at Neutral point

FIGURE 8.5: Simulation of absolute accumulated harmonic current magnitude at the bushing and neutral points

8.2.1 Frequency Domain PD Signal Extraction

The model equations developed in this thesis assume that PD signal propagation can be modeled in the predominantly capacitive region ($i_L \approx 0$) or when the transmission line analogy is applicable ($i_L \neq 0$). To determine which model is applicable, PD signal data can be transformed into the frequency domain and filtered to study variation of the accumulated harmonic amplitude. As an example, consider the circuit configuration of Figure 7.26, where PD signals from the surface discharge experiment were injected at the winding terminals from $x' = 7/7$ to $x' = 0/7$ on the plain disc winding.

Frequency domain PD signal extraction begins by capturing the PD signal on RFCT1 (bushing) and RFCT5 (neutral to ground). Each of the detected PDs are transformed into the frequency domain and filtered using a bandpass zero phase filter. At the bushing, the range of frequency is between 800kHz to 4MHz, and at neutral it is between 3.5MHz to 7MHz. Figures 8.6 and 8.7 show the filtered frequency spectrum for signals

measured at the bushing and neutral respectively. The filtered spectrums are obtained by considering a one cycle period of detected PDs for every point of injection into the transformer winding. The 3D view shows the spectrum in the form of a bode plot where the peak magnitude represents the pole position along the winding.

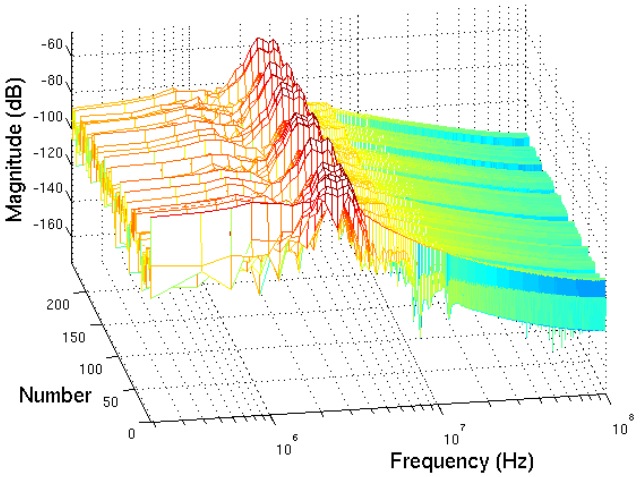

(a) 3D view extraction

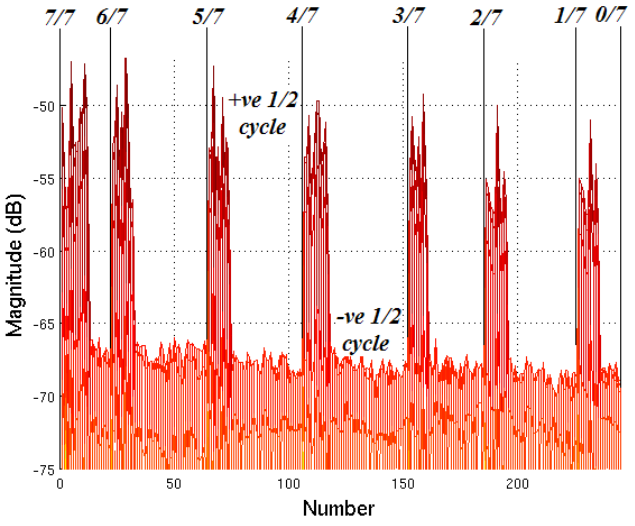

(b) Side view

FIGURE 8.6: Frequency domain extraction of surface discharge measurement on the plain winding at RFCT1 (Bushing) for 800kHz to 4MHz frequency range

The side view (Figures 8.6(b) and 8.7(b)) is a plot of the Magnitude (dB) versus Number of detected PDs for both positive half cycle and negative half cycle. The higher magnitudes represent PDs ocurring during the positive half cycle and the lower magnitudes represents PDs occuring within the negative half cycle of the applied voltage causing the surface discharge. Both Figure 8.6(b) and Figure 8.7(b) show that as the injection of surface discharge PD moves from $x' = 7/7$ to $x' = 0/7$, the captured PD signal at the bushing shows a decreased value of its magnitude and increased magnitude at the neutral to ground connection.

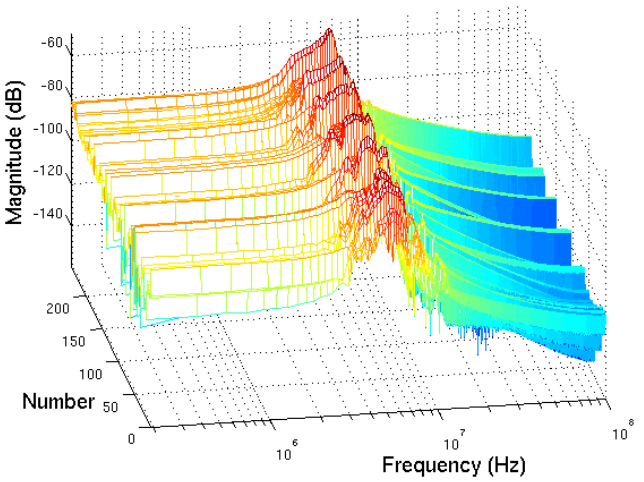

(a) 3D view extraction

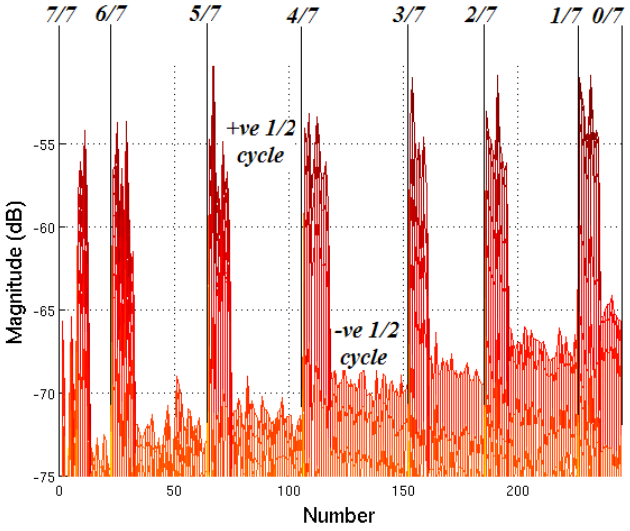

(b) Side view

FIGURE 8.7: Frequency domain extraction of surface discharge measurement on the plain winding at RFCT5 (Neutral) for 3.5MHz to 7MHz frequency range

The extraction of the PD data from surface discharge events can be achieved with isolation between the positive and the negative half cycle within the frequency spectrum. Therefore, Figure 8.8 and Figure 8.9 show the spectrum for the positive half cycle derived from Figure 8.6 and Figure 8.7 respectively. By isolating the positive and negative half cycles, the level distribution from $x' = 7/7$ to $x' = 0/7$ is much clearer.

By using the same circuit arrangement, the PD in void source is used to inject PD signals into the interleaved winding. Figures 8.10 and 8.11 show the PD signal spectrum extraction at 8MHz to 20MHz for PD signals from a void measured at the bushing (RFCT1) and the neutral to ground (RFCT5) respectively. As can be seen from the 2D view extraction, the void PDs also have a similar pattern to surface discharge in air. There is a decreasing PD magnitudes at the bushing and increasing magnitudes at the neutral for the injection of PD signals from $x' = 7/7$ to $x' = 0/7$.

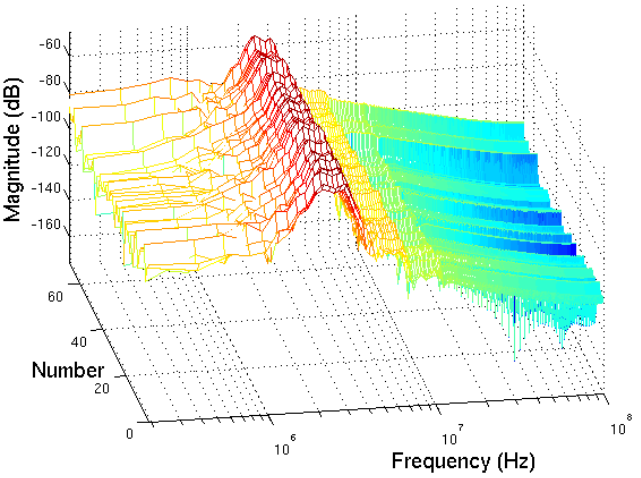

(a) 3D view extraction

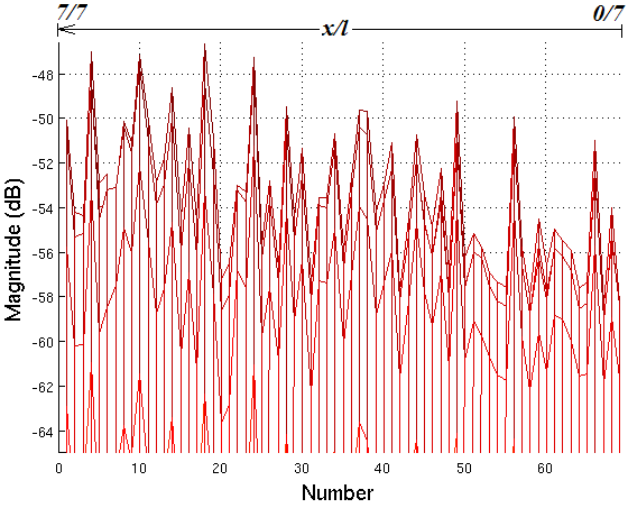

(b) Side view

FIGURE 8.8: Frequency domain extraction of surface discharge measurement from Figure 8.6(b) on the plain winding at RFCT1 (Bushing) for positive half cycle between 800kHz to 4MHz frequency range

Therefore, the level of the PD signal magnitudes injected at different points along a transfomer winding, could be used as information of PD location along the transformer winding. The information may be related with the level of PD magnitude under the predominantly capacitive linear relationship between the two terminals ends [80]. However from the analysis, comparing between bushing measurements and neutral measurements, PDs measured at the neutral have a more linear relationship compared to PDs measured at the bushing. As in the case of nonlinear distribution relationship shown in Figure 8.8(b) and Figure 8.10(b) a model for simulation of Figure 8.5 may be used. Hence model equations from (8.3) and (8.6) are used in the proposed technique developed in this thesis.

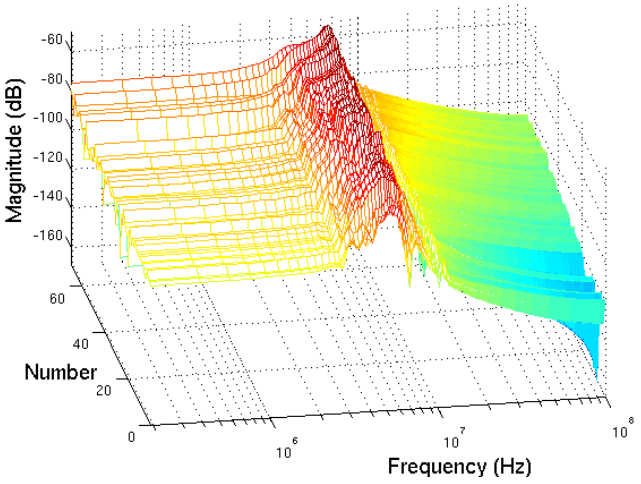

(a) 3D view extraction

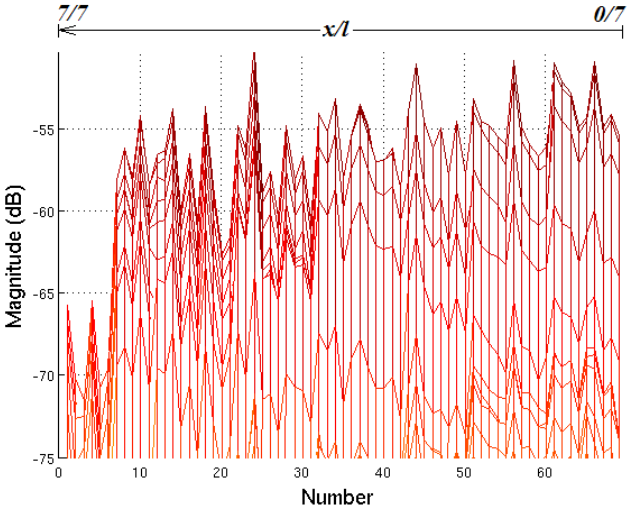

(b) Side view

FIGURE 8.9: Frequency domain extraction of surface discharge measurement from Figure 8.7(b) on the plain winding at RFCT5 (Neutral) for positive cycle between 3.5MHz to 7MHz frequency range

8.3 Minimum Mean Error

To detect the position of partial discharge along a transformer winding, a Minimum Mean Error (MME) technique based on the two ends (bushing and neutral) measurements is introduced. Suppose, I_B and I_N are the harmonic current obtained from measurments using RFCTs at the bushing and neutral respectively, with a unit of mV. Let $\widetilde{I_B}$ and $\widetilde{I_N}$ be the estimated harmonic current from the model Equations (8.6) and (8.3) at bushing and neutral points respectively.

The difference between current measurement and estimation at the Bushing and Neutral terminals are:

$$\epsilon_B = |\widetilde{I_B}| - |I_B| \tag{8.8}$$

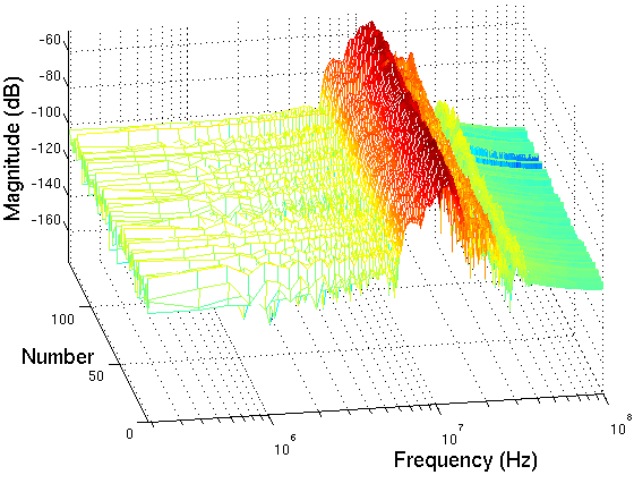

(a) 3D view extraction

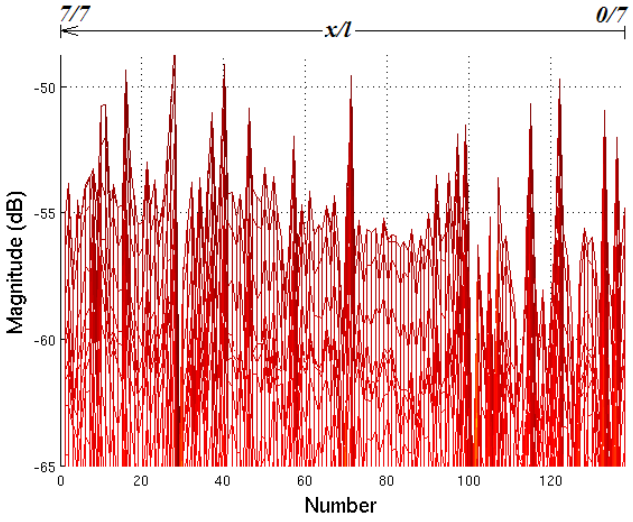

(b) Side view

FIGURE 8.10: Frequency domain extraction of PD in void measurement on the interleaved winding at RFCT1 (Bushing) for 8MHz to 20MHz frequency range

$$\epsilon_N = |\widetilde{I_N}| - |I_N| \tag{8.9}$$

The mean error between the two terminals is:

$$\overline{\epsilon_{BN}} = \frac{\epsilon_B + \epsilon_N}{2} \tag{8.10}$$

A matrix containing the different errors can be constructed as follows:

$$\widehat{\epsilon_B} = \begin{bmatrix} \epsilon_{B_1} & \epsilon_{B_2} & \dots & \epsilon_{N_2} \end{bmatrix} \tag{8.11a}$$

$$\widehat{\epsilon_N} = \begin{bmatrix} \epsilon_{N_1} & \epsilon_{N_2} & \dots & \epsilon_{N_\mathcal{K}} \end{bmatrix} \tag{8.11b}$$

$$\widehat{\epsilon_{BN}} = \begin{bmatrix} \overline{\epsilon_{BN_1}} & \overline{\epsilon_{BN_2}} & \dots & \overline{\epsilon_{BN_\mathcal{K}}} \end{bmatrix} \tag{8.11c}$$

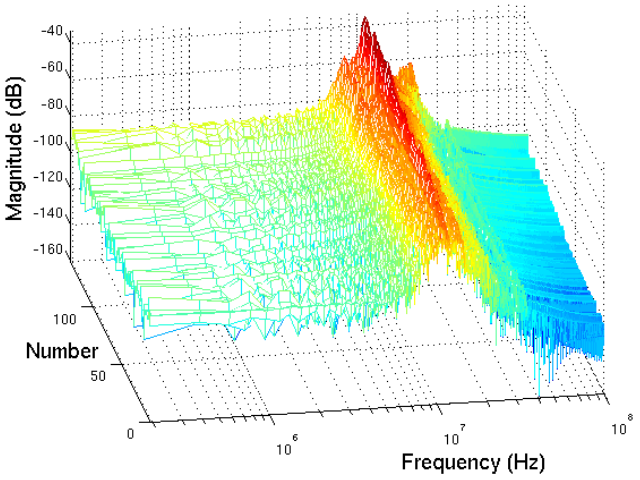

(a) 3D view extraction

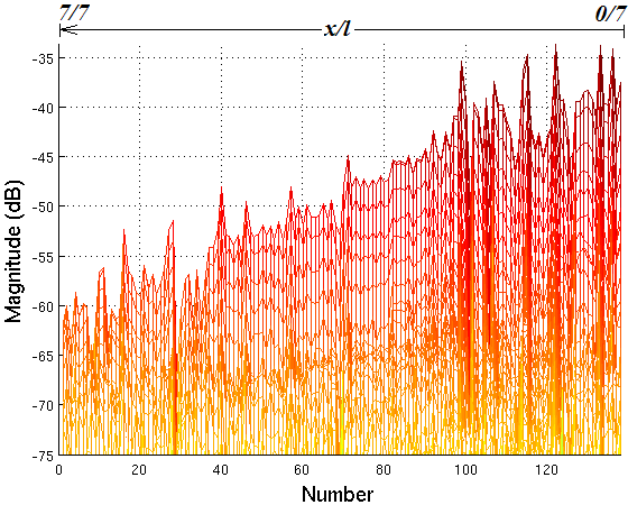

(b) Side view

FIGURE 8.11: Frequency domain extraction of PD in void measurement on the plain winding at RFCT5 (Neutral) for 8MHz to 20MHz frequency range

This will give a set of matrix of the same size $[1 \times \mathcal{K}]$, where $\mathcal{K}$ is the number of sectional windings or disc pairs with $\mathfrak{y} = 1, 2, \ldots, \mathcal{K}$. Then a Mean Error (ME) matrix of ϵ_B, ϵ_N and $\overline{\epsilon_{BN}}$ can be constructed as follows:

$$ME = \begin{bmatrix} {\epsilon_B}^T & {\epsilon_N}^T & {\epsilon_{BN}}^T \end{bmatrix} \tag{8.12}$$

where the size of the matrix ME is now equal to $[\mathcal{K}, \mathcal{J}]$, where $\mathcal{J}$ is the number of set of errors. Then the mean error $\overline{ME}$ is calculated by:

$$\overline{ME} = \frac{ME}{\mathcal{J}} \tag{8.13}$$

The position of the PD source at a specific disc pair can be found by finding $\mathfrak{y}'$ at a specific absolute minimum mean error (MME) position where

$$\mathfrak{y}' \Longrightarrow MME = \left| min\{\overline{ME_{1\mathfrak{y}}}\} \right| \tag{8.14}$$

Figure 8.12 shows simulation results using the MME technique to identify the source of a PD signal within a transformer winding. The two end measurements are used as target estimation points based on the calculation of errors. The plots are arranged to represent the matrix formation of the end terminals (bushing and neutral) errors between measured values and estimated values represented by the matrix (8.11) are based on the calculated parameters of α and V_B.

The possible position of the PD source can be identified analytically by finding $\mathfrak{y}'$ or graphically by looking at the minimum deviation of the error with respect to a zero line. The zero line represents the accuracy of the estimation such that the smaller the deviation of ϵ_B, ϵ_B and $\overline{\epsilon_{BN}}$ from zero, the better the accuracy of the estimate of the possible position of the PD.

An experiment using the plain disc winding in the circuit arrangement shown in Figure 5.17 was undertaken. An impulse of $50\mu s$ rise time and $5\mu s$ pulse width was injected between $x = 7/7$ to $x = 0/7$. Both voltage and current measurements were recorded and calibrated using a digital signal oscilloscope. The time domain response of the current measurements from both end terminals were compared to determine τ, hence the accumulated harmonic waveforms were identified. A zero phase lowpass filter was employed to remove any unwanted noise.

To estimate the fixed distribution constant, α, it is necessary to consider both measurement points at the bushing and neutral terminals. Therefore, once τ has been identified two values of α can be obtained, that is by transformation of the two time domain response captured at the winding ends into the frequency domain and applying [80];

$$\alpha = cosh^{-1}\left\{ \frac{1}{|H(\omega)|} \right\} \tag{8.15}$$

Now α defines α_B and α_N allowing the solution of model Equations (8.6) and (8.3).

Figure 8.13 shows the MME technique to locate the PD source based on the model distribution curve of Figure 8.4. By using a visual inspection the results from the MME technique show very good estimation of the location of the PD source. The estimation of PD location for $x' = 4/7$ and $x' = 3/7$ show a very accurate estimation with a small deviation from the zero line. However for the source at $x' = 6/7$, $x' = 5/7$, $x' = 2/7$ and

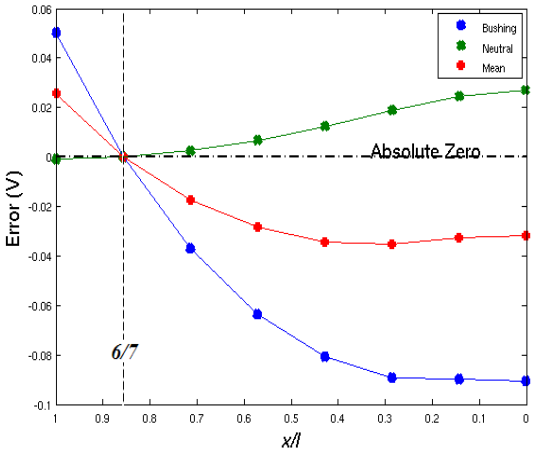

(a) $x' = 6/7$

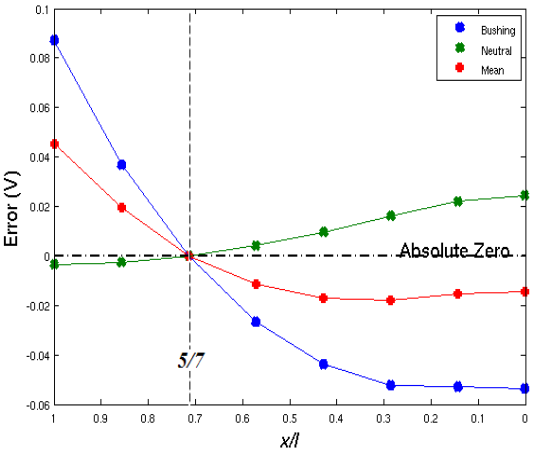

(b) $x' = 5/7$

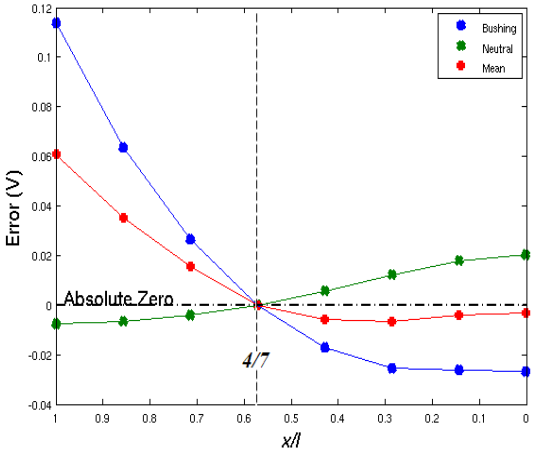

(c) $x' = 4/7$

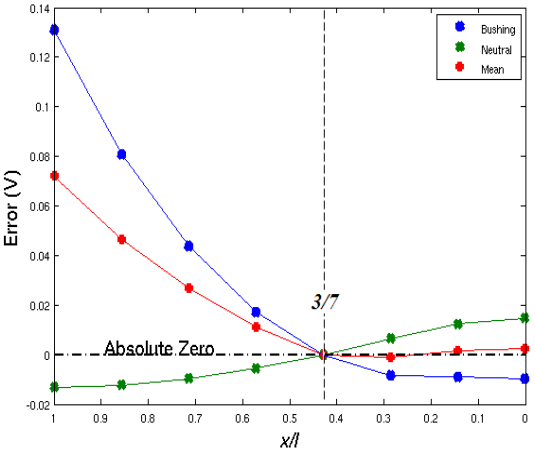

(d) $x' = 3/7$

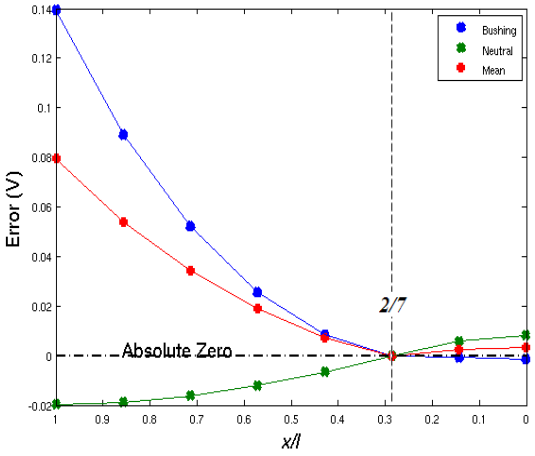

(e) $x' = 2/7$

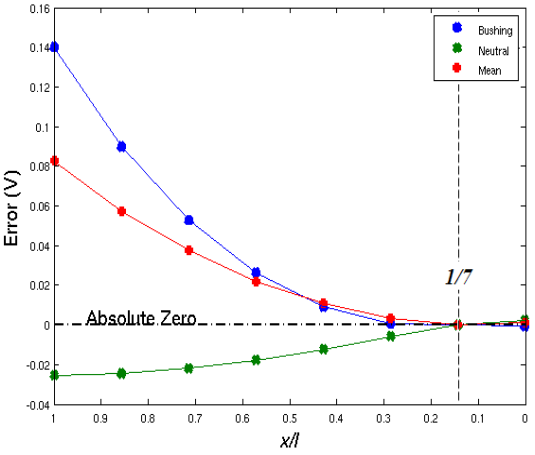

(f) $x' = 1/7$

FIGURE 8.12: Simulation of mean error from equation model

$x' = 1/7$ show a significant deviation from the zero line, this is believed to be due to the poor estimation of V_B and α. All the parameters under consideration used to estimate the location of PDs are tabulated in Table 8.1.

TABLE 8.1: MME parameters

x'	f_L	f_U	V_B	V_N	α_B	α_N	MME
6/7	100kHz	450kHz	0.042V	0V	1.5846	1.5834	4.6×10^{-3}
5/7	100kHz	450kHz	0.087V	0V	1.5851	1.5844	5.8×10^{-3}
4/7	100kHz	500kHz	0.190V	0V	1.5850	1.5854	0.0345
3/7	40kHz	400kHz	0.26V	0V	1.5849	1.5863	4.7×10^{-3}
2/7	30kHz	450kHz	0.291V	0V	1.5849	1.5874	3.4×10^{-3}
1/7	30kHz	350kHz	0.315V	0V	1.5856	1.5883	5.0×10^{-4}

8.3.1 MME and Partial Discharge Location

To demonstrate the MME technique with real PD measurements via RFCTs, experiments of PD injection on to the transformer winding were conducted for the circuit configuration shown in Figure 7.26. The points of interest for the PD measurement are at RFCT1 and RFCT5 which is the measurement point at bushing and neutral to ground connection respectively.

Using the technique of data extraction described in Section 7.1.2 the captured waveforms from RFCT1 and RFCT5 were transformed into the frequency domain using Fast Fourier Transforms (FFT). The accumulated harmonic amplitude was then identified from its bode plot diagram and filtered using a band pass zero phase filter. The filtered waveforms were then reconstructed into the time domain using an Inverse Fast Fourier Transform (IFFT) to obtain time domain representations of the filtered waveforms at the bushing and neutral to ground connections. The amplitude estimation of the accumulated harmonic waveform was found by simply taking the maximum absolute value of the inversed transform signals.

For every detected PD waveform, the MME was calculated to obtain an estimated location of the PD source. To improve the accuracy of the error calculation, the terminal points along the transformer winding were further refined into one hundred terminal points. A 3D plot was constructed for the axis of Phase (degree), distance x/l and Number or $\phi - \frac{x}{l} - n$. The position of the PD source is found by considering the highest number of estimated PD sources at the position x/l.

For the estimation of surface discharge PD source, analysis is divided into two categories, since the magnitude of the PDs are different in each half cycle. The positive half cycle and the negative half cycle were treated separately, in which the value of I_{Boff} and I_{Noff} were estimated at different values for both half cycles.

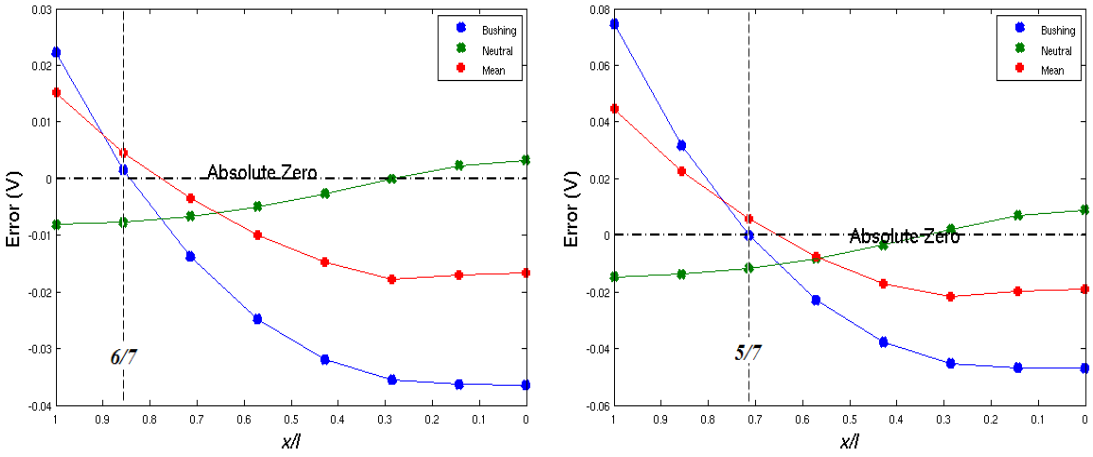

(a) $x' = 6/7$

(b) $x' = 5/7$

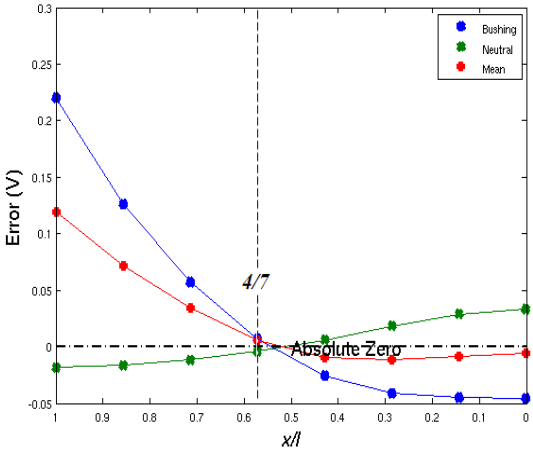

(c) $x' = 4/7$

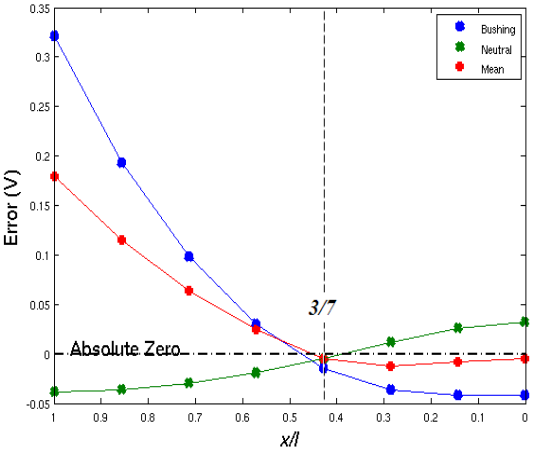

(d) $x' = 3/7$

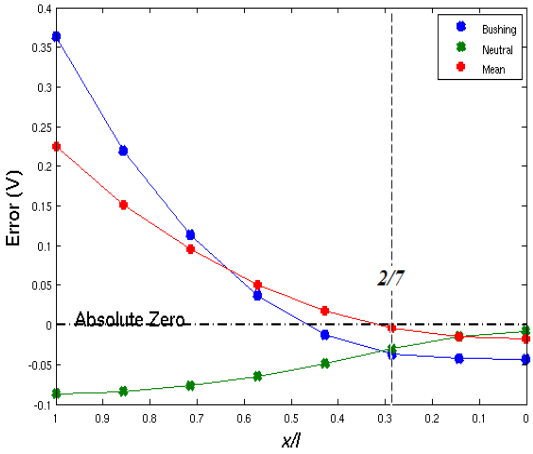

(e) $x' = 2/7$

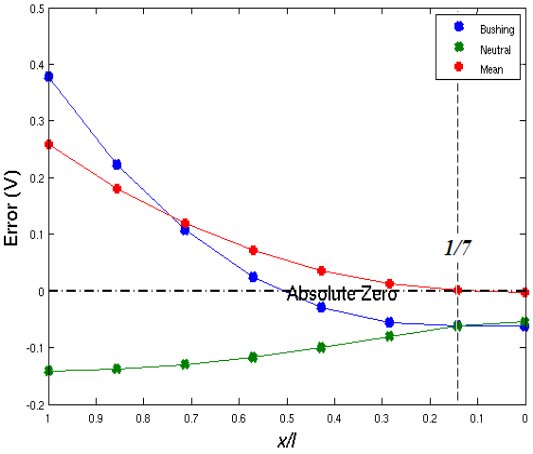

(f) $x' = 1/7$

FIGURE 8.13: Estimation of mean error from measured current

Figure 8.14 shows an estimation of location based on the positive cycle of measured PD signals from surface discharge by MME technique with the $\phi - \frac{x}{l} - n$ plot on plain winding. The PD was injected at $x' = 6/7$ or $x' = 85.7\%$ from the neutral connection, and the captured PDs at bushing were filtered between $f_L = 800$kHz to $f_U = 4$MHz and at neutral point was between $f_L = 3.5$MHz to $f_U = 7$MHz. The estimation of location of PD can be seen clearly from the side view of Figure 8.14(c). The top view of Figure 8.14(b) shows the concentration of estimated charge close to the point of injection.

The location estimation based on data for the negative half cycle, was found for the value of $I_{Boff} = 0.0035$ as shown in Figure 8.15. The peak value was estimated to be at $x' = 85\%$ from the side view. As can be seen from the top view of the $\phi - \frac{x}{l} - n$ plot, the distribution of PD charge is more concentrated and localized.

Using an identical experimental procedure, surface discharge source location for the interleaved winding is shown in Figure 8.16 and 8.17 for the positive half cycle and negative half cycle estimation respectively. PD was injected at $x' = 3/7$ or $x' = 42.8\%$, and the estimated offset currents are $I_{Boff} = 0.99$ and $I_{Boff} = 0.025$ for positive and negative half cycle respectively.

For the PD void source, the estimation of location can be undertaken simultaneously for both positive and negative half cycles. This is due to the symmetrical property of the PD signals. PDs from the void source were injected at $x' = 4/7$ or $x' = 57.1\%$ on the interleaved winding. The PD signals were filtered for $f_L = 8$MHz and $f_U = 20$MHz on both bushing and neutral terminals. Figure 8.18 shows the PD location estimation on both positive and negative half cycles with estimated $I_{Boff} = 0.139$. Note that, all the PD location estimations from Figure 8.14 to 8.18 are assume that the value of the offset current at the neutral, I_{Noff} is approximately zero.

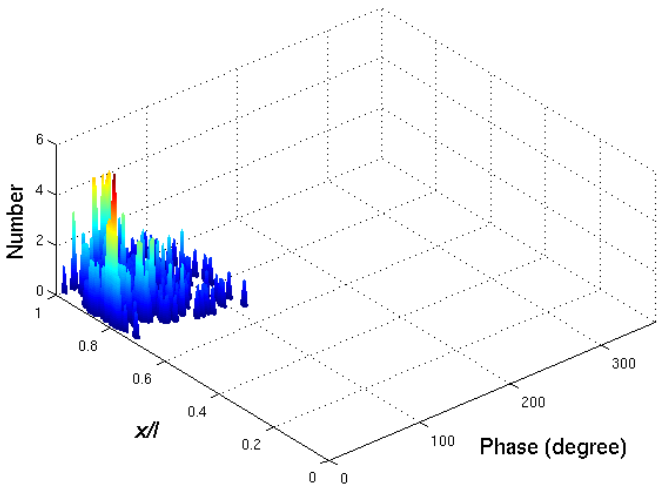

(a) 3D view of positive half cycle

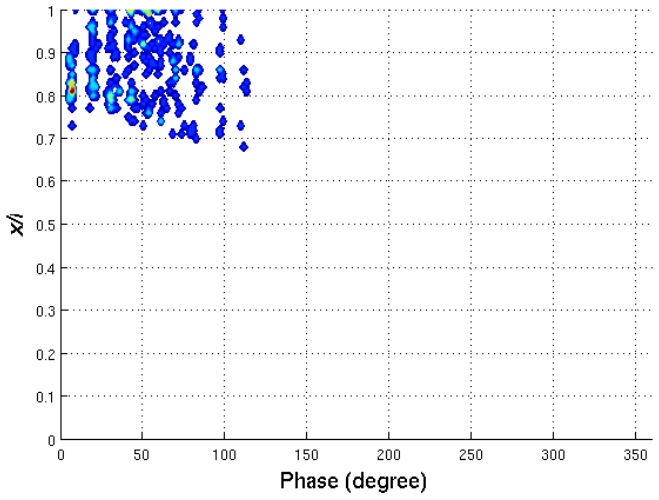

(b) Top view

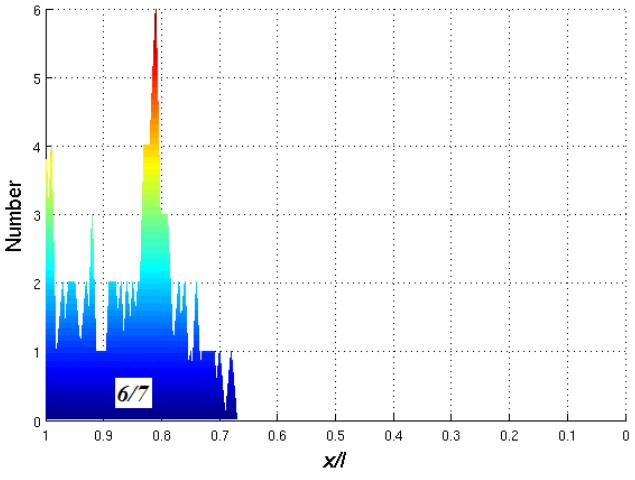

(c) Side view

FIGURE 8.14: Estimation of PD position of positive half cycle using MME technique from surface discharge in air injected at $x' = 6/7$ on plain winding: $I_{Boff} = 0.018$; Bushing: $f_L = 800$kHz, $f_U = 4$MHz. Neutral: $f_L = 3.5$MHz, $f_U = 7$MHz.

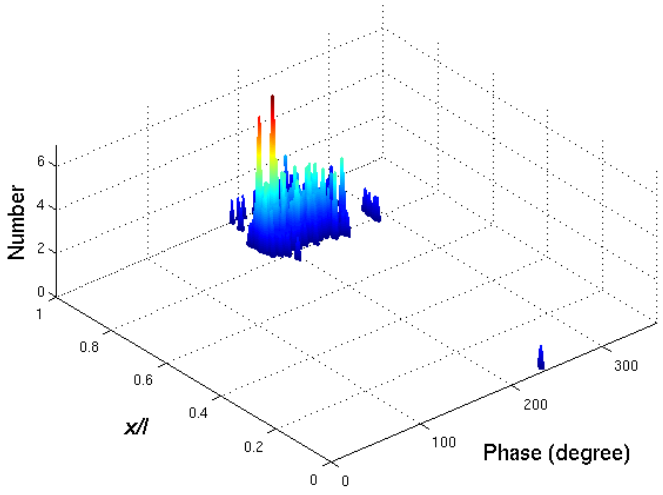

(a) 3D view of negative half cycle

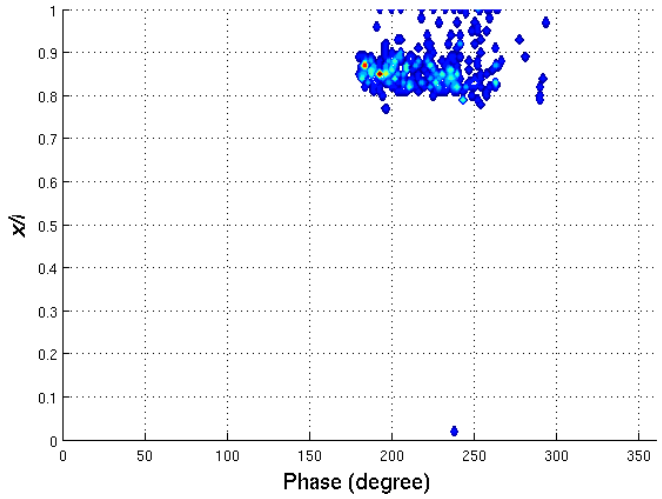

(b) Top view

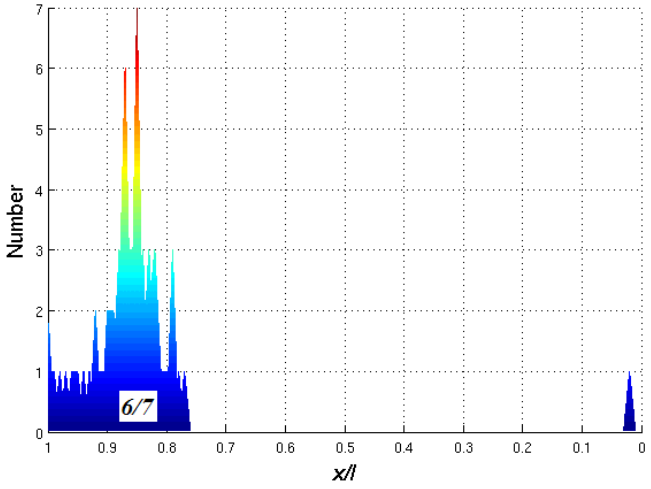

(c) Side view

FIGURE 8.15: Estimation of PD position of negative half cycle using MME technique from surface discharge in air injected at $x' = 6/7$ on plain winding $I_{Boff} = 0.0035$; Bushing: $f_L = 800$kHz, $f_U = 4$MHz. Neutral: $f_L = 3.5$MHz, $f_U = 7$MHz.

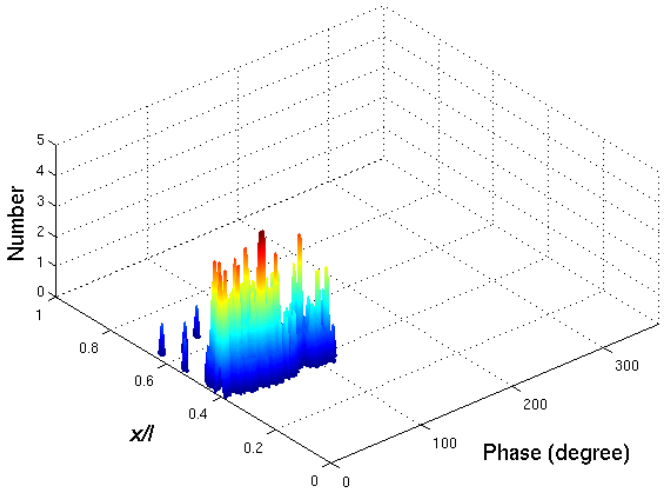

(a) 3D view of positive half cycle

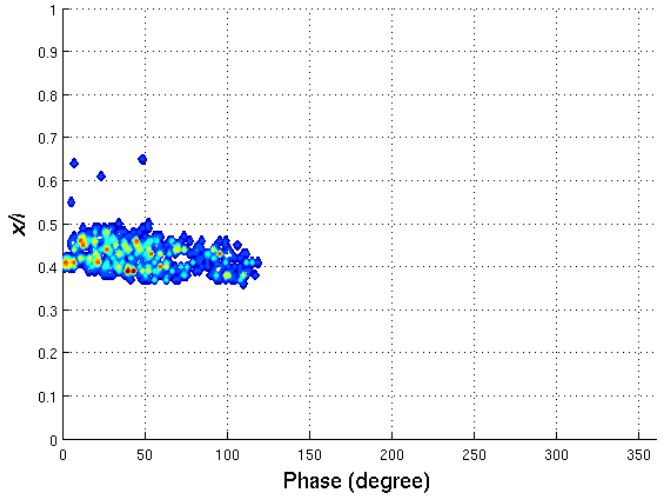

(b) Top view

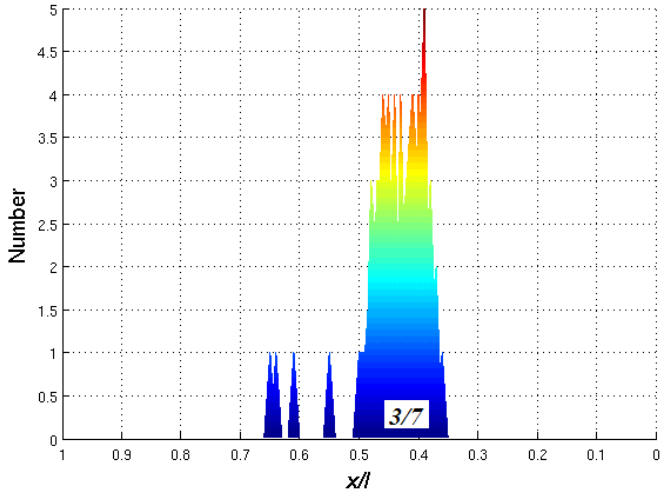

(c) Side view

FIGURE 8.16: Estimation of PD position of positive half cycle using MME technique from surface discharge in air injected at $x' = 3/7$ on interleaved winding: $I_{Boff} = 0.99$.; Bushing: $f_L = 800$kHz, $f_U = 4$MHz. Neutral: $f_L = 3.5$MHz, $f_U = 7$MHz.

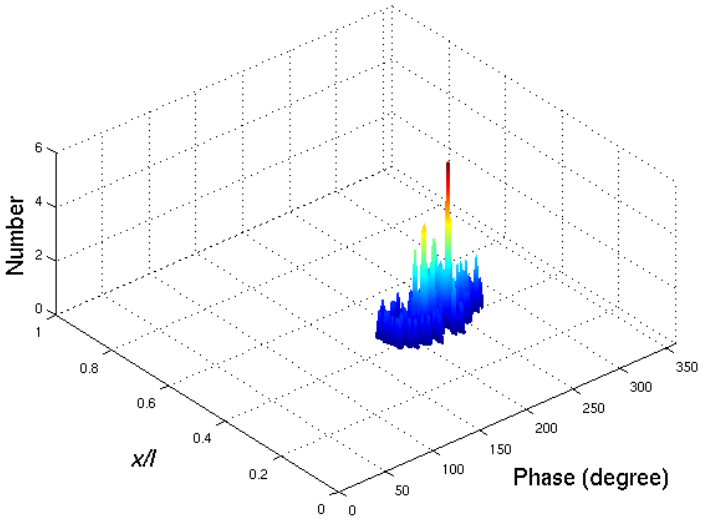

(a) 3D view of negative half cycle

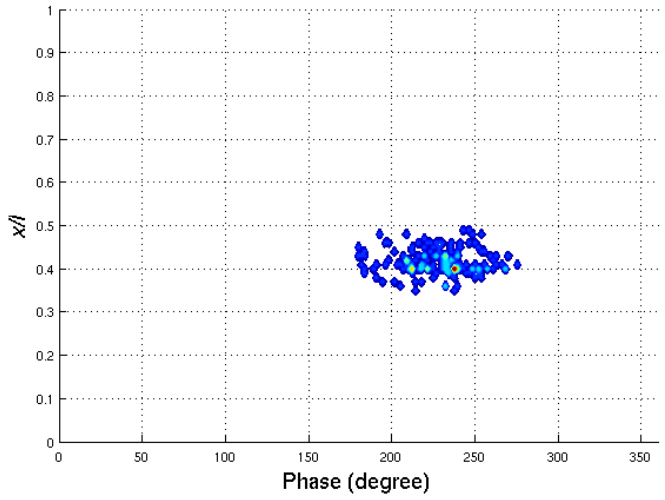

(b) Top view

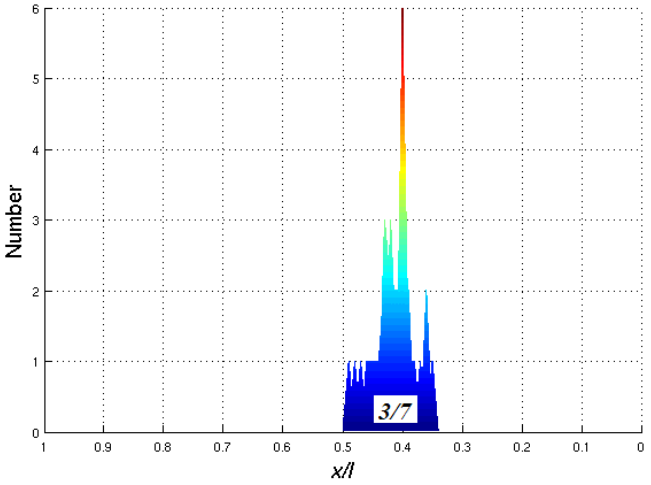

(c) Side view

FIGURE 8.17: Estimation of PD position of positive half cycle using MME technique from surface discharge in air injected at $x' = 3/7$ on interleaved winding: $I_{Boff} = 0.025$.; Bushing: $f_L = 800$kHz, $f_U = 4$MHz. Neutral: $f_L = 3.5$MHz, $f_U = 7$MHz.

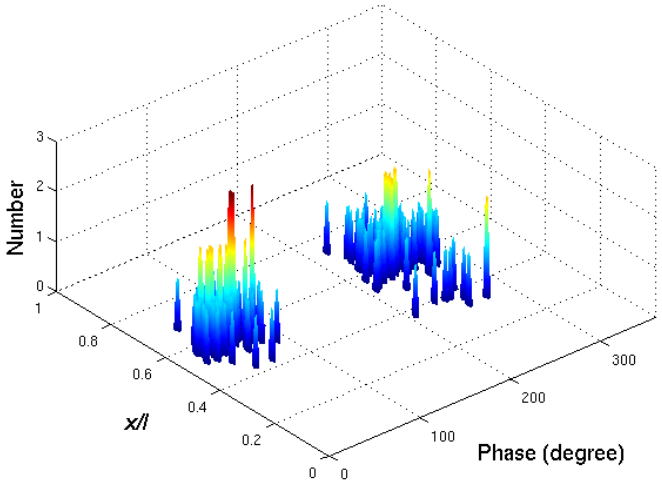

(a) 3D view

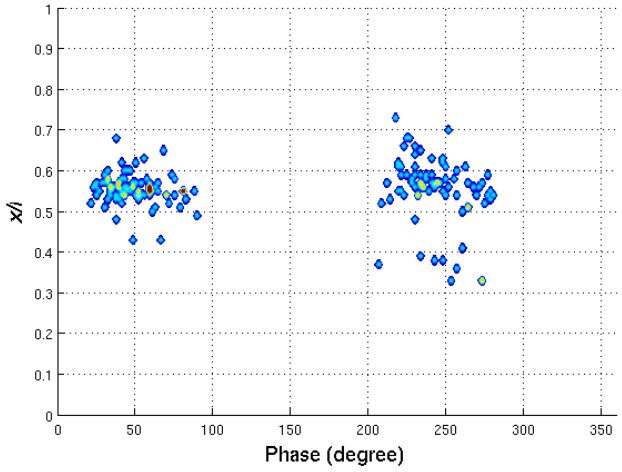

(b) Top view

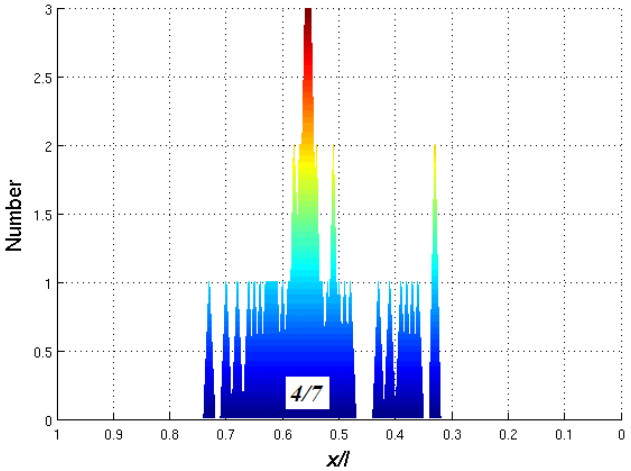

(c) Side view

FIGURE 8.18: Estimation of PD position using MME technique from PD in void injected at $x' = 4/7$ on interleaved winding $I_{Boff} = 0.139V$.; Bushing: $f_L = 8$MHz, $f_U = 20$MHz. Neutral: $f_L = 8$MHz, $f_U = 20$MHz.

8.4 Summary

Accumulated harmonic waveforms have been shown to contain considerable information about the location of partial discharge along the windings. Pulses with different widths and rise times generate different levels of accumulated harmonic waves. The current amplification factor in the time domain has been found to have a near identical solution for the predominantly capacitive region and the transmission line mode of the transformer winding response. The magnitude estimation detailed in this chapter, however, only estimates the closest possible value of the PD magnitudes at the winding ends, but does not give an accurate value at the PD source itself. Thus it is only possible to estimate the location by analysing the error deviation from measured magnitudes.

The current distribution based on the amplification factor of the split winding analysis model has the ability to estimate the amplitude of the current in the mV range at the bushing and neutral points. A new technique of MME has been introduced to locate the PD source location with the calculation of minimum deviation from the zero line. The arrangement of current amplitude error in a matrix form gives a graphical representation of the possible location of PD sources which is also derived using the MME technique.

Chapter 9

Partial Discharge Magnitude Estimation

Partial discharge magnitude estimation is important for evaluating the severity of any fault. The estimation considers the high frequency region of the derived models. From Chapter 8, the estimation of PD source location is essential prior to the estimation of PD magnitude along a transformer winding.

The model description under consideration is based on the predominantly capacitive region which gives a fixed distribution solution. Once the location of a PD source is estimated, the knowledge of location can be used to determine the magnitude of the PD. A bandpass filter is used to select the frequency of interest for the estimation of PD magnitude. The regions of interest are based on the peak pole positions that carry the information about the dominant harmonic component.

As the fixed distribution model equation is derived based on a lumped capacitive model, the point of estimation considered in this Chapter is defined along the winding length of both the interleaved and plain winding. The assumption made in this Chapter is that, the bushing used in the experiment is PD free up to 45kV. The sensors involved in PD magnitude estimation are RFCT2, RFCT3, RFCT4 and RFCT5.

9.1 PD Magnitude Estimation at Intermidiary Points along the Winding

The estimation is based on the model description in Chapters 3 and 4. This section investigates the harmonic components of PDs measured at different points using RFCTs based on the circuit arrangement of Figure 7.26. The end terminals measurements are used as input references to estimate the intermediary PD levels.

9.1.1 D'Alembert Solution to PDs

As has been shown in Chapter 4, the determination of a signal level at the source x' can be found by solution of D'Alembert formula. The analytical solution derived from Equation (4.56) is the solution of standing wave oscillations in the x-t plane. In other words, the oscillation levels are based on the travelling wave in a transformer winding that starts from $x = x'$ to $x = l$ and $x = 0$. The travelling waves are influenced by the circuit configurations which can be represented by the lumped parameter model.

In the case of waves that travel before reaching a transition point represented by the transformer winding, the circuit configuration and the ground connection do not have an influence to the source waveform. Hence the D'Alembert solution can also determine the original source of waves before the transition point. Figure 9.1 shows a graphical representation of a rectangular travelling wave on an x-t plane at a source point. The figure shows that $F(x,t)$ represents the waveform at the source just before reaching the x-plane, and at $t = 5\delta t$, $1/2F(x,t)$ is the waveform on the x-plane at the source point. Note that at this point, the area of the waveform at $t = 0$ to $t = 5\delta t$ are the same, where δt is a small change of time.

With reference to Figure 7.26, RFCT3 is the current sensor of PD propagation before reaching the transformer winding at the source point, and RFCT4 is the current sensor of PD signal propagation at the transformer. Hence, according to D'Alembert solution from the graphical representation of Figure 9.1 the relationship between the magnitude of RFCT3 and RFCT4 is:

$$RFCT3 \approx 2 \times RFCT4 \tag{9.1}$$

with a bounded length of transformer winding for the source between, $l > x' > 0$. An experimental result of measurements using RFCT3 and RFCT4 and the interleaved winding is shown in Figure 9.2 and Figure 9.3. Results obtained for void discharges using the plain winding are included in Appendix F. Partial discharge signal from a surface discharge source were injected along the interleaved winding from $x' = 7/7$ to $x' = 0/7$. As the relationship of the RFCTs from Equation (9.1), is easily identified by measuring the amplitude of PD waveforms, thus the results presented are based on the $\phi - q - n$ pattern and only differ by the magnitudes of the measurements. The results show that the PD magnitudes measured by the RFCTs are in agreement with the relationship from Equation (9.1). Where the PD levels are between 120mV to 450mV measured by RFCT3 and 60mV to 225mV measured by RFCT4 during the positive half cycle.

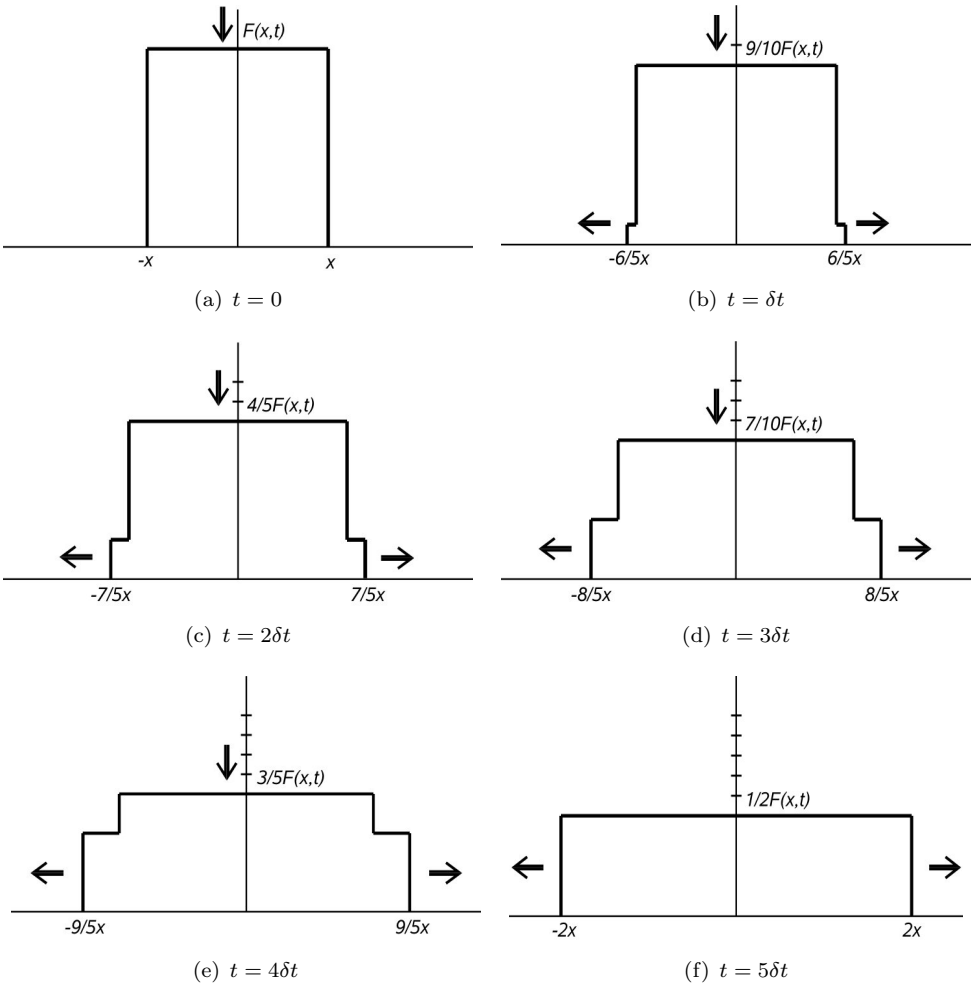

(a) $t = 0$ (b) $t = \delta t$

(c) $t = 2\delta t$ (d) $t = 3\delta t$

(e) $t = 4\delta t$ (f) $t = 5\delta t$

FIGURE 9.1: Graphical representation of D'Alembert solution

However, for PD signal injection at $x' = 0/7$, the level of PD signal measured by RFCT3 is between 150mV to 450mV, whereas PD signals measured by RFCT4 are between 50mV to 150mV, i.e RFCT3 data has a three times higher value than that of RFCT4. This is due to the circuit configuration at the winding end (neutral to ground connection), where, when applying a PD current at the neutral to ground connection, the amount of current flowing to the ground is divided by the existing neutral to ground connection measured by RFCT5 which also measuring the same source, please refer to Figure 7.36 (Section 7.3).

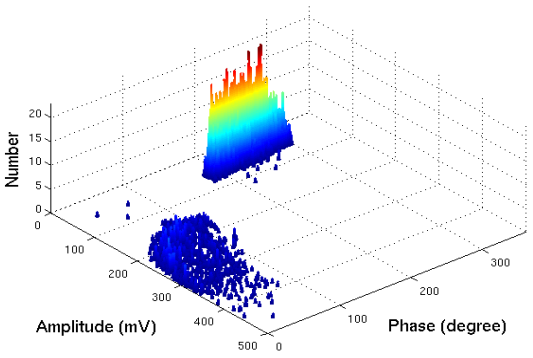

(a) $x' = 7/7$, RFCT3

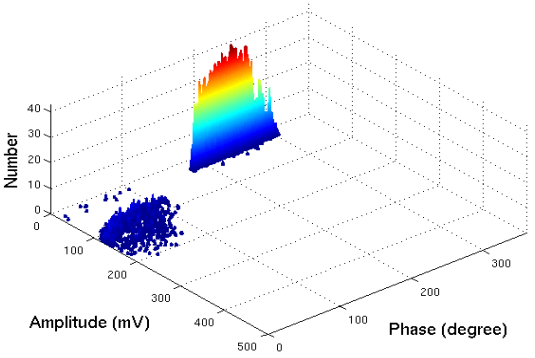

(b) $x' = 7/7$, RFCT4

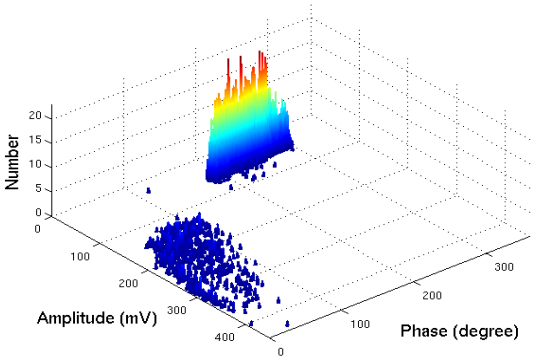

(c) $x' = 6/7$, RFCT3

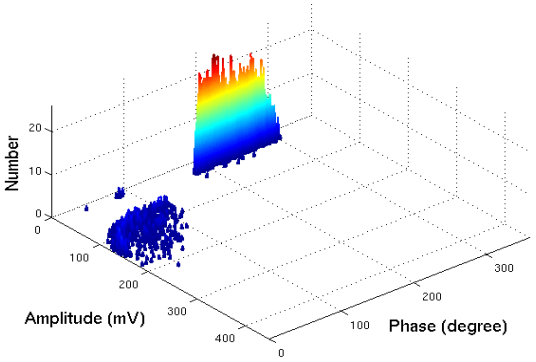

(d) $x' = 6/7$, RFCT4

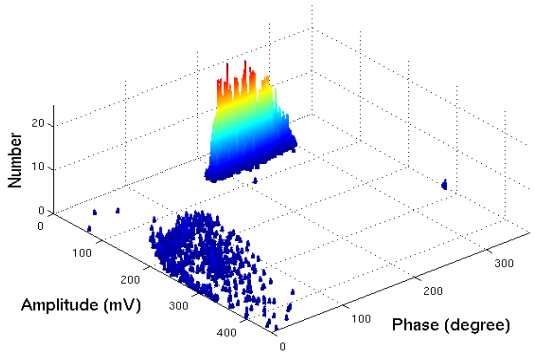

(e) $x' = 5/7$, RFCT3

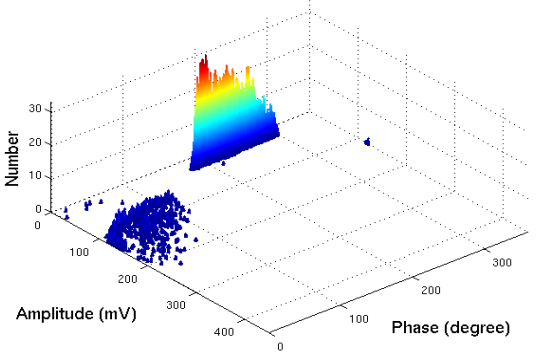

(f) $x' = 5/7$, RFCT4

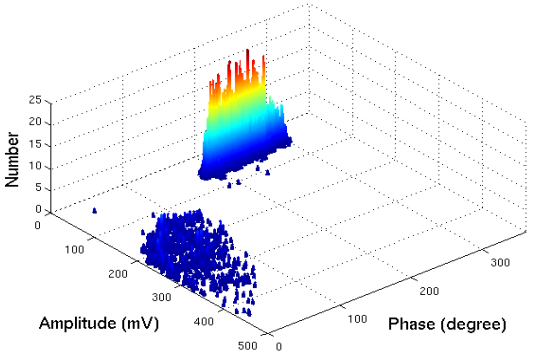

(g) $x' = 4/7$, RFCT3

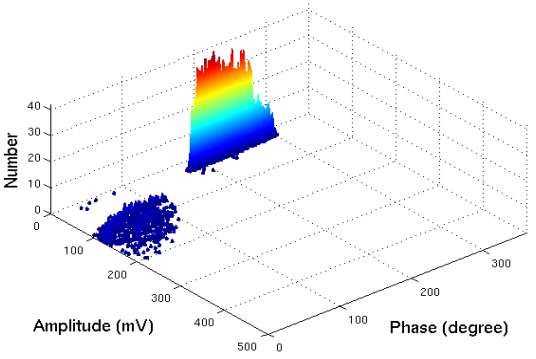

(h) $x' = 4/7$, RFCT4

FIGURE 9.2: Comparison of measurement from RFCT3 and RFCT4 at different $x' = 7/7$ to $x' = 4/7$ for interleaved winding

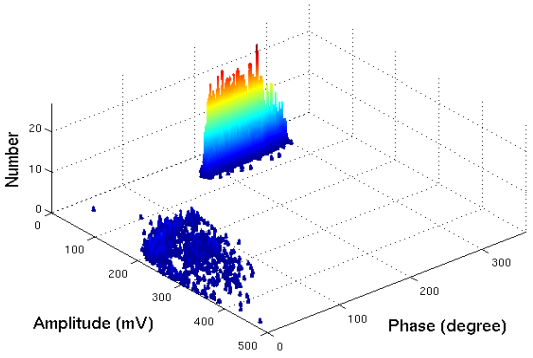

(a) $x' = 3/7$, RFCT3

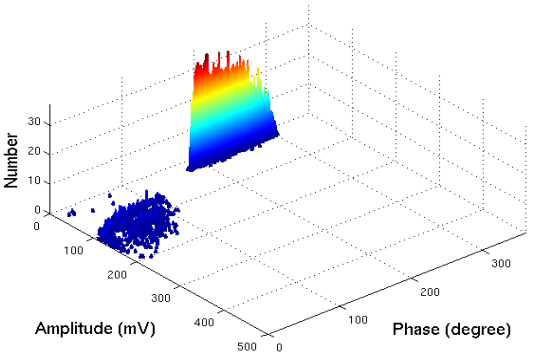

(b) $x' = 3/7$, RFCT4

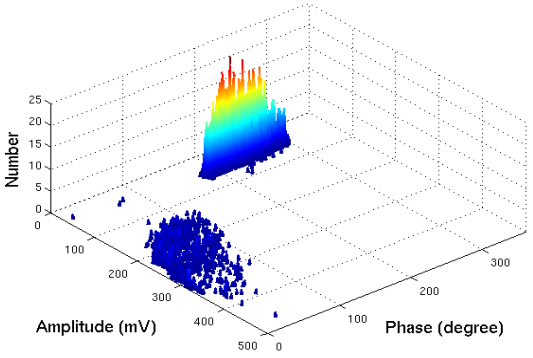

(c) $x' = 2/7$, RFCT3

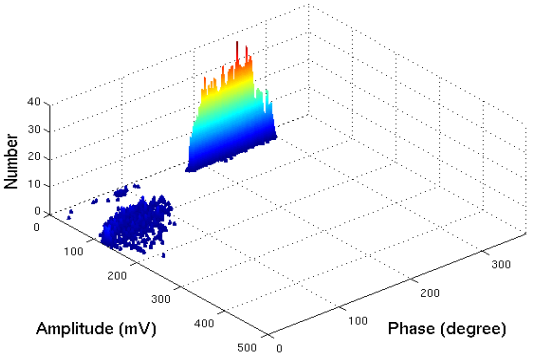

(d) $x' = 2/7$, RFCT4

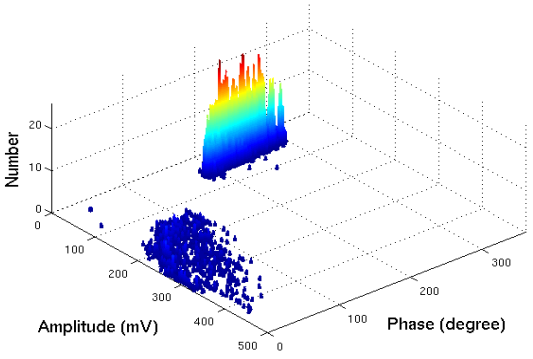

(e) $x' = 1/7$, RFCT3

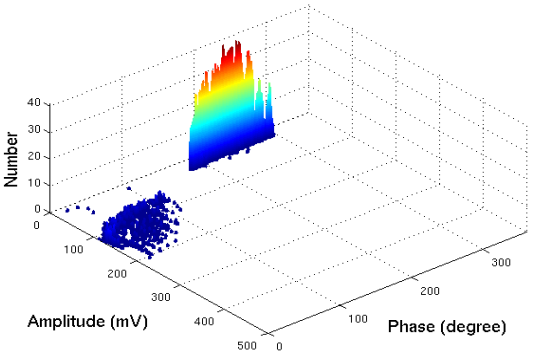

(f) $x' = 1/7$, RFCT4

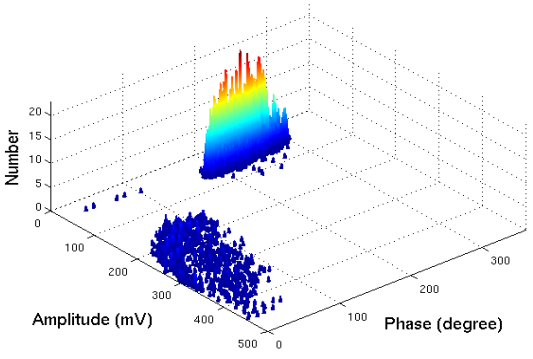

(g) $x' = 0/7$, RFCT3

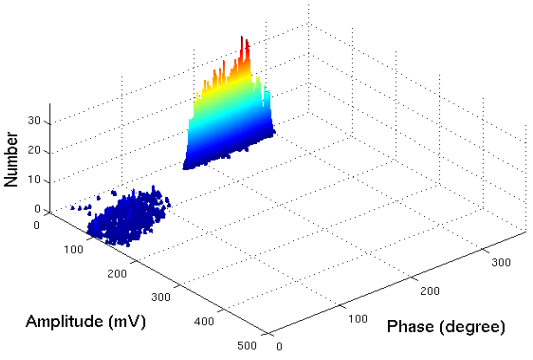

(h) $x' = 0/7$, RFCT4

FIGURE 9.3: Comparison of measurement from RFCT3 and RFCT4 at different $x' = 3/7$ to $x' = 0/7$ for interleaved winding

9.1.2 The Current Capacitive Model Equation

The current capacitive model equation is based on the current flowing out of the transformer winding. Hence, under predominantly capacitive conditions with $i_L \approx 0$, Equations (B.1) and (B.3) are relevant. If the definition of current flowing in the shunt capacitor K, is

$$i_k = K\frac{\partial^2 v}{\partial x \partial t} \tag{9.2}$$

Then substitution of Equation (B.1) and Equation (B.3) into (9.2), yields two general equations for current flowing out of the transformer winding as:

$$i_b(x) = K\alpha_B \frac{\partial}{\partial t}\Big[-C\,sin(j\alpha_B x) + D\,cos(j\alpha_B x)\Big] \tag{9.3}$$

$$i_n(x) = K\alpha_N \frac{\partial}{\partial t}\Big[A\,sinh(\alpha_N x) + B\,cosh(\alpha_N x)\Big] \tag{9.4}$$

Where $i_n(x)$ and $i_b(x)$ are the current flowing towards the neutral to ground connection and towards bushing respectively. Using the same boundary conditions as in Equations (B.6) and (B.7) i.e;

$$i_b = I_B \qquad at \qquad x = l \tag{9.5a}$$

$$i_n = I_N \qquad at \qquad x = 0 \tag{9.5b}$$

$$i_b(x) = i_n(x) \qquad at \qquad x = x' \tag{9.6a}$$

$$\frac{di_b(x)}{dx} = \frac{di_n(x)}{dx} \qquad at \qquad x = x' \tag{9.6b}$$

the current distribution in the predominantly capacitive region can also be based on a split winding analysis. Solving the Equations (9.3) to (9.6) simultaneously, and writing the differential operator $\frac{\partial}{\partial t}$ as ρ, yields:

$$A = \frac{-Csin(j\alpha_B x') + Dcos(j\alpha_B x') - Bcosh(\alpha_N x')}{sinh(\alpha_N x')} \tag{9.7}$$

$$B = \frac{I_N}{K\rho\alpha_N} \tag{9.8}$$

$$C = \frac{\frac{I_B}{\alpha_B}\Big[cos(j\alpha_B x')cosh(\alpha_N x') + sin(j\alpha_B x')sinh(\alpha_N x')\Big] - \frac{I_N}{\alpha_N}cos(j\alpha_B l)}{K\rho\widehat{F}} \tag{9.9}$$

$$D = \frac{\frac{I_B}{\alpha_B}\Big[sin(j\alpha_B x')cosh(\alpha_N x') - cos(j\alpha_B x')sinh(\alpha_N x')\Big] - \frac{I_N}{\alpha_N}sin(j\alpha_B l)}{K\rho\widehat{F}} \tag{9.10}$$

where

$$\begin{aligned}\widehat{F} = cos(j\alpha_B l)\Big[sin(j\alpha_B x')cosh(\alpha_N x') - cos(j\alpha_B x')sinh(\alpha_N x')\Big] \\ - sin(j\alpha_B l)\Big[cos(j\alpha_B x')cosh(\alpha_N x') + sin(j\alpha_B x')sinh(\alpha_N x')\Big]\end{aligned} \tag{9.11}$$

α_B and α_N are the estimated fixed distribution constants at the bushing and neutral respectively, and can be calculated using Equation (8.15), for which α is taken as an absolute value. All the constants A, B, C and D, have a common denominator of $K\rho$, and this cancels when substituting the constants back into Equations (9.3) and (9.4). Therefore, an estimation of intermediary current level at a point x' is possible with a measured value of I_B and I_N at the bushing and neutral terminals respectively, regardless of any value of shunt capacitor K.

9.1.3 Peaks Poles Estimation

An experiment using surface discharge injection into the interleaved winding was conducted to demonstrate the level of PD signal at points along the winding. RFCT2, RFCT4 and RFCT5 of Figure 7.26 were all triggered on the oscilloscope with a zero crossing detector fed from the high voltage a.c supply. The injection of PD signal was at $x' = 1/7$ or $x' = 14.3\%$ from the neutral to ground connection.

Figure 9.4 shows the frequency spectrum of the detected PD signals at the three RFCTs. The Bode plot represents a duration of PD signal monitoring for 25 cycles and a total of 1422 detected PD signals for both positive and negative half cycles occured during this time interval.

At high frequency, under the influence of the predominantly capacitive region, the propagated signals will experience no loss with same range frequencies and will have almost the same phase difference from a point of the applied wave to the measurement points. Hence, Figures 9.4(a), 9.4(b) and 9.4(c) are labeled with four peak poles, which are identified as the peak frequency components that exist along the transformer winding from the source point to the end winding terminals. With reference to Figure 9.4 the four pole peaks are labeled as *1st*, *2nd*, *3rd* and *4th*. The *1st* has a peak pole value at a frequency between 1.7MHz to 2.2MHz, *2nd* between 9.5MHz to 11MHz, *3rd* between 30MHz to 40MHz and *4th* between 50MHz to 70MHz.

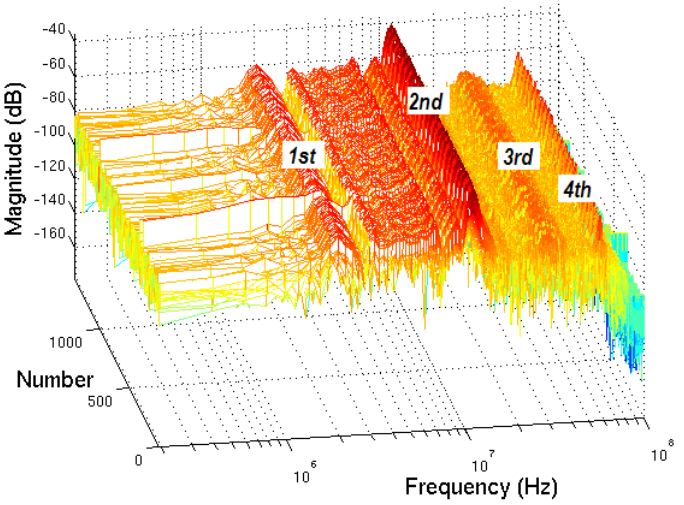

(a) PD at $x' = 1/7$, measured at $x = 7/7$ (RFCT2)

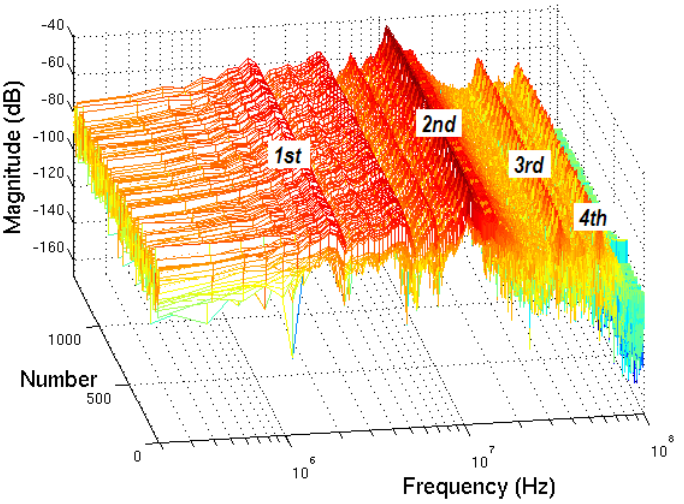

(b) PD at $x' = 1/7$, measured at $x' = 1/7$ (RFCT4)

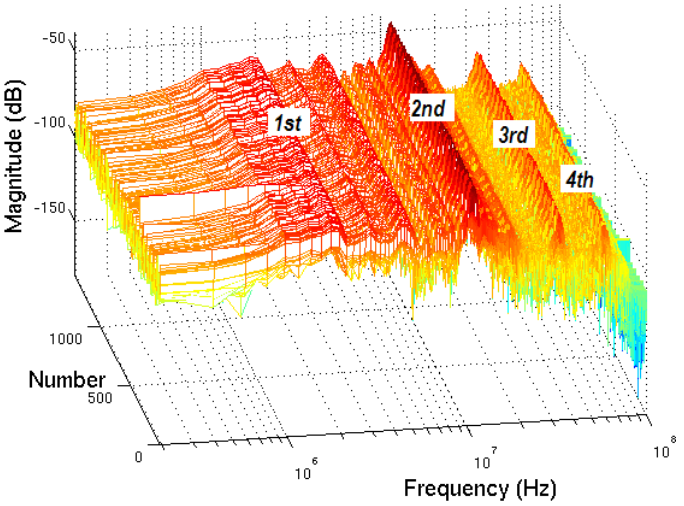

(c) PD at $x' = 1/7$, measured at $x = 0/7$ (RFCT5)

FIGURE 9.4: Frequency domain spectrum of surface discharge in air on interleaved winding over $0.5s$, injection at $x' = 1/7$

Figures 9.5 to 9.8 show extractions of the time domain detected PDs filtered using the frequency ranges relating to the four poles for the three RFCTs. Using a zero phase bandpass filtering technique, the filtered time domain signal estimation has an unaffected phase compared to the original waveform. The results show that at the frequencies of the main poles, the time domain waveforms have a similar waveshape but different amplitudes.

For every detected and filtered waveform, a maximum absolute value is estimated that represents I_B and I_N for the bushing terminal and neutral to ground measurements respectively. The measured values are then applied to the model Equations of (9.3) and (9.4) to provide an estimation based on measurements at bushing and neutral terminals respectively. The value of α_B and α_N are calculated from the maximum peak pole magnitudes in the frequency domain. An estimation of the intermediary current level at x' measured by RFCT4 is determined using the D'Alembert solution as follows;

$$i(x') = \frac{i_b(x') + i_n(x')}{2} \tag{9.12}$$

Figures 9.9 to 9.12 show the comparison results of the corresponding filtered waveforms. The comparison considers the maximum absolute magnitude and is plotted in the $\phi - q - n$ pattern. With reference to Figure 9.9, the PD pattern on the positive half cycle shows a good approximation, however for the negative half cycle, the measured PD waveforms have higher magnitudes. This is due to the accumulated harmonic waveform that contributes to the overall amplitudes at low frequencies and lower magnitudes. However as shown in Figures 9.10, 9.11 and 9.12, the $\phi - q - n$ estimation using the predominantly capacitive regions is more accurate at higher frequencies when considering the different peak pole magnitudes.

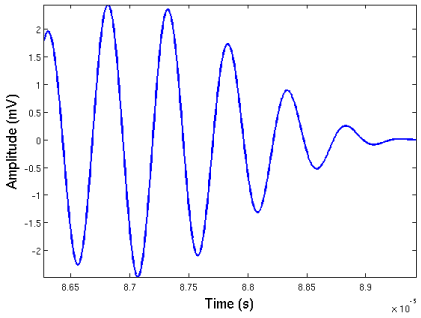

(a) Filtered PD waveform at $x = 7/7$

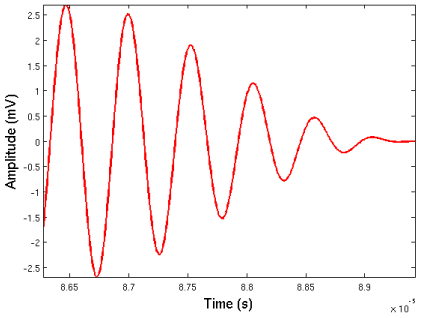

(b) Filtered PD waveform at $x' = 1/7$

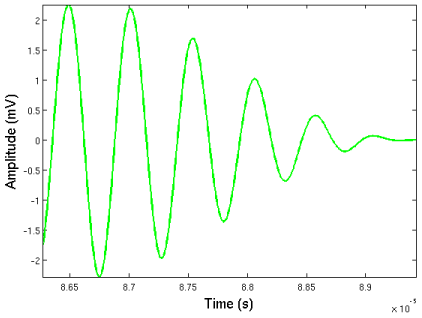

(c) Filtered PD waveform at $x = 0/7$

FIGURE 9.5: Time domain PD waveform filtered at $f_L = 1.7$MHz, $f_U = 2.2$MHz ($1st$ peak), injection at $x' = 1/7$ on interleaved winding

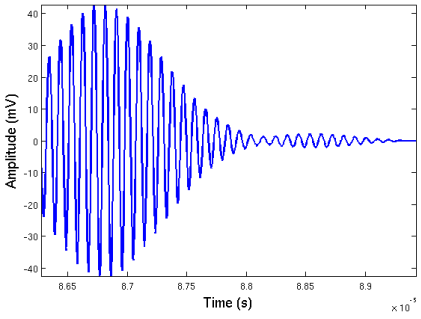

(a) Filtered PD waveform at $x = 7/7$

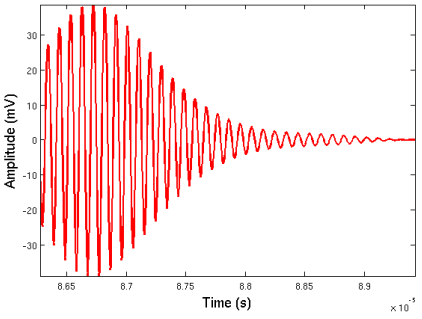

(b) Filtered PD waveform at $x' = 1/7$

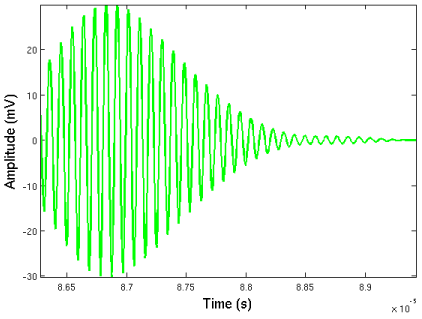

(c) Filtered PD waveform at $x = 0/7$

FIGURE 9.6: Time domain PD waveform filtered at $f_L = 9.5$MHz, $f_U = 11$MHz ($2nd$ peak), injection at $x' = 1/7$ on interleaved winding

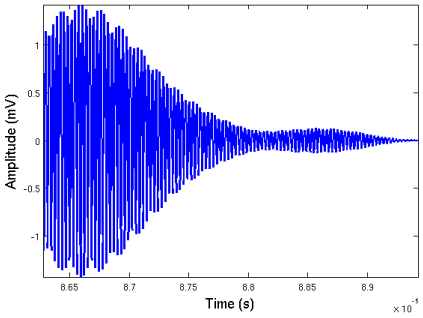

(a) Filtered PD waveform at $x = 7/7$

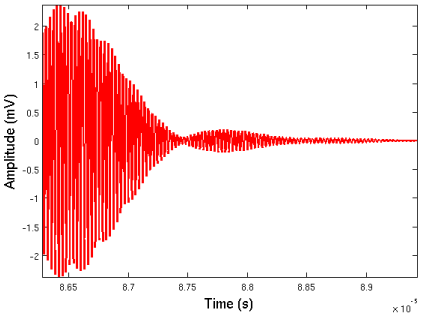

(b) Filtered PD waveform at $x' = 1/7$

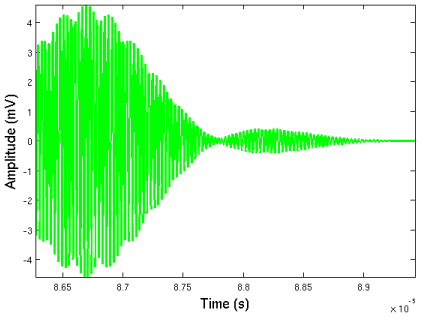

(c) Filtered PD waveform at $x = 0/7$

FIGURE 9.7: Time domain PD waveform filtered at $f_L = 32$MHz, $f_U = 33$MHz ($3rd$ peak), injection at $x' = 1/7$ on interleaved winding

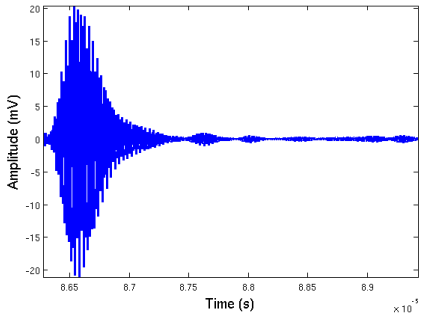

(a) Filtered PD waveform at $x = 7/7$

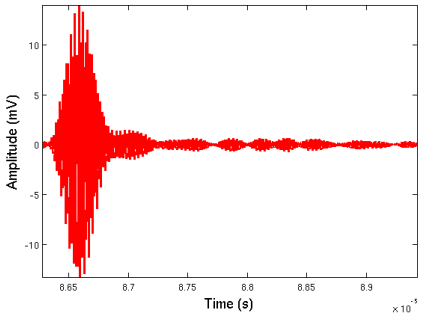

(b) Filtered PD waveform at $x' = 1/7$

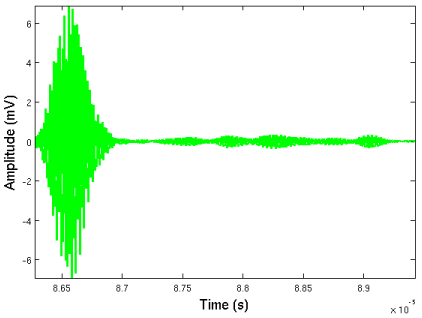

(c) Filtered PD waveform at $x = 0/7$

FIGURE 9.8: Time domain PD waveform filtered at $f_L = 54$MHz, $f_U = 60$MHz ($4th$ peak), injection at $x' = 1/7$ on interleaved winding

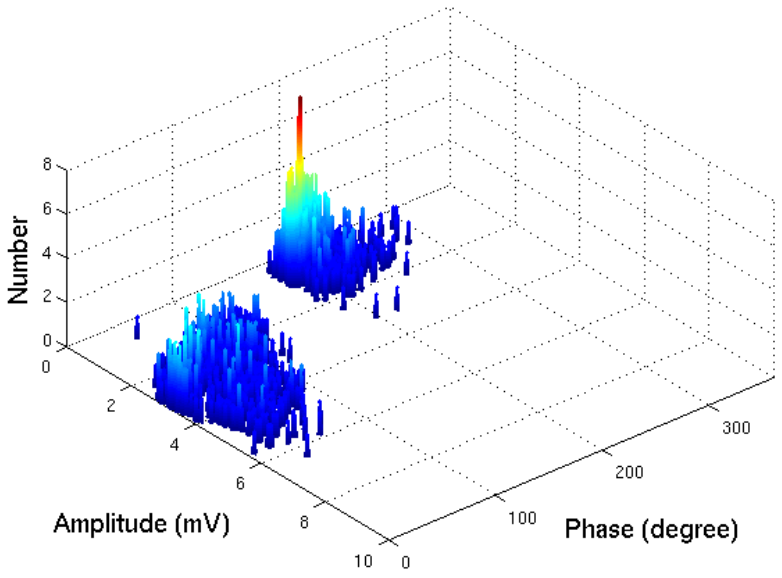

(a) Measured at $x' = 1/7$

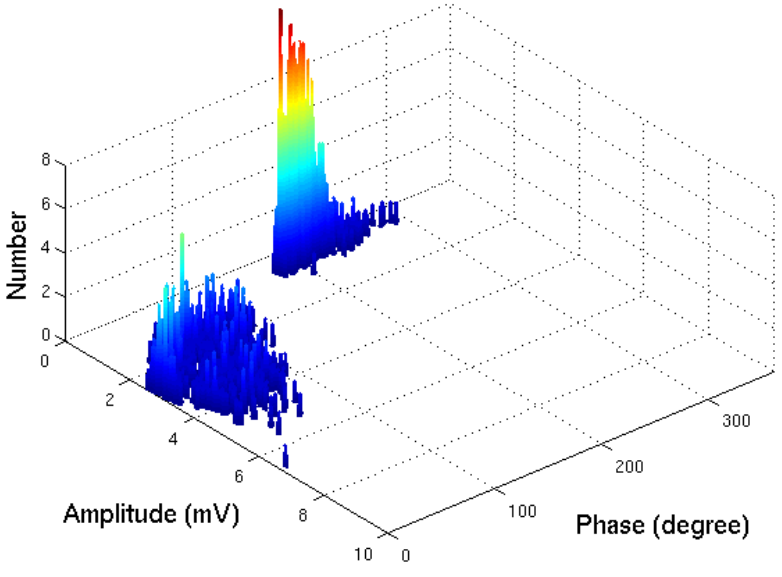

(b) Model estimation at $x' = 1/7$

FIGURE 9.9: Surface discharge pattern measured and estimated, filtered at f_L = 1.7MHz, f_U = 2.2MHz, injection at $x' = 1/7$ on interleaved winding

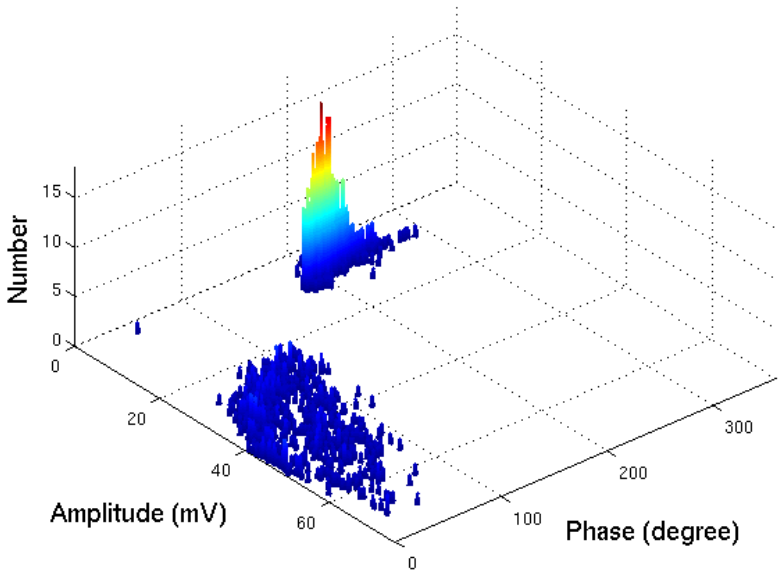

(a) Measured at $x' = 1/7$

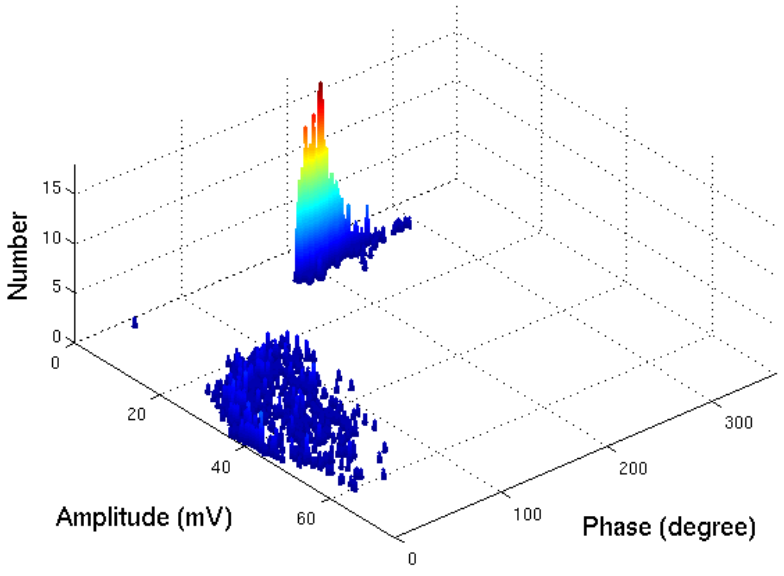

(b) Model estimation at $x' = 1/7$

FIGURE 9.10: Surface discharge pattern measured and estimated, filtered at $f_L = 9.5$MHz, $f_U = 11$MHz, injection at $x' = 1/7$ on interleaved winding

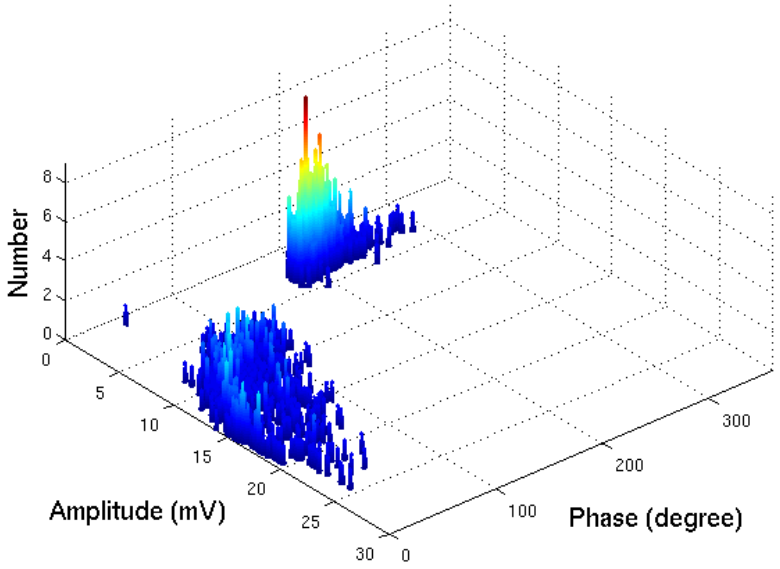

(a) Measured at $x' = 1/7$

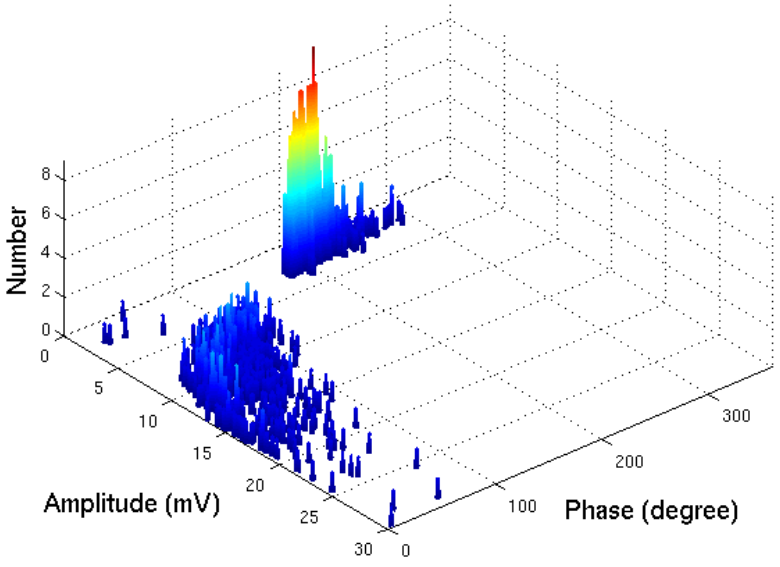

(b) Model estimation at $x' = 1/7$

FIGURE 9.11: Surface discharge pattern measured and estimated, filtered at $f_L = 30\text{MHz}$, $f_U = 40\text{MHz}$, injection at $x' = 1/7$ on interleaved winding

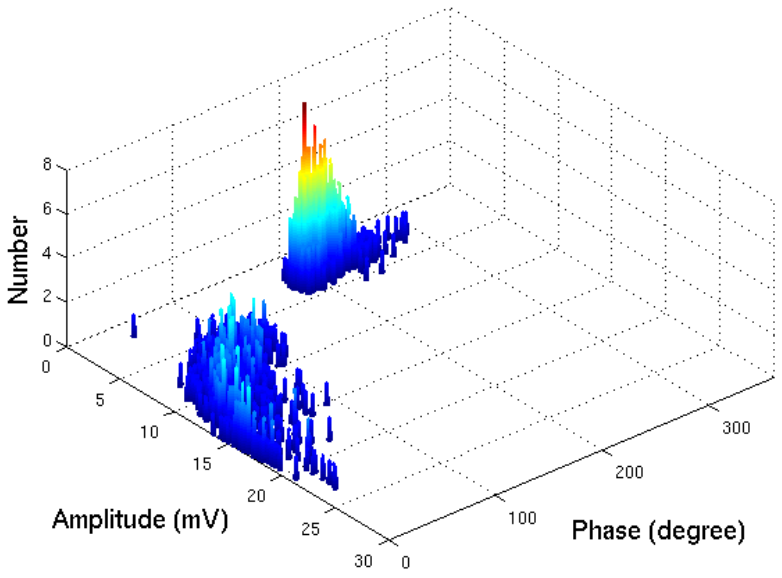

(a) Measured at $x' = 1/7$

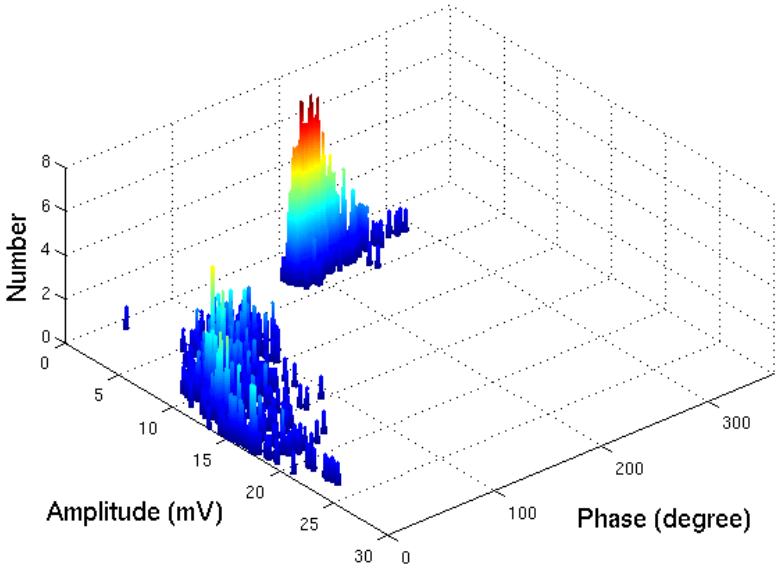

(b) Model estimation at $x' = 1/7$

FIGURE 9.12: Surface discharge pattern measured and estimated, filtered at $f_L = 50\text{MHz}$, $f_U = 70\text{MHz}$, injection at $x' = 1/7$ on interleaved winding

9.1.4 Estimation over a Wider Frequency Range

Using the analysis of Section 9.1.3, PD magnitude estimation under the predominantly capacitive region is also possible for a wide frequency range. The estimation will include a considerable number of similar peak poles at localized positions in frequency domain along a transformer winding. Hence, this allows an estimation of PD magnitudes based on the range of frequencies that are similar to the original PD source at point $x = x'$ and at measurement points $x = l$ and $x = 0$. As PD magnitudes are variable and often buried in a noisy system, the estimation over a wide frequency range within the predominantly capacitive distribution also involves the same process of frequency transformation and zero phase filtering.

Using partial discharges from a void, an experiment of PD signal injection into both transformer winding types, interleaved winding and plain winding, was undertaken and data recorded on the DSO using sampling rate at 200MHz. The total recorded data length was 100MS, equivalent to 0.5s or 25 cycles of applied voltage.

PD signals from the void source were injected at $x' = 4/7$ on the interleaved winding, and measurements made using RFCT2, RFCT4 and RFCT5. Figure 9.13 shows an example of the PD signal waveform from a cylindrical void filtered between f_L =7MHz to f_U =90MHz. The maximum levels of absolute value were calculated at both the bushing terminal, RFCT2 (I_B), and the neutral to ground connection, RFCT5 (I_N), in order to estimate the level of the source measured by RFCT4. Figure 9.14 shows the $\phi - q - n$ pattern of the PD signals from the void for over a period of 50 cycles (25 cycles per measurement). The Figure shows a close agreement between the estimated pattern by the model equation (Figure 9.14(b)) and the measurement pattern at $x' = 4/7$ (Figure 9.14(a)).

The experiment was repeated on the plain winding with the PD signal injection from the void source at $x' = 5/7$. Figure 9.15 shows an extraction of a time domain PD waveform for the range between $68.8\mu s$ to $71.9\mu s$. The frequency domain extraction of Figure 9.15(d) shows the filtered spectrum of the extracted PD at the two end measurements and the source. Figure 9.16 shows the comparison of the measured $\phi - q - n$ PD pattern and the estimated $\phi - q - n$ pattern of the PD signal at $x' = 5/7$. Again, the pattern shows a good match between the measurement and the estimation. Note that the absolute maximum value of the time domain extraction shows that the PD level measured at the bushing tap point is the highest, followed by that at the source point and then the neutral to ground connection.

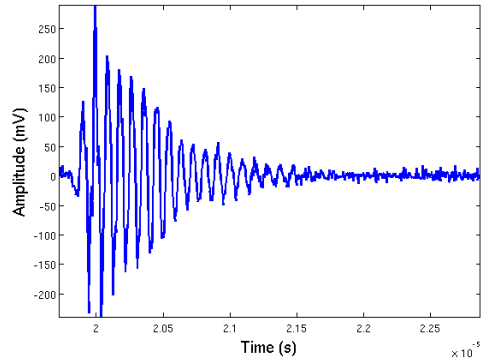

(a) Filtered PD waveform at $x = 7/7$, max $|i_b(l)| = 288.9mV$

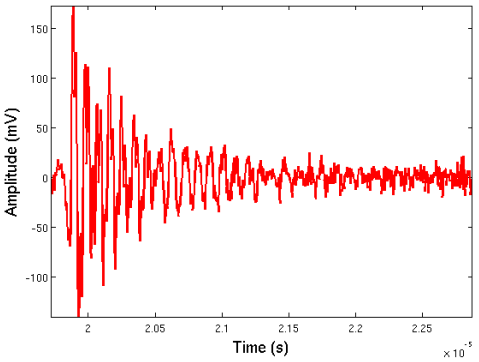

(b) Filtered PD waveform at $x' = 4/7$, max $|i(4/7)| = 172.9mV$

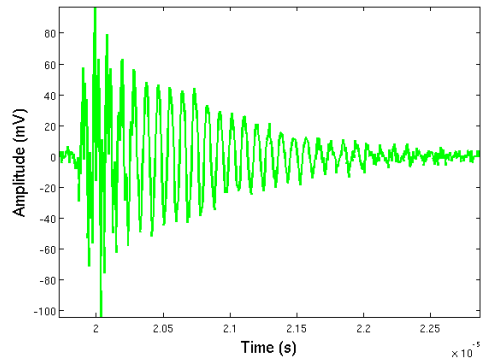

(c) Filtered PD waveform at $x = 0/7$, max $|i_n(0)| = 104.3mV$

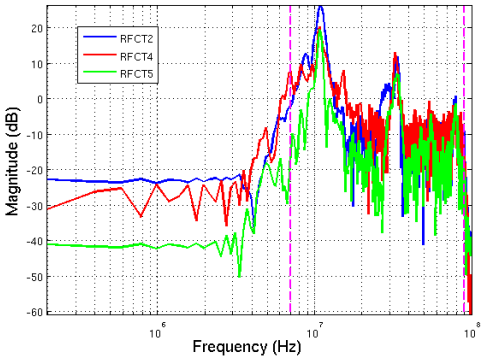

(d) The filtered spectrum

FIGURE 9.13: Extraction of PD waveform from void with 200MHz sampling frequency, filtered at $f_L = 7$MHz, $f_U = 90$MHz, injection at $x' = 4/7$ on interleaved winding

An investigation of the higher frequency range is achieved by adopting a higher sampling rate. The surface discharge source was injected into the plain winding at $x' = 2/7$ and measured at RFCT2, RFCT4 and RFCT5 using a 1GHz sampling frequency. With the higher sampling rate, the period of monitoring and measurement is limited to only 10 cycles of applied voltage (5 cycles per measurement). Figure 9.17 shows the time domain extraction of PD waveforms measured at bushing tap point, the source and neutral to ground connection were filtered between $f_L = 7$MHz to $f_U = 150$MHz. The wide frequency range is selected based on the visible number of peaks poles and also eleminating the background noise above 200MHz. The result of Figure 9.18 shows a close agreement of the $\phi - q - n$ patterns between measurement and estimation for a wider frequency range and for higher frequencies above 100MHz.

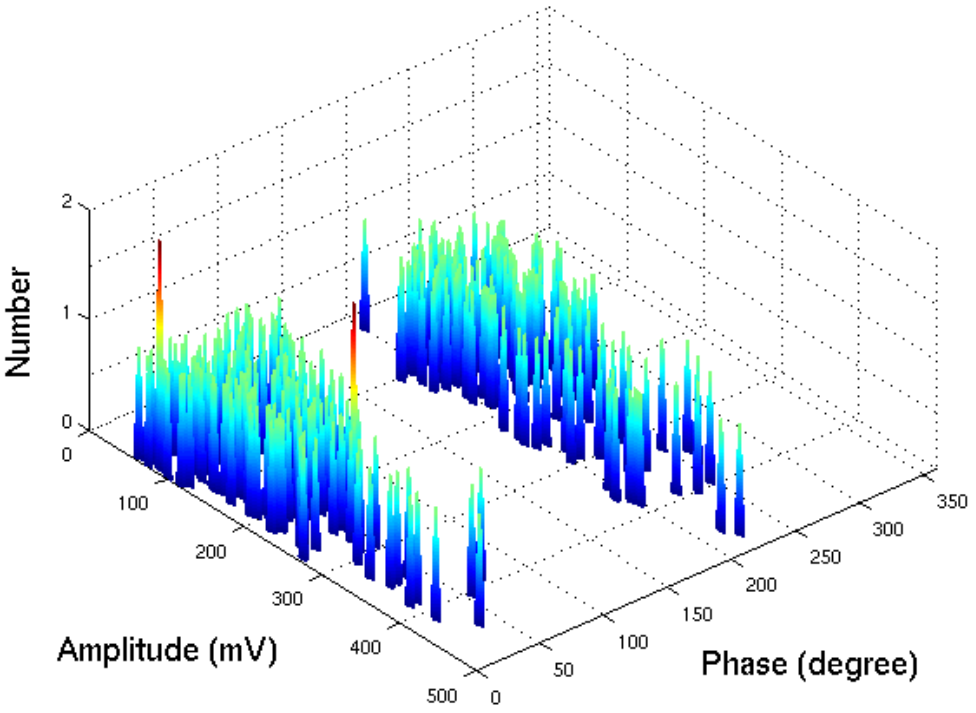

(a) Measured at $x' = 4/7$

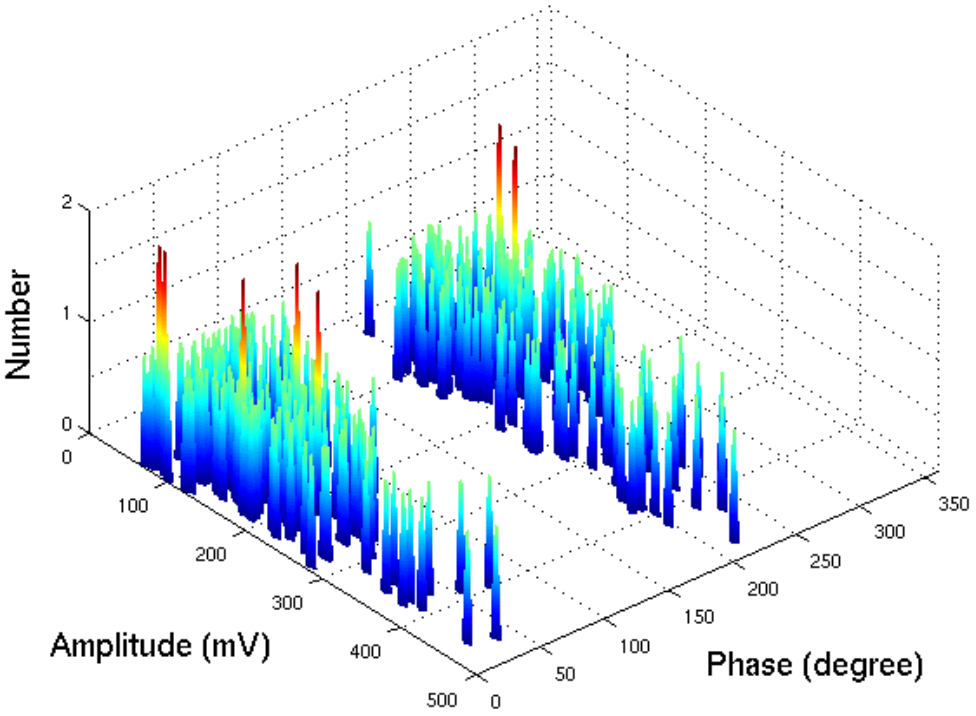

(b) Model estimation at $x' = 4/7$

FIGURE 9.14: PD from void pattern measured and estimated, filtered at $f_L = 7$MHz, $f_U = 90$MHz, injection at $x' = 4/7$ on interleaved winding. 50 cycles of data.

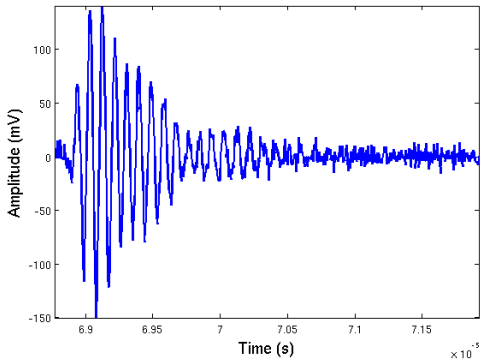

(a) Filtered PD waveform at $x = 7/7$, max $|i_b(l)| = 150.3mV$

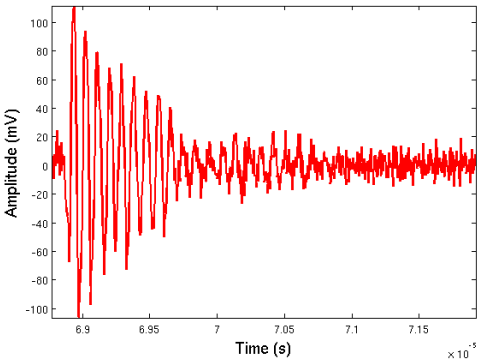

(b) Filtered PD waveform at $x' = 5/7$, max $|i(5/7)| = 111.6mV$

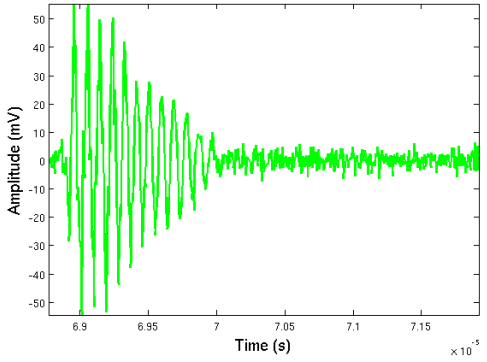

(c) Filtered PD waveform at $x = 0/7$, max $|i_n(0)| = 55.4mV$

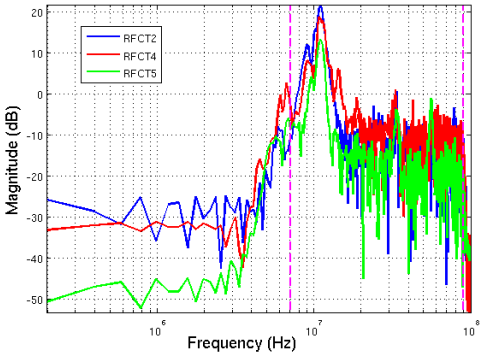

(d) The filtered spectrum

FIGURE 9.15: Extraction of PD waveform from void with 200MHz sampling frequency, filtered at $f_L = 7$MHz, $f_U = 90$MHz, injection at $x' = 5/7$ on plain winding

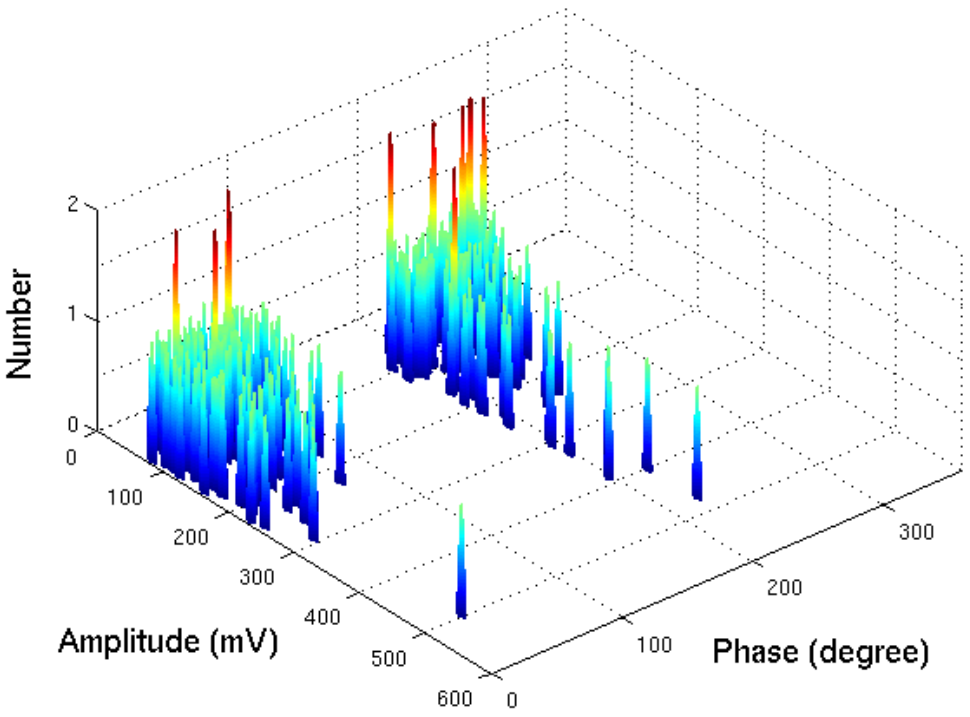

(a) Measured at $x' = 5/7$

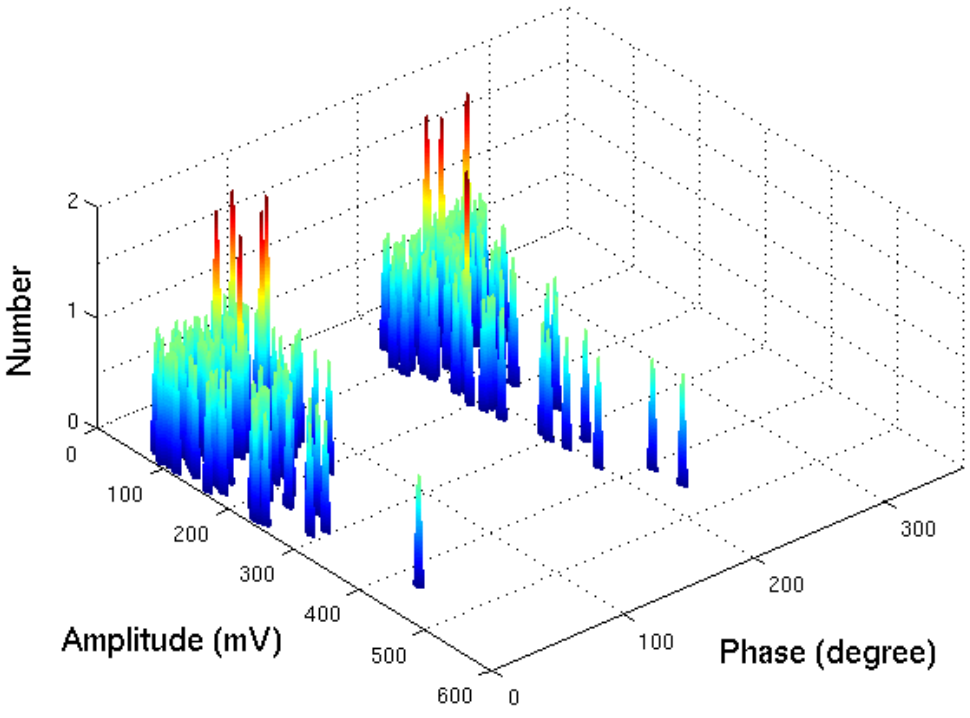

(b) Model estimation at $x' = 5/7$

FIGURE 9.16: PD from void pattern measured and estimated, filtered at $f_L = 7$MHz, $f_U = 90$MHz, injection at $x' = 5/7$ on plain winding. 50 cycles of data

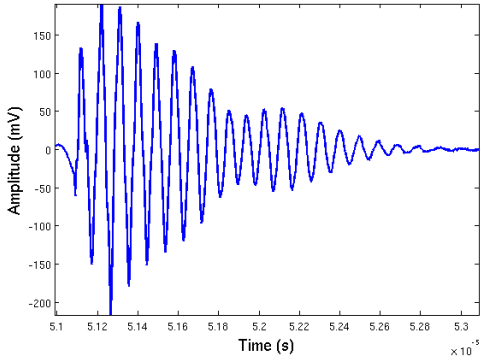

(a) Filtered PD waveform at $x = 7/7$, max $|i_b(l)| = 216.6mV$

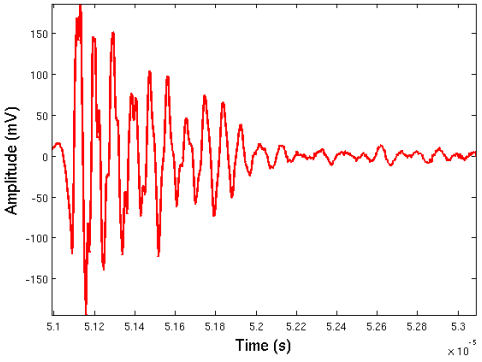

(b) Filtered PD waveform at $x' = 2/7$, max $|i(5/7)| = 193.9mV$

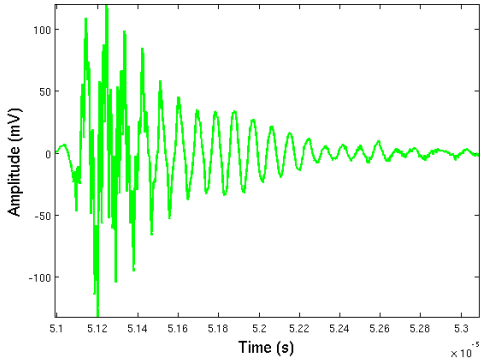

(c) Filtered PD waveform at $x = 0/7$, max $|i_n(0)| = 131.9mV$

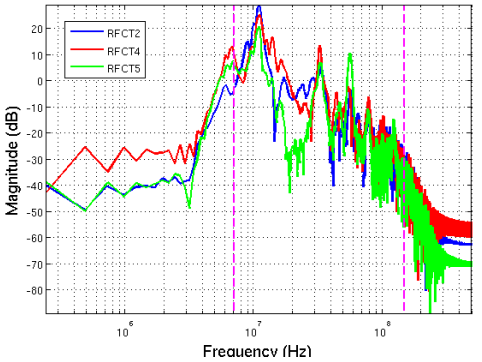

(d) The filtered spectrum

FIGURE 9.17: Extraction of PD waveform from surface discharge measurement with 1GHz sampling frequency, filtered at $f_L = 7$MHz, $f_U = 150$MHz, injection at $x' = 2/7$ on plain winding

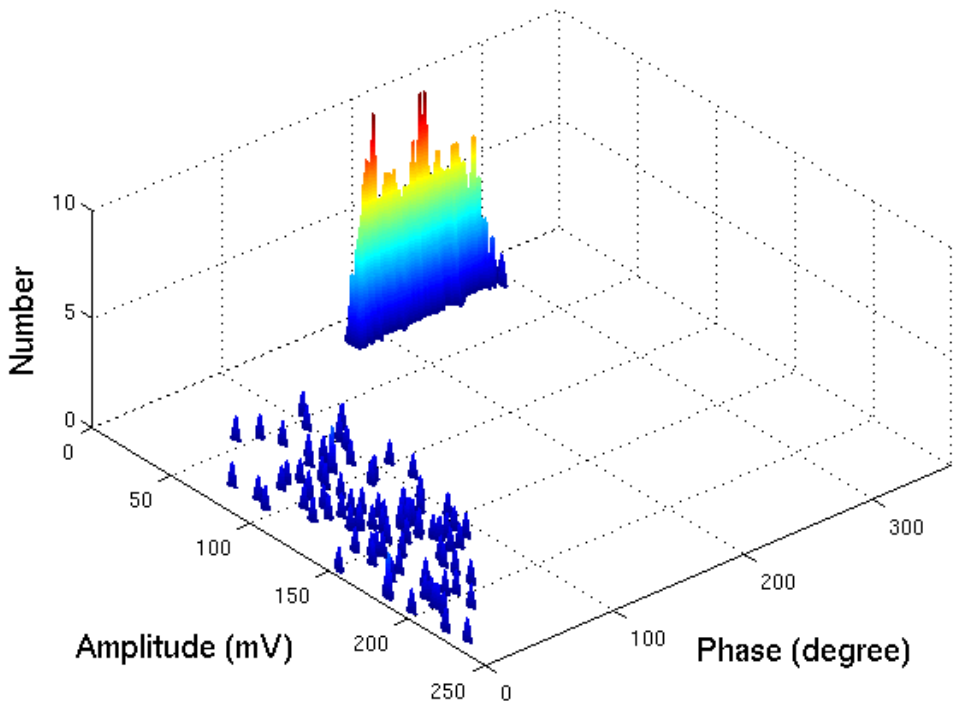

(a) Measured at $x' = 2/7$

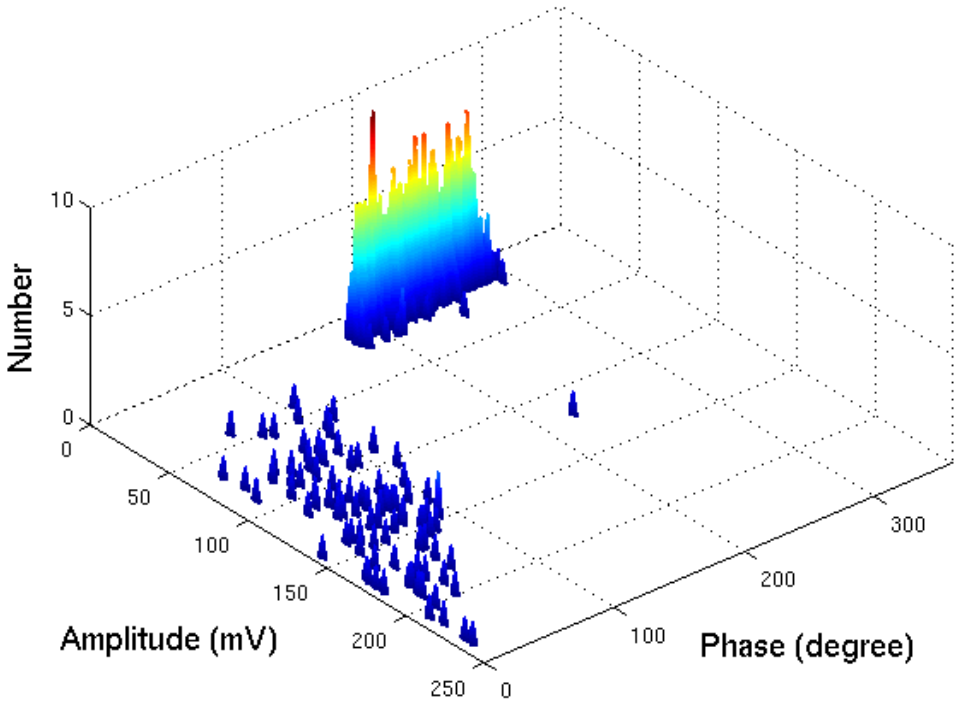

(b) Model estimation at $x' = 2/7$

FIGURE 9.18: Surface discharge pattern measured and estimated, filtered at f_L = 7MHz, f_U = 150MHz, injection at $x' = 2/7$ on plain winding. 10 cycles of data

9.2 Summary

A technique for PD magnitude estimation based on the lumped capacitive network model has been presented. With similar analysis to the capacitive network for a voltage distribution, the solution derived based on the current derivation is used to provide an analytical model solution for PD current propagation. The model equation consider the source position at x' for the source to ground connection, measured by RFCT4. Hence, an estimation of PD level under the predominantly capacitive region, can be made by setting the value of intermediary position x equivalent to x', provided that x' is known (This has been determined using the method outlined in Chapter 8).

However, the real PD magnitude value from the source is from the PD signals travelling before entering the transformer windings (measured by the RFCT3). This can be estimated using the D'Alembert solution of a travelling wave in the $x-t$ plane. It has been demonstrated that magnitudes measured at RFCT3 are approximately twice those measured at RFCT4.

It also has been shown that at high frequencies, the range of frequencies between 7MHz to 150MHz are suitable to model PD current propagation within the capacitive lumped parameter model. This is provided that all the PD signals have a considerable number of similar peaks in the frequency domain. However, the estimation is mainly for the absolute magnitude in the time domain and for $\phi-q-n$ pattern analysis. Therefore, a full waveform estimation has not been considered as it would require a full time domain equation model based on Duhamel's principle.

In summary, having estimated the source position of a PD signal based on measurements at the Bushing and Neutral to Earth terminals, it is then possible to estimate the real charge (pC).

Chapter 10

Discussion, Conclusions and Future Work

10.1 Discussion

Partial discharge propagation in a transformer winding at high frequencies can be analysed by studying the effect of a transient incident signal. Under transient conditions, the transformer excitation patterns will reveal its harmonic components in the frequency domain. The steeper the onset of the pulse applied wave to the transformer winding, the higher the level of oscillation. It has been shown in Chapter 3 that with an incident angle similar to the dirac delta function, $\delta(t)$, of an infinite rectangular wave , the response signals will have an infinite transition at $t = 0$.

The windings can be modelled using a fixed distribution equation based on a lumped capacitive model. The choice of lumped capacitive model represents a high frequency transition impulse like signal. Hence an estimation of PD location and magnitude is possible using the lumped capacitive model to represent the way the PD signals propagate from the source to the terminal winding ends.

The use of a lumped capacitive model for PD propagation is only suitable if certain requirements are met. As discussed in earlier chapters, with the influence of a predominantly capacitive network in ideal conditions, the PD signals will experience no loss and have same phase values between input and measured output.

However, difficulties may arise as PD signals are variable and contain non-uniform high frequency oscillations. It has been shown that not all the PD signal components of the original waveform are transfered to the end winding terminals (bushing and neutral) and captured by the RFCTs. The PD signals may experience loss and attenuation during the propagation due to multipath propagation and other unknown obstacles. Hence, the PD estimation technique presented in this thesis under the influence of predominantly

capacitive region only considers the harmonic peaks which are assumed to retain the essential components of the original PD signal from its source.

In estimating PD levels, a full estimation of the original waveform may be necessary, in order to achieve better results and accuracy. The full equation based on Duhamel's principle may explain the waveform oscillations as a result of a reverberation process. Analytically this involves two main components, a fixed distribution component and a harmonic decay component. It has been derived that, even at high frequencies with the use of predominantly capacitive model, Equations (8.1) and (8.4) show that the amplitude of the harmonic level can be determined which is influenced by the offset level of the PD currents. Hence a technique for estimating the offset level has to be developed. Thus for better accuracy it is essential to evaluate the full time domain waveform estimation, but this requires excessive effort to estimate the standing wave parameters based on Duhamel's principle.

As PDs travel from the source to the measuring points at the ends of windings, D'Alembert's solution has been demonstrated to be capable of estimating the original magnitude of the PD signal source. The circuit arrangement of Figure 7.26, is only a laboratory arrangement to investigate PD propagation in transformer windings by finding the relationship between RFCT3 and RFCT4. The ultimate aim of PD estimation is to estimate the original PD magnitudes at the source that is measured by RFCT3 in the experiment. The experiment also can be carried out with a typical arrangement without connection of source at x' to the ground (no RFCT4). The estimation technique thus will be by estimating the intermediary PD level at x' based on the reference measurements at bushing tap points and neutral to ground connection. The two estimation values can be calculated for the PD level from bushing and PD level from neutral at estimated point $x = x'$ ($\approx$ RFCT4). The summation of the two values becomes the estimated magnitude of the original PD source.

The main issue in PD monitoring of a high voltage transformer is the location of the PD source. The technique presented using a MME calculation, estimates the minimum error of the estimated end terminal PD levels from the measured one. This however, will not give an accurate value of the estimated PD level at the terminal ends. As shown in Figures 8.12 and 8.13, the error estimation as x' moves near to the ground connection are close to the absolute zero line. Hence problems arise when estimating PD locations that are close to the neutral to ground connection terminal.

There are occasions when PDs occur at more than one place within a transformer winding. Using a terminal ends measurement, this may look like a single source of PD. The technique introduced however is based on the assumption that the winding is a single input single output system (SISO), so for a multi-input, multi-output system (MIMO) analysis it may be necessary to employ different source location techniques. In addition, prior to PD location, a system identification process may be needed to distinguish

between more then one different PD source.

In real transformer design, a single phase of a high voltage transformer consists of high voltage winding and low voltage winding. The winding arrangements are such that, the high voltage windings are located on the outer side and low voltage winding is located on the inner side. The interaction between the two windings is represented by the flux interlinkages between the low voltage winding and the high voltage winding, which can be electrically modelled as equivalent inductances. At higher frequencies, the lumped capacitance model has to take into account the capacitances between windings (interwinding capacitance). The value of interwinding capacitance may differ from the value of the series capacitances within transformer windings which need to be identified by its physical dimensions. Thus as PD occurs within a transformer winding, the interwinding capacitances will become a medium of travelling waves for the waves to travel between the windings at high frequencies. In this case the measurement of PDs is possible either on the high voltage side or the low voltage side of transformer winding pair by using RFCTs. Hence for a single phase of a transformer, two measurements at the bushings may be necessary to correlate the PD source under investigation. However, additional techniques such as system identification will need to be employed to isolate the real source location of the PDs.

10.2 Conclusion of the Thesis

This research has presented techniques for representing the reverberation process of high frequency signals under transient conditions and the way the PD signals propagate along a transformer winding. The transformer model windings involved in the experiments were a plain winding and an interleaved winding. The two windings differ by their physical construction and parameters, but obtained results have shown that both can be represented using the lumped circuit model with RLC transmission line parameter model and the lumped capacitive model.

It was found that, at certain rise times of the applied wave, the natural frequency of the transformer winding will be excited. Similarly, in the case of partial discharge signals, where PDs are variable and have short rise times, the signals travelling from the source to the end terminals contain information about the original source signal by means of harmonic frequencies. Hence, it is possible to estimate the PD source location and its magnitude.

The derived model and the techniques presented can be further developed and explored to represent partial discharge propagation in high voltage transformers. The standing wave analytical solution has demonstrated that from the level of signal oscillation at high frequencies it is possible to estimate the source position by specifying the nomalized distance, x, from neutral to ground terminal and estimating the standing waves

parameters from the measured waveforms at bushing and neutral. Hence this approach has an advantage of not requiring the electrical physical parameters of the transformer winding or even its physical dimensions, which may change over the time and also change due to high voltage stress and mechanical stress.

Due to limited access to transformer windings, parameters of interest are derived from the standing wave formulas. With known equations, approximation of PD waveforms is achievable with the help of NLSE. This involves an iterative procedure to minimize errors between the measured PD waveform and the estimated PD waveform. Despite the uniqueness of the NLSE technique, a suitable choice of value for the initial parameters is an important factor in determining the accuracy and the convergence of the estimation.

The use of the D'Alembert solution has shown the capability of solving initial boundary value problems. As PDs originate at a point along a transformer winding, the levels of PDs at the source are approximately double the magnitudes of the PD signals measured at the transformer winding terminals. Thus in estimating the level of PDs at the source point, two criteria have to be considered, namely, the source level in the transformer winding and the law of bound charge. The source level can be interpreted based on travelling wave theory, whereas the law of bound charge is the formation of floating charge in the source before and after the disharge in the transformer winding. This will involve a technique of waveform deformation as in Figure 9.1 with a constant charge integration over a duration of time during the process.

Analysing this it is necessary to consider Duhamel's principle. It has the capability of determining the source signal with time varying function. Hence, the PD signal in a HV transformer can be explained using a time varying boundary conditions model. The aim of the model is to provide the PD propagation level approximation which finally solves the problem of determining the real PD magnitudes.

10.2.1 Research Contributions

The research contributions of this thesis can be divided into two categories. First is the development of the model description and derivation of PD propagation within a transformer winding, and secondly are the development of experimental procedures to validate the proposed analytical approach.

The first contribution is concerned with an analytical solution based on the voltage winding distribution towards the bushing and neutral points. The solutions are derived based on the divergence of current within a lumped capacitive network which allows an estimate of the level of the signal voltage at the point of source x'. It also has the capability to estimate the voltage level at any point x along the transformer winding. Hence, a representation of the voltage distribution along a transformer winding can be established which defines the voltage level caused by the source current.

Additionally, the reverberation process of travelling waves that exist due to inductive elements within the lumped circuit parameter model are explained using a standing wave solution. The solution was derived analytically where the windings are divided into two to come up with a split winding analysis towards the bushing and neutral to ground connections. At the source, an analytical solution is derived using D'Alembert's solution to represent the oscillation and the harmonic level in the time domain and the frequency domain. This in turn has the ability to estimate the harmonic content that exists due to the resonant poles of the winding.

A time varying boudary conditions model is derived to explain the reverberation process caused by PDs or arbitrary applied waveforms injected at intermidiary points along a transformer winding. Unlike the homogeneous solution with constant boundary conditions, the time varying boundary conditions solution for a PD signal is for an unknown source signal represented by the PD waveform. In the homogeneous model problem, the solutions of voltage distribution are explained in simpler forms. Hence, a time varying boundary conditions model based on Duhamel's principle is derived to represent PD signal propagation within a transformer winding.

The second category of contribution is the development of PD experiments with the various points of PD injection along the transformer windings. A circuit arrangement allows measurement of PD propagation at different points. Based on the principle of waves travelling on the x-t plane, the source magnitudes of PDs can be found using the D'Alembert solution. Hence, by considering the absolute maximum value of filtered PDs in time domain, an estimated $\phi - q - n$ pattern can represent the magnitude levels at the point source x'.

A technique for PD location is introduced based on the estimation of errors between the measured PD levels and the consequent estimated PD levels at the winding ends. By estimating the levels of offset current and the calculated fixed distribution constant, α, the accumulated harmonic amplitude can be estimated and this contains information about PD location.

Finally, the derivation and estimation of PD current propagation under the predominantly capacitive region of the winding response. Using a similar analysis to the fixed distibution solution for the voltage distribution allows the current distribution of the PD propagation signal to be derived. Hence within the predominantly capacitive region, the PD level in the time domain can be estimated at the source point x', for a range of frequencies up to 150MHz. i.e within the useful bandwidth of the RFCT sensors.

10.3 Recommendations for Future Work

The research has provided the potential to explore further development of PD monitoring using RFCT sensors. Further investigations may need to be undertaken for different types of winding with longer stacks.

The method based on split winding analysis can be used with fully capacitive domain frequencies. At very high frequencies the visible peak poles for PD spectrum are between 7MHz to 150MHz. Hence, the use of split winding analysis can be further explored for different types of PD such as corona and floating partial discharge in oil.

Since the developed model does not consider a PD source within the bushing, it is essential to produce a combined model incoporating the existing transformer model as well as a bushing model.

As a real transformer is constructed with low voltage windings and high voltage windings, it is essential to investigate PD signal propagation with the presence of interlinkages and the interwinding capacitances. Thus a further development of the model description under the influence of PD signal initiation with two windings in a toroidal arrangement is necessary.

Appendix A

Transformer Model Construction

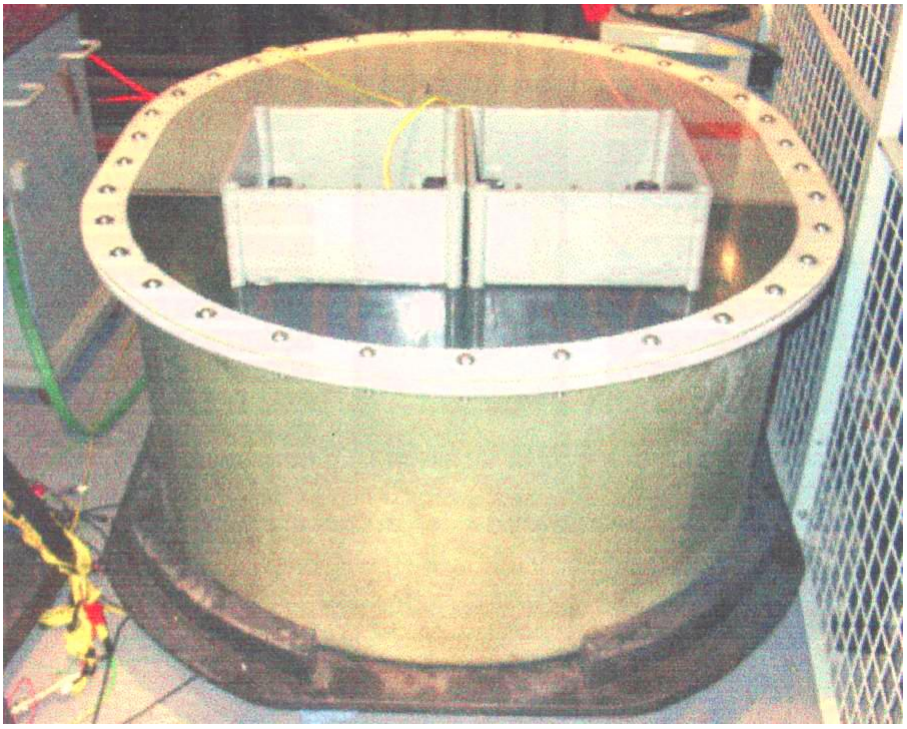

FIGURE A.1: Transformer model [102]

A.1 Transformer Model Construction

The single transformer model winding was constructed in 2004 and it was originally designed and produced by Alstom Transformer and National Grid Company. It was then further redesigned into experimental model in Tony Davies High Voltage Laboratory, University of Southampton. The windings of the transformer are connected for a pair of disc from outside via metal terminals [102].

A.2 The winding design

The experimental design consists two types of windings, interleaved disc winding and plain disc winding. Four static plate are used to separate the between the two. The static plates are made of metal, where the metal plates were rounded and wrapped with crepe paper in order to minimize PD under high voltage stress.

A.3 The tank design

The outer container of the transformer is made from plastic. A test was carried out [102] to simulate the state of a real transformer tank, so the parameters of the transformer model, such as capacitance of the winding to the tank wall and capacitance of the ends of the windings to ground.

A.4 Construction parameters

Table A.1: Physical dimensions

Parameters	**Dimensions**
Number of discs per winding	14
Number of turns per disc	14
Total number of turns per winding	24
Mean length of per turn	1810 mm
Width of spacers	40 mm
Radial depth of disc	85 mm
Physical axial length of per winding	150 mm
Width of the conductor	3.0 mm
Height of the conductor	7.0 mm
Duct dimension between two adjacent discs	3.0 mm
Thickness between the end disc and static ring	3.0 mm
Thickness of static ring	5.0 mm
Turn insulation	1.0 mm
Inside diameter of winding	475 mm
Outside diameter of winding	650 mm
Distance from winding to the outer wall of tank	100 mm
Distance from winding to the inner core	50 mm
Distance from upper static ring to bottom	50 mm
Distance from lower static to top pressure plate	50 mm
Total mass	730 kg

Appendix B

Alternative Solution for Current Divergence

B.1 Alternative Solution for Current Divergence

The solution of the PDE from Equation (3.16) will have general solutions as follows:

$$v_n(x) = A\,cosh(\alpha x) + B\,sinh(\alpha x) \tag{B.1}$$

for the solution towards neutral and

$$v_b(x) = \mathfrak{A}\,cosh[\alpha(l-x)] + \mathfrak{B}\,sinh[\alpha(l-x)] \tag{B.2}$$

for the solution towards bushing. Where A, $\mathfrak{A}$, B and $\mathfrak{B}$ are arbitrary constants. From the definition of hyperbolic function and trigonometric function; by the derivation of absolute value of α in [80] (if in any case for the complex term of α, $j\alpha$ becomes α); and from pseudofinal distribution of transformer windings [45]; hence Equation (B.2) can be written in the following form:

$$v_b(x) = C\,cos\,(j\alpha x) + D\,sin\,(j\alpha x) \tag{B.3}$$

Where the arbitrary constants of C and D are equal to:

$$C = \mathfrak{A}\,cos\,(j\alpha l) - j\mathfrak{B}\,sin\,(j\alpha l) \tag{B.4}$$

and

$$D = \mathfrak{A}\, sin\,(j\alpha l) + j\mathfrak{B}\, cos\,(j\alpha l) \tag{B.5}$$

The two Equations (B.1) and (B.3) require definition of boundary conditions in order to be effectively solved. The boundary conditions are [44];

$$v_b(x) = V_B \qquad at \qquad x = l \tag{B.6a}$$
$$v_n(x) = V_N \qquad at \qquad x = 0 \tag{B.6b}$$

$$v_b(x') = v_n(x') \qquad at \qquad x = x' \tag{B.7a}$$
$$\frac{dv_b(x')}{dx} = \frac{dv_n(x')}{dx} \qquad at \qquad x = x' \tag{B.7b}$$

Regardless of the value of the terminal impedance at the bushing, $Z_b(p)$, and at neutral point, $Z_n(p)$, V_B and V_N are the terminal conditions considered for analysis and can be obtained from measurement. Hence According to the conditions defined in (B.6),

$$A = V_N \tag{B.8a}$$
$$C\, cos\,(j\alpha l) + D\, sin\,(j\alpha l) = V_B \tag{B.8b}$$

and applying (B.7), yields:

$$C\, cos\,(j\alpha x') + D\, sin\,(j\alpha x') = A\, cosh\,(\alpha x') + B\, sinh\,(\alpha x') \tag{B.9a}$$
$$-C\, sin\,(j\alpha x') + D\, cos\,(j\alpha x') = A\, sinh\,(\alpha x') + B\, cosh\,(\alpha x') \tag{B.9b}$$

Solving (B.8) and (B.9) simultaneously yields expressions for the variables B, C and D;

$$B = \frac{-C\, sin\,(j\alpha x') + D\, cos\,(j\alpha x') - V_N sinh\,(\alpha x')}{cosh\,(\alpha x')} \tag{B.10}$$

$$C = \frac{V_B\big(cosj\alpha x'\, tanh\alpha x' - sinj\alpha x'\big) + V_N sinj\alpha l\big(cosh\alpha x' - sinh\alpha x'\, tanh\alpha x'\big)}{cosj\alpha l\big(cosj\alpha x'\, tanh\alpha x' - sinj\alpha x'\big) + sinj\alpha l\big(cosj\alpha x' + sinj\alpha x'\, tanh\alpha x'\big)} \tag{B.11}$$

$$D = \frac{V_B\big(cosj\alpha x' + sinj\alpha x'\, tanh\alpha x'\big) - V_N cosj\alpha l\big(cosh\alpha x' - sinh\alpha x'\, tanh\alpha x'\big)}{cosj\alpha l\big(cosj\alpha x'\, tanh\alpha x' - sinj\alpha x'\big) + sinj\alpha l\big(cosj\alpha x' + sinj\alpha x'\, tanh\alpha x'\big)} \tag{B.12}$$

B.2 Solution For The Injection At Winding Ends

In the case of travelling waves injected at the winding ends, solutions may again be divided into two explicit formulas. One for the PDE that represents the wave travelling to the neutral end, and one for the PDE representing the wave that travels towards the bushing end.

Suppose a wave is injected at terminal neutral end, then Equation (B.3) will be the solution of the voltage distribution. Hence, by taking $x' = 0$; and solving for (B.11) and (B.12) the new equation becomes:

$$C = V_N\big|_{x'=0} \tag{B.13}$$

$$D = \left.\frac{V_B - V_N cos\,(j\alpha l)}{sin\,(j\alpha l)}\right|_{x'=0} \tag{B.14}$$

Therefore the solution for the winding distribution becomes:

$$V_b(x) = V_N cos\,(j\alpha x) + \left.\frac{V_B - V_N cos\,(j\alpha l)}{sin\,(j\alpha l)} sin\,(j\alpha x)\right|_{x'=0} \tag{B.15}$$

Using the similar analysis for the wave source at bushing tap point, where $x' = l$, and the boundary solutions of (B.8), the Equation (B.1) becomes the model propagation of the travelling wave and the new solution for the constants becomes:

$$B = \left.\frac{-C\,sin\,(j\alpha l) + D\,cos\,(j\alpha l) - V_N sinh\,(\alpha l)}{cosh\,(\alpha l)}\right|_{x'=l} \tag{B.16}$$

$$C = \left.\frac{V_B\big(cos\,j\alpha l\,tanh\,\alpha l - sin\,j\alpha l\big) + V_N sin\,j\alpha l\big(cosh\,\alpha l - sinh\,\alpha l\,tanh\,\alpha l\big)}{tanh\,\alpha l}\right|_{x'=l} \tag{B.17}$$

$$D = \left.\frac{V_B\big(cos\,j\alpha l + sin\,j\alpha l\,tanh\,\alpha l\big) - V_N cos\,j\alpha l\big(cosh\,\alpha l - sinh\,\alpha l\,tanh\,\alpha l\big)}{tanh\,\alpha l}\right|_{x'=l} \tag{B.18}$$

where

$$V_n(x) = V_N cosh\,(\alpha x) - \left.\frac{C\,sin\,(j\alpha l) - D\,cos\,(j\alpha l) + V_N sinh\,(\alpha l)}{cosh\,(\alpha l)} sinh\,(\alpha x)\right|_{x'=l} \tag{B.19}$$

Appendix C

Split Winding Analysis Solutions: LCK Circuit

C.1 Split Winding Analysis: Solution Towards Neutral

Consider the following general solution:

$$\begin{aligned}\psi_n(x,t) = &\big(Acosh\beta x + Bsinh\beta x\big) \\ &+ \sum\Big(E_{sn}sin\lambda x\, cos\omega t + F_{sn}sin\lambda x\, sin\omega t \\ &\qquad + G_{sn}cos\lambda x\, cos\omega t + H_{sn}cos\lambda x\, sin\omega t\Big)\end{aligned} \tag{C.1}$$

with initial conditions as follows:

$$\frac{\partial^2 v_n}{\partial x^2} - \frac{C_g}{K}v_n = 0 \qquad and \qquad \frac{\partial \psi_n(x,t)}{\partial t} = 0 \tag{C.2}$$

and boundary conditions:

$$\psi_n(l,t) = V_B(t) \qquad and \qquad \psi_n(0,t) = 0; \tag{C.3}$$

Therefore, the initial conditions of the first solution are equal to the initial distribution solution of Equation (3.19). Comparison of the general solution of Equation (C.1) at $t = 0$, with the initial distribution (Equation (3.19)) and expressing the term as half

range fourier sine series (see Appendix D) gives:

$$\begin{aligned}\sum_{s=1}^{\infty}\frac{2}{s\pi}\Big[A\Big(1-coss\pi\,cosh\alpha l\Big)-Bcoss\pi\,sinh\alpha l\Big]sin\frac{s\pi x}{l}\\ =\sum_{s=1}^{\infty}\frac{2}{s\pi}\Big[A\Big(1-coss\pi\,cosh\beta l\Big)-Bcoss\pi\,sinh\beta l\Big]sin\frac{s\pi x}{l}\\ +\sum_{s=1}^{\infty}\Big(E_{sn}sin\lambda x+G_{sn}cos\lambda x\Big)\end{aligned}\tag{C.4}$$

By inspection:

$$\lambda=\frac{s\pi}{l}\qquad and\qquad G_{sn}=0;\tag{C.5}$$

Therefore E_{sn} is equivalent to:

$$E_{sn}=\frac{2coss\pi}{s\pi}\Big[A\Big(cosh\beta l-cosh\alpha l\Big)+B\Big(sinh\beta l-sinh\alpha l\Big)\Big]\tag{C.6}$$

To satisfy the second initial condition, by differentiating (4.17) with respect to t and substituting for $t=0$, F_{sn} and H_{sn} can be further defined:

$$\sum_{s=1}^{\infty}\omega_{sn}\left(F_{sn}sin\frac{s\pi x}{l}+H_{sn}cos\frac{s\pi x}{l}\right)=0\tag{C.7}$$

However, H_{sn} can be found for the boundary condition at $x=0$, therefore

$$\sum_{s=1}^{\infty}\Big(G_{sn}cos\omega t+H_{sn}sin\omega t\Big)=0\tag{C.8}$$

Since G_{sn} is zero, hence it follows that H_{sn} is also zero. Therefore from (C.7), it is evident that F_{sn} is equal to zero, since ω_{sn} is a nonzero term. Thus the complete solution for a wave travelling towards the neutral is equivalent to:

$$\begin{aligned}\psi_n(x,t)=\big(Acosh\beta x+Bsinh\beta x\big)\\ +\sum_{s=1}^{\infty}\frac{2(-1)^s}{s\pi}\,\zeta_n sin\Big(\frac{s\pi x_n}{l}\Big)\,cos(\omega_{sn}t)\end{aligned}\tag{C.9}$$

Where

$$\zeta_n=\Big[A\big(cosh\beta l-cosh\alpha l\big)+B\big(sinh\beta l-sinh\alpha l\big)\Big]\tag{C.10}$$

and

$$x_n = \frac{x}{x'} - 1 \tag{C.11}$$

C.2 Split Winding Analysis: Solution Towards Bushing

Similar to solution towards Neutral, the following is considered

$$\begin{aligned}\psi_b(x,t) = &\big(Ccos\beta x + Dsin\beta x\big) \\ &+ \sum E_{sb}sin\lambda x\, cos\omega t + F_{sb}sin\lambda x\, sin\omega t \\ &\qquad + G_{sb}cos\lambda x\, cos\omega t + H_{sb}cos\lambda x\, sin\omega t\end{aligned} \tag{C.12}$$

With the initial conditions towards bushing:

$$\frac{\partial^2 v_b}{\partial x^2} - \frac{C_g}{K} v_b = 0 \qquad and \qquad \frac{\partial \psi_b(x,t)}{\partial t} = 0, \tag{C.13}$$

and boundary conditions:

$$\psi_b(l,t) = V_B(t) \qquad and \qquad \psi_b(0,t) = 0; \tag{C.14}$$

Taking into consideration the initial distribution condition and writing the initial fixed distribution equation as a quarter range sine series (see Appendix D) the general solution becomes:

$$\begin{aligned}&\sum_{s_o}^{\infty} \frac{4}{s_o\pi}\left[C + \frac{2l}{s_o\pi} sin\frac{s_o\pi}{2}\Big(-C\alpha sin\alpha l + D\alpha cos\alpha l\Big)\right] sin\frac{s_o\pi x}{2l} \\ &\qquad = \sum_{s_o}^{\infty} \frac{4}{s_o\pi}\left[C + \frac{2l}{s_o\pi} sin\frac{s_o\pi}{2}\Big(-C\beta sin\beta l + D\beta cos\beta l\Big)\right] sin\frac{s_o\pi x}{2l} \\ &\qquad + \sum_{s_o}^{\infty} E_{sb}sin\lambda x + G_{sn}cos\lambda x\end{aligned} \tag{C.15}$$

Comparing both sides for terms $sin\lambda x$ and $cos\lambda x$ yields

$$G_{sb} = 0 \qquad and \qquad \lambda = \frac{s_o\pi}{2l} \tag{C.16}$$

Hence;

$$E_{sb} = \frac{8l}{s_o^2\pi^2} \sin \frac{s_o\pi}{2} \Big[C\Big(\beta sin\beta l - \alpha sin\alpha l\Big) + D\Big(\alpha cos\alpha l - \beta cos\beta l\Big) \Big] \tag{C.17}$$

Substituting the value for $x = 0$ for the Neutral end boundary condition, the general solution gives:

$$\sum_{s_o}^{\infty} \Big(G_{sb} cos\omega t + H_{sb} sin\omega t \Big) = 0 \tag{C.18}$$

Since G_{sb} is equivalent to zero, therefore it follows that H_{sb} is also zero. Differentiating (4.24) with respect to t and for time is zero gives:

$$\sum_{s_o}^{\infty} \omega_{sb} \Big(F_{sb} sin\frac{s\pi}{2l} + H_{sb} cos\frac{s\pi}{2l} \Big) = 0 \tag{C.19}$$

Therefore F_{sb} is zero, which consequently makes the general solution for the waves travelling towards bushing tap point similar to those travelling towards the neutral. Therefore the complete solution for the wave travelling towards bushing is:

$$\begin{aligned} \psi_b(x,t) = &\Big(Ccos\beta x + Dsin\beta x \Big) \\ &+ \sum_{s_o=1}^{\infty} \frac{8l}{s_o^2\pi^2} \, sin\frac{s_o\pi}{2} \, \zeta_b sin\Big(\frac{s_o\pi x_b}{2l} \Big) cos\omega_{sb} t \end{aligned} \tag{C.20}$$

Where

$$\zeta_b = \Big[C\big(\beta sin\beta l - \alpha sin\alpha l\big) + D\big(\alpha cos\alpha l - \beta cos\beta l\big) \Big] \tag{C.21}$$

and

$$x_b = x - x' \tag{C.22}$$

Appendix D

Fourier Range Sine Cosine Series

D.1 Half Range Fourier Sine Series: Fixed Distribution Towards Neutral

Let

$$\phi_n(x) = A cosh\alpha x + B sinh\alpha x \tag{D.1}$$

The half range Fourier Sine Series state that:

$$\phi_n(x) = \sum_{s=1}^{\infty} a_n sin\frac{s\pi x}{l} \tag{D.2a}$$

$$where \qquad a_n = \frac{2}{l}\int_0^l \phi_n(x) sin\frac{s\pi x}{l} dx \tag{D.2b}$$

$$\therefore \qquad a_n = \frac{2}{l}\int_0^l (A cosh\alpha x + B sinh\alpha x) sin\frac{s\pi x}{l} dx \tag{D.3}$$

Using integration by part:

$$\begin{aligned} a_n = &\left[\Big(A cosh\alpha x + B sinh\alpha x\Big)\Big(-\frac{2}{s\pi} cos\frac{s\pi x}{l}\Big)\right]_0^l \\ &+ \int_0^l \frac{2}{s\pi} cos\frac{s\pi x}{l}\big(A\alpha sinh\alpha x + B\alpha cosh\alpha x\big) dx \end{aligned} \tag{D.4}$$

Considering only the first term:

$$\begin{aligned} a_n &= \left[\Big(Acosh\alpha l + Bsinh\alpha l\Big)\Big(-\frac{2}{s\pi}coss\pi\Big) + \frac{2A}{s\pi}\right] \\ &= \frac{2}{s\pi}\left[A - coss\pi\Big(Acosh\alpha l + Bsinh\alpha l\Big)\right] \\ &= \frac{2}{s\pi}\left[A\Big(1 - coss\pi\, cosh\alpha l\Big) - Bcoss\pi\, sinh\alpha l\right] \end{aligned} \tag{D.5}$$

Substitute back into equation D.2a, the half range sine series for fixed distribution equation towards neutral therefore is:

$$\phi_n(x) = \sum_{s=1}^{\infty} \frac{2}{s\pi}\left[A\Big(1 - (-1)^s cosh\alpha l\Big) - B(-1)^s sinh\alpha l\right] sin\frac{s\pi x}{l} \tag{D.6}$$

D.2 Quarter Range Fourier Sine Series: Fixed Distribution Towards Bushing

The initial fixed distribution towards bushing is:

$$\phi_b(x) = Ccos\alpha x + Dsin\alpha x \tag{D.7}$$

The quarter range sine series is:

$$\phi_b(x) = \sum_{s_{odd}=1}^{\infty} b_n sin\frac{s\pi x}{2l} \tag{D.8a}$$

$$where \qquad b_n = \frac{2}{l}\int_0^l \phi_b(x) sin\frac{s\pi x}{2l} dx \tag{D.8b}$$

$$\therefore \quad b_n = \frac{2}{l}\int_0^l \Big(Ccos\alpha x + Dsin\alpha x\Big) sin\frac{s\pi x}{2l} dx \tag{D.9}$$

Using intergration by part:

$$\begin{aligned} b_n = &\left[\Big(Ccos\alpha x + Dsin\alpha x\Big)\Big(-\frac{4}{s\pi}cos\frac{s\pi x}{2l}\Big)\right]_0^l \\ &+ \int_0^l \frac{4}{s\pi} cos\frac{s\pi x}{2l}\Big(-C\alpha sin\alpha x + D\alpha cos\alpha x\Big) dx \end{aligned} \tag{D.10}$$

Therefore

$$b_n = \frac{4}{s\pi}C + \frac{8l}{s^2\pi^2} sin\frac{s\pi}{2}\Big(-C\alpha sin\alpha l + D\alpha cos\alpha l\Big) \tag{D.11}$$

Substitue D.11 into equation D.8a, the fixed distribution equation towards bushing in quarter range sine series is:

$$\phi_b(x) = \sum_{s_{odd}=1}^{\infty} \frac{4}{s\pi}\left[C + \frac{2l}{s\pi} sin\frac{s\pi}{2}\Big(-C\alpha sin\alpha l + D\alpha cos\alpha l\Big)\right] sin\frac{s\pi x}{2l} \tag{D.12}$$

Appendix E

Experimental Apparatus

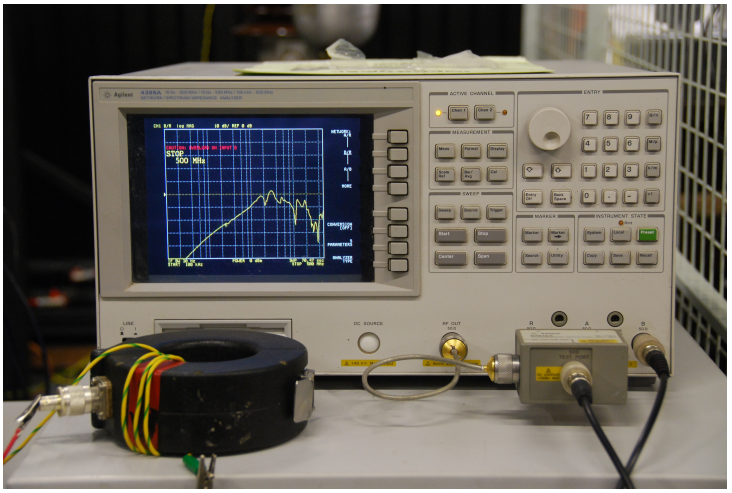

FIGURE E.1: Frequency response measurement of the RFCT with a network analyser

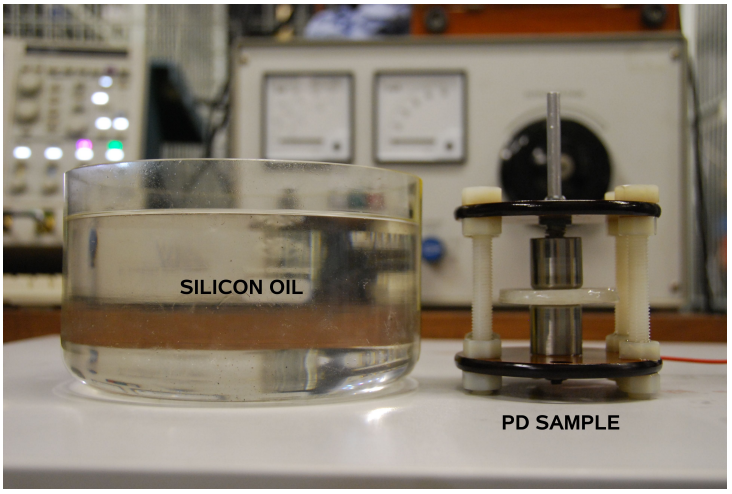

FIGURE E.2: Cylindrical void with silicon oil

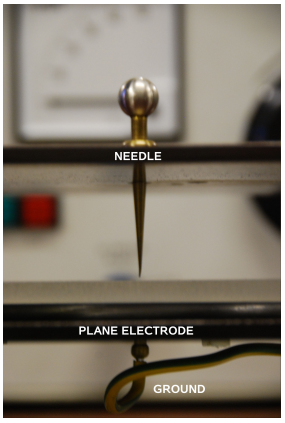

FIGURE E.3: Needle to plane for surface discharge experiment

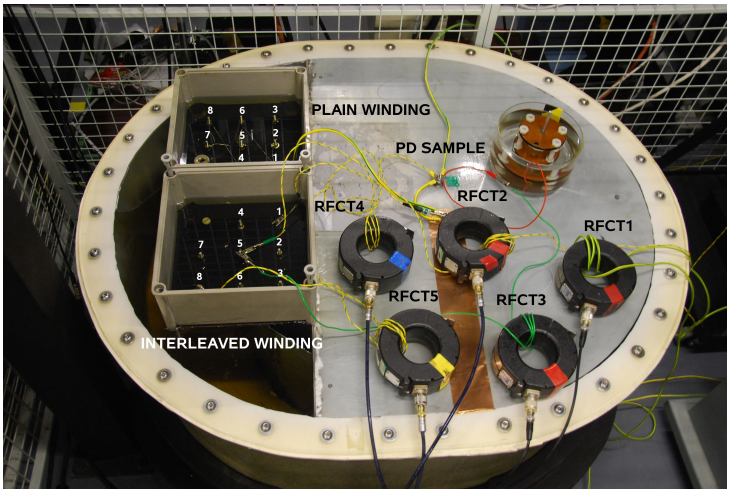

FIGURE E.4: Experimental setup with five RFCTs

FIGURE E.5: 60kV bushing

Appendix F

Comparison of RFCT3 and RFCT4 on Plain Winding

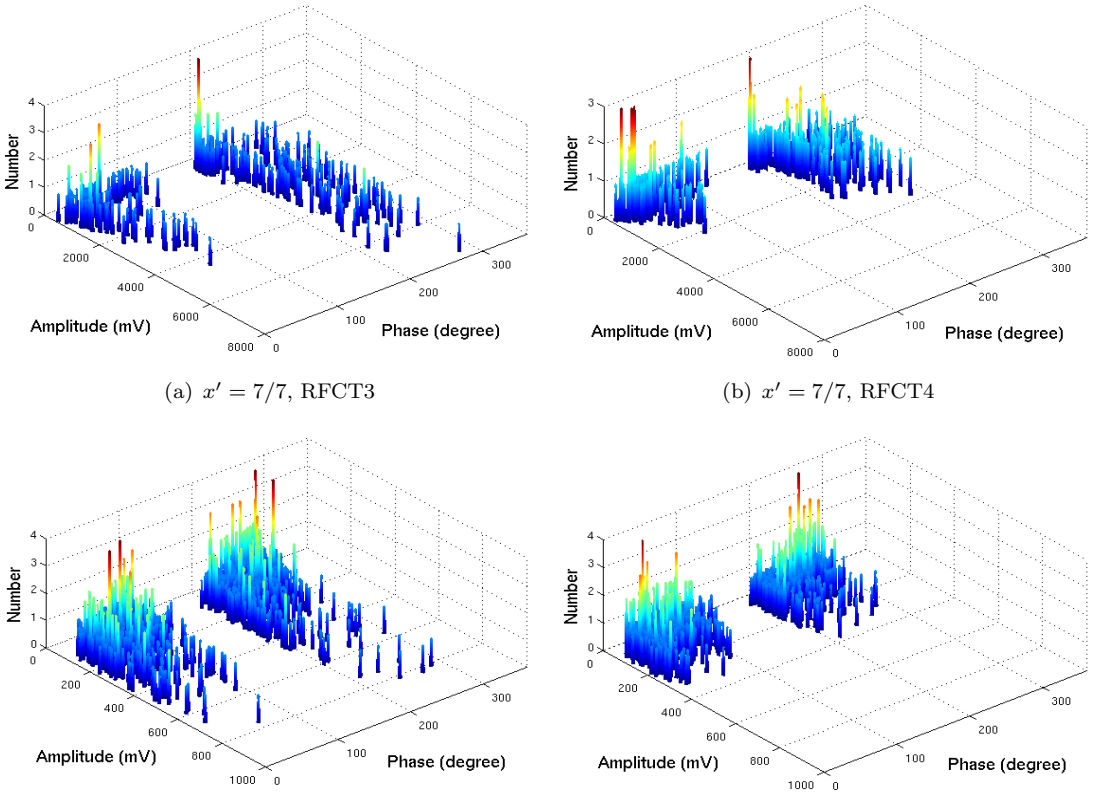

(a) $x' = 7/7$, RFCT3

(b) $x' = 7/7$, RFCT4

(c) $x' = 6/7$, RFCT3

(d) $x' = 6/7$, RFCT4

FIGURE F.1: Comparison of measurement from RFCT3 and RFCT4 at $x' = 7/7$ to $x' = 6/7$ for plain winding

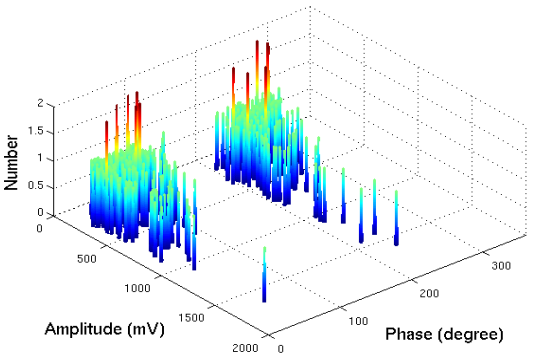

(a) $x' = 5/7$, RFCT3

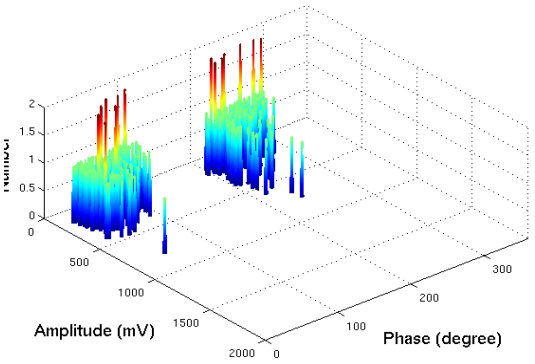

(b) $x' = 5/7$, RFCT4

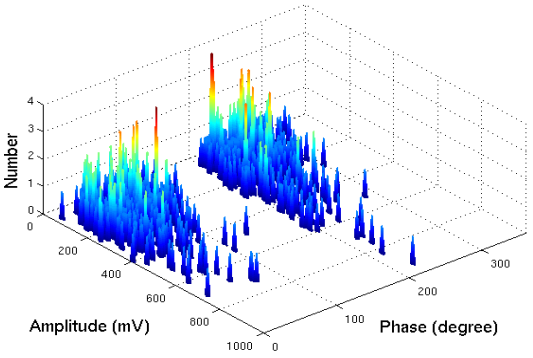

(c) $x' = 4/7$, RFCT3

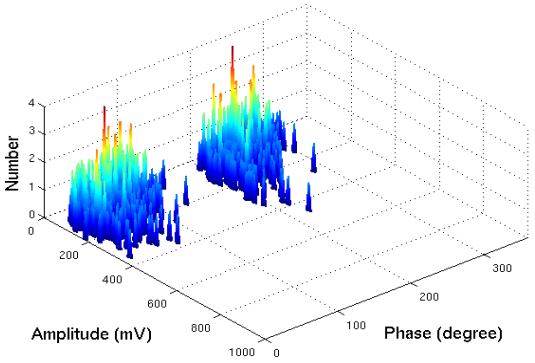

(d) $x' = 4/7$, RFCT4

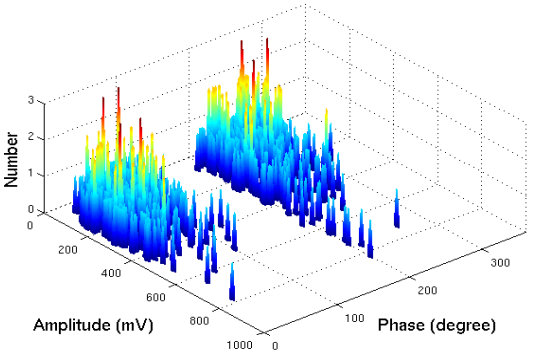

(e) $x' = 3/7$, RFCT3

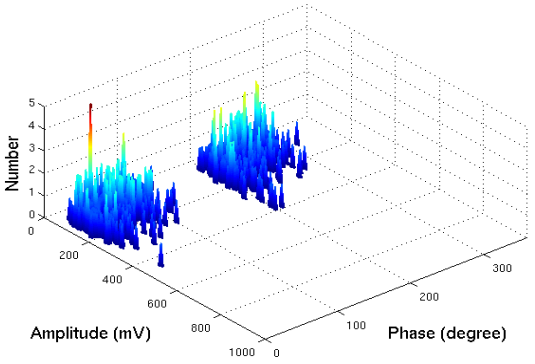

(f) $x' = 3/7$, RFCT4

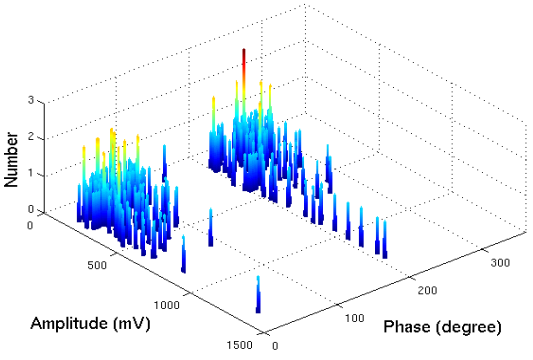

(g) $x' = 2/7$, RFCT3

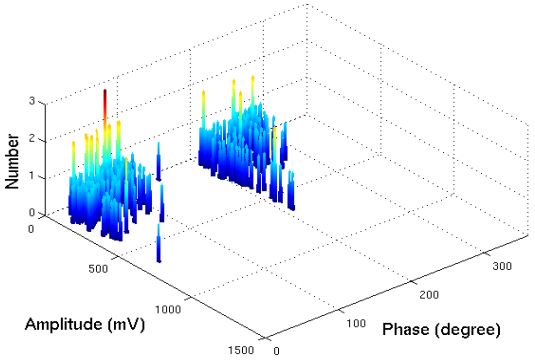

(h) $x' = 2/7$, RFCT4

FIGURE F.2: Comparison of measurement from RFCT3 and RFCT4 at $x' = 5/7$ to $x' = 2/7$ for plain winding

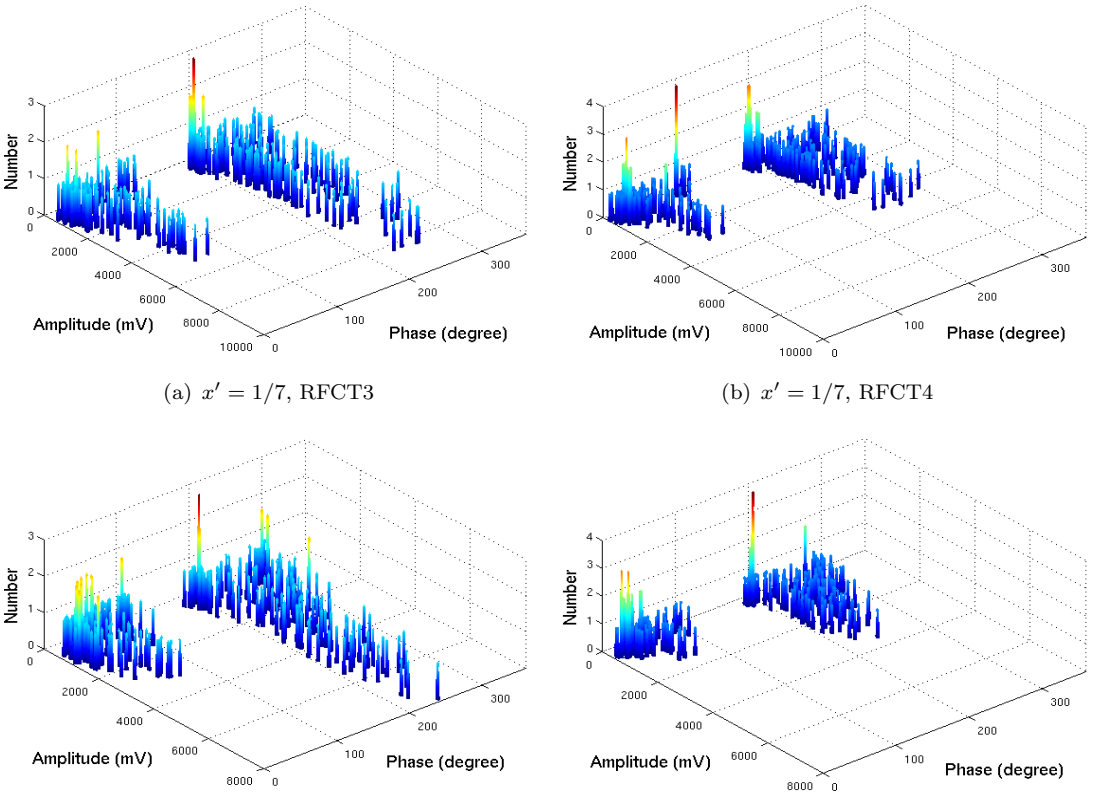

(a) $x' = 1/7$, RFCT3

(b) $x' = 1/7$, RFCT4

(c) $x' = 0/7$, RFCT3

(d) $x' = 0/7$, RFCT4

FIGURE F.3: Comparison of measurement from RFCT3 and RFCT4 at $x' = 1/7$ to $x' = 0/7$ for plain winding

References

[1] O. Seevers, *Power Systems Handbook: Design, Operation and Maintenance*. Prentice Hall, 1991.

[2] CIGRE Working Group 05, "An international survey on failures in large power transformers in service," *ELECTRA*, pp. 21–48, May 1983.

[3] M. Wang, A. Vandermaar, and K. Srivastava, "Review of condition assessment of power transformers in service," *IEEE Electrical Insulation Magazine*, vol. 18, no. 6, pp. 12–25, 2002.

[4] C. Bengstsson, "Status and trends in transformer monitoring," *IEEE Transactions on Power Delivery*, vol. 11, pp. 1379–1384, July 1996.

[5] C. Homagk and T. Leibfried, "Practical experience on transformer insulation condition assessment," *International Conference on Properties and Application of Dielectric Material*, pp. 238–241, June 2006.

[6] A. Nesbitt and B. Stewart, "Condition monitoring of power transformers through partial discharge measurement: problems associated with pulse distortion in the winding," *IEEE Transactions on Power Delivery*, vol. 10, pp. 1171–1176, July 1997.

[7] M. Minhas, J. Reynders, and P. D. Klerk, "Failures in power system transformers and appropriate monitoring techniques," *Eleventh International Symposium on High Voltage Engineering, 1999*, vol. 1, pp. 94–97, 23-27 July 1999.

[8] L. Pettersson, "Estimation of the remaining service life of power transformers and their insulation," *ELECTRA*, pp. 65–71, Dec 1990.

[9] J. Singh, Y. R. Sood, and R. K. Jarial, "Condition monitoring of power transformers - bibliography survey," *IEEE Electrical Insulation Magazine*, vol. 24, pp. 11–25, May/June 2008.

[10] S. D. J. McArthur, S. M. Strachan, and G. Jahn, "The design of a multi-agent transformer condition monitoring system," *IEEE Transaction on Power Systems*, vol. 19, no. 4, p. 18451852, 2004.

[11] T. K. Saha, "Review of modern diagnostics techniques for assessing insulation condition in aged transformer," *IEEE Transactions on Power Delivery*, vol. 10, no. 15, pp. 903–917, 2003.

[12] Y. Han and Y. H. Song, "Condition monitoring techniques for electrical equipment-a literature survey," *IEEE Transactions on Power Delivery*, vol. 18, no. 1, pp. 4–13, 2003.

[13] Y. C. Huang, "Condition assessment of power transformers using genetic-based neural networks," *IEE Proceedings on Science, Measurement and Technology*, vol. 150, no. 1, pp. 19–24, 2003.

[14] H. Y. Chang and H. C. Ming, "Evolving wavelet networks for power transformer condition monitoring," *IEEE Transactions on Power Delivery*, vol. 17, no. 2, pp. 412–416, 2002.

[15] H. Yang, C. C. Liao, and J. H. Chou, "Fuzzy learning vector quantization networks for power transformer condition assessment," *IEEE Transactions on Dielectrics and Electrical Insulation*, vol. 8, no. 1, pp. 143–149, 2001.

[16] J. Fuhr and T. Aschwanden, "Experience with diagnostic tools for condition assessment of large power transformers," *Conference Record; IEEE International Symposium on Electrical Insulation, 2004*, pp. 508–511, 2004.

[17] T. Leibfried, "Online monitors keep transformers in service," *IEEE Computer Applications in Power*, pp. 36–42, July 1998.

[18] M. D. Judd, S. D. J. McArthur, J. McDonald, and O. Farish, "Intelligent condition monitoring and asset management, partial discharge monitoring for power transformer," *Power Engineering Journal*, pp. 297–304, Dec 2002.

[19] D. Lin, L. Jiang, F. Li, D. Zhu, K. Tan, C. Wang, X. Jin, T. Cheng, and C. Wu, "A novel on-line PD monitoring and diagnostic system for power transformers," *Annual Report Conference on Electrical Insulation and Dielectric Phenomena*, pp. 748–751, 2002.

[20] A. S. Kumar, R. Gupta1, K. Udayakumar, and A.Venkatasami1, "Online partial discharge detection and location techniques for condition monitoring of power transformers: a review," *International Conference on Condition Monitoring and Diagnosis, CMD 2008, Beijing, China*, pp. 927–931, 21-24 April 2008.

[21] B. H. Ward, "A survey of new techniques in insulation monitoring of power transformers," *IEEE Electrical Insulation Magazine*, vol. 17, pp. 16–23, July 2001.

[22] R. Schwarz, M. Muhr, and S. Pack, "Partial discharge detection in oil with optical methods," *IEEE International Conference on Dielectric Liquids 2005. ICDL 2005.*, pp. 245–248, July 2005.

[23] A. Wang, Y. Liu, and P. Duncan, "Optical fiber acoustic sensors for inside-transformer on-line detection of partial discharges," *EPRI Internal Report*, April 2000.

[24] S. Fujita, N. Hosokawa, and Y. Shibuya, "Experimental investigation of high frequency voltage oscillation in transformer windings," *IEEE Transaction on Power Delivery*, vol. 13, pp. 1201–1207, Oct 1998.

[25] M. Judd, L. Yang, and I. Hunter, "Partial discharge monitoring of power transformers using UHF sensors. Part 1: sensors and signal interpretation," *IEEE Electrical Insulation Magazine*, vol. 21, no. 2, pp. 5–14, 2005.

[26] M. Judd, L. Yang, and I. Hunter, "Partial discharge monitoring for power transformer using UHF sensors. Part 2: field experience," *IEEE Electrical Insulation Magazine*, vol. 21, no. 3, pp. 5–13, 2005.

[27] C. Zhou, D. M. Hepburn, X. Song, and M. Michel, "Application of denoising techniques to PD measurement utilising UHF, HFCT, acoustic sensors and IEC60270," *2009 20th International Conference and Exhibition on Electricity Distribution, Prague*, vol. Paper 0260, pp. 1–4, 8-11 June 2009.

[28] C. Zhou, D. M. Hepburn, X. Song, and M. Michel, "Application of combined PD sensor for GIS PD detection and condition monitoring," *International Conference on Condition Monitoring and Diagnosis, Beijing, China, CMD 2008*, pp. 456–460, 21-24 April 2008.

[29] S. Birlasekaran and W. H. Leong, "Comparison of Known PD Signals With the Developed and Commercial HFCT Sensors," *IEEE Transactions on Power Delivery*, vol. 22, no. 3, pp. 1581–1590, 2007.

[30] S. H. Lee, S. Y. Jung, and B. W. Lee, "Partial discharge measurements of cryogenic dielectric materials in an HTS transformer using HFCT," *IEEE Transactions on Applied Superconductivity*, vol. PP, no. 99, pp. 1–1, 2010.

[31] IPEC Limited, "High Frequency Current Transducer," *IPEC ASM Solution*, July 2010.

[32] A. O. Soysal and A. Semlyen, "Practical transfer function estimation and its application to wide frequency range representation of transformers," *IEEE Transactions on Power Delivery*, vol. 8, pp. 1627–1637, July 2001.

[33] C. C. Brozio and H. J. Vermeulen, "Wideband equivalent circuit modelling and parameter estimation methodology for two-winding transfomers," *IEE Proceedings on Generation, Transmission and Distribution*, vol. 150, pp. 487–492, July 2003.

[34] A. Keyhani, S. W. Chua, and S. A. Sebo, "Maximum likelihood estimation of transformer high frequency parameters from test data," *IEEE Transaction on Power Delivery*, vol. 6, pp. 858–865, April 1991.

[35] D. J. Wilcox, M. Conlon, and W. G. Hurley, "Calculation of self and mutual impedance for coils on ferromagnetic cores," *IEE Proceedings of Science, Measurement and Technology*, vol. 135, pp. 470–476, September 1988.

[36] D. J. Wilcox, W. G. Hurley, T. P. McHale, and M. Conlon, "Calculation of self and mutual impedances between sections of transformer windings," *IEE Proceedings-Generation, Transmission and Distribution*, vol. 136, pp. 308–314, September 1989.

[37] D. J. Wilcox, W. G. Hurley, T. P. McHale, and M. Conlon, "Application of modified modal theory in the modelling of practical transformers," *IEE Proceedings-Generation, Transmission and Distribution*, vol. 139, Nov 1992.

[38] W. G. Hurley and D. J. Wilcox, "Calculation of leakage inductance in transformer windings," *IEEE Transaction on Power Electronics*, vol. 9, no. 1, pp. 121–126, 1994.

[39] A. Keyhani, H. Tsai, and S. Sebo, "Modelling and parameter estimation of power transformers for the study of high frequency system transients," *Proceedings of the 32nd Midwest Symposium on Circuits and Systems*, vol. 1, pp. 258–264, August 1989.

[40] J. Pleite, E. Olas, A. Barrado, A. Lzaro, and J. Vzquez, "Transformer modeling for FRA techniques," *IEEE/PES*, vol. 1, pp. 317–321, Oct 2002.

[41] S. M. Islam, "Detection of shorted turns and winding movements in large power transformers using frequency response analysis," *IEEE Power Society*, vol. 3, pp. 2233–2238, 2000.

[42] M. Wang, A. J. Vandermaar, and K. D. Srivastava, "Improved detection of power transformer winding movement by extending the FRA high frequency range," *IEEE Transaction on Power Delivery*, vol. 3, pp. 1930–1938, July 2005.

[43] E. Rahimpour, J. Christian, K. Feser, and H. Mohseni, "Transfer function method to diagnose axial displacement and radial deformation of transformer windings," *IEEE Transactions on Power Delivery*, vol. 18, pp. 493–505, April 2003.

[44] L. V. Bewley, *Traveling Waves on Transmission Systems*. 180 Varick Street, New York 14, N.Y: Dover Publication, Inc, 2nd edition ed., 1951.

[45] K. Karsai, D. Kerenyi, and L. Kiss, *Large Power Transformer*. Elsevier Science Ltd, Nov 1987.

[46] K. Pedersen, M. E. Lunow, J. Holboell, and M. Henriksen, "Detailed high frequency models of various winding types in power transformers," *International Conference on Power Systems Transients (IPST05), Montreal, Canada*, vol. Paper No. IPST05-100, 19-23 June 2005.

[47] A. D. Podoltsev, I. N. Kucheryavaya, and B. B. Lebedev, "Analysis of effective resistance and eddy-current losses in multiturn winding of high-frequency magnetic components," *IEEE Transactions on Magnetics*, vol. 39, pp. 539–548, Jan 2003.

[48] Y. Shibuya and S. Fujita, "High frequency model of transformer winding," *Electrical Engineering in Japan*, vol. 146, no. 3, pp. 8–16, 2004.

[49] E. Bjerkan and H. K. Hidalen, "High frequency FEM-based power transformer modeling: Investigation of internal stresses due to network-initiated overvoltages," *International Conference on Power Systems Transients (IPST05), Montreal, Canada*, vol. Paper No. IPST05-106, 19-23 June 2005.

[50] P. T. M. Vaessen, "Transformer model for high frequencies," *IEEE Transaction on Power Delivery*, vol. 3, pp. 1761–1768, Oct 1988.

[51] A. Morched, L. Marti, and J. Ottevangers, "A high frequency transformer model for the EMTP," *IEEE Transactions on Power Delivery*, vol. 8, pp. 1615–1626, July 1993.

[52] O. Moreau, P. Guuinic, R. Dorr, and Q. Su, "Comparison between the high frequency characteristics of transformer interleaved and ordinary disk windings," *IEEE Power Engineering Society Winter Meeting, 2000*, vol. 3, pp. 2187 – 2192, 23-27 Jan 2000.

[53] C. Koley, P. Purkait, and S. Chakravorti, "Time-frequency representation of resistance for modelling of transformer winding under impulse test," *IEEE Transactions on Power Delivery*, vol. 21, pp. 1367–1374, July 2006.

[54] S. Chimklai and J. R. Marti, "Simplified three-phase transformer model for electromagnetic transient studies," *IEEE Transaction on Power Delivery*, vol. 10, pp. 1316–1325, July 1995.

[55] L. V. Bewley, "Transient oscillations in distributed circuits with special reference to transformer windings," *Transactions of the American Institute of Electrical Engineers*, vol. 50, pp. 1215–1233, December 1931.

[56] S. M. Islam and G. Ledwich, "Locating transformer faults through sensitivity analysis of high frequency modeling using transfer function approach," *Conference Record of the 1996 IEEE International Symposium on Electrical Insulation*, vol. 1, pp. 38 – 41, June 1996.

[57] A. Keyhani, H. Tsai, and A. Abur, "Maximum likelihood estimation of high frequency machine and transformer winding parameters," *IEEE Transaction on Power Delivery*, vol. 5, pp. 212–219, January 1990.

[58] A. Akbari, P. Werle, H. Borsi, and E. Gockenbach, "A continuous parameter high frequency model based on travelling waves for transformer diagnostic purposes,"

Conference Record of the 2002 IEEE International Symposium on Electrical Insulation, pp. 154–157, April 7-10 2002.

[59] L. Fangcheng, L. Yunpeng, L. Lei, and L. Chengrong, "Pulse propagation model of partial discharge in transformer winding," *Proceedings of 2005 International Symposium on Electrical Insulating Materials*, pp. 729–732, June 5-9 Kitakyushu, Japan, 2005.

[60] D. J. Wilcox and M. Condon, "Time-domain model for multiconductor power transmission lines," *IEE Proc.-Gener. Transm. Distrib*, vol. 145, pp. 473–479, July 1998.

[61] K. Pedersen, M. E. Lunow, J. Holboell, and M. Henriksen, "A hybrid transformer model for determination of partial discharge location in transformer winding," *IEEE Transactions on Dielectrics and Electrical Insulation*, vol. 14, pp. 436–443, April 2007.

[62] G. B. Gharehpetian, H. Mohseni, and K. Moller, "Hybrid modelling of inhomogeneous transformer winding for very fast transient overvoltage studies," *IEEE Transaction on Power Delivery*, vol. 13, pp. 157–163, Jan 1998.

[63] D. F. Leon and A. Semlyen, "Complete transformer model for electromagnetic transients," *IEEE Transaction on Power Delivery*, vol. 9, pp. 231–239, Jan 1994.

[64] S. Markalous, S. Tenbohlen, and K. Feser, "Detection and location of partial discharges in power transformers using acoustic and electromagnetic signals," *IEEE Transactions on Dielectrics and Electrical Insulation*, vol. 15, pp. 1576–1583, December 2008.

[65] S. Markalous and T. Strehl, "New approaches in arrival time-based PD location in transformers," *IEEE Conference on Electrical Insulation and Dielectric Phenomena, Kansas City*, pp. 652–655, Oct 2006.

[66] L. Yang, M. Judd, and G. Costa, "Simulating Propagation of UHF Signals for PD Monitoring in Transformers Using the Finite Difference Time Domain Technique," *Conference on Electrical Insulation and Dielectric Phenomena, CEIDP 2004*, pp. 410–413, 2004.

[67] L. Lundgaard, "Partial discharge. XIV. acoustic partial discharge detection-practical application," *IEEE Electrical Insulation Magazine*, vol. 8, pp. 34 – 43, Sept.-Oct. 1992.

[68] P. Eleftherion, "Partial discharge. XXI. acoustic emission based pd source location in transformers," *IEEE Electrical Insulation Magazine*, vol. 11, pp. 22 – 26, Nov.-Dec 1995.

[69] J. Fuhr, "PD-Source Localization in the Insulating System of Large Power Transformers," *IEEE International Symposium on Electrical Insulation 2006*, pp. 424–427, June 2006.

[70] J. Fuhr, "Procedure for identification and localization of dangerous PD sources in power transformers," *IEEE Transaction on Dielectrics and Electrical Insulation*, vol. 12, pp. 1005–1014, October 2005.

[71] A. Akbari, P. Werle, P. Borsi, and E. Gockenbach, "Transfer function based partial discharge localization in power transformer: A feasibility study," *IEEE Electrical Insulation Magazine*, vol. 18, pp. 22–32, Sept/Oct 2002.

[72] E. Gockenbach, "Partial discharge detection and localization in power transformers," *Conference on Electrical Insulation and Dielectric Phenomena*, pp. 466–469, October 2004.

[73] A. Akbari, P. Werle, H. Borsi, and E. Gockenbach, "High Frequency Transformer Model For Computation of Sectional Winding Transfer Functions Used For Partial Discharge Localisation," *12th International Symposium on High Voltage Engineering (ISH)*, Bangalore, India 2001.

[74] M. Naderi, M. Vakilian, T. Blackburn, B. Phung, and H. Zhang, "A method for studying partial discharges location and propagation within power transformer winding based on the structural data," *International Symposium on Electrical Insulating Materials*, vol. 2, pp. 490–493, 5-9 June 2005.

[75] S. Hettiwatte, Z. Wang, and P. Crossley, "Investigation of propagation of partial discharges in power transformers and techniques for locating the discharge," *EE Proceedings, Science, Measurement and Technology*, vol. 152, pp. 25–30, Jan 2005.

[76] Z. Wang, S. Hettiwatte, and P. Crossley, "A measurements-based discharge location algorithm for plain disc winding power transformers," *IEEE Transactions on Dielectrics and Electrical Insulation*, vol. 12, pp. 416–422, June 2005.

[77] S. Hettiwatte, P. Crossley, Z. Wang, A. Darwin, and G. Edwards, "Simulation of a transformer winding for partial discharge propagation studies," *IEEE Power Engineering Society Winter Meeting*, vol. 2, pp. 1394–1399, 27-31 Jan 2002.

[78] M. Naderi, M. Vakilian, T. Blackburn, B. P. H. Nam, and R. Ghaemmaghami, "Simulation of partial discharge propagation and location in Abetti winding based on structural data," *The 7th International Power Engineering Conference, IPEC 2005*, 29 Nov -2 Dec 2005.

[79] Z. Wang, P. Crossley, and K. Cornick, "Partial discharge location in power transformers using the spectra of the terminal current signals," *Eleventh International Symposium on High Voltage Engineering*, vol. 5, pp. 58 – 61, 23-27 Aug 1999.

[80] R. E. James, B. T. Phung, and Q. Su, "Application of digital filtering techniques to the determination of partial discharge location in transformers," *IEEE Transaction on Electrical Insulation*, vol. 24, pp. 657–668, August, 1989.

[81] H. Tatizawa and G. F. Burani, "Analysis and location of partial discharges in power transformers by means of electrical methods," *16th International Conference and Exhibition on Electricity Distribution*, vol. 1, p. 4, 18-21 Jun 2001.

[82] Z. Wang, P. Crosley, K. Cornick, D. Zhu, A. Shields, and I. Kemp, "Partial discharge location in power transformers," *IEE Proceedings on Science, Measurement and Technology*, vol. 147, pp. 249 – 255, Sep 2000.

[83] M. Eldery, T. Abdel-Galil, E. El-Saadany, and M. Salama, "Identification of partial discharge locations in transformer winding using PSD estimation," *IEEE Transactions on Power Delivery*, vol. 21, pp. 1022 – 1023, April 2006.

[84] D. Wenzel, H. Borsi, and E. Gockenbach, "A new method of partial discharge localization on transformers via the karhunen-loeve-transform," *International Conference on Properties and Applications of Dielectric Materials*, vol. 2, pp. 622–625, July 1994.

[85] J. Martinez, R. Walling, B. Mork, J. Martin-Arnedo, and D. Durbak, "Parameter Determination for Modelling System Transients - Part III: Transformers," *IEEE Transactions on Power Delivery*, vol. 20, pp. 2051–2062, July 2005.

[86] E. C. Levy, "Complex curve fitting," *IRE Transaction on Automatic Control*, vol. AC, pp. 37–44, May 1959.

[87] C. K. Sanathanan and J. Koerner, "Transfer function systhesis as a ratio of two complex polynomials," *IEEE Transaction on Automatic Control*, vol. 8, pp. 56–58, Jan 1963.

[88] P. A. Payne, "An improved technique for transfer function systhesis from frequency response data," *IEEE Transaction on Automatic Control*, vol. 15, pp. 480–483, Aug 1970.

[89] P. Guillaume, R. Pintelon, and J. Schoukens, "Robust parametric transfer function estimation using complex logarithmic frequency response data," *IEEE Transactions on Automatic Control*, vol. 40, pp. 1180–1190, July 1995.

[90] A. Banos and F. Gomez, "Parametric identification of transfer functions from frequency response data," *Computing and Control Engineering Journal*, vol. 6, pp. 137–144, June 1995.

[91] P. Stoica and T. Sundin, "Transfer function estimation using elemental sets," *IEEE Transactions on Power Delivery*, vol. 6, pp. 269 – 272, Oct 1999.

[92] S. M. Islam, K. M. Coates, and G. Ledwich, "Identification of high frequency transformer equivalent circuit using matlab from frequency domain data," *Industry Applications Conference, 1997. Thirty-Second IAS Annual Meeting, IAS '97*, vol. 1, pp. 357–364, Oct 1997.

[93] A. Keyhani, S. Pilltla, and A. Abur, "Identification of high frequency transformer model parameters," *Electric Power Systems Research*, vol. 42, pp. 127–133, 1997.

[94] H. Akcay, S. M. Islam, and B. Ninness, "Subspace-based identification of power transformer models from frequency response data," *IEEE Transactions on Instrumentation and Measurement*, vol. 48, pp. 700–704, June 1999.

[95] G. M. V. Zambrano, A. C. Ferreira, and L. P. Caloba, "Power transformer equivalent circuit identification by artificial neural network using frequency response analysis," *IEEE Power Engineering Society General Meeting 2006*, p. 6, 18-22 June 2006.

[96] G. J. Burke, E. K. Miller, S. Chakrabarti, and K. Demarest, "Using model-based parameter estimation to increase the efficiency of computing electromagnetic transfer functions," *IEEE Transactions on Magnetics*, vol. 25, pp. 2807–2809, July 1989.

[97] B. Gustavsen and A. Semlyen, "Rational approximation of frequency domain responses by vector fitting," *IEEE Transaction on Power Delivery*, vol. 14, pp. 1052–1061, July 1999.

[98] A. Semlyen and B. Gustavsen, "Vector fitting by pole relocation for the state equation approximation of nonrational transfer matrices," *Circuits Systems Signal Process*, vol. 19, no. 6, pp. 549–566, 2000.

[99] B. Gustavsen, "Improving the pole relocating properties of vector fitting," *IEEE Transaction on Power Delivery*, vol. 21, pp. 1587–1592, July 2006.

[100] B. Gustavsen, "Computer code for rational approximation of frequency dependent admittance matrices," *IEEE Transaction on Power Delivery*, vol. 17, pp. 1093–1098, Oct 2002.

[101] L. V. Bewley, "Equivalent circuits of transformers and reactors to switching surges," *Transactions of the American Institute of Electrical Engineers*, vol. 58, pp. 797–802, December 1939.

[102] B. Han, *Partial Discharge Monitoring of Power Transformer*. Doctor of philosophy, School of Electrical and Computer Science, University of Southampton, School of Electrical and Computer Science, SO17 1BJ, Jan 2004.

[103] L. V. Bewley, "Travelling waves initiated by switching," *Transactions of the American Institute of Electrical Engineers*, vol. 58, pp. 18–27, January 1939.

[104] L. V. Bewley, "Transient oscillations of mutually coupled windings," *Transactions of the American Institute of Electrical Engineers*, vol. 51, pp. 299–308, June 1932.

[105] D. J. Wilcox, M. Condon, D. Leonard, and T. McHale, "Time domain modelling of power transformers using modal analysis," *IEE Proceedings - Electric Power Applications*, vol. 144, pp. 77–84, Mar 1997.

[106] L. Bewley, J. H. Hagenguth, and F. R. Jackson, "Methods of determining natural frequencies in coils and windings," *Transactions of the American Institute of Electrical Engineers*, vol. 60, pp. 1145–1150., March 1941.

[107] A. Tanskanen, "Transmission line modelling using wave equation standing-wave solutions as basis functions," *European Conference on Circuit Theory and Design, 2007, ECCTD 2007, 18th*, pp. 659 – 662, 2007.

[108] S. Farlow, *Partial Differential Equation for Scientist and Engineers.* John Wiley & Sons, New York, 1993.

[109] N. Huang and S. Shen, *Hilbert-Huang Transform and Its Applications.* 5 Toh Tuck Link, Singapore 596224, World Scientific Publishing Company, 30 Oct 2005.

[110] K. Dutton, S. Thompson, and B. Barraclough, *The Art of Control Engineering.* Prentice Hall, 1997.